Surface enhanced Raman scattering (SERS) bioimaging of complex 3D cellular systems

PhD thesis
Elisa Lenzi

Supervised by: Professor Luis Liz-Marzán and
Dr. Dorleta Jiménez de Aberasturi

Donostia - San Sebastián, 2022

eman ta zabal zazu
Universidad del País Vasco
Euskal Herriko Unibertsitatea

Surface enhanced Raman scattering (SERS) bioimaging of complex 3D cellular systems

A manuscript submitted to the University of the Basque Country

For the degree of doctor in sciences

Presented by **Elisa Lenzi**

Under the supervision of:

Luis Manuel Liz Marzán (Bionanoplasmonic Lab/CIC Biomagune)

Dorleta Jiménez de Aberasturi (Bionanoplasmonic Lab/CIC Biomagune)

San Sebastián - Donostia, 2022

CIC biomaGUNE
MEMBER OF BASQUE RESEARCH & TECHNOLOGY ALLIANCE

eman ta zabal zazu
Universidad del País Vasco
Euskal Herriko Unibertsitatea

Resumen

Esta tesis se ha centrado en la optimización de la dispersión Raman mejorada en superficie (SERS), como técnica de bioimagen para el estudio cultivos celulares tridimensionales (3D) como modelos de tumores. Para esta técnica, es necesario emplear como agentes de contraste nanopartículas (NPs) de oro codificadas con moléculas activas en SERS (o etiquetas SERS). Una vez diseñadas y sintetizadas, se ha planteado el estudio de la interacción de estas etiquetas SERS con diferentes células cancerígenas, así como su evolución en el tiempo, con el objetivo de optimizar la tomografía SERS como método emergente de bioimagen, que puede aportar información complementaria a las técnicas comúnmente utilizadas. Las principales ventajas de SERS sobre la que probablemente es la técnica más utilizada, la microscopía de fluorescencia, incluyen la posibilidad de multiplexado y la estabilidad a largo plazo de la señal, permitiendo así obtener imágenes más detalladas del sistema biológico y durante periodos de tiempo más largos. El uso de nano-etiquetas para la obtención de imágenes es cada vez más popular, debido a que no solo se pueden aplicar para la observación de células individuales, sino también para investigar en detalle las características de la formación de tumores y la dinámica de los procesos metastásicos en el microentorno natural. En este contexto, en comparación con otras modalidades de bioimagen, las imágenes SERS ofrecen biocompatibilidad (ausencia de toxicidad), alta especificidad y sensibilidad, así como capacidad de multiplexado.

Esta tesis se ha realizado en el marco de un proyecto europeo ERC Advanced Grant 4DBIOSERS (n° 787510), cuyo objetivo es el desarrollo de andamios celulares plasmónicos tridimensionales. Dichos andamios proporcionan un soporte para el crecimiento de tumores de cáncer de mama de forma realista, de forma que se puedan estudiar la evolución y la dinámica de las diferentes células que los componen. Mediante la incorporación de nanopartículas de oro en la estructura de los andamios de soporte, es posible asimismo monitorizar en tiempo real la liberación de biomarcadores tumorales relevantes. Esta tesis se ha estructurado por tanto en torno a tres objetivos principales: I) síntesis y caracterización de etiquetas SERS con características ópticas adecuadas y evaluación de su rendimiento en imagen SERS; II) estudio de la interacción de las etiquetas SERS con células tumorales; III) optimización de los parámetros de medida de bioimagen por SERS en modelos celulares 3D.

A continuación se presenta un breve resumen de cada uno de los capítulos en los que se estructura la tesis.

En el **Capítulo 1** se presenta una introducción general de los principales aspectos biológicos, técnicos y analíticos necesarios para comprender la descripción del trabajo. En concreto, se explican los principios básicos de la técnica SERS y las características que hacen que esté recibiendo cada vez más atención de cara a aplicaciones biológicas y médicas. Las principales

ventajas del SERS radican en su alta sensibilidad, obteniendo límites de detección bajos que permiten alcanzar incluso concentraciones atomolares, y su especificidad molecular basada en las características vibracionales (huella molecular) de cada molécula. La técnica está basada en la espectroscopia Raman, que consiste en la dispersión inelástica de la luz incidente, pero a diferencia de esta última, SERS es mucho más sensible pudiendo llegar a detectar incluso moléculas individuales gracias a una muy elevada amplificación de la señal Raman. En la bibliografía se pueden encontrar valores de amplificación de la señal SERS hasta en una magnitud de 10^{10}-10^{11} veces la dispersión Raman normal. Se han identificado dos mecanismos como los principales responsables de dicha mejora de la señal Raman: el mecanismo de amplificación electromagnética (en inglés electromagnetic enhancement mechanism, EEM) y el mecanismo de amplificación química (chemical enhancement mechanism, CEM). El primero se produce como resultado de la amplificación de la luz por excitación de resonancias plasmónicas superficiales localizadas (LSPR) en nanomateriales plasmónicos, mientras que el segundo mecanismo implica procesos de transferencia de carga, es decir, cuando la luz incidente entra en resonancia con algún estado electrónico se puede producir la transferencia de carga entre el metal y la molécula. Sin embargo, se ha aceptado de forma general que la principal contribución a la mayoría de los procesos SERS es debida al EEM. En este mecanismo, cuando se irradia con una luz incidente adecuada una molécula que se encuentra adsorbida o cerca de la superficie de una partícula plasmónica, el campo electromagnético local amplificado, generado por una LSPR, interactúa con los modos vibracionales de la molécula produciendo una dispersión Raman. En consecuencia, la señal dispersada se potencia y cuando tanto el campo incidente como la señal Raman dispersada están en resonancia con la frecuencia del plasmón, el factor de amplificación (EF) de la señal SERS es proporcional a $|E|^4$, donde E es el aumento del campo en la superficie de la nanopartícula. Esto permite obtener una espectroscopia vibracional ultrasensible que resulta de especial utilidad en aplicaciones como la obtención de imágenes y la detección de analitos en experimentos biológicos, en los que otras técnicas no invasivas no son capaces de proporcionar información del sistema a largo plazo.

En esta tesis, se ha planteado el uso de SERS como técnica de imagen para el análisis e interpretación de modelos celulares tumorales en 3D. Según las estadísticas mundiales, el cáncer se ha convertido en uno de los problemas más graves que afectan directamente a la salud pública y por ello es imprescindible llevar a cabo investigación dirigida al desarrollo de métodos de diagnóstico precoz y terapias más eficaces. El cáncer se define como un proceso de crecimiento celular irregular que da lugar a aglomerados de células, que son capaces de invadir tejidos o de desplazarse a otros lugares del cuerpo para formar nuevos tumores mediante el proceso denominado de metástasis. Se ha demostrado que ciertas variaciones producidas en el microambiente tumoral pueden afectar en gran medida a la forma en la que los tumores crecen y se extienden. El microambiente tumoral, formado por células no

malignas y otros componentes no celulares conocidos como matriz extracelular (ECM). Esta última desempeña funciones vitales en los procesos biológicos, ya que proporciona un soporte a las células, un anclaje para la adhesión celular, un depósito de agua y diferentes factores de crecimiento, además de facilitar la señalización intracelular.

Uno de los principales obstáculos de cara a encontrar una terapia para el cáncer es la gran variedad de tejidos y tipos de células que pueden verse afectados. Aunque se pueden observar algunas características comunes entre pacientes diferentes, en general es extremadamente difícil generalizar los hallazgos científicos. En particular, se ha registrado que el 90% de las muertes asociadas al cáncer se deben al proceso de metástasis del tumor original. Por este motivo, un conocimiento exhaustivo tanto de las células cancerosas como de la ECM es igualmente importante para desarrollar nuevas terapias contra el cáncer. Esta tesis se ha centrado en el cáncer de mama, que a nivel mundial resulta el más comúnmente diagnosticado en mujeres. Hasta ahora, los métodos de diagnóstico convencionales requieren una elevada cantidad de células para identificar eficazmente los rastros de cáncer, lo cual en muchos casos es inviable, por lo que es necesario desarrollar técnicas de imagen más sofisticadas. En cuanto a los modelos *in vitro*, se ha demostrado que los cultivos 3D recrean más fielmente las características morfológicas de las células, su potencial de proliferación y diferenciación y las interacciones célula-célula y célula-ECM, asimismo la transducción de señales se acerca más a la situación *in vivo* que en los cultivos tradicionales 2D. Se ha demostrado también que los sistemas 3D se caracterizan por una mayor estabilidad y una vida más larga, llegando hasta más de 3 semanas, lo cual supone un avance significativo en comparación con los cultivos 2D (menos de una semana).

En el **Capítulo 2** se presenta un método de cuantificación para evaluar la señal de una única partícula codificada (etiqueta SERS). Dichas etiquetas SERS constan de un núcleo formado por una NP de un metal noble, la cual está recubierta por una monocapa de moléculas activas en Raman (Raman reporters, RaRs), y habitualmente se recubre con otra capa protectora o revestimiento, la cual a su vez puede ser funcionalizada selectivamente con biomoléculas de reconocimiento específico. Cuando las etiquetas SERS interactúan con una fuente de luz, como un láser, dispersan una señal Raman de alta intensidad que es la huella vibracional de los RaRs colocados sobre la superficie de la nanopartícula, y por esta razón pueden utilizarse como etiquetas. Una de las dificultades que persisten, de cara a la aplicación de las etiquetas SERS en bioimagen, está relacionada con la falta de conocimiento de la señal de una única etiqueta. A pesar de las considerables mejoras logradas en la síntesis de NPs metálicas, esta incertidumbre se debe principalmente a la dificultad y complejidad de controlar los factores que influyen en la señal SERS, como por ejemplo el número de RaRs en la superficie de la NP. Por lo tanto, en una primera etapa de esta tesis se ha desarrollado una aplicación (App) denominada “SERSTEM”, que permite correlacionar mapas de imágenes SERS con imágenes de microscopía electrónica de transmisión (TEM), con el objetivo de evaluar el número de

etiquetas presentes en una zona determinada, basándose en su señal SERS. Dicha App se ha diseñado para relacionar la posición de las nanopartículas a través de imágenes de TEM con la señal SERS recogida de las mismas áreas obtenidas tras secar gotas de dispersiones coloidales de dichas etiquetas SERS. Las señales SERS se identificaron utilizando un microscopio Raman confocal, y utilizando una técnica de análisis de datos que basada en análisis por regresión lineal múltiple (MLRA). De esta manera, el análisis hace de filtro para excluir automáticamente las señales SERS que no presentan suficiente similitud con el espectro de referencia, así como el ruido de fondo. Este procedimiento nos ha permitido estimar la intensidad de la señal en uno de los picos principales de cada una de las moléculas RaR utilizadas, pudiendo así determinar la señal de SERS por partícula (SSpP). Este valor se ha utilizado asimismo para predecir el número de NPs en una región 2D, obteniendo valores en concordancia con los esperados, y que pudieron ser validados a través del número de nanopartículas contadas en TEM. Esta herramienta analítica, desarrollada para obtener el número de NPs etiquetadas en áreas determinadas de 2D, a partir de los mapas obtenidos por imagen SERS, fue optimizada también para obtener una estimación fiable del número de NPs internalizadas en células, lo cual correspondería a un volumen en 3D que se describe en el Capítulo 3.

Por lo tanto, en el trabajo descrito en el **Capítulo 3** se llevó a cabo una evaluación de la cantidad intracelular de etiquetas SERS, a partir de un análisis basado en medidas de SERS 3D de células cancerígenas de mama (MCF7) vivas. El hecho de trabajar con células vivas añade un grado de dificultad, ya que ha de evitarse cualquier posible citotoxicidad debida a una exposición excesiva al haz láser. Esta metodología se ha desarrollado con el objetivo de caracterizar de forma dinámica y en tiempo real la internalización celular de las NPs, su dilución debida a la división celular y/o la posible exocitosis de las NPs desde el interior de las células. Entre los resultados de este trabajo se incluye el seguimiento de la dilución de etiquetas SERS hacia sus células hijas durante más de dos semanas. De esta forma se ha podido corroborar la capacidad de identificación a largo plazo de estas etiquetas SERS sin que las células sufran ningún tipo de efectos de toxicidad. Durante las medidas se observó una disminución de la intensidad SERS de las etiquetas incluidas en las células a lo largo del tiempo, lo cual se analizó sobre la base de procesos de división celular y de exocitosis ya mencionados, identificando finalmente la división celular como la principal fuente de dilución de las NPs, después de 1 día *in vitro* (DIV). La cuantificación de las etiquetas SERS mediante imagen SERS en 3D, una técnica no invasiva que sin embargo está todavía en fase de desarrollo, nos permitió identificar parámetros importantes necesarios para la obtención de dichas imágenes. En particular, el largo tiempo de permanencia de las etiquetas SERS (más de 2 semanas), junto con su naturaleza no tóxica y su alta capacidad de detección multiplexada, ha confirmado que pueden ser excelentes candidatas para su uso como agentes de contraste SERS en modelos celulares 3D o *in vivo*, incluso a bajas concentraciones.

Los resultados obtenidos se utilizaron a continuación en el **Capítulo 4**, para estudiar sistemas celulares 3D cada vez más complejos, controlando todos los parámetros que puedan afectar a las bioimágenes SERS. Como un primer sistema complejo, se utilizó como soporte de cultivo un andamio celular impreso en 3D a partir de un copolímero de ácido poli(láctico–co–glicólico) (PLGA), marcado con etiquetas SERS y con moléculas poliméricas marcadas con fluoróforos, el cual facilitó el crecimiento de una capa tridimensional entrelazada de fibroblastos dermales humanos (HDF). El tejido generado, de 100 μm de espesor, se utilizó para evaluar el nivel de profundidad al que se puede llegar mediante la técnica de imagen SERS, estimando los parámetros necesarios para obtener imágenes SERS nítidas y claras, usando como fuente de irradiación un láser a 785 nm. Como elemento de control, se estudió la potencia del láser necesaria para obtener una intensidad suficientemente alta de la señal SERS sin inducir efectos de fototoxicidad debidos a las etiquetas SERS, la cual resultó ser de 30 mW, con un tiempo de integración de 0.05 s en un microscopio confocal Raman. Se estableció además que el paso espacial en las imágenes SERS que permite generar una imagen en 3D debía de ser de 5 μm^3, pudiendo así distinguir dos poblaciones celulares en un mismo volumen tridimensional mientras las células se mantienen vivas, proliferan y migran. De esta forma, se analizó una área lo suficientemente grande como para lograr una caracterización significativa de una muestra milimétrica que contiene millones de células. Por último, se verificó la estabilidad y ausencia de fotodegradación de la señal de las etiquetas SERS dentro de un entorno celular vivo, de forma que se pueden obtener imágenes del modelo celular 3D durante un período de aproximadamente 3 semanas. Tras establecer dichos parámetros de medida, se utilizó la técnica para caracterizar un modelo celular 3D más complejo donde el objetivo es recrear el entorno tumoral de un cáncer de mama. Concretamente, se utilizó un andamio basado en un hidrogel impreso en 3D y funcionalizado con NPs de oro (AuNPs) sin el recubrimiento de RaRs, a fin de utilizar dichos andamios no sólo como referencia de imagen SERS, sino también como sensores plasmónicos de metabolitos tumorales. Para caracterizar las propiedades de detección de estos andamios híbridos, se utilizó una molécula modelo, en este caso el ácido 4-mercaptobenzoico (MBA), que permitió observar una adsorción homogénea del analito por todo el andamio. De cara a la amplificación de la señal Raman de detección, se identificaron nanoparticulas de oro con forma de cilindros (AuNRs) como las más eficientes, a una concentración en la tinta de bioimpresión de $[Au^0]$ = 1 mM. En estas condiciones, se evaluó como límite de detección de la molécula de MBA 100 nM en disolución acuosa, y se pudo identificar hasta a 1500 μm de profundidad desde la superficie del andamio, que se estableció como el límite de detección de la señal SERS en la dirección (Z). Tras verificar las propiedades de detección de estas plataformas plasmónicas, se utilizó como analito un biomarcador habitualmente segregado por las células cancerígenas, en concreto la adenosina. A pesar de que fue necesario utilizar un mayor tiempo de incubación (24 horas), fue posible detectar una señal de intensidad reducida, pero suficiente para detectar la biomolécula en condiciones realistas (habituales en casos clínicos). Estos resultados indican

que sería posible de monitorizar la producción de biomarcadores relevantes a lo largo del tiempo. Por último, estos andamios basados en hidrogeles impresos en 3D se utilizaron también como soportes para el crecimiento de células cancerígenas, monitorizando la evolución del sistema mediante el uso combinado de imágenes SERS y detección de biomoléculas. Se llevaron a cabo medidas en 3D y en profundidad sobre áreas extensas de dichos sistemas, identificando así la localización espacial de las células. En concreto, se plantaron en los andamios células previamente marcadas con etiquetas SERS. Para ello se incorporaron las células marcadas en un gel biocompatible que sirve de matriz extracelular dentro del modelo 3D. De esta forma, se observó el crecimiento y la extensión de las células dentro de los andamios cargados con NPs plasmónicas. Una vez construidos, estos sistemas se usaron para determinar su capacidad para detectar, en medios celulares, la presencia de metabolitos relacionados con el cáncer mediante la comparación de la señal SERS obtenida a partir de células sanas (MCF10) y de células malignas (MCF7). Se analizaron también las medidas de SERS de células malignas tratadas y no tratadas con un fármaco anticancerígeno, concretamente Fulvestrant, para determinar el efecto del fármaco mediante la técnica de SERS. Efectivamente, se observaron cambios alrededor de los desplazamientos Raman a 960 cm^{-1} y 1227 cm^{-1}, los cuales podrían estar relacionados con la presencia de diferentes biomoléculas producidas por células sanas y malignas. Por otra parte, la presencia de dos picos con desplazamientos Raman a 751 cm^{-1} y 1001 cm^{-1} en las células tratadas con Fulvestrant, sugirió la posible detección de metabolitos relacionados con el fármaco anticancerígeno.

Aunque obviamente será necesario realizar más investigaciones, los resultados obtenidos en esta tesis han revelado un gran potencial de las técnicas analíticas relacionadas con SERS para detección y bioimagen. Tanto la metodología desarrollada para establecer los parámetros de medida como los valores obtenidos, resultarán de gran utilidad para poder analizar modelos celulares 3D y obtener una mejor comprensión de estos sistemas.

Abbreviations

1NAT	1-naphthalenethiol
2NAT	2-naphthalenethiol
2D	Two-dimensional
3D	Three-dimensional
AFM	Atomic force microscopy
Ag	Silver
AuNP	Gold nanoparticle
AuNR	Gold nanorod
AuNS	Gold nanostar
BPT	Biphenyl-4-thiol
BSA	Bovine serum albumin
BT	Benzenethiol
CA	Cluster analysis
CCD	Charge-coupled device
cDMEM	Complete DMEM
CEM	Chemical enhancement mechanism
CRM	Confocal Raman microscopy
CT	X-Ray computer tomography
DA	Discriminant analysis
DIV	Day *in vitro*
DIW	Direct ink writing
ECM	Extra cellular matrix
EEM	Electromagnetic enhancement mechanism
EF	Enhancement factor
ELISA	Enzyme-linked immunosorbent assay
EMT	Epithelial-mesenchymal transition
FBS	Fetal bovine serum
GFP	Green fluorescent protein
GLV	Grey limit value
HAMA	Methacrylated hyaluronic acid
HCA	Hierarchical clustering analysis
HDF	Human fibroblast
ICP-MS	Inductively coupled plasma mass spectroscopy
LDA	Linear discriminant analysis
LSPR	Localized surface plasmon resonance
MBA	4-Mercaptobenzoic acid
MBT	4-Methylbenzenethiol

ML	Machine learning
MLRA	Multiple linear regression analysis
MRI	Magnetic resonance imaging
NIR	Near infrared
NIR-I	First biologically transparency window
NIR-II	Second biologically transparency window
NIR-III	Third biologically transparency window
NP	Nanoparticle
PA	Poly-L-arginine hydrochloride
PAc	Photoacoustic
PCA	Principal component analysis
PCR	Principal component regression
PDMS	Polydimethylsiloxane
PEG	O-[2-(3-mercaptopropionylamino)ethyl]-O'-methylpolyethylene glycol
PEGDA	Poly(ethylene glycol) diacrylate
PET	Positron emission tomography
PLGA	Poly(D,L-lactide-co-glycolide)
PLS	Partial least square
PMA	Dodecylamine/polyisobutylene-alt-maleic anhydride
PTT	Photothermal therapy
RaR	Raman active molecule
RFP	Red fluorescent protein
SA	Supervised analysis
SEM	Scanning electron microscopy
SERRS	Surface-enhanced resonance Raman scattering
SERS	Surface-enhanced Raman scattering
SHERS	Surface-enhanced hyper Raman scattering
SORS	Spatially offset Raman spectroscopy
SSpP	SERS signal per particle
SVM	Support vector machines
TCA	True component analysis
TECARS	Tip-enhanced coherent anit-Stokes Raman spectroscopy
TEM	Transmission electron microscopy
TERS	Tip-enhanced Raman spectroscopy
UV-Vis	Ultraviolet/Visible

Aims and scope

This thesis has been focused on Surface-Enhanced Raman Scattering (SERS) as a bioimaging technique, in particular for the observation of three-dimensional (3D) biological systems of tumorous cells. For this technique, we employed SERS-encoded nanoparticles (or SERS tags) as contrast agents. We thus studied the interaction of SERS tags with cancer cells, highlighting their application for the study of novel 3D cell cultures, and aiming at the optimization of SERS tomography as an emerging bioimaging method. In particular, breast cancer was chosen as a cellular model considering that it is readily accessible by optical methods.[1] This thesis has been carried out in the framework of the ERC Advanced Grant 4DBIOSERS (n° 787510), which aims at the development of novel nanocomposite 3D plasmonic scaffolds that support tissue growth to acquire a better understanding of tumour evolution and dynamics, monitoring in real time its progression and the release of relevant tumour biomarkers. The thesis was structured into three main tasks: I) synthesis and characterization of SERS tags with tailored optical features and evaluation of their SERS performance; II) study of the interaction of SERS tags with cells; III) optimization of SERS measurement parameters in 3D cell models.

In what follows, a brief outline is presented for each chapter in which the thesis is structured. After a general introduction (**Chapter 1**), where the main aspects of the biological, technical and analytical backgrounds are introduced, a quantification method is presented to evaluate the number of SERS tags, based on their SERS signal (**Chapter 2**). This methodology was then used to analyse the data acquired in each of the subsequent studies. This analytical tool, initially developed for two-dimensional (2D) SERS mapping, was then optimized for the observation of 3D systems. Described in **Chapter 3** is an investigation of the interaction between SERS tags and cells, where the main objective was the identification of measurement parameters required for live-cell imaging of single cells, thereby paving the way for a quantitative characterization of the uptake of nanoparticles by cells, in 3D. Finally, in **Chapter 4** the measurement parameters required for 3D imaging of large complex cellular models have been optimized.

1. Introduction

Contents

1.1 Cancer: unresolved medical issues

Cancer is one of the main causes of death worldwide. The incidence and mortality of cancer are increasing every year. According to global cancer statistics, 19.3 million new cases were diagnosed in 2020 and 10 million deaths were associated to cancer. [2] Therefore, cancer has become one of the most serious problems which affect directly public health and it motivates research to improve early diagnosis and efficient therapies, thus involving not only biomedical sciences but also indirectly related disciplines such as physics and engineering. Current therapies for cancer treatment include surgery, chemotherapy, radiotherapy, targeted therapy and immunotherapy. Although great advances have been achieved, especially in the field of targeted and immune therapies, the highest death rate is still related to tumour recurrence and cancer spreading throughout the body after systemic antitumoral treatments. [3]

With more than 100 known variants, cancer represents a group of diseases which involve the abnormal growth of cells with the potential of invading or colonizing healthy cells or parts of the body. This irregular growth process gives rise to lumps of tissue, called tumours which can be cancerous (malignant) or benign depending on their rate of growth and spreading.[4] Whereas benign tumours tend to grow slowly and not spread, malignant tumours can invade nearby tissues or travel to distant places in the body to from new tumours through the process called metastasis. The related metastatic cancer cells present some of the molecular features of the original cancer cells, such as the presence of specific chromosomic changes. In fact, cancer is caused by one or more abnormalities of genes that control the way in which the cells function, especially how they grow and divide.

The different types of cancer are usually called by a name related to the organs or tissues where they formed. Carcinomas are cancers that arise in epithelial cells that line bodily cavities. Sarcomas are cancers that arise in mesenchymal stem cells (multipotent stromal cells that can differentiate into a variety of cell types, such as bone cells, muscle cells, etc.) in bone, muscles, blood vessels, and other tissues. Leukaemia, lymphomas and myeloma are cancers related to blood, which arise from the bone marrow (leukaemia and multiple myelomas) or the lymphoid tissues (lymphomas). They do not need to form tumours, as they are present in the bloodstream and lymph fluid, from where they take the nutrients to survive. Brain and spinal cord tumours are named based on the type of cells in which they formed and where the tumour first formed in the central nervous system. [4] One of the major obstacles toward finding a therapy or cure for cancer is this wide variety of tissue and cell types affected, and while some common features may be observed among patients, on the whole it is extremely difficult to generalize scientific findings. Moreover, the ability of cancer cells to generate metastases and undergo invasion, migrating to other

sites of the body and changing position within the tissue is also a key aspect. In fact, about 90% of the deaths associated with cancer are due to the formation of distant metastases, far and different from the original tumour. Cancer cells are able to move from the original site by reorganizing their cytoskeleton in finger-like protrusions and attaching to other cells or the extracellular matrix, via proteins present on the outside of their membrane.[5] When reaching the vascular basement membrane, which consists of a thick layer of proteins, cells are able to cleaver and cross it, by producing certain enzymes, called matrix metalloproteinases, which are also involved in the angiogenesis formation.[6] Once in the blood flow, the cells can re-enter the tissues in other locations and give rise to the formation of new tumours. The efficiency of this reintegration is much higher than the actual metastasising process, and therefore it is still critical to differentiate between cellular spreading and metastatic development. The obstacles to the formation of secondary tumours are related to the hostile environment that cancer cells find in the new site. Differently from the initial growth, the expansion of the tumour requires a sufficient degree of oxygenation and nutrients, which can be supported only by angiogenesis.[7] Considering all these variables that affect metastatic processes, which in many cancer cases are still unknown, there is a clear need to study these cell movement processes in live tissue, and bioimaging is an excellent tool to do so.

In the earliest stages of cancer or metastasis formation, it may not always be straightforward to distinguish between normal and cancer cells. Moreover, conventional diagnostic methods, such as morphological analysis of tissues (histopathology) or magnetic resonance imaging (MRI) require highly proliferated cells to effectively identify cancer traces.[8] Consequently, more sophisticated imaging techniques are required to investigate these aspects, which would be applied to understand the cancer biology, to make specific prognosis and to design individual treatments. While macroscopic imaging techniques, such as MRI or X-ray computed tomography (CT), grant anatomical information, microscopic imaging techniques are applied not only for the localization of the tumour but also for the visualization of the production of cancer-related biomolecules (cancer biomarkers). Some examples are positron emission tomography (PET), fluorescence imaging tomography and multiphoton microscopy. Their experimental use is devoted to the study of biological processes involved in tumour growth and response to the application of therapeutic drugs.[9] In this context, the application of such imaging techniques is mainly dedicated to studies over time and *in vivo*. In particular, a huge effort has been made in applying nanotechnologies for cellular labelling. Important improvements in the production of NPs have allowed to obtain highly specific nano-tags, which can be used to label particular cellular parts or products. In this way, it is possible to recognize and label, by means of both direct and indirect procedures, cancer cells for imaging.[10] Nano-tags can be applied not only to observe single cells, but also to investigate

in depth the characteristics of tumour formation and the dynamics of metastatic processes in the natural microenvironment.[11] In this context, compared to alternative imaging modalities, SERS imaging offers no-toxicity, high specificity, sensitivity and multiplexing capability. The tuneability properties in the near-infrared (NIR) of the SERS labels, make them ideal for *in vivo* use, enhancing the image contrast by minimizing the background signal. Furthermore, the long-term stability of the signal ensures the characterisation of biological samples over long periods of time. [12] For these reasons, the SERS technique has a great potential in studying cancer progression and can lead to a better insight of the disease.

The comprehensive understanding of cancer cells and the microenvironment that supports their malignant behaviour are of equal importance toward developing novel therapeutics against cancer. It has been demonstrated that variations in the tumour microenvironment can largely affect the way in which the tumour grows and spreads.[13,14] The tumour microenvironment consists of non-malignant cells and a non-cellular component, known as the extracellular matrix (ECM) (**Figure 1.1**). The cellular component includes stromal fibroblasts, specialized mesenchymal cell types distinctive of each tumour environment, immune cells like microglia, macrophages and lymphocytes, and blood vessels with endothelial cells.[15] The ECM comprises the interstitial elements within tissue or organs, and plays vital roles for biological processes by providing architectural support, anchorage for cell adhesion, a reservoir for water and various growth factors, as well as inductions for intracellular signalling pathways. It is constituted mainly by two groups of proteins, fibrous and glycosaminoglycan proteins, which are crosslinked and distributed evenly, forming the mesh structure for tissue. The former group includes collagen, fibronectin, elastin, and laminin, while the latter consists of hyaluronic acid, chondroitin sulphate, keratan sulphate and heparan sulphate. The deregulation of the ECM is a remarkable indication of cancer, e.g., the stiffness of the ECM is influenced by the malignant cells, and in turn alters the characteristics of the cancer cells. Also, the communication between cancer cells and the ECM activate several pathways related to mechanotransduction. [16]

Generally, the reciprocal interactions of tumour cells with the ECM and cellular non-neoplastic components of the tumour microenvironment control the majority of the stages of tumorigenesis, including clonal evolution, cancer heterogeneity, epithelial–mesenchymal transition (EMT), migration, invasion, development of metastasis, neovascularization, apoptosis and chemotherapeutic drug resistance. A better understanding of these elements can be achieved by the use of cancer models, while preserving the key characteristics of the original tumour. Recent advances in 3D

platforms, such as lab-on-a-chip and microfluidic devices have allowed to better simulate the function and biology of the tumour microenvironment using 3D cellular models. [17]

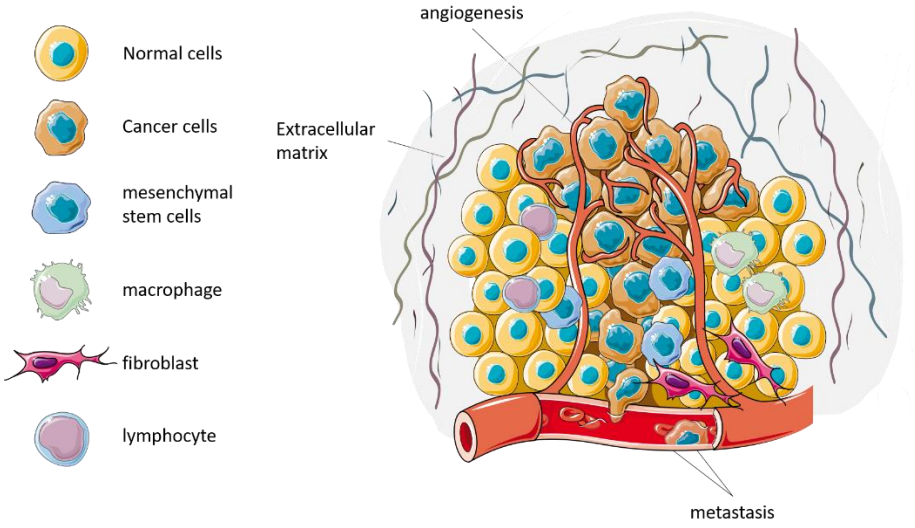

Figure 1.1 *Tumour microenvironment. The non-cancerous component includes cells called tumour stroma, such as fibroblasts and endothelial cells, as well as immune cells like macrophages and lymphocytes. They assist in angiogenesis, tumour progression and metastasis formation. The non-cellular component, namely the extracellular matrix, is formed by a network of macromolecules, mostly structural proteins, glycoproteins and proteoglycans.*

1.2 3D cellular models

Currently, two-dimensional (2D) platforms, in which a flat monolayer of cells are cultured in the presence of the necessary nutrients provided by a cell culture medium, are still the most commonly used method for cell-based assays, because it is easy, convenient and cost-effective. However, it is not a realistic imitation of the *in vivo* architecture and microenvironment, which play a key role in many processes, as mentioned above. In fact, several aspects differ from the *in vivo* situation, such as the morphological characteristics of cells, the proliferation and differentiation potential, cell-cell and cell-surrounding matrix interactions, and signal transduction. Hence, 3D cell culture systems emerge as promising approaches to overcome these issues, offering an *in vitro* cell-based assay with more physiological relevance, especially the behavioural similarity to *in vivo* cells. Indeed, cells of multicellular organisms capable of forming tissues, are arranged in 3D and include complex interactions within cell populations and between cells and their environments. An example of 3D cellular model is the spheroid, which is an agglomeration of cells realized through the liquid overlay technique (explained in **Section 1.2.1**). The formation of these cellular aggregates within the matrix or the culture medium, indicates that the model is close enough to the natural environment to induce morphological alterations.

Another important aspect that can be reproduced in 3D models is cellular heterogeneity. This concept refers to the presence of cells at various development stages, including proliferating, quiescent, apoptotic, hypoxic and necrotic cells, due to gradients of nutrients and oxygen level. This feature is typical of *in vivo* natural tissues, organs and tumours. Moreover, it has been shown that 3D cultures are characterized by a greater stability and longer lifetimes, expanding the cell confluence limitation of 2D cultures (less than a week) up to 3 weeks. Hence, these new kinds of cell cultures allow long-term experiments, such as the study of enduring effects of drugs on cellular responses.[18]

The numerous different characteristics of 3D cellular models compared with those traditional have been widely exploited in cancer research, and particularly in breast cancer. Breast cancer is the most frequently diagnosed cancer in women worldwide, with approximately 2.3 million new cases and 68,500 deaths globally in 2020. Most breast cancer-related deaths are caused by their metastasis to vital organs, which indicates the importance of early diagnosis and effective treatment. If the invasive breast cancer is located only in the breast, the 5-years survival rate of women with this disease is of 99%. However, if the cancer has spread to the regional lymph nodes, the 5-year survival rate is lower, corresponding to 86%, which drops to 28% when the cancer has spread to a distant part of the body.[19] Not only malignant cells but also stromal cells of breast cancer greatly influence the progression of the tumour by altering the cell phenotypes, secreting signalling molecules, supporting tumour invasion and modifying the tumour microenvironment. Therefore, reliable breast cancer models based on cancer cells derived from patients, surrounded by healthy cells to recreate the *in vivo* tumour microenvironment through the use of 3D cultures, are of high importance.[20] Moreover, by using such models it is possible to study the processes of migration and dissemination toward adjacent tissues, which extend over long periods of time. Several works have been reported, on the development of 3D *ex vivo* platforms for the screening of therapeutic compounds.[21–26] Another application of 3D cellular models of breast cancer cells is the assessment of tumour tissue response to agents that mitigate or treat injury, such as radiation-induced fibrosis. [27]

1.2.1 Types of 3D cellular cultures

Among the wide range of 3D cell cultures, we can distinguish multicellular spheroid formation (liquid overlay culture and hanging drop method), hydrogel-based cultures, bioreactor-based cultures, scaffold-based and bio-printed cultures

The liquid overlay culture is the simplest one, created using inert substrates, such as agarose or a protein based biocompatible gel (such as Matrigel or Geltrex), which promote support and cellular aggregation, preventing the cells to adhere on the surface of the

container. It should be noted however, that the number and size of the formed spheroids are difficult to monitor (**Figure 1.2A**).

The hanging drop method, which started as non-dripping drops process of well-defined cellular seeding density, has been improved by using bioassay dishes where the cells are forced to accumulate at their round bottoms. The technique is very simple and exceedingly reproducible in generating tightly packed spheroids with a highly organized structure together with their produced ECM. The main drawbacks are the limited volume of the cell suspension and the procedure for changing the culture medium (**Figure 1.2B**).

Hydrogels are networks of cross-linked hydrophilic polymeric material, which can be both synthetic and natural (such as collagen and alginate), with a high-water content. They exhibit a soft tissue-like stiffness, with mechanical properties resembling a natural ECM. It is also possible to integrate hydrogels with other cell culture models, like cell spheroid cultures, scaffold-based cell cultures and microchip-based cell cultures, to improve the delivery of soluble or signalling molecules. However, the disadvantages of hydrogels are related to the uncertainty and complexity in composition, which is influenced by pH-based gelling mechanisms that can affect sensitive cells (**Figure 1.2C**).

Bioreactor-based cell culture models comprise a system where a cell suspension with the optimal cell density is filled into a chamber under continuous agitation, either by gently stirring, rotating the chamber, or perfusing culture media through a scaffold using a pump system. These models have been created for intensive cell expansion and large-scale biomolecule production, such as antibodies or growth factors. However, the large-scale production of spheroids is characterized by heterogeneity in size and number (**Figure 1.2D**).

The 3D scaffold approach is also called “top-down”, meaning that it involves seeding cells into biodegradable polymeric scaffolds to form tissue constructs. The cells are expected to populate the scaffold and create the appropriate ECM and microarchitecture, often with the aid of perfusion, growth factors and/or mechanical stimulation. Although this method has been reported in some cases to fail in recreating the intricate microstructural features of tissue, it allows a high degree of reproducibility, fundamental in a field intrinsically susceptible to variations, thereby allowing their use to understand a variety of processes. 3D scaffold structures can be made of a wide range of materials and possess different porosities, permeability, surface chemistries and mechanical characteristics. They are in general porous, biocompatible, and biodegradable, to provide appropriate microenvironments where cells naturally reside, supporting mechanical, physical, and biochemical requirements for cell growth and function. Moreover, the biocompatibility of the porous matrix can be enhanced by the addition of biomolecules such as growth factors, either to the bulk matrix or by attaching them to pore walls. Several biopolymers have

been used to generate porous structures, including collagen, gelatine, silk, chitosan, and alginate, with different biodegradation rates. Various techniques have been developed for the fabrication of scaffolds, such as foaming, freeze-drying, phase separation, solvent casting and particulate leaching (**Figure 1.2E**). [28,29]

The fabrication of scaffolds by 3D-bioprinting methods has gained popularity because they offer high reproducibility and degree of complexity. This "bottom-up" approach, based on building different modular tissues, is a powerful tool because many tissues are made of repeating functional units. Tissue models are generated by computer-aided equipment, in which materials are precisely printed out layer by layer, solidified or crosslinked through various methods. Hence, the technique involves computational modelling, ink/bioink preparation and deposition, and subsequent maturation of printed products (**Figure 1.2F**). 3D-printed scaffolds show a precise microporous structure toward promoting cell adhesion and allowing the diffusion of biomolecules. They can be prepared from a single component (metal, ceramics or polymers), but can also be composites or cell-laden materials, depending on the application. They furnish simultaneously tissue growth and mechanical support, and can be used to deliver bioactive molecules or to monitor the evolution of a 3D culture.[30] Depending on the application, 3D printed biostructures can reach several millimetres or centimetres. Examples of scaffolds printed with cell-laden material are vascular-like tubes, kidney, cartilage and artificial skin.[31] For example, it has been reported the use of 3D bioprinting methodology to reproduce the ECM environment for the development of a cervical tumour model, using a bioink made of gelatin, fibrinogen and HeLa cells. [32] Both single and combined materials have been used to 3D-print complex structures that can be used as supports for the 3D cellular growth of large tissues such as bone or vessels. In particular, the use of polymeric scaffolds has been indicated as largely versatile and biocompatible. It has been reported, for example, the use of poly(propylene fumarate) to realize a biodegradable vascular graft *in vivo*, [33] as well as pours polyvinyl alcohol (PVA)-based hydrogels to realize a synthetic scaffold for articulating cartilage. [34]

In this thesis, 3D-printed polymeric scaffolds have been used to build 3D cellular models, on which the advantages briefly reported here were combined with the possibility of creating a 3D SERS platform to monitor the evolution of 3D cell cultures during their growth. We therefore provide a more detailed introduction to this kind of 3D cellular models in the following section.

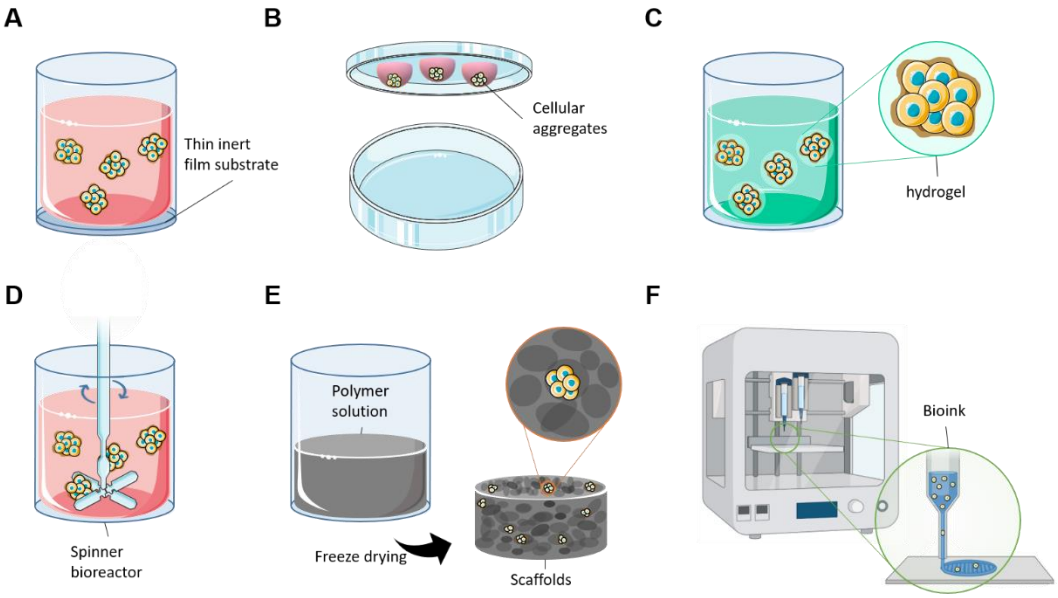

Figure 1.2 *3D culture techniques.* ***A)*** *Liquid overlaid culture,* ***B)*** *hanging drop,* ***C)*** *example of hydrogel surrounded 3D culture in solution,* ***D)*** *spinner bioreactors,* ***E)*** *example of scaffold supported 3D culture and* ***F)*** *3D bio printing.*

1.2.2 3D cultures aided by 3D-printed scaffolds

As mentioned above, a versatile possibility to create 3D cellular cultures involves the aid of 3D-printed scaffolds. In fact, the availability of biocompatible polymeric inks allows to print well-defined 3D microscopic structures, which confer mechanical support to the cellular culture and also promote cell adhesion and infiltration, e.g., of nutrients. The choice of material, printing process and design strategies for the scaffold are guided from the features of the desired final product. For example, tissue scaffolds constructed from polycaprolactone using fused deposition modelling have more flexible structure and biodegradability, with respect to titanium scaffolds printed by selective laser sintering.[35] The scaffolds are classified depending on the printing technique, the principal three techniques being: extrusion-based, inkjet-based and laser-assisted bioprinting. [31,36] The extrusion-based bioprinting technique, also known as direct ink writing (DIW), comprises a computer-controlled extrusion head, from where the material in the form of a paste (such as the Nivea cream) or a thick ink is dispensed, in continuous flow, by an extrusion nozzle. There are two main ways of printing through extrusion, with and without material melting. [37] In the Fused deposition modelling (FDM) method, the material, e.g. poly(D,L-lactide) (PLA) or poly(D,L-lactide-co-glycolide) (PLGA), is melted by heating prior to extrusion from the nozzle.[38] This method is used mainly for printing scaffolds that will be subsequently loaded with cells. In the pressure-assisted micro syringe (PAM) method, the material can be extruded with a pneumatic mechanism, a piston or a screw.[39] The non-contact inkjet-based method consists of pushing a fluid through the nozzle, which breaks

it into a stream of droplets that are charged and deflected using field plates onto the substrate during printing. [40] The liquid droplets are projected from the nozzle through different forces, such as thermal or acoustic. By using this technique, it is possible to print very low viscosity materials (0.001-0.010 Pascal·s), such as molten polymer resins and UV or thermally curable photopolymer resins.[41] The light-assisted bioprinting method comprises the photopolymerization of biomaterials. Among them, we can identify two principal methods, the digital light processing and laser-based printers. The former method uses a laser to cure a polymer, such as PEG diacrylate (PEGDA), glycidyl methacrylate-modified hyaluronic acid (GM-HA) or gelatine methacrylate (GelMA). [42] The method can be improved by including stereolithography projection, to modulate the light and project an optical pattern onto the photopolymer solution, such as PLA-based resin or Poly(ethylene oxide) /poly(ethylene glycol) (PEGDA) hydrogels. On the other hand, there are several types of laser-based printers, which work by focusing a laser beam though a high magnification objective lens to induce polymerization or material transfer on the sample slide.[43]

1.2.2.1 3D-printed hydrogel-based scaffolds

Among all the possible materials, hydrogels are the best candidates for tissue engineering applications in the wet state. They are currently being used in 3D printing of scaffolds, due to their ease of chemical design, formulation and functionalization. They can also replicate the properties of biological tissues, with collagen and ECM-like properties. They consist of a polymeric network with hydrophilic chains, which are crosslinked either covalently or physically via intra- or inter-molecular attraction. Their hydrophilic structures allow them to hold considerable amounts of water or any aqueous biological fluids, up to 10-1000 times their original weight or volume. [44] The presence of crosslinks causes hydrogels to swell without dissolution in aqueous environments, providing a hydrated and mechanically stable environment where molecules and cells can perfuse. Moreover, their porous structure can stimulate natural ECM and exhibit high cell seeding density and homogeneous cell distribution within the scaffold. In addition, hydrogel components can respond remarkably well to various external stimuli such as light, temperature, ions, pH or biochemical signals. Three main classes of hydrogels can be distinguished, depending on their source, i.e., natural, synthetic, and hybrid. The first ones, which are derived from proteins, polysaccharides or decellularized tissues, are biodegradable, generally nontoxic, and with less adverse effects compared to the synthetic ones. [45–48] Some examples are hyaluronic acid, alginate, dextran hydrogels, and cellulose- and chitosan-based hydrogels. [49] On the other hand, synthetic hydrogels exhibit more versatile and easy-controlled physical and chemical properties, and higher mechanical resistance. [50–52] Among the most commonly used ones are Gelatin-Methacryloyl (GelMA), Poly(ethylene glycol) (PEG),

PEGDA and Poly(ethylene oxide) (PEO), Poly (hydroxyethyl methacrylate) PHEMA, Polyacrylamide (PAAm), and Polyvinyl alcohol (PVA) hydrogels and their derivatives.[49] Printing of hydrogels is usually carried out by extrusion-based DIW printing and inkjet printing, followed by laser irradiation. In the first case, after printing, cross-linking or UV-curing are typically used to accelerate gel formation, strengthen the whole matrix structure, and tune polymer degradation.[53] Natural hydrogels, such as alginate or collagen-based hydrogels, can be directly extruded for the design of 3D scaffolds or even used for freeform reversible embedding of suspended hydrogels (FRESH).[54]

In an interesting modification, the integration of organic or inorganic NPs in the hydrogel matrix can improve its structural integrity, giving strength to the scaffold while introducing the possibility for their application in different fields, such as detection of biomolecules, electronics, and soft robotics. [55–57] New categories can be defined depending on their environmental stimuli-responsiveness, such as reversible changes of shape and volume in response to variations in pH, temperature, light, electric and magnetic fields.[58] The most important physical parameters are mechanical properties, like strength, flexibility and elasticity, which facilitate movement or diffusion of bioactive reagents, biodegradability rate, and porosity, in turn facilitating adequate cell growth and flow, as well as swelling, which is also crucial for diffusion and transport. Indeed, the principal requirements for a proper biological performance are biocompatibility, cell adhesion, vascularization, which indicates the adequate interconnectivity and branching of the pores, and bioactivity. The latter refers to the ability of the scaffold to control and sustain the release of bioactive factors, promoting diffusion and ECM formation.[59]

In this thesis, the incorporation of NPs in polymeric inks has been exploited for different approaches. Before going into further detail, a more basic introduction of NPs is provided, starting by a definition of nanotechnology.

1.3 Nanoparticles

Nanotechnology represents an interdisciplinary field between chemistry, physics, biology and engineering. It involves materials and interactions at molecular or even atomic levels (between 0.1 and 100 nm). The small dimensions confer the materials with different optical, chemical and magnetic properties, compared to their bulk counterparts. It has been considered that the nano-era started in the second half of the 20th century, with the famous lecture by the physicist Richard Feynman “There’s plenty of room at the bottom: an invitation to enter a new field of physics”, in 1959. Impressively, a nano-related challenge proposed at the end of the lecture was achieved within less than 30 years.[60]

The application of nanotechnology in the field of medicine has offered many advantages, considering that their small dimensions allow nanomaterials to pass through biological

membranes, becoming in this way better dispersed and bioavailable. These features have improved drug delivery systems and the temporal permanence of nanomaterials within the living body. Moreover, the small dimensions increase the total surface of the administered material, improving its reactivity and the potential surface conjugation or the interaction with other larger molecules. Indeed, the ability of tailoring NPs properties such as material, shape, dimension and surface functionalization has rendered them one of the main characters in the modern research fields of non-invasive diagnostics, targeted treatments and monitoring of biological systems. [61] However, the interaction of nanomaterials with living cells or subcellular structures is not yet perfectly understood. The higher permeability and bioavailability at the nanoscale carry the risk of penetration and accumulation within certain tissues, which may cause oncogenesis. [62] For these reasons, the study of the interaction of nanoparticles with living cells has become as important as the development of the nanomaterials themselves. Several studies have been conducted to understand the interaction of nanoparticles with cells and subcellular molecules such as proteins, ribonucleic acids (DNA and RNA) receptors and enzymes. [63–65] Regarding the chemical composition, it is possible to distinguish three main groups of NPs: organic (liposomes and polymers), carbon-based (graphene, carbon nanotubes, fullerenes, etc.) and inorganic (metals, metal oxides, ceramics, quantum dots, etc.). Selected examples are schematically reported in ***Figure* 1.3**. [66]

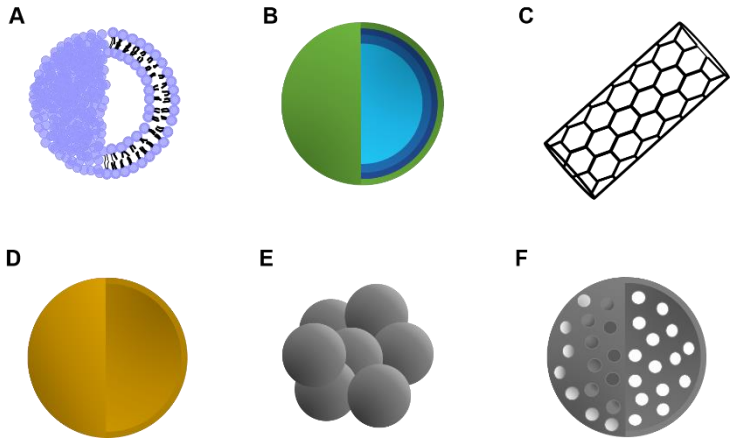

Figure 1.3 *Schematic examples of nanoparticle types: for organic NPs* ***A****) lipidic NP and* ***B****) layered biopolymer;* ***C****) carbon nanotube; for inorganic NPs,* ***D****) gold sphere,* ***E****) iron oxide nanoflower, and* ***F****) mesoporous silica.*

Organic NPs made of polymers are mostly presented as nanospheres or nanocapsules. They can absorb other molecules at the outer boundary or completely encapsulate them within the particles, depending on the application. [67–69] Lipid-based NPs are made by a solid lipidic core and a matrix containing lipophilic molecules, which are stabilized by surfactants and emulsifiers. Their main application concerns the transport and delivery of drugs or RNA.[70–72] The three major classes of carbon-based NPs are graphene, fullerenes

and carbon nanotubes, which are made of carbon atoms, respectively organized as single layer of two-dimensional honeycomb lattice, globular hollow cages and elongated tubular structures. All of them have raised great interest due to their electronic properties. [73,74] Regarding inorganic nanomaterials, ceramics and semiconductor-based NPs have shown applications in catalysis and photocatalysis, also due to their singular electronic properties. [75–78] Lastly, metal NPs feature unique optoelectronic properties that make them ideal for applications in very diverse fields. [79,80]

1.3.1 Metal nanoparticles

Among all metals, gold (Au) and silver (Ag) NPs are characterized by respectively chemical inertness and antibacterial activity, rendering them suitable for biomedical applications. Moreover, their optical properties can be precisely tuned by changing the NP shape and dimensions, from the visible range of the electromagnetic spectrum to the near-IR (NIR) (as explained in the following section), thereby widening their application in the biological field. Indeed, much effort has been invested in the development and improvement of reliable diagnostic tools based on this type of NPs. In particular, both quick [81–84] and extremely precise methods of diagnostic, treatments or long-term monitoring have been developed. [85]

1.3.2 Optical properties of metal nanoparticles

The optical properties of metallic plasmonic NPs depend on the Localized Surface Plasmon Resonances (LSPRs), namely, collective oscillations of conduction electrons of the NPs in resonance with an external electromagnetic radiation that interacts with them (***Figure 1.4***). Upon this optical excitation, the NPs exhibit strong absorption and scattering properties in the Ultraviolet/Visible (UV/Vis) range, due to the generation of a highly enhanced localized electromagnetic field. [86] These properties can be tuned by changing the size and shape of the NPs. An example are anisotropic NPs, such as gold nanorods (AuNRs), which possess an extinction band that can be varied from ca. 680 to 1100nm by changing their shape.[87]

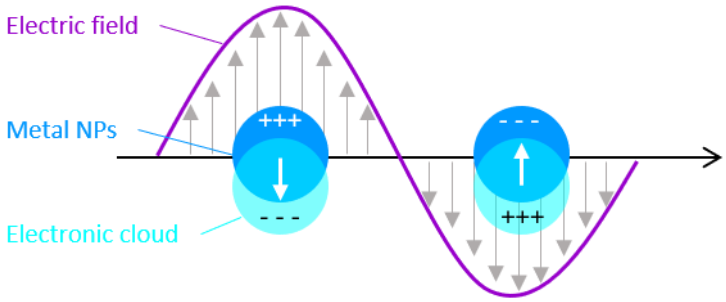

Figure 1.4 *Localized surface plasmon generated when incident light interacts with a metal nanostructure smaller than the electric field wavelength.*

These phenomena can be mathematically described through the general solution of Maxwell's equations proposed by Mie in 1908 and extended to ellipsoidal gold and silver particle geometries by Gans in 1912-1915. [88–90] Hence, in the case of particles smaller than the light wavelength, the equation that describe the extinction E(λ) i.e., the sum of the absorption and scattering terms, is the following:

$$E(\lambda) = \frac{24\,\pi N_A a^3 \epsilon_m^{3/2}}{\lambda \ln(10)} \left[\frac{\epsilon_i}{(\epsilon_r + \chi\epsilon_m)^2 + \epsilon_i^2}\right] \qquad \textbf{\textit{Equation 1.1}}$$

Where N_A is the density of NPs, a is the radius of the sphere, ε_m is the dielectric constant of the medium surrounding the sphere, λ is the wavelength of the incident radiation, ε_i and ε_r are the imaginary and real components of the nanoparticle's dielectric function, respectively, and χ represents the shape factor that accounts for deviations from spherical particle geometries. Therefore, the LSPR of an isolated metallic NP depends firstly on the radius (a) and material (ε_i and ε_r) of the particle, and then on the dielectric constant of the environment ε_m. Additionally, the shape of the NP, the presence of a covering shell, the orientation and the interparticle interaction are responsible for changes in the surface plasmon resonances. [79,91]

We have focused on anisotropic NPs, specifically AuNRs and gold nanostars (AuNSs), which are characterized by highly confined LSPRs at edges and corners, also called intrinsic hot spots. In here, the confined oscillating metal charges produce an enhanced near-field that is stronger than the one generated in spherical NPs. Consequently, these points are the ones that contribute the most in the re-emitted radiation. In particular, AuNRs present two plasmon bands, corresponding to longitudinal and transverse plasmon resonance modes (***Figure 1.5A***). The longitudinal band has the highest intensity and can be tuned by varying the aspect ratio of the NRs. For AuNSs, a principal peak can be observed, as well as a less intense shoulder at lower wavelength, respectively corresponding to the tips and core plasmon modes. Decreasing the diameter of the nanostar causes a shift towards lower wavelengths and narrowing of the main peak, while the shoulder becomes more intense (***Figure 1.5B***). [79,92]

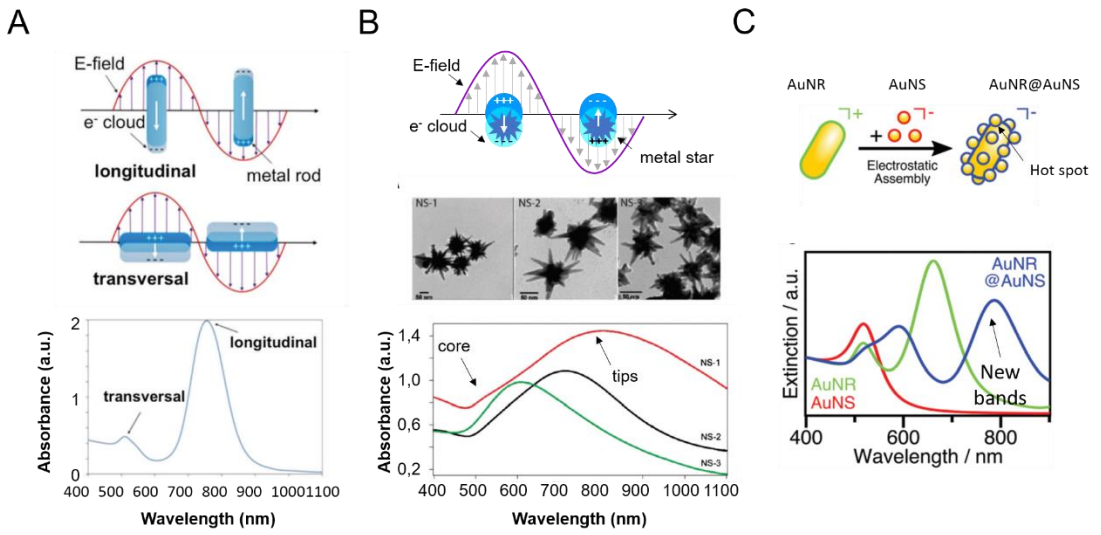

Figure 1.5 *Anisotropic NPs:* ***A)*** *Typical absorbance spectrum of Au NRs with evidenced the longitudinal and transversal plasmon modes. Reproduced from ref*[79]*;* ***B)*** *Typical absorbance spectrum of Au NSs, with the core and tips contributions, as a function of NS dimensions. Reproduced from ref* [92]*;* ***C)*** *Extrinsic hot spot generated via electrostatic assembly of NPs. Reproduced from ref* [93]*.*

Another type of hot spots called extrinsic, are those formed between two NPs positioned at a very short separation distance (1-10nm), or on top of a solid support. In this situation, the coupled plasmon modes of the two NPs or the NP and the substrate, induce new highly localized fields at the narrow gaps within the junctions. An example is reported in ***Figure 1.5C***, where several hot spots have been created through electrostatic assembly of small spheres around a single NR. The extinction spectrum of the assembly shows different bands with respect to the single NPs spectra, presenting a combination of their main peaks. [93]

1.3.3 Surface-enhanced Raman scattering (SERS)

The SERS effect was discovered in 1974 by Fleischmann and co-workers, who observed a considerably enhanced inelastic scattering from pyridine when in close contact with a rough silver electrode.[94] Increasing attention has been given to SERS techniques, in particular toward biological and medical applications.[95] Both low detection limits, down to attomolar concentrations,[96,97] and precise molecular specificity, due to the characteristic vibrational fingerprint of each molecule, are the main highlights of SERS.

This vibrational spectroscopic technique could reach the detection of even single molecules, when they are in close contact with the nanoparticle surface (within 10 nm). In fact, it has been reported that the SERS signal can be enhanced up to 10^{10} – 10^{11} times, compared to normal Raman scattering. [12,98,99] It has been established that two mechanisms are responsible for the enhancement effect: the electromagnetic enhancement mechanism

(EEM) and the chemical enhancement mechanism (CEM). However, it is now generally agreed that the principal contribution to most SERS processes comes from the EEM. The former is the result of the amplification of the light by excitation of LSPRs in plasmonic nanomaterials, whereas the latter involves charge transfer mechanisms, when the incident light is in resonance with metal-molecule charge transfer electronic states. [100]

In the EEM, when light interacts with a metallic nanosphere on which a molecule is adsorbed, the local enhanced electromagnetic field generated by a LSPR, interacts with the molecule to produce Raman scattering. Consequently, the scattered signal is enhanced and when both the incident field and the scattered Raman signal are in resonance with the plasmon frequency, the enhancement factor (EF) of the SERS signal reaches the value of $|E|^4$, where E is the field enhancement at the nanoparticle surface. To carry out on-resonance measurements and thereby achieve a large Raman scattering enhancement, it is crucial to tailor the LSPR of the substrate relative to the laser excitation wavelength. These adjustments can be done, as mentioned above, considering the tuneable optical properties of the NPs, by changing their size and shape. In practical use, the EF related to both the two mechanisms is experimentally evaluated at a single excitation wavelength, as the ratio between the SERS intensity and the Raman intensity:

$$EF = \frac{[I_{SERS}/N_{SERS}]}{[I_{RS}/N_{RS}]} \qquad \textit{Equation 1.2}$$

Where I_{SERS} is the surface-enhanced Raman intensity caused by N_{SERS} molecules and I_{RS} is the normal Raman intensity produced by N_{RS} molecules. This equation describes the Raman enhancement, which accounts for the enhancements of both the incident excitation and the resulting scattered light. [98]

The high SERS signal enhancement allows the detection of analytes close to the NPs surface, with high specificity and at very low concentrations. Hence, plenty of investigations have been performed in applying the SERS technique to sense low abundant species, or to improve the sensitivity of existing methods, such as immunoassays used to find the presence of pathogens in clinical analysis.[101] Additionally, the stability and reproducibility of the SERS signals, as well as the multiplexing capacity related to narrow spectral peaks (ca. 1-2 nm),[102] make the technique perfectly suitable to perform imaging. Nevertheless, to compensate the extremely low intrinsic Raman cross sections of most biomolecules it is a common procedure to use other labelling molecules with comparatively higher cross sections, i.e., Raman reporters (RaRs).[103] Hence, it is possible to distinguish two strategies for both SERS detection and imaging, namely the direct and indirect approaches. In the former case, those moieties with high affinity for binding the metallic NPs are directly adsorbed onto their surface and the enhanced Raman

signal is detected. [104–106] One of the main issues with the direct (or label-free) approach in colloidal suspension is the possibility of aggregation or clustering of the NPs, which causes irreproducibility in quantification. In the indirect approach, molecules with large Raman cross section are adsorbed or covalently bounded to the NP, to create a so-called SERS tag which is subsequently attached through surface functionalization to the biological element under investigation. This approach is better suited for the high complex and constantly evolving biological environment. Therefore, the identification and localization of an analyte is indirectly related to the Raman spectrum of the selected RaR. [107–110] The advantages of the indirect approach in bioimaging over other classical techniques,[111,112] are related to the long-term stability of the RaR molecules, which results in highly reproducible SERS signals, and reduced background autofluorescence noise.[113]

The definition, composition and principal applications of the SERS tags are presented in the following sections.

1.4 SERS tags

SERS tags consist of a core made by a noble metal (typically Au or Ag), which acts as the plasmonic electromagnetic field enhancer, covered with a monolayer of RaR molecules,[114] usually surrounded by a protective layer or coating shell, which can be in turn selectively functionalized with targeting biomolecules as represented in ***Figure 1.6A***.

1.4.1 SERS tags composition

1.4.1.1 The core

The core of a SERS tag is made of one or more plasmonic metal NPs and provides a largely enhanced electromagnetic field when an LSPR is excited by the incoming light. In imaging experiments, high SERS signal intensity and reproducibility relay on the efficiency of the enhancement process. The optical response of the nanoparticle cores depends mainly on their chemical composition, size, shape, and on the refractive index of the surrounding medium, which influence the LSPR frequency. As mentioned above, the most commonly employed metals are silver and gold. In fact, silver is the most efficient plasmonic metal,[115] while gold is the most widely used material in biomedicine, considering its high biocompatibility due to low toxicity and the excellent control over the synthesis of Au NPs.[80] In particular, for Au NPs, the major effect on LSPR is given by their shape, e.g. whereas small gold nanospheres present a plasmon resonance in the visible (c.a. 520 nm),[116,117] the LSPRs of anisotropic NPs such as NRs can be tuned from the visible into the NIR region (up to 1500 nm).[118] This characteristic makes them perfectly suitable for biological applications, considering that the so-called biological transparency windows are in the NIR. These are defined as the regions with optimum light transmission in tissue, due to maximum penetration and minimal autofluorescence noise. In particular, the first

window (NIR-I) is located at 650-950 nm, the second (NIR-II) is defined from 1.0 to 1.35 μm and the third one (NIR-III) from 1.5 to ~1.8 μm).[119,120] In addition, NPs characterized by sharp tips and edges, such as star-like morphologies (i.e. NSs), have resulted to be efficient electric field enhancers, and therefore have acquired a high relevance in the biological field.[121,122]

Furthermore, great attention has been given to the fabrication of multiparticle cores due to the formation of plasmonic hot spots. These are regions at the interparticle gaps with locally high enhancement, where ideally RaR molecules are placed to obtain high SERS signals. [123–126] Some examples of multiple cores proposed for the realization of efficient SERS tags are controlled assemblies of NPs such as dimers,[127] larger clusters[124,128] and switchable core-satellite Au-SiO_2 heteroassemblies.[129] Actually, several challenges remain for the production of highly homogeneous and controlled NPs and assemblies, and recent efforts have been directed to overcome these issues. Significant improvements in morphological monodispersity and reproducibility in Au NSs,[130] as well as methods to improve encapsulation of nanoparticle clusters, e.g. using microfluidic systems, have been reported.[131]

1.4.1.2 The encoding layer

The encoding layer consists of RaR molecules, which provide the characteristic spectral fingerprint of the SERS tag that is enhanced when in contact with the plasmonic metal core. Hence ,the production of a large library of SERS tags with different Raman codes,[103,132] depends on the availability of different RaR molecules used and can be improved by simply modifying the chemical structure of RaR molecules. The possibility of having such a large number of different SERS tags offers important applications in multiplexed bioimaging, acquiring relevance with respect to other classical imaging techniques, such as fluorescence. For multiplexing purposes, the overall number of vibrational Raman bands, as well as the spectral overlap between selected RaRs should be minimized. A relatively high Raman cross section is a fundamental requirement in the selection of RaR molecules, but still a wide variety of molecules including for example standard fluorophores (crystal violet, Nile blue, etc.) is available. In general, this condition is obtained when the molecules contain highly polarizable moieties, such as double and triple bonds. In the case that the RaR displays an electronic transition in resonance with the excitation laser wavelength, the resulting Surface Enhanced Resonance Raman Scattering (SERRS) effect, generates even higher signal intensity than normal SERS.[103,133] Among the most commonly used RaRs are thiolated aromatic molecules, which can readily adsorb onto gold surfaces. Some examples are biphenyl-4-thiol (4-BPT), 1-naphthalenethiol (1NAT), 2-naphthalenethiol (2-NAT), benzenethiol (BT), 4-Mercaptobenzoic acid (MBA), 4-methylbenzenethiol (MBT), etc. It has been reported that

a monolayer of RaR molecules uniformly covering the metal surface should provide intense, stable and reliable signals. [102,134] Although the quantification of the amount of RaR molecules attached to NPs is still a challenge, techniques such as mass spectrometry can be used to determine the ligand shell morphology and provide a better understanding of SERS tags.[135] Also, it has been reported the creation of tags as result of the combination of different RaR molecules on the same NP substrate, which can be detected across a wider range of excitation wavelengths.[136] Recently, custom made RaR molecules have been produced to improve the performance of existing RaRs, such as e.g. resonant modified dyes that incorporate functional groups for an easier adsorption onto NPs. Oher examples are novel RaRs such as olefin or alkyne moieties realized through specific synthetic procedures, which are characterized by strong and characteristic vibrational Raman bands.[137]

1.4.1.3 The protecting shell

The external layer that composes the SERS tags improves their colloidal stability and also provides insulation.[114] Indeed, the main functions of the protecting layer are avoiding detachment of RaR molecules, preventing potential contamination of the signal due to interfering molecules present in the surrounding medium, reducing any eventual toxicity of the NPs and decreasing NPs interactions that can lead to plasmon coupling. Although the choice of the protecting shell depends on the specific application, it is possible to define biomolecules, such as bovine serum albumin (BSA), amphiphilic or other polymers, such as polyethylene glycol (PEG), and inorganic shells, most often SiO_2, as the most commonly used.[108,129] Although silica coatings often suffer from degradation and agglomeration problems when exposed for long time to cellular media,[138] they provide a highly versatile encapsulation in terms of porosity, shell thickness, synthetic reproducibility and biodegradability (***Figure 1.6B***).[139–142] Polymers such as heterofunctional PEG with a thiol end-group or additional functional groups (e.g. –COOH) are also largely used as NP stabilizers, with a strong binding to the Au NP surface and the possibility of conjugation to amine groups, e.g. to attach antibodies through EDC-NHS chemistry.[143] However, it necessary to finely tune the polymer/RaR ratio to maintain a high SERS signal, considering the binding competition for the Au NP surface between PEG-SH and RaR molecules.[102,144] Encapsulation of RaR molecules can also be accomplished by means of crosslinked polymers, such as poly(N-isopropylacrylamide) (pNIPAM).[113] On a different strategy, amphiphilic polymers (such as dodecylamine/polyisobutylene-alt-maleic anhydride, PMA) provide highly stable and biocompatible coatings, based on the interactions between hydrophobic RaR molecules covering NPs surface and the hydrophobic block of PMA[102,145] (***Figure 1.6C***).[146] Alternatively a biocompatible protecting shell can also be realized by using liposomes[147] or high molecular weight proteins, which

can easily bind onto the Au NP surface through either covalent bonds or physical interactions.[148] One of the most common choices is the BSA globular protein, which provides the particles with both stability and protection.[149] Finally, the deposition of few-layer graphene onto AuNPs has been reported to form so-called graphene-isolated-Au nanocrystals (GIANs), in which graphene acts simultaneously as a label and a protective layer (***Figure 1.6D***).

1.4.1.4 The external targeting ligands

The presence of targeting ligands such as specific antibodies, proteins, aptamers or peptides bonded on the external surface on the external layer allow SERS tags to selectively recognize specific body regions or tissues.[150,151] The resulting specifically functionalized NPs have been widely used to target cancer cells for both *in vitro* and *in vivo* imaging. [152,153]

In the case of polymeric external shells, the connection with antibodies and proteins is often based on direct binding, namely either 1-ethyl-3-(3-dimethylaminopropyl)carbodiimide (EDC) chemistry, forming stable amide bonds, or click chemistry. When silica shells are used as the outer layer, silane chemistry is often used for further functionalization. A strategy to obtain the site-specific immobilization of antibodies involves the attachment of a peptide linker onto the NPs. An example is Protein A, which presents high affinity toward the Fc fragment of both human and rabbit Immunoglobulin G (IgG). This method facilitates an ordered immobilization, thereby achieving maximum selectivity while leaving the reactive site of the antibody available for targeting. Another option is based on biotin-modified proteins or aptamers, bound to avidin or streptavidin-modified NPs.[154] In some cases, it is also possible to directly link the appropriate biomolecules to AuNPs via adsorption or electrostatic interaction.[108] One of the most common strategies when using peptides employs covalent coupling of cysteine-terminated peptides to the particle surface via S-Au bonds. Additionally, it has been reported the use of BSA as a linker between peptides (via the crosslinker 3-maleimido benzoic acid N-hydroxysuccinimide) and NPs (via electrostatic interactions), conferring better solubility and stability to the peptide.[155]

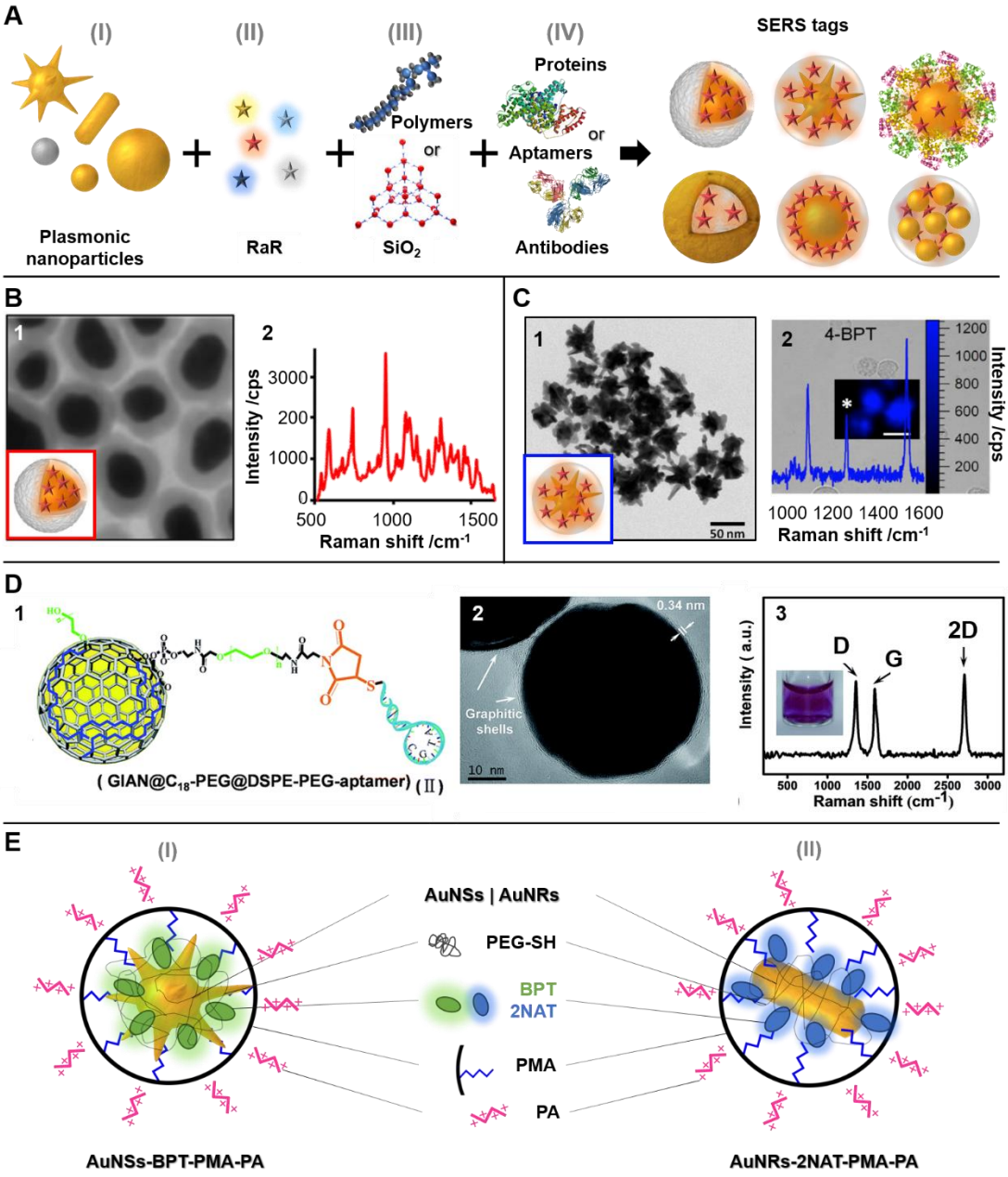

Figure 1.6 *A) Schematic representation of the basic elements of single core and multiple core SERS tags:* ***(I)*** *inorganic cores;* ***(II)*** *Raman reporter molecules;* ***(III)*** *coatings made of different materials (proteins, polymers, silica, etc.);* ***(IV)*** *recognition moieties.* ***B****) PEGylated, silica coated SERS-nanotags containing the NIR dye IR780 perchlorate as RaR:* ***B.1)*** *Transmission electron microscopy (TEM) image and sketch (inset);* ***B.2)*** *SERS spectrum using 785 nm laser excitation. Reproduced with permission from ref* [156]*.* ***C****) BPT-SERS-encoded Au NSs with an amphiphilic polymer protective layer:* ***C.1)*** *TEM image and sketch (inset);* ***C.2)*** *Coloured SERS maps of tag-labelled cells. The white scale bar corresponds to 20 µm. Reproduced with permission from ref* [102]*.* ***D****) Graphene-isolated–Au nanocrystals (GIANs):* ***D.1)*** *Scheme of aptamer-functionalized GIANs;* ***D.2)*** *TEM image;* ***D.3)*** *SERS spectrum of aqueous GIANs suspension highlighting graphene main peaks. Reproduced from ref* [157]*.* ***E****) Schematic representation of the general types of SERS tags used in this thesis: the*

two different gold cores are encoded with a Raman reporter molecule, i.e., BPT for AuNSs and 2NAT for AuNRs, stabilized with PMA and functionalized with an external positively charged layer of poly-L-arginine hydrochloride (PA). The final SERS tags are thus defined as (I) AuNSs-BPT-PMA-PA and (II) AuNRs-2NAT-PMA-PA, respectively.

In this thesis, mainly gold anisotropic NPs, such as NSs and NRs have been used (***Figure 1.6E (I)*** and ***(II)***, respectively). The NPs were encoded with BPT, 2NAT, MBT, and BT RaRs, and wrapped with PMA to enhance their stability and apply them in aqueous solutions, via a phase-transfer methodology. The whole structure was then further functionalized with the cationic polyelectrolyte poly-L-arginine hydrochloride (PA), to achieve positively charged SERS tags that are easily uptaken by the cells. Details of the preparations are presented in the experimental section of **Chapter 2**.

1.4.4 SERS tags applications: sensing and imaging

The characteristic properties of SERS tags are particularly useful for many applications, including imaging and sensing in long-term experiments, where other non-invasive techniques are not able to monitor the system over time. In fact, a fundamental advantage of SERS tags, with respect to commonly used fluorophore labels, is their resistance to photobleaching.[111] This feature allows the localization and monitoring of the labelled elements over extended periods of time, with negligible loss of the SERS signal. Moreover, their tunability in the NIR region provides access to deeper light penetration in biological systems, increasing the range of potential applications. Lastly, the non-invasive character of the SERS technique makes SERS tags suitable for *in vivo* experiments, avoiding the need for fixing cells, which is crucial to understand cellular behaviour in real life conditions. Although still few *in vivo* imaging studies have been reported,[158] their properties make them desirable for high resolution imaging of 3D cellular tissue models. Notwithstanding the excellent characteristics of SERS imaging, these kinds of 3D cellular systems are noticeably complex and there are still several aspects that have to be further studied.[111] The short penetration depth of the excitation laser light (ca. 2-5 mm)[159] is one of the main limitations for the application of SERS imaging in deep human body tissues/tumours. A possible alternative in such cases may be through direct access to the area of interest, as has been done with an endoscopic probe equipped for SERS imaging.[160] Several authors have reported the use of SERS tags in *in vivo* biomarker sensing, for both detection and treatment of cancer-cells. Indeed, SERS detection can be applied in all those situations where the analyte concentration is extremely low, thanks to its ultra-sensitive character.[110] Furthermore, SERS can be combined in dual or multimode platforms,[161,162] for simultaneous imaging and sensing,[163] and/or therapeutic treatments as for example, photothermal therapy.[164] Further details of SERS imaging and sensing are addressed in the following sections.

1.5 SERS imaging

Considering all the aspects formerly explained, SERS imaging appears as an ideal option in those cases where a minimally invasive technique is required, capable of monitoring the samples over extended periods of time. An example is the development of new materials for biomedical applications, which requires cytotoxicity tests to be carried out[145] through experiments with living cells. Another situation where SERS imaging appears as an ideal choice, is in studies related to long term monitoring, e.g., about the effects of anticancer drugs, which requires the use of methods that do not modify the cellular environment.

1.5.1 SERS imaging of 2D cellular models

Regarding 2D cell cultures, SERS tags have been demonstrated to be particularly useful to separately monitor mixtures of different cell types. For example, it has been demonstrated that five different cancer cell lines can be specifically imaged and followed within a quintuple cell co-culture for more than 24 h, without visible damage to the cells.[102] SERS tags with specific cell receptors can be used to discriminate cells, as has been reported by using SERS tags carrying different antibodies, which selectively attach to cellular receptors and clearly allow to distinguish tumour from healthy cells.[113] Moreover, by integrating multiplex targeting and multicolour coding with multimodal detection, promising improvements have been achieved in multispectral imaging of individual tumour cells within complex biological environments. [165]

Besides all the features mentioned above, another important advantage of SERS imaging compared to commonly used techniques, such as fluorescence, is the possibility to combine imaging with and without labels. In this respect, a simultaneous triplex 3D imaging of cellular nucleus and membrane has been reported, based on the co-localization of very narrow peaks in the Raman spectra of both labelled and non-labelled NPs.[166] The combination of both approaches, SERS tags for 3D imaging and label-free SERS analysis to monitor selected biomolecules (biomarkers) is a suitable pathway to obtain a complete characterization of the biological system.

1.5.2 SERS imaging of 3D cellular models

It has been discussed above that commonly used 2D cell models are not suitable to simulate the natural microenvironment and therefore, the design of realistic 3D *in vitro* models is required.[167,168] Indeed, the use of scaffold-supported models that recreate a dynamic situation, where cells can migrate, is rapidly increasing.[169] However, the ability to characterize the internal structure of these models or their evolution is still rather limited. The most commonly used technique to characterize 3D structures is confocal fluorescence microscopy, even though it presents various drawbacks, such as limited

penetration depth, autofluorescence from cells, photobleaching and overlapping signals due to broad emission bands. Hence, considering the advantages of the SERS technique, its application in imaging is emerging as a promising alternative to monitor 3D cell ensembles. It has been reported the use of SERS tags to perform 3D SERS imaging of single cells, [170–174] but less examples are reported for a cellular complex tissue-like structure.[175] A label-free SERS based approach has been shown for the analysis of intracellular responses at different depth layers of a 3D culture model, in a spheroid structure, upon exposure to different drugs. [176] In another work, SERS tags were used to image a 3D cell culture model with a "sandwich" structure, over a millimetric distance in depth.[107] It has also been reported the development of a hierarchical 3D SERS-active structure to increase signal collection along the z-direction.[177] Actually, the implementation of SERS in the bioimaging field is still in progress due to several challenges related to the spatial and temporal resolution of existing instruments. The sensitivity and resolution of the measurements are determined by several aspects. Light source parameters such as wavelength, spectral linewidth, frequency and power stability, spectral purity, beam quality, output power, etc. are important for any kind of measurement. In biological samples, irradiation wavelengths are restricted to the NIR region to increase the penetration depth, even if the Raman-scattering efficiency is weaker than at shorter wavelengths. In this respect, one of the most often used laser wavelengths is 785 nm. It presents a good balance between scattering efficiency, low fluorescence, detector efficiency and cost-efficiency.[178] Moreover, wavelength specific charge couple device (CCD) detectors with improved precision and optimized laser-detector coupling, are increasingly available.

To overcome the problems related to spatial resolution, improved SERS-related techniques are arising. It is possible for example, to introduce a spatial filter to eliminate the out-of-focus signal, such as pinholes, which enable the confocal Raman microscopy (CRM) configuration to reach resolutions of 0.5-1.0 μm.[179] Moreover, it is possible to implement atomic force microscopy (AFM) systems with confocal Raman spectrometers to allow resolution in the nanoscale. In this configuration, also called tip-enhanced Raman spectroscopy (TERS), an opto-mechanical coupling that confines the laser on a metal-coated tip, which acts as both focal enhancer and nano-source of light, is employed.[180] The detection of single molecules with high sensitivity and resolution has been achieved by combining TERS with non-linear coherent Raman scattering phenomena, namely tip-enhanced coherent anti-Stokes Raman scattering (TECARS).[181] On the other hand, it is possible to combine SERS with spatially offset Raman spectroscopy (SORS), to yield enhanced Raman signals at much greater sub-surface levels, up to 25 mm of depth.[182,183] Additionally, the use of non-linear excitation, i.e. surface enhanced hyper Raman Scattering (SHERS), allows to reduce the illumination area and consequently to obtain

more precise data in deep 3D samples, in a similar manner to two-photon fluorescence microscopy.[184] Immuno-SERS microscopy, characterized by single-nanoparticle sensitivity, is quickly taking relevance due to the capability of rapidly imaging large tissue areas (namely, 30msec per pixel acquired).[185] In most of these cases, it is possible to equip the machine with ultrafast lasers reaching femtosecond or picosecond timescales, to study molecular motion and molecule-plasmon interactions at a single molecule level.[186,187] Moreover, home-made spectrometers, coupled with the implementation of structured line illumination in slit-scanning microscopy can lead to rapid ultra-resolution.[188]

In bioimaging, high resolution, fast acquisition time and increased penetration depth are all highly desirable features. The implementations reported above to achieve these valuable characteristics, generate a massive amount of data and also require sophisticated procedures of data analysis. In particular, improved applications are required for the analysis and representation of 3D images. The general approach focuses on reducing the dimensionality of the system, without losing information related to the variability of the samples, to be able to distinguish and classify the different elements inside the system. In parallel to the classical procedures, such as principal component analysis (PCA)[189] or linear regression analysis,[190] multivariate analysis is becoming more and more popular due to its ability to face multidimensionality problems. The treatment and analysis of data are addressed in **Section 1.7**.

1.5.3 *In vivo* imaging

The SERS imaging application in *in vivo* measurements has focused on identifying the presence and location of tumours, thereby guiding surgical tumour removal. [191] Occasionally, it has been combined with complementary imaging techniques for multimodal imaging. [162] In *in vivo* SERS imaging studies, SERS tags are injected into the animal,[81] and either accumulate in a tumour due to the enhanced permeation and retention (EPR) effect[192] or specifically target certain cells or tumours via direct injection or biorecognition of surface ligands. Much effort is being devoted toward developing new instrumentation for *in vivo* SERS imaging to overcome the limitations due to the short penetration depth of the excitation laser beam. It has been reported, a small animal Raman imaging (SARI) system that allows for rapid imaging over a relatively large area (>6 cm^2), with high spatial resolution. [193] Furthermore, it has been shown a non-invasive and multiplexing method characterized by high sensitivity, that surpasses the multiplicity limit of previous preclinical tumour imaging methods, and could enable the evaluation of multiple bio-molecules within the tumour microenvironment in living subjects. [194] Another surgical application has been introduced, coupling an optical fibre probe with a clinical endoscope. The combination of both systems is a significant advancement for

simultaneous *in vivo* identification of cancer receptors,[163] ultimately leading to real-time image-guided resection (pre and intra-operative)[195] and/or drug delivery. [196]

1.5.4 Multimodal imaging

The demand of the combination of mutually compatible imaging techniques, which can provide complementary information, is based on the need to obtain as much information as possible, toward accurate disease diagnosis. The combination of fluorescence and SERS labels is probably the most common dual imagining technique. For example, fluorescent polystyrene beads coated with SERS-labelled AuNSs have been demonstrated efficient systems as dual imaging probes.[161,197,198]

Another common combination is with MRI. There are examples in the literature, of Janus plasmonic–magnetic (Au–Fe_2O_3) NPs that showed multimodal imaging performance for CT, MRI, Photoacoustic (PAc) and SERS. [162] Moreover, it has been reported the functionalization of Au NPs with Gd organometallic complexes to obtain probes that can be imaged with SERS, MRI and PAc, aiming at visualize brain tumour margins with high precision.[199]

SERS NPs can be combined not only with other imaging techniques, but also with selective treatment techniques such as photothermal therapy (PTT). An imaging guide through SERS and PAc for photothermal therapy has been reported, using antibody-conjugated Au@Ag NRs decorated with DTNB nanoprobes (5,5'-Dithiobis-(2-nitrobenzoic acid)). [200] It has also been reported the application of SERS in combination with PAc and PPT for deep tumours, using gold nanostructures tuned in the NIR-II. [201] AuNSs,[202] as well as Raman reporter-coupled Ag@Au NSs and gold nanobipyramids, [203,204] have been used for *in vivo* tumour imaging and photothermal therapy. In this regard, a novel treatment is the application of plasmonic gold NSs as photothermal inducers for synergistic immune-photothermal nanotherapy. [205]

1.6 SERS detection

As previously discussed, the ultra-sensitivity provided by SERS is one of the main reasons that make this technique an attractive candidate for the design of systems for the detection of biomolecules at extremely low concentration, such as *in vivo* and *in vitro* indirect detection. In fact, the high sensitivity and specificity of SERS tags can lead to detection at a single-cell level, via the specific binding through a targeting moiety. As mentioned, the *in vivo* detection is focused on endoscopic systems where biomarker-targeted nanoparticles are injected and then localized through the use of endoscopes or optical-fibre devices equipped to acquire the Raman signal.[206] There are several examples of applications for the identification of biomarker expressed by cancer cells [207] or other diseases, [208] as well as viral and bacterial microorganisms. [209]Another application of SERS

ultra-detection involves SERS-based *in vitro* immunoassay devices. These tools are commonly used to detect a specific target molecule in solution using antibodies and antigens, for example the Enzyme-Linked Immunosorbent Assay (ELISA) test. The SERS-based devices offer improved detection, especially in those cases where the extremely low amounts of solution lead to failure in standard systems.[122] In particular, an improvement of ca. two orders of magnitude with respect to the sensitivity of conventional immunoassays has been reported, for different types of biomolecules and microorganisms, including proteins, bacteria and viruses.[210]

1.7 Data analysis

Often, the identification and quantification of components in biological samples by spectroscopic methods is difficult to observe in raw data, considering the diverse and complex nature of the samples. Therefore, to obtain meaningful information and for a deeper insight, it is necessary to process and analyse the data. The data analytical methods that deal with only one variable are defined as univariate methods. Some examples are first and second order derivatives, curve fitting and various bands intensity/area under the curve ratios, which help to visualize band shift, peak broadening and changes in intensity. However, each one of these single contributions is generally not enough to understand a set of spectroscopic data and an analysis that takes into consideration all the information is required. Multivariate data analysis consists of an analytical method that deals with more than one variable at a time, perceiving the relationships between the variables and ultimately combining them into a multivariate model. This is based on the idea of using these models routinely to predict newly acquired data of a similar type. The advantage of these multivariate statistical methods is the capability to analyse the vast spectral distribution and thoroughly discriminate between spectra of different samples that show only very minor changes. Various data mining methods such as PCA, linear discriminant analysis (LDA), multiple linear regression analysis (MLRA), cluster analysis (CA), and partial least squares (PLS), are examples of known analysis employed in the field of Raman spectroscopy. The effective application of these methods requires the pre-treatment of data, eliminating noise and unwanted signals and enhancing discriminating featured signals. Sometimes, they assist the pre-processing procedure, reducing and correcting interferences to analyse spectral variations. [211]

1.7.1 Data pre-treatment

Data pre-processing consists firstly of the removal of cosmic rays. These are very strong sharp emission line signals generated due to high-energy particles passing randomly through the CCD of the spectroscope and generating many electrons interpreted as a

signal. Another challenge in using Raman spectroscopy for biological samples is the strong intrinsic fluorescence from many biomolecules. Similarly, ambient light and detector thermal noise may contribute to the background of the signal. Therefore, various processing methods such as polynomial fitting, first and second order differentiation, frequency domain filtering, etc. have been used for baseline removal. Detector noise and intensity fluctuations of the used radiation source are other components that can affect the signal. In this case, the signal to noise ratio can be improved by increasing the integration time during the measurement or by using smoothing filters on the raw data. In some cases, it can be useful to apply normalization methods to take care of disparity in intensity levels, due to different instrument conditions, such as laser alignment or laser power levels. Finally, it is important to omit from the data set those spectra that are very divergent from the group (outliers), caused by factors like instrumental artifacts or similar.

1.7.2 Multivariate data analysis

Generally, the analysis starts by representing the data in a matrix form, where each pixel of the measured mapping is represented by one column of wavenumber and another one of intensities. Each signal or observation consists of two parts: the relevant signal, which is the actual representation of the underlying chemical information and the noise that is the irrelevant part, including spectral noise. Generally, the application of multivariate analysis involves separating the relevant signal from the noise, by using intrinsic variable correlations in a given data set. Many multivariate data analysis techniques are available, depending on the final aim of the application, i.e., data description and modelling, classification and clustering, or regression and prediction. In the case of data description and modelling, PCA is the principally used analysis method, while for discrimination, classification and clustering, LDA and CA can be applied to divide the data into two or more groups. In the case of data regression and prediction, where two sets of variables are related and quantified with respect to each other, MLRA and PLS analysis can be applied. It is possible to divide the multivariate data procedures into two broad groups: unsupervised and supervised methods. The first one defines those procedure where no supervising guidance is available, namely reference spectra or labels. These are useful to discover hidden structures in the unlabelled data and are often used as precursors to supervised methods on huge data sets. Examples are PCA, k-means and Hierarchical Clustering Analysis (HCA). In the supervised methods instead, the classes to be discriminated are labelled before the analysis starts. Indeed, it is possible to divide the process into two steps. The first one is called training phase and it consists of a passive modelling, which uses a training data set to find patterns in the data. Then, the model parameters are applied on the rest of the data, during a second phase called prediction or

testing phase. Among the most used methods, it is possible to identify the Discriminant Analysis (DA), MLRA, Principal Component Regression (PCR), PLS and Support Vector Machines (SVM). In the case of a very large data sets, unsupervised methods are first applied to divide the data in clusters and label the observations with the dominant class label. Hence, data are classified and fed to supervised methods for further classification.

1.7.2.1 Multivariate linear regression

In linear regression, the objective is to determine the relationship between several x-variables, called independent or explanatory (x_1, x_2,…,x_N), and one dependent variable y, called also response. The linearity of the model refers to the linear relationship assumed between the x-variables and the y-variable. In the simple linear regression, there is only one explanatory variable, while the multiple linear regression is a generalized version. A model for N non interacting x-variables linearly correlated to y can be written as:

$$y_i = b_0 + b_1 x_{i1} + b_2 x_{i2} + \cdots + b_N x_{iN} + e_i \qquad \textit{Equation 1.3}$$

where b_i (i = 0,1,…, p) are regression coefficients describing the effect of each calculated term and e_i is the model error. Both in simple and multiple linear regression, the size of the coefficient for each independent x-variable indicates the magnitude of the effect that variable is having on the independent variable y. In the case of a single independent variable x, the b value suggests the y variation respect to x, while in case of multiple x, each b_i value is related to the variation of the respective x_i, considering all the other independent variables constant. This linear relationship can be achieved by means of a model, where the observed result, i.e., the response (y), is described as a function of the x-variables. When the dimensions of y and x are generalized, the model is called multivariate linear regression and **Equation 3** can be expressed in matrix form, as $\mathbf{y = Xb + e_y}$. The regression vector **b** can be generally estimated with a least-squares fit minimizing the sum of squared residuals, as follows:

$$\boldsymbol{b} = (\boldsymbol{X}^T\boldsymbol{X})^{-1}\boldsymbol{X}^T\boldsymbol{y} \qquad \textit{Equation 1.4}$$

These b values represent the underlying regression model, which is learned during the training phase. Then, they can be used to predict y-values from new measurements of x. [212,213] They can be also calculated through several techniques depending on the data. [214] To address the strength of the linear relationship between x and y, it is possible to calculate the parameter defined R^2:

$$R^2 = \frac{\Sigma(\hat{y} - \bar{y})^2}{\Sigma(y - \bar{y})^2} \qquad \textit{Equation 1.5}$$

Where $\hat{y}$ indicates the estimated value and $\bar{y}$ is the mean value. This represents the percentage of the variability in y that is explained by using x to predict y, which can assume values in the range $0 \leq R^2 \leq 1$. The closer R^2 is to 1, the closer the model will be to the data. It is a rough indicator of the worth of the regression model, very important in the case of predictions based on the model. However, it is necessary to use the p-value to determine whether the relationships observed among the variables x and the response y are also existing in the larger population, or differently said, if they are statistically significant. The p-value for each independent variable tests the null hypothesis that the variable (x) has no correlation with the dependent variable (y). If there is no correlation, there is no association between the changes in the independent variable and the shifts in the dependent variable. This indicates that, there is no sufficient evidence to conclude that there is an effect at the population level. Hence, if the p-value for a variable is less than the significance level, the data provide enough evidence to reject the null hypothesis for the entire population. The data favour instead the hypothesis that the independent variable is associated with changes in the dependent variable at the population level, indicating a statistically significant variable. On the other hand, if the p-value is greater than the significance level there is not sufficient evidence in the data to exclude the null hypothesis. More in detail, the p value is determined comparing the t statistic on the x variable with values in the Student's t distribution, which describes how the mean of a sample with a certain number of observations (i = 0,1,..., p) is expected to behave. The t statistic is defined as the coefficient (b) divided by its standard error, which is an estimation of the standard deviation of the coefficient.

1.7.3 Big data

The definition of big data changes constantly with evolving data and is driven by technology, but it is possible to identify some common characteristics over time: very large volume of diverse forms of data at a very high rate of generation. [215] This is something that involves also SERS bio-imaging data. In fact, in analysing an imaging, all the considerations previously done about a single spectrum, are similarly applied to the whole mapping data set. This aspect highlights how quickly the analysis consuming time can increase when imaging data analysis is performed. This brings up the needed of developing algorithms to standardize some of the steps required, gaining speed in the analysis. To give an example, let us consider a general 2D Raman image of a cell of average dimensions of 20 × 20 × 10 μm. The image field should be at least four times bigger with

respect to the cell area, to place it in the middle of the image, namely an area of 40 × 40 μm. To image the cells with sharp details, it is necessary to use at least 1 μm of step size, which means 40 × 40 = 1600 points collected inside the mapping. Still, each point is a Raman spectrum, which should be treated as explained before, i.e., performing pre-treatment (cosmic rays removal, baseline correction, etc.) and then applying the analysis. If we move to 3D analysis, every step should be multiplied by the number of layers that the sample has been scanned along the z direction, for example 10 layers (maintaining 1 μm of resolution also in z). And yet studying the results obtained, probably it could be necessary to change some parameters and repeat the analysis from the beginning.

It is clear how much time the analysis process can require and how easily the resolution is pushed towards the implementation of programs that can semi-automatise the analysis. However, totally blind automatic algorithms are not desirable, considering that some parameters vary strongly from one mapping to another and cannot be standardised. A wrong interpretation may profoundly influence the results and thus, it is important to support the algorithm during some passages. The algorithm can be generated on different platforms, such as python-based, MATLAB, R-based, etc. The procedures generally consist of two parts, the acquisition and pre-treatment data, and then the more analytical part. The acquisition is a crucial step, which depends strongly on the accessibility of the generated data. In fact, not all Raman microscopes allow the operator to obtain quickly the data in an accessible form, such as .txt extension for example. In some cases, a conversion of the data is required and not always such a conversion produces easily interpretable data. Data conversion is another element that strongly influences the total employed time for data analysis. After the acquisition step, the data can be organized in an easy and understandable manner to perform data pre-treatment. In general, in spectroscopy the pre-treatment should be done to prepare the data for an easier analysis, highlighting the real information stored in the data set without modifying it. For example, in Raman spectroscopy, this means not to remove the baseline, in the case it is necessary to know the influence of fluorescence contributions, or to apply a normalization on the data to spectral elements (like peak intensity or area) which are expected not to change or influence the evolution of interest. Subsequently, the actual analysis is applied onto the prepared data and, depending on the data and the elements under study, a different protocol is implemented. Some examples of analysis have been given in the previous section, but there are still plenty of options, reported in the references.

Among all the possibilities, it is important to stress out the emerging trend of using the machine learning (ML) approach in combination with multivariate data analysis.[216] Machine learning arises in the context of too vast and complex data sets for parsing without computational assistance. The fundamental scope is to train models that can be

used to classify observations into discrete groups, learn which features determine the variability in the samples, or predict the outcome of new experiments. The algorithms built for these scopes, learn from the training data itself to refine the accuracy of their prediction, typically minimizing a mathematical error function. The combination of this intuitive technique and the multivariate analysis, allows largely to take advantage of the merits of both techniques.

Thesis contents

The contents of this thesis have been developed on the basis of the considerations presented so far, which provide a general overview over theoretical and experimental aspects, and the state of the art of biological, technical and analytical background of the work. In particular, the first part of the thesis focused on developing an algorithm based on multivariate analysis to treat and analyse the SERS data, regarding the biological models chosen. In more detail, the MCF7 breast cancer cell line has been mainly investigated *in vitro*, both in simple 2D and more complex 3D cultures. The 3D cellular models have been realized by seeding the cells in complex structures, such as polymeric and hydrogel-based 3D-printed scaffolds, while letting them grow in real-like conditions. Considering that few investigations regarding 3D SERS bioimaging have been presented so far (see 3D cellular models in **Section 1.2**), the thesis focused also on the study of the interaction of SERS tags with cells, to characterize fundamental aspects, such as the dwelling time of the NPs inside cells or the eventual phototoxicity induced by the NIR laser. In addition, we explored in the thesis the optimization of the parameters for 3D measurements, aiming at obtaining sharp images, which are spatially and temporarily representative of the biological sample under examination. Hence, the most important parameters, such as laser power, exposure time, maximum volume scanned, while maintaining a step size which ensures enough spatial and temporal accuracies, have been investigated for different 3D SERS-labelled complex samples.

References:

(1) Ansari, B.; Morton, M. J.; Adamczyk, D. L.; Jones, K. N.; Brodt, J. K.; Degnim, A. C.; Jakub, J. W.; Lohse, C. M.; Boughey, J. C. Distance of Breast Cancer From the Skin and Nipple Impacts Axillary Nodal Metastases. *Ann. Surg. Oncol.* **2011**, *18*, 3174–3180. https://doi.org/10.1245/S10434-011-1957-Z.

(2) Sung, H.; Ferlay, J.; Siegel, R. L.; Laversanne, M.; Soerjomataram, I.; Jemal, A.; Bray, F. Global Cancer Statistics 2020: GLOBOCAN Estimates of Incidence and Mortality Worldwide for 36 Cancers in 185 Countries. *CA. Cancer J. Clin.* **2021**, *71*, 209–249. https://doi.org/10.3322/CAAC.21660.

(3) Waks, A. G.; Winer, E. P. Breast Cancer Treatment: A Review. *JAMA* **2019**, *321*, 288–300. https://doi.org/10.1001/JAMA.2018.19323.

(4) Cooper, G. M. The Development and Causes of Cancer. In *The Cell: A Molecular Approach.*; Associates, S., Ed.; Sinauer Associates, 2000.

(5) Aseervatham, J. Cytoskeletal Remodeling in Cancer. *Biology (Basel).* **2020**, *9*, 385. https://doi.org/10.3390/BIOLOGY9110385.

(6) Quintero-Fabián, S.; Arreola, R.; Becerril-Villanueva, E.; Torres-Romero, J. C.; Arana-Argáez, V.; Lara-Riegos, J.; Ramírez-Camacho, M. A.; Alvarez-Sánchez, M. E. Role of Matrix Metalloproteinases in Angiogenesis and Cancer. *Front. Oncol.* **2019**, *9*, 1370. https://doi.org/10.3389/FONC.2019.01370.

(7) Welch, D. R.; Hurst, D. R. Defining the Hallmarks of Metastasis. *Cancer Res.* **2019**, *79*, 3011–3027. https://doi.org/10.1158/0008-5472.CAN-19-0458.

(8) Condeelis, J.; Weissleder, R. In Vivo Imaging in Cancer. *Cold Spring Harb. Perspect. Biol.* **2010**, *2*, a003848. https://doi.org/10.1101/CSHPERSPECT.A003848.

(9) Kapsokalyvas, D.; van Zandvoort, M. A. M. J. Molecular Imaging in Oncology: Advanced Microscopy Techniques. *Recent Results Cancer Res.* **2020**, *216*, 533–561. https://doi.org/10.1007/978-3-030-42618-7_16.

(10) Zhang, Y.; Li, M.; Gao, X.; Chen, Y.; Liu, T. Nanotechnology in Cancer Diagnosis: Progress, Challenges and Opportunities. *J. Hematol. Oncol.* **2019**, *12*, 137. https://doi.org/10.1186/S13045-019-0833-3.

(11) Tanaka, K.; Toiyama, Y.; Okugawa, Y.; Okigami, M.; Inoue, Y.; Uchida, K.; Araki, T.; Mohri, Y.; Mizoguchi, A.; Kusunoki, M. In Vivo Optical Imaging of Cancer Metastasis Using Multiphoton Microscopy: A Short Review. *Am. J. Transl. Res.* **2014**, *6*, 179–187. https://doi.org/24936213.

(12) Langer, J.; Jiménez de Aberasturi, D.; Aizpurua, J.; Alvarez-Puebla, R. A.; Auguié, B.; Baumberg, J. J.; Bazan, G. C.; Bell, S. E. J.; Boisen, A.; Brolo, A. G.; et al. Present and Future of Surface-Enhanced Raman Scattering. *ACS Nano* **2020**, *14*, 28–117. https://doi.org/10.1021/acsnano.9b04224.

(13) Bissell, M. J.; Hines, W. C. Why Don't We Get More Cancer? A Proposed Role of the Microenvironment in Restraining Cancer Progression. *Nat. Med.* **2011**, *17*, 320–329. https://doi.org/10.1038/NM.2328.

(14) Soysal, S. D.; Tzankov, A.; Muenst, S. E. Role of the Tumor Microenvironment in Breast Cancer. *Pathobiology* **2015**, *82*, 142–152. https://doi.org/10.1159/000430499.

(15) Bremnes, R. M.; Dønnem, T.; Al-Saad, S.; Al-Shibli, K.; Andersen, S.; Sirera, R.; Camps, C.; Marinez, I.; Busund, L. T. The Role of Tumor Stroma in Cancer

Progression and Prognosis: Emphasis on Carcinoma-Associated Fibroblasts and Non-Small Cell Lung Cancer. *J. Thorac. Oncol.* **2011**, *6*, 209–217. https://doi.org/10.1097/JTO.0B013E3181F8A1BD.

(16) Huang, J.; Zhang, L.; Wan, D.; Zhou, L.; Zheng, S.; Lin, S.; Qiao, Y. Extracellular Matrix and Its Therapeutic Potential for Cancer Treatment. *Signal Transduct. Target. Ther. 2021 61* **2021**, *6*, 153. https://doi.org/10.1038/s41392-021-00544-0.

(17) Baghban, R.; Roshangar, L.; Jahanban-Esfahlan, R.; Seidi, K.; Ebrahimi-Kalan, A.; Jaymand, M.; Kolahian, S.; Javaheri, T.; Zare, P. Tumor Microenvironment Complexity and Therapeutic Implications at a Glance. *Cell Commun. Signal. 2020 181* **2020**, *18*, 59. https://doi.org/10.1186/S12964-020-0530-4.

(18) Chaicharoenaudomrung, N.; Kunhorm, P.; Noisa, P. Three-Dimensional Cell Culture Systems as an in Vitro Platform for Cancer and Stem Cell Modeling. *World J. Stem Cells* **2019**, *11*, 1065–1083. https://doi.org/10.4252/WJSC.V11.I12.1065.

(19) Breast cancer https://www.cancer.net/cancer-types/breast-cancer/statistics.

(20) Augustine, R.; Kalva, S. N.; Ahmad, R.; Zahid, A. A.; Hasan, S.; Nayeem, A.; McClements, L.; Hasan, A. 3D Bioprinted Cancer Models: Revolutionizing Personalized Cancer Therapy. *Transl. Oncol.* **2021**, *14*, 101015. https://doi.org/10.1016/J.TRANON.2021.101015.

(21) Malakpour Permlid, A.; Rocci, P.; Fredlund, E.; Fält, F.; Önell, E.; Johansson, F.; Oredsson, S. Unique Animal Friendly 3D Culturing of Human Cancer and Normal Cells. *Toxicol. Vitr.* **2019**, *60*, 51–60. https://doi.org/10.1016/J.TIV.2019.04.022.

(22) Dunne, L. W.; Huang, Z.; Meng, W.; Fan, X.; Zhang, N.; Zhang, Q.; An, Z. Human Decellularized Adipose Tissue Scaffold as a Model for Breast Cancer Cell Growth and Drug Treatments. *Biomaterials* **2014**, *35*, 4940–4949. https://doi.org/10.1016/J.BIOMATERIALS.2014.03.003.

(23) Jensen, C.; Teng, Y. Is It Time to Start Transitioning From 2D to 3D Cell Culture? *Front. Mol. Biosci.* **2020**, *7*, 33. https://doi.org/10.3389/FMOLB.2020.00033/BIBTEX.

(24) Imamura, Y.; Mukohara, T.; Shimono, Y.; Funakoshi, Y.; Chayahara, N.; Toyoda, M.; Kiyota, N.; Takao, S.; Kono, S.; Nakatsura, T.; et al. Comparison of 2D- and 3D-Culture Models as Drug-Testing Platforms in Breast Cancer. *Oncol. Rep.* **2015**, *33*, 1837–1843. https://doi.org/10.3892/OR.2015.3767.

(25) Saraiva, D. P.; Matias, A. T.; Braga, S.; Jacinto, A.; Cabral, M. G. Establishment of a 3D Co-Culture With MDA-MB-231 Breast Cancer Cell Line and Patient-Derived Immune Cells for Application in the Development of Immunotherapies. *Front. Oncol.* **2020**, *10*, 1543. https://doi.org/10.3389/FONC.2020.01543.

(26) Reynolds, D. S.; Tevis, K. M.; Blessing, W. A.; Colson, Y. L.; Zaman, M. H.; Grinstaff, M. W. Breast Cancer Spheroids Reveal a Differential Cancer Stem Cell Response to Chemotherapeutic Treatment. *Sci. Rep.* **2017**, *7*, 10382. https://doi.org/10.1038/s41598-017-10863-4.

(27) Yakavets, I.; Francois, A.; Benoit, A.; Merlin, J. L.; Bezdetnaya, L.; Vogin, G. Advanced Co-Culture 3D Breast Cancer Model for Investigation of Fibrosis Induced by External Stimuli: Optimization Study. *Sci. Reports 2020 101* **2020**, *10*, 21273. https://doi.org/10.1038/s41598-020-78087-7.

(28) Vila-Parrondo, C.; García-Astrain, C.; Liz-Marzán, L. M. Colloidal Systems toward 3D Cell Culture Scaffolds. *Adv. Colloid Interface Sci.* **2020**, *283*, 102237.

https://doi.org/10.1016/J.CIS.2020.102237.

(29) Nichol, J. W.; Khademhosseini, A. Modular Tissue Engineering: Engineering Biological Tissues from the Bottom Up. *Soft Matter* **2009**, *5*, 1312–1319. https://doi.org/10.1039/B814285H.

(30) Nikolova, M. P.; Chavali, M. S. Recent Advances in Biomaterials for 3D Scaffolds: A Review. *Bioact. Mater.* **2019**, *4*, 271–292. https://doi.org/10.1016/J.BIOACTMAT.2019.10.005.

(31) Murphy, S. V.; Atala, A. 3D Bioprinting of Tissues and Organs. *Nat. Biotechnol.* **2014**, *32*, 773–785. https://doi.org/10.1038/NBT.2958.

(32) Zhao, Y.; Yao, R.; Ouyang, L.; Ding, H.; Zhang, T.; Zhang, K.; Cheng, S.; Sun, W. Three-Dimensional Printing of Hela Cells for Cervical Tumor Model in Vitro. *Biofabrication* **2014**, *6*, 035001. https://doi.org/10.1088/1758-5082/6/3/035001.

(33) Melchiorri, A. J.; Hibino, N.; Best, C. A.; Yi, T.; Lee, Y. U.; Kraynak, C. A.; Kimerer, L. K.; Krieger, A.; Kim, P.; Breuer, C. K.; et al. 3D-Printed Biodegradable Polymeric Vascular Grafts. *Adv. Healthc. Mater.* **2016**, *5*, 319–325. https://doi.org/10.1002/ADHM.201500725.

(34) Sánchez-Téllez, D. A.; Téllez-Jurado, L.; Rodríguez-Lorenzo, L. M. Hydrogels for Cartilage Regeneration, from Polysaccharides to Hybrids. *Polym.* **2017**, *9*, 671. https://doi.org/10.3390/POLYM9120671.

(35) Yao, Q.; Wei, B.; Guo, Y.; Jin, C.; Du, X.; Yan, C.; Yan, J.; Hu, W.; Xu, Y.; Zhou, Z.; et al. Design, Construction and Mechanical Testing of Digital 3D Anatomical Data-Based PCL–HA Bone Tissue Engineering Scaffold. *J. Mater. Sci. Mater. Med. 2015 261* **2015**, *26*, 51. https://doi.org/10.1007/S10856-014-5360-8.

(36) Yan, Q.; Dong, H.; Su, J.; Han, J.; Song, B.; Wei, Q.; Shi, Y. A Review of 3D Printing Technology for Medical Applications. *Engineering* **2018**, *4*, 729–742. https://doi.org/10.1016/J.ENG.2018.07.021.

(37) Vaezi, M.; Zhong, G.; Kalami, H.; Yang, S. Extrusion-Based 3D Printing Technologies for 3D Scaffold Engineering. In *Functional 3D Tissue Engineering Scaffolds*; Deng, Y., Jordan, K., Eds.; Woodhead Publishing, 2018; Vol. 14, pp 235–254. https://doi.org/https://doi.org/10.1016/B978-0-08-100979-6.00010-0.

(38) Mustapha, K. B.; Metwalli, K. M. A Review of Fused Deposition Modelling for 3D Printing of Smart Polymeric Materials and Composites. *Eur. Polym. J.* **2021**, *156*, 110591. https://doi.org/10.1016/J.EURPOLYMJ.2021.110591.

(39) Aguilar-De-leyva, Á.; Linares, V.; Casas, M.; Caraballo, I. 3D Printed Drug Delivery Systems Based on Natural Products. *Pharmaceutics* **2020**, *12*, 620. https://doi.org/10.3390/PHARMACEUTICS12070620.

(40) Guo, Y.; Patanwala, H. S.; Bognet, B.; Ma, A. W. K. Inkjet and Inkjet-Based 3D Printing: Connecting Fluid Properties and Printing Performance. *Rapid Prototyp. J.* **2017**, *23*, 562–576. https://doi.org/10.1108/RPJ-05-2016-0076.

(41) Ko, S. H. Advanced Inkjet Technology for 3D Micro-Metal Structure Fabrication. In *Micromanufacturing Engineering and Technology: Second Edition*; William Andrew Publishing, 2015; pp 425–439. https://doi.org/10.1016/B978-0-323-31149-6.00018-9.

(42) Zhang, J.; Hu, Q.; Wang, S.; Tao, J.; Gou, M. Digital Light Processing Based Three-Dimensional Printing for Medical Applications. *Int. J. Bioprinting* **2020**, *6*, 242.

https://doi.org/10.18063/IJB.V6I1.242.

(43) Zhu, W.; Ma, X.; Gou, M.; Mei, D.; Zhang, K.; Chen, S. 3D Printing of Functional Biomaterials for Tissue Engineering. *Curr. Opin. Biotechnol.* **2016**, *40*, 103–112. https://doi.org/10.1016/J.COPBIO.2016.03.014.

(44) Ahmed, E. M. Hydrogel: Preparation, Characterization, and Applications: A Review. *J. Adv. Res.* **2015**, *6*, 105–121. https://doi.org/10.1016/J.JARE.2013.07.006.

(45) Martin, V.; Ribeiro, I. A.; Alves, M. M.; Gonçalves, L.; Claudio, R. A.; Grenho, L.; Fernandes, M. H.; Gomes, P.; Santos, C. F.; Bettencourt, A. F. Engineering a Multifunctional 3D-Printed PLA-Collagen-Minocycline-NanoHydroxyapatite Scaffold with Combined Antimicrobial and Osteogenic Effects for Bone Regeneration. *Mater. Sci. Eng. C* **2019**, *101*, 15–26. https://doi.org/10.1016/J.MSEC.2019.03.056.

(46) Wang, P.; Berry, D.; Moran, A.; He, F.; Tam, T.; Chen, L.; Chen, S. Controlled Growth Factor Release in 3D-Printed Hydrogels. *Adv. Healthc. Mater.* **2020**, *9*, 1900977. https://doi.org/10.1002/ADHM.201900977.

(47) Murphy, R.; Walsh, D. P.; Hamilton, C. A.; Cryan, S. A.; In Het Panhuis, M.; Heise, A. Degradable 3D-Printed Hydrogels Based on Star-Shaped Copolypeptides. *Biomacromolecules* **2018**, *19*, 2691–2699. https://doi.org/10.1021/ACS.BIOMAC.8B00299/SUPPL_FILE/BM8B00299_SI_003.AVI.

(48) Liu, Q.; Li, Q.; Xu, S.; Zheng, Q.; Cao, X. Preparation and Properties of 3D Printed Alginate–Chitosan Polyion Complex Hydrogels for Tissue Engineering. *Polym. 2018, Vol. 10, Page 664* **2018**, *10*, 664. https://doi.org/10.3390/POLYM10060664.

(49) Gyles, D. A.; Castro, L. D.; Silva, J. O. C.; Ribeiro-Costa, R. M. A Review of the Designs and Prominent Biomedical Advances of Natural and Synthetic Hydrogel Formulations. *Eur. Polym. J.* **2017**, *88*, 373–392. https://doi.org/10.1016/J.EURPOLYMJ.2017.01.027.

(50) Janarthanan, G.; Shin, H. S.; Kim, I. G.; Ji, P.; Chung, E. J.; Lee, C.; Noh, I. Self-Crosslinking Hyaluronic Acid–Carboxymethylcellulose Hydrogel Enhances Multilayered 3D-Printed Construct Shape Integrity and Mechanical Stability for Soft Tissue Engineering. *Biofabrication* **2020**, *12*, 045026. https://doi.org/10.1088/1758-5090/ABA2F7.

(51) Tessmar, J. K.; Göpferich, A. M. Customized PEG-Derived Copolymers for Tissue-Engineering Applications. *Macromol. Biosci.* **2007**, *7*, 23–39. https://doi.org/10.1002/MABI.200600096.

(52) Christensen, R. K.; Von Halling Laier, C.; Kiziltay, A.; Wilson, S.; Larsen, N. B. 3D Printed Hydrogel Multiassay Platforms for Robust Generation of Engineered Contractile Tissues. *Biomacromolecules* **2020**, *21*, 356–365. https://doi.org/10.1021/ACS.BIOMAC.9B01274.

(53) Cidonio, G.; Glinka, M.; Dawson, J. I.; Oreffo, R. O. C. The Cell in the Ink: Improving Biofabrication by Printing Stem Cells for Skeletal Regenerative Medicine. *Biomaterials* **2019**, *209*, 10–24. https://doi.org/10.1016/J.BIOMATERIALS.2019.04.009.

(54) Lee, A.; Hudson, A. R.; Shiwarski, D. J.; Tashman, J. W.; Hinton, T. J.; Yerneni, S.; Bliley, J. M.; Campbell, P. G.; Feinberg, A. W. 3D Bioprinting of Collagen to Rebuild

Components of the Human Heart. *Science (80-.).* **2019**, *365*, 482–487. https://doi.org/10.1126/SCIENCE.AAV9051/SUPPL_FILE/AAV9051S9.MP4.

(55) Zhai, X.; Ma, Y.; Hou, C.; Gao, F.; Zhang, Y.; Ruan, C.; Pan, H.; Lu, W. W.; Liu, W. 3D-Printed High Strength Bioactive Supramolecular Polymer/Clay Nanocomposite Hydrogel Scaffold for Bone Regeneration. *ACS Biomater. Sci. Eng.* **2017**, *3*, 1109–1118. https://doi.org/10.1021/ACSBIOMATERIALS.7B00224.

(56) Jaiswal, M. K.; Xavier, J. R.; Carrow, J. K.; Desai, P.; Alge, D.; Gaharwar, A. K. Mechanically Stiff Nanocomposite Hydrogels at Ultralow Nanoparticle Content. *ACS Nano* **2016**, *10*, 246–256. https://doi.org/10.1021/ACSNANO.5B03918.

(57) Ashammakhi, N.; Ahadian, S.; Zengjie, F.; Suthiwanich, K.; Lorestani, F.; Orive, G.; Ostrovidov, S.; Khademhosseini, A. Advances and Future Perspectives in 4D Bioprinting. *Biotechnol. J.* **2018**, *13*, 1800148. https://doi.org/10.1002/BIOT.201800148.

(58) Tijing, L. D.; Dizon, J. R. C.; Ibrahim, I.; Nisay, A. R. N.; Shon, H. K.; Advincula, R. C. 3D Printing for Membrane Separation, Desalination and Water Treatment. *Appl. Mater. Today* **2020**, *18*, 100486. https://doi.org/10.1016/J.APMT.2019.100486.

(59) Advincula, R. C.; Dizon, J. R. C.; Caldona, E. B.; Viers, R. A.; Siacor, F. D. C.; Maalihan, R. D.; Espera, A. H. On the Progress of 3D-Printed Hydrogels for Tissue Engineering. *MRS Commun.* **2021**, *11*, 539–553. https://doi.org/10.1557/S43579-021-00069-1/FIGURES/4.

(60) Ball, P. Feynman' s fancy https://www.chemistryworld.com/features/feynmans-fancy/3004592.article.

(61) Hu, Z.; Ott, P. A.; Wu, C. J. Towards Personalized, Tumour-Specific, Therapeutic Vaccines for Cancer. *Nat. Rev. Immunol.* **2017**, *18*, 168–182. https://doi.org/10.1038/nri.2017.131.

(62) Nikalje, A. P. Nanotechnology and Its Applications in Medicine. *Med. Chem. (Los. Angeles).* **2015**, *5*, 1–9. https://doi.org/10.4172/2161-0444.1000247.

(63) Jong, W. H. De; Borm, P. J. Drug Delivery and Nanoparticles: Applications and Hazards. *Int. J. Nanomedicine* **2008**, *3*, 133–149. https://doi.org/10.2147/IJN.S596.

(64) Oberdörster, G.; Stone, V.; Donaldson, K. Toxicology of Nanoparticles: A Historical Perspective. *Nanotoxicology* **2007**, *1*, 2–25. https://doi.org/10.1080/17435390701314761.

(65) Ma, D.-D.; Yang, W.-X. Engineered Nanoparticles Induce Cell Apoptosis: Potential for Cancer Therapy. *Oncotarget* **2016**, *7*, 40882–40903. https://doi.org/10.18632/ONCOTARGET.8553.

(66) Matteis, V. De; Rinaldi, R. Toxicity Assessment in the Nanoparticle Era. In *Advances in Experimental Medicine and Biology*; Springer, Cham, 2018; Vol. 1048, pp 1–19. https://doi.org/10.1007/978-3-319-72041-8_1.

(67) Mansha, M.; Khan, I.; Ullah, N.; Qurashi, A. Synthesis, Characterization and Visible-Light-Driven Photoelectrochemical Hydrogen Evolution Reaction of Carbazole-Containing Conjugated Polymers. *Int. J. Hydrogen Energy* **2017**, *42*, 10952–10961. https://doi.org/10.1016/J.IJHYDENE.2017.02.053.

(68) Rao, J. P.; Geckeler, K. E. Polymer Nanoparticles: Preparation Techniques and Size-Control Parameters. *Prog. Polym. Sci.* **2011**, *36*, 887–913. https://doi.org/10.1016/j.progpolymsci.2011.01.001.

(69) Ellah, N. H. A.; Abouelmagd, S. A. Surface Functionalization of Polymeric Nanoparticles for Tumor Drug Delivery: Approaches and Challenges. *Expert Opin. Drug Deliv.* **2017**, *14*, 201–214. https://doi.org/10.1080/17425247.2016.1213238.

(70) Rawat, M. K.; Jain, A.; Singh, S. Studies on Binary Lipid Matrix Based Solid Lipid Nanoparticles of Repaglinide: In Vitro and in Vivo Evaluation. *J. Pharm. Sci.* **2011**, *100*, 2366–2378. https://doi.org/10.1002/JPS.22435.

(71) Mashaghi, S.; Jadidi, T.; Koenderink, G.; Mashaghi, A. Lipid Nanotechnology. *Int. J. Mol. Sci.* **2013**, *14*, 4242–4282. https://doi.org/10.3390/IJMS14024242.

(72) Puri, A.; Loomis, K.; Smith, B.; Lee, J.-H.; Yavlovich, A.; Heldman, E.; Blumenthal, R. Lipid-Based Nanoparticles as Pharmaceutical Drug Carriers: From Concepts to Clinic. *Crit. Rev. Ther. Drug Carr. Syst.* **2009**, *26*, 523–580. https://doi.org/10.1615/CritRevTherDrugCarrierSyst.v26.i6.10.

(73) Astefanei, A.; Núñez, O.; Galceran, M. T. Characterisation and Determination of Fullerenes: A Critical Review. *Anal. Chim. Acta* **2015**, *882*, 1–21. https://doi.org/10.1016/J.ACA.2015.03.025.

(74) Aqel, A.; El-Nour, K. M. M. A.; Ammar, R. A. A.; Al-Warthan, A. Carbon Nanotubes, Science and Technology Part (I) Structure, Synthesis and Characterisation. *Arab. J. Chem.* **2012**, *5*, 1–23. https://doi.org/10.1016/J.ARABJC.2010.08.022.

(75) Sigmund, W.; Yuh, J.; Park, H.; Maneeratana, V.; Pyrgiotakis, G.; Daga, A.; Taylor, J.; Nino, J. C. Processing and Structure Relationships in Electrospinning of Ceramic Fiber Systems. *J. Am. Ceram. Soc.* **2006**, *89*, 395–407. https://doi.org/10.1111/J.1551-2916.2005.00807.X.

(76) Thomas, S.; Harshita, B. S. P.; Mishra, P.; Talegaonkar, S. Ceramic Nanoparticles: Fabrication Methods and Applications in Drug Delivery. *Curr. Pharm. Des.* **2015**, *21*, 6165–6188. https://doi.org/10.2174/1381612821666151027153246.

(77) Ali, S.; Khan, I.; Khan, S. A.; Sohail, M.; Ahmed, R.; Rehman, A. ur; Ansari, M. S.; Morsy, M. A. Electrocatalytic Performance of Ni@Pt Core–Shell Nanoparticles Supported on Carbon Nanotubes for Methanol Oxidation Reaction. *J. Electroanal. Chem.* **2017**, *795*, 17–25. https://doi.org/10.1016/j.jelechem.2017.04.040.

(78) Sun, S.; Murray, C. B.; Weller, D.; Folks, L.; Moser, A. Monodisperse FePt Nanoparticles and Ferromagnetic FePt Nanocrystal Superlattices. *Science (80-.).* **2000**, *287*, 1989–1992. https://doi.org/10.1126/SCIENCE.287.5460.1989.

(79) Reguera, J.; Langer, J.; Jiménez De Aberasturi, D.; Liz-Marzán, L. M. Anisotropic Metal Nanoparticles for Surface Enhanced Raman Scattering. *Chem. Soc. Rev.* **2017**, *46*, 3866–3885. https://doi.org/10.1039/c7cs00158d.

(80) Dreaden, E. C.; Alkilany, A. M.; Huang, X.; Murphy, C. J.; El-Sayed, M. A. The Golden Age: Gold Nanoparticles for Biomedicine. *Chem. Soc. Rev.* **2012**, *41*, 2740–2779. https://doi.org/10.1039/C1CS15237H.

(81) Henry, A. I.; Sharma, B.; Cardinal, M. F.; Kurouski, D.; Van Duyne, R. P. Surface-Enhanced Raman Spectroscopy Biosensing: In Vivo Diagnostics and Multimodal Imaging. *Anal. Chem.* **2016**, *88*, 6638–6647. https://doi.org/10.1021/acs.analchem.6b01597.

(82) Nayak, S.; Blumenfeld, N. R.; Laksanasopin, T.; Sia, S. K. Point-of-Care Diagnostics: Recent Developments in a Connected Age. *Anal. Chem.* **2017**, *89* (1), 102–123. https://doi.org/10.1021/acs.analchem.6b04630.

(83) Basile, K.; Kok, J.; Dwyer, D. E. Point-of-Care Diagnostics for Respiratory Viral Infections. *Expert Rev. Mol. Diagn.* **2018**, *18*, 75–83. https://doi.org/10.1080/14737159.2018.1419065.

(84) Klonoff, D. C. Point-of-Care Blood Glucose Meter Accuracy in the Hospital Setting. *Diabetes Spectr.* **2014**, *27*, 174–179. https://doi.org/10.2337/diaspect.27.3.174.

(85) Lewins, J. S. Future Directions in Minimally Invasive Intervention. *Trans. Am. Clin. Climatol. Assoc.* **2017**, *128*, 346–352.

(86) Willets, K. A.; Duyne, R. P. Van. Localized Surface Plasmon Resonance Spectroscopy and Sensing. *Annu Rev Phys Chem* **2007**, *58*, 267–297. https://doi.org/10.1146/ANNUREV.PHYSCHEM.58.032806.104607.

(87) Li, P.; Wu, Y.; Li, D.; Su, X.; Luo, C.; Wang, Y.; Hu, J.; Li, G.; Jiang, H.; Zhang, W. Seed-Mediated Synthesis of Tunable-Aspect-Ratio Gold Nanorods for Near-Infrared Photoacoustic Imaging. *Nanoscale Res. Lett.* **2018**, *13*, 313. https://doi.org/10.1186/S11671-018-2734-8.

(88) Mie, G. Beiträge Zur Optik Trüber Medien, Speziell Kolloidaler Metallösungen. *Ann. Phys.* **1908**, *330*, 377–445. https://doi.org/10.1002/ANDP.19083300302.

(89) Gans, R. Über Die Form Ultramikroskopischer Goldteilchen. *Ann. Phys.* **1912**, *342*, 881–900. https://doi.org/10.1002/ANDP.19123420503.

(90) Gans, R. Über Die Form Ultramikroskopischer Silberteilchen. *Ann. Phys.* **1915**, *352*, 270–284. https://doi.org/10.1002/ANDP.19153521006.

(91) Liz-Marzán, L. M. Tailoring Surface Plasmons through the Morphology and Assembly of Metal Nanoparticles. *Langmuir* **2006**, *22*, 32–41. https://doi.org/10.1021/LA0513353.

(92) Indrasekara, A. S. D. S.; Meyers, S.; Shubeita, S.; Feldman, L. C.; Gustafsson, T.; Fabris, L. Gold Nanostar Substrates for SERS-Based Chemical Sensing in the Femtomolar Regime. *Nanoscale* **2014**, *6*, 8891–8899. https://doi.org/10.1039/C4NR02513J.

(93) Kuttner, C.; Höller, R. P. M.; Quintanilla, M.; Schnepf, M. J.; Dulle, M.; Fery, A.; Liz-Marzán, L. M. SERS and Plasmonic Heating Efficiency from Anisotropic Core/Satellite Superstructures. *Nanoscale* **2019**, *11*, 17655–17663. https://doi.org/10.1039/C9NR06102A.

(94) Fleischmann, M.; Hendra, P. J.; McQuillan, A. J. Raman Spectra of Pyridine Adsorbed at a Silver Electrode. *Chem. Phys. Lett.* **1974**, *26*, 163–166. https://doi.org/10.1016/0009-2614(74)85388-1.

(95) Alvarez-Puebla, R. A.; Liz-Marzán, L. M. SERS-Based Diagnosis and Biodetection. *Small* **2010**, *6*, 604–610. https://doi.org/10.1002/SMLL.200901820.

(96) Zengin, A.; Tamer, U.; Caykara, T. Fabrication of a SERS Based Aptasensor for Detection of Ricin B Toxin. *J. Mater. Chem. B* **2015**, *3*, 306–315. https://doi.org/10.1039/C4TB00290C.

(97) Rodríguez-Lorenzo, L.; Álvarez-Puebla, R. A.; Pastoriza-Santos, I.; Mazzucco, S.; Stéphan, O.; Kociak, M.; Liz-Marzán, L. M.; García de Abajo, F. J. Zeptomol Detection Through Controlled Ultrasensitive Surface-Enhanced Raman Scattering. *J. Am. Chem. Soc.* **2009**, *131*, 4616–4618. https://doi.org/10.1021/ja809418t.

(98) Stiles, P. L.; Dieringer, J. A.; Shah, N. C.; Duyne, R. P. Van. Surface-Enhanced Raman Spectroscopy. *Annu. Rev. Anal. Chem. (Palo Alto. Calif).* **2008**, *1*, 601–626.

https://doi.org/10.1146/ANNUREV.ANCHEM.1.031207.112814.

(99) Almehmadi, L. M.; Curley, S. M.; Tokranova, N. A.; Tenenbaum, S. A.; Lednev, I. K. Surface Enhanced Raman Spectroscopy for Single Molecule Protein Detection. *Sci. Reports 2019 91* **2019**, *9*, 12356. https://doi.org/10.1038/s41598-019-48650-y.

(100) Sharma, B.; Frontiera, R. R.; Henry, A. I.; Ringe, E.; Van Duyne, R. P. SERS: Materials, Applications, and the Future. *Mater. Today* **2012**, *15*, 16–25. https://doi.org/10.1016/S1369-7021(12)70017-2.

(101) Kamińska, A.; Winkler, K.; Kowalska, A.; Witkowska, E.; Szymborski, T.; Janeczek, A.; Waluk, J. SERS-Based Immunoassay in a Microfluidic System for the Multiplexed Recognition of Interleukins from Blood Plasma: Towards Picogram Detection. *Sci. Rep.* **2017**, *7*, 10656. https://doi.org/10.1038/s41598-017-11152-w.

(102) Jiménez de Aberasturi, D.; Serrano-Montes, A. B.; Langer, J.; Henriksen-Lacey, M.; Parak, W. J.; Liz-Marzán, L. M. Surface Enhanced Raman Scattering Encoded Gold Nanostars for Multiplexed Cell Discrimination. *Chem. Mater.* **2016**, *28*, 6779–6790. https://doi.org/10.1021/acs.chemmater.6b03349.

(103) Fabris, L. SERS Tags: The Next Promising Tool for Personalized Cancer Detection? *ChemNanoMat* **2016**, *2*, 249–258. https://doi.org/10.1002/cnma.201500221.

(104) Ayas, S.; Cinar, G.; Ozkan, A. D.; Soran, Z.; Ekiz, O.; Kocaay, D.; Tomak, A.; Toren, P.; Kaya, Y.; Tunc, I.; et al. Label-Free Nanometer-Resolution Imaging of Biological Architectures through Surface Enhanced Raman Scattering. *Sci. Reports 2013 31* **2013**, *3*, 2624. https://doi.org/10.1038/srep02624.

(105) Ren, W.; Liu, J.; Guo, S.; Wang, E. SERS Imaging for Label-Free Detection of the Phospholipids Distribution in Hybrid Lipid Membrane. *Sci. China Chem. 2011 548* **2011**, *54*, 1334–1341. https://doi.org/10.1007/S11426-011-4312-0.

(106) García-Astrain, C.; Lenzi, E.; Jiménez de Aberasturi, D.; Henriksen-Lacey, M.; Binelli, M. R.; Liz-Marzán, L. M. 3D-Printed Biocompatible Scaffolds with Built-In Nanoplasmonic Sensors. *Adv. Funct. Mater.* **2020**, *30*, 2005407. https://doi.org/10.1002/ADFM.202005407.

(107) Jiménez de Aberasturi, D.; Henriksen-Lacey, M.; Litti, L.; Langer, J.; Liz-Marzán, L. M. Using SERS Tags to Image the Three-Dimensional Structure of Complex Cell Models. *Adv. Funct. Mater.* **2020**, *30*, 1909655. https://doi.org/10.1002/adfm.201909655.

(108) Fabris, L. Gold-Based SERS Tags for Biomedical Imaging. *J. Opt. (United Kingdom)* **2015**, *17*, 114002. https://doi.org/10.1088/2040-8978/17/11/114002.

(109) Cialla-May, D.; Zheng, X. S.; Weber, K.; Popp, J. Recent Progress in Surface-Enhanced Raman Spectroscopy for Biological and Biomedical Applications: From Cells to Clinics. *Chem. Soc. Rev.* **2017**, *46*, 3945–3961. https://doi.org/10.1039/c7cs00172j.

(110) Lenzi, E.; Jiménez de Aberasturi, D.; Liz-Marzán, L. M. Surface-Enhanced Raman Scattering Tags for Three-Dimensional Bioimaging and Biomarker Detection. *ACS Sensors* **2019**, *4*, 1126–1137. https://doi.org/10.1021/acssensors.9b00321.

(111) Strozyk, M. S.; de Aberasturi, D. J.; Gregory, J. V.; Brust, M.; Lahann, J.; Liz-Marzán, L. M. Spatial Analysis of Metal–PLGA Hybrid Microstructures Using 3D SERS Imaging. *Adv. Funct. Mater.* **2017**, *27*, 1701626. https://doi.org/10.1002/adfm.201701626.

(112) Strozyk, M. S.; Jimenez de Aberasturi, D.; Liz-Marzán, L. M. Composite Polymer Colloids for SERS-Based Applications. *Chem. Rec.* **2018**, *18*, 807–818. https://doi.org/10.1002/tcr.201700082.

(113) Bodelõn, G.; Montes-García, V.; Fernández-Lõpez, C.; Pastoriza-Santos, I.; Pérez-Juste, J.; Liz-Marzán, L. M. Au@pNIPAM SERRS Tags for Multiplex Immunophenotyping Cellular Receptors and Imaging Tumor Cells. *Small* **2015**, *11*, 4149–4157. https://doi.org/10.1002/smll.201500269.

(114) Wang, Y.; Schlücker, S. Rational Design and Synthesis of SERS Labels. *Analyst* **2013**, *138*, 2224–2238. https://doi.org/10.1039/c3an36866a.

(115) Wang, Y.; Yan, B.; Chen, L. SERS Tags: Novel Optical Nanoprobes for Bioanalysis. *Chem. Rev.* **2013**, *113*, 1391–1428. https://doi.org/10.1021/cr300120g.

(116) Brust, M.; Walker, M.; Bethell, D.; Schiffrin, D. J.; Whyman, R. Synthesis of Thiol-Derivatised Gold Nanoparticles in a Two-Phase Liquid–Liquid System. *J. Chem. Soc., Chem. Commun.* **1994**, 801–802. https://doi.org/10.1039/C39940000801.

(117) Bastús, N. G.; Comenge, J.; Puntes, V. Kinetically Controlled Seeded Growth Synthesis of Citrate-Stabilized Gold Nanoparticles of up to 200 Nm: Size Focusing versus Ostwald Ripening. *Langmuir* **2011**, *27*, 11098–11105. https://doi.org/10.1021/la201938u.

(118) Scarabelli, L.; Sánchez-Iglesias, A.; Pérez-Juste, J.; Liz-Marzán, L. M. A "Tips and Tricks" Practical Guide to the Synthesis of Gold Nanorods. *J. Phys. Chem. Lett.* **2015**, *6*, 4270–4279. https://doi.org/10.1021/acs.jpclett.5b02123.

(119) Hemmer, E.; Venkatachalam, N.; Hyodo, H.; Hattori, A.; Ebina, Y.; Kishimoto, H.; Soga, K. Upconverting and NIR Emitting Rare Earth Based Nanostructures for NIR-Bioimaging. *Nanoscale* **2013**, *5*, 11339–11361. https://doi.org/10.1039/c3nr02286b.

(120) Hemmer, E.; Benayas, A.; Légaré, F.; Vetrone, F. Exploiting the Biological Windows: Current Perspectives on Fluorescent Bioprobes Emitting above 1000 Nm. *Nanoscale Horizons* **2016**, *1*, 168–184. https://doi.org/10.1039/C5NH00073D.

(121) Guerrero-Martínez, A.; Barbosa, S.; Pastoriza-Santos, I.; Liz-Marzán, L. M. Nanostars Shine Bright for You: Colloidal Synthesis, Properties and Applications of Branched Metallic Nanoparticles. *Curr. Opin. Colloid Interface Sci.* **2011**, *16*, 118–127. https://doi.org/10.1016/j.cocis.2010.12.007.

(122) Li, T. Da; Zhang, R.; Chen, H.; Huang, Z. P.; Ye, X.; Wang, H.; Deng, A. M.; Kong, J. L. An Ultrasensitive Polydopamine Bi-Functionalized SERS Immunoassay for Exosome-Based Diagnosis and Classification of Pancreatic Cancer. *Chem. Sci.* **2018**, *9*, 5372–5382. https://doi.org/10.1039/c8sc01611a.

(123) Halas, N. J.; Lal, S.; Chang, W.-S.; Link, S.; Nordlander, P. Plasmons in Strongly Coupled Metallic Nanostructures. *Chem. Rev.* **2011**, *111*, 3913–3961. https://doi.org/10.1021/cr200061k.

(124) Kim, H.-M.; Kim, D.-M.; Jeong, C.; Park, S. Y.; Cha, M. G.; Ha, Y.; Jang, D.; Kyeong, S.; Pham, X.-H.; Hahm, E.; et al. Assembly of Plasmonic and Magnetic Nanoparticles with Fluorescent Silica Shell Layer for Tri-Functional SERS-Magnetic-Fluorescence Probes and Its Bioapplications. *Sci. Rep.* **2018**, *8*, 13938. https://doi.org/10.1038/s41598-018-32044-7.

(125) Khlebtsov, B.; Pylaev, T.; Khanadeev, V.; Bratashov, D.; Khlebtsov, N. Quantitative and Multiplex Dot-Immunoassay Using Gap-Enhanced Raman Tags. *RSC Adv.*

2017, *7*, 40834–40841. https://doi.org/10.1039/c7ra08113h.

(126) Wang, Y.; Serrano, A. B.; Sentosun, K.; Bals, S.; Liz-Marzán, L. M. Stabilization and Encapsulation of Gold Nanostars Mediated by Dithiols. *Small* **2015**, *11*, 4314–4320. https://doi.org/10.1002/smll.201500703.

(127) Vilar-Vidal, N.; Bonhommeau, S.; Talaga, D.; Ravaine, S. One-Pot Synthesis of Gold Nanodimers and Their Use as Surface-Enhanced Raman Scattering Tags. *New J. Chem.* **2016**, *40*, 7299–7302. https://doi.org/10.1039/c6nj01389a.

(128) Yang, Y.; Wang, Y.; Jin, S.-M.; Xu, J.; Hou, Z.; Ren, J.; Wang, K.; Lee, E.; Zhang, L.; Zhang, Y.; et al. 3D Confined Assembly of Polymer-Tethered Gold Nanoparticles into Size-Segregated Structures. *Mater. Chem. Front.* **2019**, *3*, 209–215. https://doi.org/10.1039/C8QM00560E.

(129) Rodríguez-Fernández, D.; Langer, J.; Henriksen-Lacey, M.; Liz-Marzán, L. M. Hybrid Au–SiO2 Core–Satellite Colloids as Switchable SERS Tags. *Chem. Mater.* **2015**, *27*, 2540–2545. https://doi.org/10.1021/acs.chemmater.5b00128.

(130) Atta, S.; Beetz, M.; Fabris, L. Understanding the Role of AgNO 3 Concentration and Seed Morphology in the Achievement of Tunable Shape Control in Gold Nanostars. *Nanoscale* **2019**, *11*, 2946–2958. https://doi.org/10.1039/C8NR07615D.

(131) Scarabelli, L.; Schumacher, M.; Jimenez de Aberasturi, D.; Merkl, J.-P.; Henriksen-Lacey, M.; Milagres de Oliveira, T.; Janschel, M.; Schmidtke, C.; Bals, S.; Weller, H.; et al. Encapsulation of Noble Metal Nanoparticles through Seeded Emulsion Polymerization as Highly Stable Plasmonic Systems. *Adv. Funct. Mater.* **2019**, *29*, 1809071. https://doi.org/10.1002/adfm.201809071.

(132) Leigh, S. Y.; Som, M.; Liu, J. T. C. Method for Assessing the Reliability of Molecular Diagnostics Based on Multiplexed SERS-Coded Nanoparticles. *PLoS One* **2013**, *8*, e62084. https://doi.org/10.1371/journal.pone.0062084.

(133) Laing, S.; Jamieson, L. E.; Faulds, K.; Graham, D. Surface-Enhanced Raman Spectroscopy for in Vivo Biosensing. *Nat. Rev. Chem.* **2017**, *1*, 0060. https://doi.org/10.1038/s41570-017-0060.

(134) Serrano-Montes, A. B.; Jimenez de Aberasturi, D.; Langer, J.; Giner-Casares, J. J.; Scarabelli, L.; Herrero, A.; Liz-Marzán, L. M. A General Method for Solvent Exchange of Plasmonic Nanoparticles and Self-Assembly into SERS-Active Monolayers. *Langmuir* **2015**, *31*, 9205–9213. https://doi.org/10.1021/acs.langmuir.5b01838.

(135) Luo, Z.; Zhao, Y.; Darwish, T.; Wang, Y.; Hou, J.; Stellacci, F. Mass Spectrometry and Monte Carlo Method Mapping of Nanoparticle Ligand Shell Morphology. *Nat. Commun.* **2018**, *9*, 4478. https://doi.org/10.1038/s41467-018-06939-y.

(136) McLintock, A.; Cunha-Matos, C. A.; Zagnoni, M.; Millington, O. R.; Wark, A. W. Universal Surface-Enhanced Raman Tags: Individual Nanorods for Measurements from the Visible to the Infrared (514–1064 Nm). *ACS Nano* **2014**, *8*, 8600–8609. https://doi.org/10.1021/nn503311d.

(137) Schütz, M.; Müller, C. I.; Salehi, M.; Lambert, C.; Schlücker, S. Design and Synthesis of Raman Reporter Molecules for Tissue Imaging by Immuno-SERS Microscopy. *J. Biophotonics* **2011**, *4*, 453–463. https://doi.org/10.1002/jbio.201000116.

(138) Yang, S.-A.; Choi, S.; Jeon, S. M.; Yu, J. Silica Nanoparticle Stability in Biological Media Revisited. *Sci. Rep.* **2018**, *8*, 185. https://doi.org/10.1038/s41598-017-18502-8.

(139) Mulvaney, S. P.; Musick, M. D.; Keating, C. D.; Natan, M. J. Glass-Coated, Analyte-Tagged Nanoparticles: A New Tagging System Based on Detection with Surface-Enhanced Raman Scattering. *Langmuir* **2003**, *19*, 4784–4790. https://doi.org/10.1021/LA026706J.

(140) Sanz-Ortiz, M. N.; Sentosun, K.; Bals, S.; Liz-Marzán, L. M. Templated Growth of Surface Enhanced Raman Scattering-Active Branched Gold Nanoparticles within Radial Mesoporous Silica Shells. *ACS Nano* **2015**, *9*, 10489–10497. https://doi.org/10.1021/acsnano.5b04744.

(141) Ott, A.; Yu, X.; Hartmann, R.; Rejman, J.; Schütz, A.; Ochs, M.; Parak, W. J.; Carregal-Romero, S. Light-Addressable and Degradable Silica Capsules for Delivery of Molecular Cargo to the Cytosol of Cells. *Chem. Mater.* **2015**, *27*, 1929–1942. https://doi.org/10.1021/cm502472g.

(142) Hanske, C.; Sanz-Ortiz, M. N.; Liz-Marzán, L. M. Silica-Coated Plasmonic Metal Nanoparticles in Action. *Adv. Mater.* **2018**, *30*, 1707003. https://doi.org/10.1002/adma.201707003.

(143) Damodaran, V. B.; Murthy, N. S. Bio-Inspired Strategies for Designing Antifouling Biomaterials. *Biomater. Res.* **2016**, *20*, 18. https://doi.org/10.1186/s40824-016-0064-4.

(144) Dinish, U. S.; Balasundaram, G.; Chang, Y. T.; Olivo, M. Actively Targeted in Vivo Multiplex Detection of Intrinsic Cancer Biomarkers Using Biocompatible SERS Nanotags. *Sci. Rep.* **2014**, *4*, 4075. https://doi.org/10.1038/srep04075.

(145) Rivera-Gil, P.; Jimenez De Aberasturi, D.; Wulf, V.; Pelaz, B.; Del Pino, P.; Zhao, Y.; De La Fuente, J. M.; Ruiz De Larramendi, I.; Rojo, T.; Liang, X.-J.; et al. The Challenge To Relate the Physicochemical Properties of Colloidal Nanoparticles to Their Cytotoxicity. *Acc. Chem. Res.* **2013**, *46*, 743–749. https://doi.org/10.1021/ar300039j.

(146) Pellegrino, T.; Manna, L.; Kudera, S.; Liedl, T.; Koktysh, D.; Rogach, A. L.; Keller, S.; Rädler, J.; Natile, G.; Parak, W. J. Hydrophobic Nanocrystals Coated with an Amphiphilic Polymer Shell: A General Route to Water Soluble Nanocrystals. *Nano Lett.* **2004**, *4*, 703–707. https://doi.org/10.1021/nl035172j.

(147) Alipour, E.; Halverson, D.; McWhirter, S.; Walker, G. C. Phospholipid Bilayers: Stability and Encapsulation of Nanoparticles. *Annu. Rev. Phys. Chem.* **2017**, *68*, 261–283. https://doi.org/10.1146/annurev-physchem-040215-112634.

(148) Alsamamra, H.; Hawwarin, I.; Sharkh, S. A.; Abuteir, M. Study the Interaction between Gold Nanoparticles and Bovine Serum Albumin: Spectroscopic Approach. *J. Bioanal. Biomed.* **2018**, *10*, 43–49. https://doi.org/10.4172/1948-593X.1000203.

(149) Brewer, S. H.; Glomm, W. R.; Johnson, M. C.; Knag, M. K.; Franzen, S. Probing BSA Binding to Citrate-Coated Gold Nanoparticles and Surfaces. *Langmuir* **2005**, *21*, 9303–9307. https://doi.org/10.1021/la050588t.

(150) Attarwala, H. Role of Antibodies in Cancer Targeting. *J. Nat. Sci. Biol. Med.* **2010**, *1*, 53–56. https://doi.org/10.4103/0976-9668.71675.

(151) Mousavizadeh, A.; Jabbari, A.; Akrami, M.; Bardania, H. Cell Targeting Peptides as Smart Ligands for Targeting of Therapeutic or Diagnostic Agents: A Systematic Review. *Colloids Surfaces B Biointerfaces* **2017**, *158*, 507–517. https://doi.org/10.1016/J.COLSURFB.2017.07.012.

(152) Nicolson, F.; Jamieson, L. E.; Mabbott, S.; Plakas, K.; Shand, N. C.; Detty, M. R.;

Graham, D.; Faulds, K. Multiplex Imaging of Live Breast Cancer Tumour Models through Tissue Using Handheld Surface Enhanced Spatially Offset Resonance Raman Spectroscopy (SESORRS). *Chem. Commun.* **2018**, *54*, 8530–8533. https://doi.org/10.1039/C8CC04267E.

(153) Kang, S.; Wang, Y.; Reder, N. P.; Liu, J. T. C. Multiplexed Molecular Imaging of Biomarker-Targeted SERS Nanoparticles on Fresh Tissue Specimens with Channel-Compressed Spectrometry. *PLoS One* **2016**, *11*, e0163473. https://doi.org/10.1371/journal.pone.0163473.

(154) Hu, Z.; Tan, J.; Lai, Z.; Zheng, R.; Zhong, J.; Wang, Y.; Li, X.; Yang, N.; Li, J.; Yang, W.; et al. Aptamer Combined with Fluorescent Silica Nanoparticles for Detection of Hepatoma Cells. *Nanoscale Res. Lett.* **2017**, *12*, 96. https://doi.org/10.1186/s11671-017-1890-6.

(155) Tkachenko, A.; Xie, H.; Franzen, S.; Feldheim, D. L. Assembly and Characterization of Biomolecule–Gold Nanoparticle Conjugates and Their Use in Intracellular Imaging. *Methods Mol Biol.* **2005**, *303*, 85–100. https://doi.org/10.1385/1-59259-901-X:085.

(156) Harmsen, S.; Rogalla, S.; Huang, R.; Spaliviero, M.; Neuschmelting, V.; Hayakawa, Y.; Lee, Y.; Tailor, Y.; Toledo-Crow, R.; Kang, J. W.; et al. Detection of Premalignant Gastrointestinal Lesions Using Surface-Enhanced Resonance Raman Scattering-Nanoparticle Endoscopy. *ACS Nano* **2019**, *13*, 1354–1364. https://doi.org/10.1021/ACSNANO.8B06808.

(157) Zou, Y.; Huang, S.; Liao, Y.; Zhu, X.; Chen, Y.; Chen, L.; Liu, F.; Hu, X.; Tu, H.; Zhang, L.; et al. Isotopic Graphene-Isolated-Au-Nanocrystals with Cellular Raman-Silent Signals for Cancer Cell Pattern Recognition. *Chem. Sci.* **2018**, *9*, 2842–2849. https://doi.org/10.1039/c7sc05442d.

(158) Du, Z.; Qi, Y.; He, J.; Zhong, D.; Zhou, M. Recent Advances in Applications of Nanoparticles in SERS in Vivo Imaging. *Wiley Interdiscip. Rev. Nanomedicine Nanobiotechnology* **2021**, *13*, e1672. https://doi.org/10.1002/WNAN.1672.

(159) Ash, C.; Dubec, M.; Donne, K.; Bashford, T. Effect of Wavelength and Beam Width on Penetration in Light-Tissue Interaction Using Computational Methods. *Lasers Med. Sci.* **2017**, *32*, 1909–1918. https://doi.org/10.1007/s10103-017-2317-4.

(160) Garai, E.; Sensarn, S.; Zavaleta, C. L.; Loewke, N. O.; Rogalla, S.; Mandella, M. J.; Felt, S. A.; Friedland, S.; Liu, J. T. C.; Gambhir, S. S.; et al. A Real-Time Clinical Endoscopic System for Intraluminal, Multiplexed Imaging of Surface-Enhanced Raman Scattering Nanoparticles. *PLoS One* **2015**, *10*, e0123185. https://doi.org/10.1371/journal.pone.0123185.

(161) Serrano-Montes, A. B.; Langer, J.; Henriksen-Lacey, M.; Jimenez de Aberasturi, D.; Solís, D. M.; Taboada, J. M.; Obelleiro, F.; Sentosun, K.; Bals, S.; Bekdemir, A.; et al. Gold Nanostar-Coated Polystyrene Beads as Multifunctional Nanoprobes for SERS Bioimaging. *J. Phys. Chem. C* **2016**, *120*, 20860–20868. https://doi.org/10.1021/acs.jpcc.6b02282.

(162) Reguera, J.; Jiménez de Aberasturi, D.; Henriksen-Lacey, M.; Langer, J.; Espinosa, A.; Szczupak, B.; Wilhelm, C.; Liz-Marzán, L. M. Janus Plasmonic–Magnetic Gold–Iron Oxide Nanoparticles as Contrast Agents for Multimodal Imaging. *Nanoscale* **2017**, *9*, 9467–9480. https://doi.org/10.1039/C7NR01406F.

(163) Jeong, S.; Kim, Y. Il; Kang, H.; Kim, G.; Cha, M. G.; Chang, H.; Jung, K. O.; Kim, Y. H.; Jun, B. H.; Hwang, D. W.; et al. Fluorescence-Raman Dual Modal Endoscopic System for Multiplexed Molecular Diagnostics. *Sci. Rep.* **2015**, *5*, 13–16.

https://doi.org/10.1038/srep09455.

(164) Sun, C.; Gao, M.; Zhang, X. Surface-Enhanced Raman Scattering (SERS) Imaging-Guided Real-Time Photothermal Ablation of Target Cancer Cells Using Polydopamine-Encapsulated Gold Nanorods as Multifunctional Agents. *Anal. Bioanal. Chem.* **2017**, *409*, 4915–4926. https://doi.org/10.1007/s00216-017-0435-2.

(165) Nima, Z. A.; Mahmood, M.; Xu, Y.; Mustafa, T.; Watanabe, F.; Nedosekin, D. A.; Juratli, M. A.; Fahmi, T.; Galanzha, E. I.; Nolan, J. P.; et al. Circulating Tumor Cell Identification by Functionalized Silver-Gold Nanorods with Multicolor, Super-Enhanced SERS and Photothermal Resonances. *Sci. Rep.* **2014**, *4*, 4752. https://doi.org/10.1038/srep04752.

(166) Chen, Y.; Bai, X.; Su, L.; Du, Z.; Shen, A.; Materny, A.; Hu, J. Combined Labelled and Label-Free SERS Probes for Triplex Three-Dimensional Cellular Imaging. *Sci. Rep.* **2016**, *6*, 19173. https://doi.org/10.1038/srep19173.

(167) Hutchinson, L.; Kirk, R. High Drug Attrition Rates—Where Are We Going Wrong? *Nat. Rev. Clin. Oncol.* **2011**, *8*, 189–190. https://doi.org/10.1038/nrclinonc.2011.34.

(168) Edmondson, R.; Broglie, J. J.; Adcock, A. F.; Yang, L. Three-Dimensional Cell Culture Systems and Their Applications in Drug Discovery and Cell-Based Biosensors. *Assay Drug Dev. Technol.* **2014**, *12*, 207–218. https://doi.org/10.1089/adt.2014.573.

(169) Chan, B. P.; Leong, K. W. Scaffolding in Tissue Engineering: General Approaches and Tissue-Specific Considerations. *Eur. Spine J.* **2008**, *17*, 467–479. https://doi.org/10.1007/s00586-008-0745-3.

(170) Zhang, Y.; Jiménez de Aberasturi, D.; Henriksen-Lacey, M.; Langer, J.; Liz-Marzán, L. M. Live-Cell Surface-Enhanced Raman Spectroscopy Imaging of Intracellular PH: From Two Dimensions to Three Dimensions. *ACS Sensors* **2020**, *5*, 3194–3206. https://doi.org/10.1021/acssensors.0c01487.

(171) de Albuquerque, C. D. L.; Schultz, Z. D. Super-Resolution Surface-Enhanced Raman Scattering Imaging of Single Particles in Cells. *Anal. Chem.* **2020**, *92*, 9389–9398. https://doi.org/10.1021/acs.analchem.0c01864.

(172) Kapara, A.; Brunton, V.; Graham, D.; Faulds, K. Investigation of Cellular Uptake Mechanism of Functionalised Gold Nanoparticles into Breast Cancer Using SERS. *Chem. Sci.* **2020**, *11*, 5819–5829. https://doi.org/10.1039/d0sc01255f.

(173) Liu, W.; Jing, C.; Liu, X.; Du, J. 3D Imaging of Single Bacterial Cells Using Surface-Enhanced Raman Spectroscopy with a Multivariate Curve Resolution Model. *Analyst* **2022**, *147*, 223–229. https://doi.org/10.1039/D1AN01879E.

(174) Jin, Q.; Li, M.; Polat, B.; Paidi, S. K.; Dai, A.; Zhang, A.; Pagaduan, J. V.; Barman, I.; Gracias, D. H. Mechanical Trap Surface-Enhanced Raman Spectroscopy for Three-Dimensional Surface Molecular Imaging of Single Live Cells. *Angew. Chemie Int. Ed.* **2017**, *56*, 3822–3826. https://doi.org/10.1002/anie.201700695.

(175) Lin, J.; Akakuru, O. U.; Wu, A. Advances in Surface-Enhanced Raman Scattering Bioprobes for Cancer Imaging. *View* **2021**, *2*, 20200146. https://doi.org/10.1002/VIW.20200146.

(176) Altunbek, M.; Çetin, D.; Suludere, Z.; Çulha, M. Surface-Enhanced Raman Spectroscopy Based 3D Spheroid Culture for Drug Discovery Studies. *Talanta* **2019**, *191*, 390–399. https://doi.org/10.1016/J.TALANTA.2018.08.087.

(177) Zhang, Q.; Lee, Y. H.; Phang, I. Y.; Lee, C. K.; Ling, X. Y. Hierarchical 3D SERS Substrates Fabricated by Integrating Photolithographic Microstructures and Self-Assembly of Silver Nanoparticles. *Small* **2014**, *10*, 2703–2711. https://doi.org/10.1002/smll.201303773.

(178) Karlsson, H. and Illy, E. How to Choose a Laser: How to choose a laser for Raman spectroscopy https://hubner-photonics.com/knowledge-bank/how-to-choose-lasers-for-raman-spectroscopy/.

(179) Giridhar, G.; Manepalli, R. R. K. N.; Apparao, G. Confocal Raman Spectroscopy. In *Spectroscopic Methods for Nanomaterials Characterization*; Elsevier, 2017; pp 141–161. https://doi.org/10.1016/B978-0-323-46140-5.00007-8.

(180) Verma, P. Tip-Enhanced Raman Spectroscopy : Technique and Recent Advances. **2017**, *117*, 6447–6466. https://doi.org/10.1021/acs.chemrev.6b00821.

(181) Kou, X.; Zhou, Q.; Wang, D.; Yuan, J.; Fang, X.; Wan, L. High-Resolution Imaging of Graphene by Tip-Enhanced Coherent Anti-Stokes Raman Scattering. *J. Innov. Opt. Health Sci.* **2019**, *12*, 1841003. https://doi.org/10.1142/S1793545818410031.

(182) Nicolson, F.; Jamieson, L. E.; Mabbott, S.; Plakas, K.; Shand, N. C.; Detty, M. R.; Graham, D.; Faulds, K. Through Tissue Imaging of a Live Breast Cancer Tumour Model Using Handheld Surface Enhanced Spatially Offset Resonance Raman Spectroscopy (SESORRS). *Chem. Sci.* **2018**, *9*, 3788–3792. https://doi.org/10.1039/c8sc00994e.

(183) Nicolson, F.; Andreiuk, B.; Andreou, C.; Hsu, H. T.; Rudder, S.; Kircher, M. F. Non-Invasive In Vivo Imaging of Cancer Using Surface-Enhanced Spatially Offset Raman Spectroscopy (SESORS). *Theranostics* **2019**, *9*, 5899–5913. https://doi.org/10.7150/THNO.36321.

(184) Madzharova, F.; Heiner, Z.; Kneipp, J. Surface Enhanced Hyper Raman Scattering (SEHRS) and Its Applications. *Chemical Society Reviews*. Royal Society of Chemistry July 2017, pp 3980–3999. https://doi.org/10.1039/c7cs00137a.

(185) Salehi, M.; Steinigeweg, D.; Ströbel, P.; Marx, A.; Packeisen, J.; Schlücker, S. Rapid Immuno-SERS Microscopy for Tissue Imaging with Single-Nanoparticle Sensitivity. *J. Biophotonics* **2012**, *6*, 785–792. https://doi.org/10.1002/jbio.201200148.

(186) Gruenke, N. L.; Cardinal, M. F.; McAnally, M. O.; Frontiera, R. R.; Schatz, G. C.; Van Duyne, R. P. Ultrafast and Nonlinear Surface-Enhanced Raman Spectroscopy. *Chem. Soc. Rev.* **2016**, *45*, 2263–2290. https://doi.org/10.1039/C5CS00763A.

(187) Milojevich, C. B.; Silverstein, D. W.; Jensen, L.; Camden, J. P. Surface-Enhanced Hyper-Raman Scattering Elucidates the Two-Photon Absorption Spectrum of Rhodamine 6G. *J. Phys. Chem. C* **2013**, *117*, 3046–3054. https://doi.org/10.1021/jp3094098.

(188) Watanabe, K.; Palonpon, A. F.; Smith, N. I.; Chiu, L. Da; Kasai, A.; Hashimoto, H.; Kawata, S.; Fujita, K. Structured Line Illumination Raman Microscopy. *Nat. Commun.* **2015**, *6*, 10095. https://doi.org/10.1038/ncomms10095.

(189) Das, G.; Gentile, F.; Coluccio, M. L.; Perri, A. M.; Nicastri, A.; Mecarini, F.; Cojoc, G.; Candeloro, P.; Liberale, C.; De Angelis, F.; et al. Principal Component Analysis Based Methodology to Distinguish Protein SERS Spectra. *J. Mol. Struct.* **2011**, *993*, 500–505. https://doi.org/10.1016/j.molstruc.2010.12.044.

(190) Li, X.; Yang, T.; Li, C. S.; Song, Y.; Lou, H.; Guan, D.; Jin, L. Surface Enhanced Raman Spectroscopy (SERS) for the Multiplex Detection of Braf, Kras, and Pik3ca

Mutations in Plasma of Colorectal Cancer Patients. *Theranostics* **2018**, *8*, 1678–1689. https://doi.org/10.7150/thno.22502.

(191) Karabeber, H.; Huang, R.; Iacono, P.; Samii, J. M.; Pitter, K.; Holland, E. C.; Kircher, M. F. Guiding Brain Tumor Resection Using Surface-Enhanced Raman Scattering Nanoparticles and a Hand-Held Raman Scanner. *ACS Nano* **2014**, *8*, 9755–9766. https://doi.org/10.1021/nn503948b.

(192) Arami, H.; Patel, C. B.; Madsen, S. J.; Dickinson, P. J.; Davis, R. M.; Zeng, Y.; Sturges, B. K.; Woolard, K. D.; Habte, F. G.; Akin, D.; et al. Nanomedicine for Spontaneous Brain Tumors: A Companion Clinical Trial. *ACS Nano* **2019**, *13*, 2858–2869. https://doi.org/10.1021/acsnano.8b04406.

(193) Bohndiek, S. E.; Wagadarikar, A.; Zavaleta, C. L.; Van de Sompel, D.; Garai, E.; Jokerst, J. V; Yazdanfar, S.; Gambhir, S. S. A Small Animal Raman Instrument for Rapid, Wide-Area, Spectroscopic Imaging. *Proc. Natl. Acad. Sci. U. S. A.* **2013**, *110*, 12408–12413. https://doi.org/10.1073/pnas.1301379110.

(194) Yu, J. H.; Steinberg, I.; Davis, R. M.; Malkovskiy, A. V.; Zlitni, A.; Radzyminski, R. K.; Jung, K. O.; Chung, D. T.; Curet, L. D.; D'Souza, A. L.; et al. Noninvasive and Highly Multiplexed Five-Color Tumor Imaging of Multicore Near-Infrared Resonant Surface-Enhanced Raman Nanoparticles In Vivo. *ACS Nano* **2021**, *15*, 19956–19969. https://doi.org/10.1021/ACSNANO.1C07470.

(195) Shi, B.; Zhang, B.; Zhang, Y.; Gu, Y.; Zheng, C.; Yan, J.; Chen, W.; Yan, F.; Ye, J.; Zhang, H. Multifunctional Gap-Enhanced Raman Tags for Preoperative and Intraoperative Cancer Imaging. *Acta Biomater.* **2020**, *104*, 210–220. https://doi.org/10.1016/J.ACTBIO.2020.01.006.

(196) Tian, F.; Conde, J.; Bao, C.; Chen, Y.; Curtin, J.; Cui, D. Gold Nanostars for Efficient in Vitro and in Vivo Real-Time SERS Detection and Drug Delivery via Plasmonic-Tunable Raman/FTIR Imaging. *Biomaterials* **2016**, *106*, 87–97. https://doi.org/10.1016/j.biomaterials.2016.08.014.

(197) Alvarez-Puebla, R. A.; Pazos-Perez, N.; Guerrini, L. SERS-Fluorescent Encoded Particles as Dual-Mode Optical Probes. *Appl. Mater. Today* **2018**, *13*, 1–14. https://doi.org/10.1016/j.apmt.2018.07.007.

(198) He, P.; Han, W.; Bi, C.; Song, W.; Niu, S.; Zhou, H.; Zhang, X. Many Birds, One Stone: A Smart Nanodevice for Ratiometric Dual-Spectrum Assay of Intracellular MicroRNA and Multimodal Synergetic Cancer Therapy. *ACS Nano* **2021**, *15*, 6961–6976. https://doi.org/10.1021/ACSNANO.0C10844.

(199) Kircher, M. F.; de la Zerda, A.; Jokerst, J. V; Zavaleta, C. L.; Kempen, P. J.; Mittra, E.; Pitter, K.; Huang, R.; Campos, C.; Habte, F.; et al. A Brain Tumor Molecular Imaging Strategy Using a New Triple-Modality MRI-Photoacoustic-Raman Nanoparticle. *Nat. Med.* **2012**, *18*, 829–834. https://doi.org/10.1038/nm.2721.

(200) Chen, S.; Bao, C.; Zhang, C.; Yang, Y.; Wang, K.; Chikkaveeraiah, B. V; Wang, Z.; Huang, X.; Pan, F.; Wang, K.; et al. EGFR Antibody Conjugated Bimetallic Au@Ag Nanorods for Enhanced SERS-Based Tumor Boundary Identification, Targeted Photoacoustic Imaging and Photothermal Therapy. *Nano Biomed. Eng.* **2016**, *8*, 315–328. https://doi.org/10.5101/nbe.v8i4.p315-328.

(201) Wang, J.; Sun, J.; Wang, Y.; Chou, T.; Zhang, Q.; Zhang, B.; Ren, L.; Wang, H. Gold Nanoframeworks with Mesopores for Raman-Photoacoustic Imaging and Photo-Chemo Tumor Therapy in the Second Near-Infrared Biowindow. *Adv. Funct. Mater.* **2020**, *30*, 1908825. https://doi.org/10.1002/ADFM.201908825.

(202) Liu, Y.; Ashton, J. R.; Moding, E. J.; Yuan, H.; Register, J. K.; Fales, A. M.; Choi, J.; Whitley, M. J.; Zhao, X.; Qi, Y.; et al. A Plasmonic Gold Nanostar Theranostic Probe for in Vivo Tumor Imaging and Photothermal Therapy. *Theranostics* **2015**, *5*, 946–960. https://doi.org/10.7150/thno.11974.

(203) Zeng, L.; Pan, Y.; Wang, S.; Wang, X.; Zhao, X.; Ren, W.; Lu, G.; Wu, A. Raman Reporter-Coupled Agcore@Aushell Nanostars for in Vivo Improved Surface Enhanced Raman Scattering Imaging and Near-Infrared-Triggered Photothermal Therapy in Breast Cancers. *ACS Appl. Mater. Interfaces* **2015**, *7*, 16781–16791. https://doi.org/10.1021/acsami.5b04548.

(204) Feng, J.; Chen, L.; Xia, Y.; Xing, J.; Li, Z.; Qian, Q.; Wang, Y.; Wu, A.; Zeng, L.; Zhou, Y. Bioconjugation of Gold Nanobipyramids for SERS Detection and Targeted Photothermal Therapy in Breast Cancer. *ACS Biomater. Sci. Eng.* **2017**, *3*, 608–618. https://doi.org/10.1021/acsbiomaterials.7b00021.

(205) Liu, Y.; Chongsathidkiet, P.; Crawford, B. M.; Odion, R.; Dechant, C. A.; Kemeny, H. R.; Cui, X.; MacCarini, P. F.; Lascola, C. D.; Fecci, P. E.; et al. Plasmonic Gold Nanostar-Mediated Photothermal Immunotherapy for Brain Tumor Ablation and Immunologic Memory. *Immunotherapy* **2019**, *11*, 1293–1302. https://doi.org/10.2217/IMT-2019-0023.

(206) Wang, Y. W.; Kang, S.; Khan, A.; Bao, P. Q.; Liu, J. T. C. In Vivo Multiplexed Molecular Imaging of Esophageal Cancer via Spectral Endoscopy of Topically Applied SERS Nanoparticles. *Biomed. Opt. Express* **2015**, *6*, 3714–3723. https://doi.org/10.1364/BOE.6.003714.

(207) Choi, N.; Dang, H.; Das, A.; Sim, M. S.; Chung, I. Y.; Choo, J. SERS Biosensors for Ultrasensitive Detection of Multiple Biomarkers Expressed in Cancer Cells. *Biosens. Bioelectron.* **2020**, *164*, 112326. https://doi.org/10.1016/j.bios.2020.112326.

(208) Song, C.; Guo, S.; Jin, S.; Chen, L.; Jung, Y. M. Biomarkers Determination Based on Surface-Enhanced Raman Scattering. *Chemosens. 2020, Vol. 8, Page 118* **2020**, *8*, 118. https://doi.org/10.3390/CHEMOSENSORS8040118.

(209) Bodelón, G.; Montes-García, V.; Costas, C.; Pérez-Juste, I.; Pérez-Juste, J.; Pastoriza-Santos, I.; Liz-Marzán, L. M. Imaging Bacterial Interspecies Chemical Interactions by Surface-Enhanced Raman Scattering. *ACS Nano* **2017**, *11*, 4631–4640. https://doi.org/10.1021/ACSNANO.7B00258.

(210) Smolsky, J.; Kaur, S.; Hayashi, C.; Batra, S. K.; Krasnoslobodtsev, A. V. Surface-Enhanced Raman Scattering-Based Immunoassay Technologies for Detection of Disease Biomarkers. *Biosensors* **2017**, *7*, 7. https://doi.org/10.3390/bios7010007.

(211) Gautam, R.; Vanga, S.; Ariese, F.; Umapathy, S. Review of Multidimensional Data Processing Approaches for Raman and Infrared Spectroscopy. *EPJ Techn Instrum* **2015**, *2*, 8. https://doi.org/10.1140/epjti/s40485-015-0018-6.

(212) Huang, Z.; Lui, H.; McLean, D. I.; Korbelik, M.; Zeng, H. Raman Spectroscopy in Combination with Background Near-Infrared Autofluorescence Enhances the In Vivo Assessment of Malignant Tissues. *Photochem. Photobiol.* **2005**, *81*, 1219–1226. https://doi.org/10.1562/2005-02-24-ra-449.

(213) Rajalahti, T.; Kvalheim, O. M. Multivariate Data Analysis in Pharmaceutics: A Tutorial Review. *Int. J. Pharm.* **2011**, *417*, 280–290. https://doi.org/10.1016/J.IJPHARM.2011.02.019.

(214) Ryan, T. P. Introduction to Multiple Linear Regression. In *Modern Regression Methods*; wiley, 2008; pp 146–189. https://doi.org/10.1002/9780470382806.ch4.

(215) Nagaraj, K.; Sharvani, G. S.; Sridhar, A. Emerging Trend of Big Data Analytics in Bioinformatics: A Literature Review. *Int. J. Bioinform. Res. Appl.* **2018**, *14*, 144–205. https://doi.org/10.1504/IJBRA.2018.089175.

(216) Brown, K. A.; Brittman, S.; Maccaferri, N.; Jariwala, D.; Celano, U. Machine Learning in Nanoscience: Big Data at Small Scales. *Nano Lett.* **2020**, *20*, 2–10. https://doi.org/10.1021/ACS.NANOLETT.9B04090.

2. Evaluation of the signal from single SERS tags

Contents

2.1 Introduction

In this chapter, a method to quantify the SERS signal from individual SERS tags is presented, as a means to apply the obtained information to SERS bioimaging. One of the remaining obstacles to implement this technique is related to the difficulty to correlate the SERS signal corresponding to a single SERS tag. This uncertainty is mainly due to the complexity in controlling the factors that influence the SERS signal, such as the Raman scattering cross-section of the molecules used (Raman reporters, RaR), the number of RaR molecules adsorbed onto the core NP and those present in the enhancement region, as well as their orientation with respect to the NP surface. The control of these factors is extremely challenging, partly because each of them is determined by a combination of other variables, which are also difficult to measure. For instance, it has been reported that the number of molecules in the enhancement region depends on both the area and the occupancy of the surface, which are still difficult quantities to be determined.[1]

Optical bioimaging techniques are usually employed to retrieve unique and quantitative information about morphological and functional cellular properties. Imaging facilities are thus useful in drug development,[2] but also serve as a powerful research tool for diagnostics[3] and monitoring,[4] among other applications.[5,6] As discussed in **Chapter 1**, although fluorescence microscopy has been the most commonly used method for bioimaging at a cellular and sub-cellular level,[7,8] it presents some drawbacks, such as quenching of the signal, auto-fluorescence from biological samples, spectral overlap between fluorescent probes, and signal loss (bleaching) during long-term experiments.[9,10] In comparison, SERS imaging can overcome some of these issues, featuring high resolution, narrow spectral peaks, no overlap issues and extended multiplexing capability,[3,11,12] thanks to the unique features of SERS tags.[13–15]

In this context, a supervised methodology has been developed and implemented in the form of an application (App), to correlate the recorded SERS intensity with the number of SERS tags, aided by associated TEM images. The App was called SERSTEM and the resulting methodology has been shown to yield a quantification of the SERS signal per NP. Even though the correlation between SERS and TEM microscopy can in principle be achieved through hybrid instruments,[16,17] such imaging capabilities are not commonly available. Correlated SERS studies have been reported to determine the SERS enhancement by measuring the same single, dimer, or cluster Ag NPs on a Raman microscope and correlating with either scanning electron microscopy (SEM)[18–21] or TEM.[22–25] Statistical analysis to correlate SERS intensity and NP cluster size has also been reported by SERS and SEM imaging.[26] These methods still involve manual correlations, which may lead to subjective bias, and therefore the SERSTEM App has been implemented to obtain a reliable correlation. This is considered to be a first step toward establishing a suitable method for SERS tag signal calibration, which has been used in the following chapters to determine the number of NPs

inside living cells. The App should be further improved for bioimaging quantification in complex samples, such as 3D models and tissues.[27]

2.2 Our system: SERS tags

SERS tags with a sufficiently uniform and intense SERS signal and good reproducibility are required to implement a reliable software that can correlate SERS and TEM imaging. Therefore, both Au nanorods (AuNRs) and nanostars (AuNSs) were synthesized, and encoded with aromatic thiols and encapsulated with an amphiphilic block co-polymer, dodecylamine-modified polyisobutylene-alt-maleic (PMA). [27,28] A schematic representation of the SERS tag preparation is provided in ***Figure 2.1*** and the details are presented in the **Experimental Section (2.7.1-2-3-4)**.

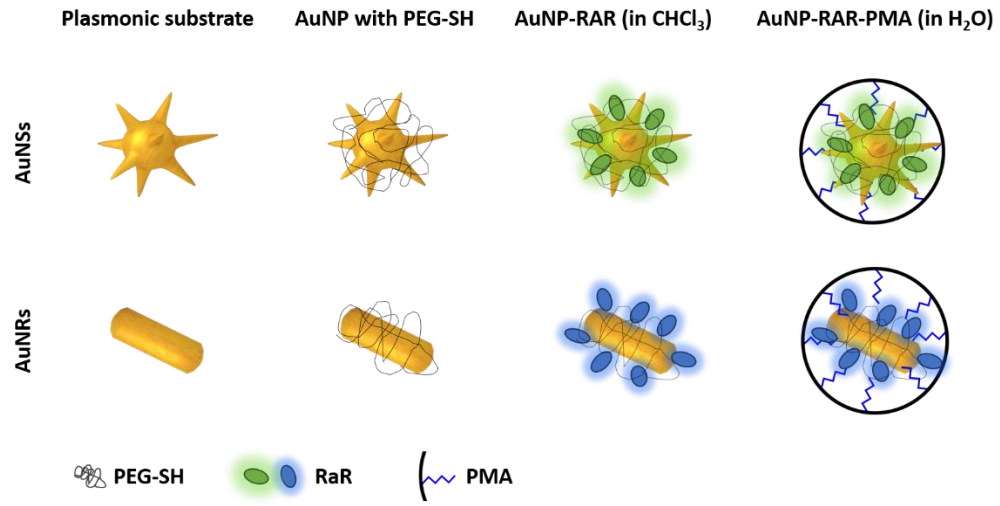

Figure 2.1 *SERS tags preparation: schematic representation of the different steps along the preparation of SERS-encoded NPs (AuNR-BT, AuNR-MBT, AuNR-2NAT and AuNS-4BPT). NPs were pre-stabilized with PEG and subsequently coated with a selected Raman tag during phase transfer from water into $CHCl_3$. The obtained hydrophobic AuNPs were then wrapped with PMA, leading to encoded AuNPs that were colloidally stable in aqueous solution.*

The selected AuNPs were synthesized with LSPRs in the NIR region, to obtain an efficient enhancement of the Raman signal using a 785 nm laser excitation, for which light transmission in biological tissue is maximized.[29,30] Shown in ***Figure 2.2A*** are representative TEM images and UV-Vis-NIR spectra for both AuNRs and AuNSs. Two different AuNR samples were prepared, with average dimensions of 33 nm × 102 nm (diameter × length, respectively), and 17 nm × 60 nm. Whereas, AuNSs were synthesized with an overall size of (70 ± 18) nm. The NPs surface was first partially protected with thiolated polyethylene glycol (PEG) . Smaller AuNRs were coated with a higher PEG concentration, thereby reducing the amount of RaR on each particle, and allowing us to analyse the influence of this parameter. In detail, 4-methyl benzenethiol (MBT), benzenethiol (BT), 2-naphthalenethiol (2NAT) and biphenyl-4-thiol (BPT) were selected as RaR molecules, due to their relatively high Raman

cross sections, and clearly distinguishable fingerprints, as previously reported.[28] The corresponding SERS spectra are shown in ***Figure 2.2B***, which were used as reference spectra for subsequent analysis. The most intense characteristic vibrations for each RaR are listed in ***Table 2.1***.

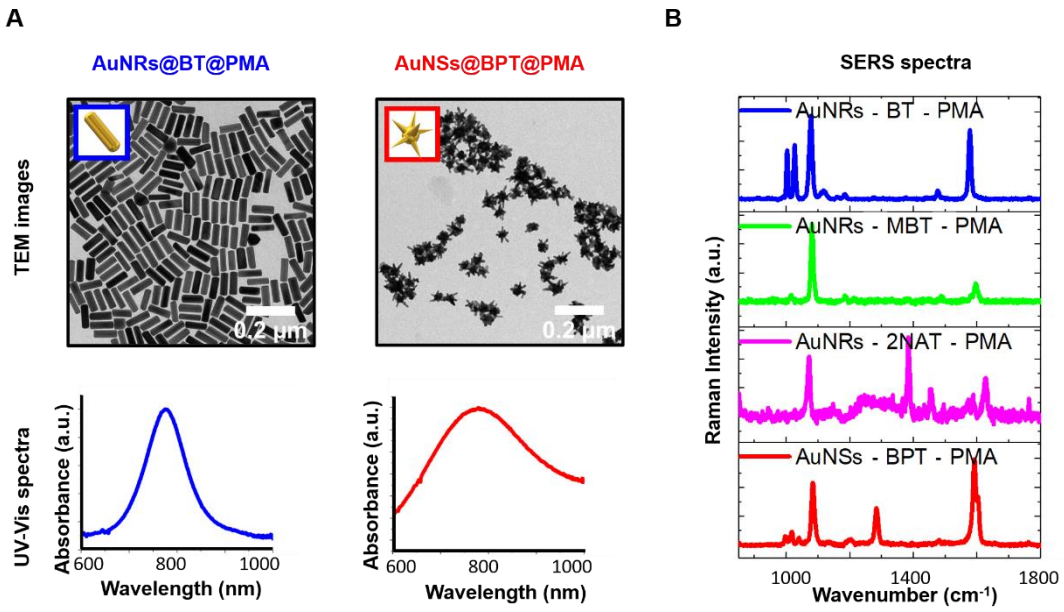

Figure 2.2 *SERS tags characterization:* ***A)*** *UV-Vis-NIR spectra and TEM images of AuNRs and AuNSs;* ***B)*** *SERS spectra collected from 5-µl drop of different SERS tags ($[Au]^0$ = 0.5mM) with 50× objective, 10s of integration time and 0.35mW of laser power.*

Table 2.1 *Characteristic and most intense vibrational bands of the RaRs used to encode SERS tags.*

RaR molecule	Vibrations
BT	1002 cm^{-1} (ring breathing) 1025 cm^{-1} (ring C-H bending) 1077 cm^{-1} (C-S stretching) 1578 cm^{-1} (symmetric C-C stretching)[31]
MBT	1082 cm^{-1} (ring C-H in plane bending) 1597 cm^{-1} (ring C-C stretching)[32]
2NAT	1070 cm^{-1} (ring C-H bending in plane) 1383 cm^{-1} (ring C-C stretching) 1626 cm^{-1} (ring C-C stretching)[33]
BPT	1084 cm^{-1} (ring C-H bending) 1285 cm^{-1} (ring C-C stretching) 1593/1604 cm^{-1} (ring C-C stretching)[34]

2.3 Sample preparation and measurements

After synthesis, the samples were prepared by drop casting an aliquot of the SERS tags colloidal dispersion onto a TEM grid, used as support, as schematically illustrated in ***Figure 2.3.A (1)***. In more detail, TEM finder grids (#CFLF400-Cu-50, Aname) labelled with easily recognizable characters were used to facilitate the identification of the same measurement area for SERS mapping and TEM imaging (see ***Figure 2.3 B***). A glow discharge treatment was applied to render the grids hydrophilic and ensure a homogeneous dispersion of NPs. The small drop of colloidal dispersion was deposited immediately after the treatment and then it was allowed to dry slowly in air, ***(2)***. To prepare the grids, different dispersions of SERS tags were used to ensure a sufficient SERS signal-to-noise ratio for the calculations to be performed, while ensuring sufficiently separated AuNPs in TEM images to be correctly counted (details are given in **Experimental Section 2.7.5**). Finally, the TEM grid was imaged with Raman microscopy and then with TEM, ***(3)-(4)***.

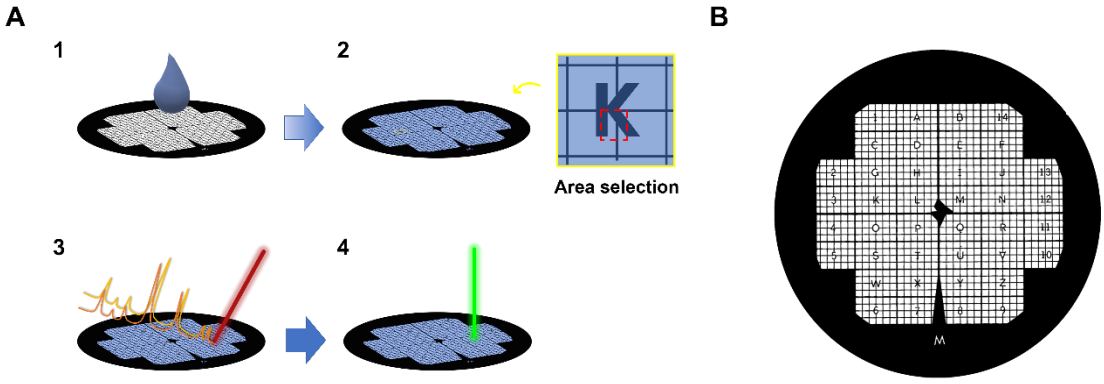

Figure 2.3 A) *Sample preparation procedure:* ***1)*** *Addition of SERS tags via drop casting of a colloidal dispersion,* ***2)*** *drying of the sample in air, showing in a yellow box a region close to one of the letters generally used as reference, and in red dashed line the area subsequently measured via* ***3)*** *SERS and* ***4)*** *TEM imaging.* ***B)*** *Sketch of a TEM grid with reference letters.*

2.3.1 SERS mapping

The selected area for SERS mapping was ca. 50 × 50 μm^2, located next to an asymmetric letter (e.g. D, G, K, P, Q or R), which displayed a flatter morphology thus avoiding loss of focus. SERS measurements were performed with a confocal Raman microscope (Renishaw inVia) equipped with 1024 × 512 CCD detectors, using a 785 nm laser excitation source (maximum output 270 mW), using a pinhole to obtain a circular laser spot geometry, and a 1200 l/mm diffraction grating. SERS maps were recorded in static mode (centre of scattered wavenumber 1400 cm^{-1}) using a 50× long working distance objective (numerical aperture, NA = 0.5; Leica Microsystems, Wetzlar, Germany) with 0.5 s integration time, at 0.6 mW laser power (except for the maps of AuNSs-BPT-PMA, which were recorded with 0.35 mW). Initially, the selected area (ca. 50 × 50 μm^2) was scanned with different map spacing to avoid oversampling. The SERS intensity map of a selected area is shown in ***Figure 2.4,*** with step

sizes of: ***A)*** 1 µm, ***B)*** 1.3 µm and ***C)*** 2 µm. By decreasing the step size, sharper SERS maps of the label were obtained, with no evidence of oversampling. Thus, the smallest step size of 1 µm in x and y was used, which allowed a complete survey of the sample. In this configuration, mappings required approximately 40 minutes to be completed. Meanwhile, the SERS tags reference spectra were collected from a drop of 5 µL of the colloidal dispersion ($[Au]^0$ = 0.5 mM) on top of a quartz slide. A 50× long working distance objective (NA=0.5; Leica Microsystems, Wetzlar, Germany) was used in expanded scan mode, with an integration time of 10s, at a laser power of 0.35mW and five accumulative scans. These spectra were later used as reference for the analysis.

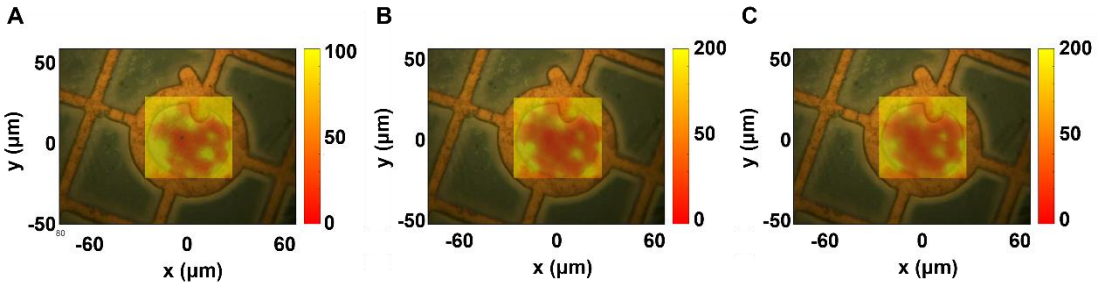

Figure 2.4 *Comparison of step sizes: SERS mappings recorded from the intensity at 1082* cm^{-1}*, with of step sizes of:* ***A)*** *1 µm* ***B)****1.3 µm and* ***C)*** *2 µm.*

2.3.2 TEM imaging

After SERS mapping, the same area was imaged using TEM, with a magnification that allowed to distinguish the morphology of the SERS tags. TEM images were acquired with a JEOL JEM-1400PLUS transmission electron microscope operating at 120 kV. To image the area that has an extension larger than the field of view, working at 3000× magnification, consecutive images with an overlap between each other of around 40% of the total image were recorded (see ***Figure 2.5***). Post-reconstruction of the whole image was carried out by a dedicated tool available on Fiji, namely the Microscopy Image Stitching Tool (MIST). [35]

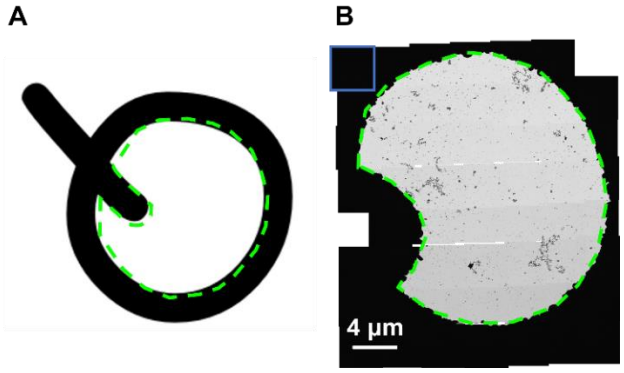

Figure 2.5 *TEM imaging:* ***A)*** *Q letter with the inner edge of the area to be acquired by TEM, evidenced in a green dashed line.* ***B)*** *Overlap image of several TEM images by the MIST tool; the blue square evidences a single TEM image acquired with 3000× magnification.*

2.4 The SERSTEM App

A code to correlate SERS and TEM measurements was developed in Matlab© R2019b environment, as a graphical interface, which has been deposited as a freely available App in collaboration with Dr. Lucio Litti of University of Padova, Padova (Italy).[36,37] The rationale behind the code is sketched in ***Figure 2.6***, and the various steps followed through the use of the App are described in the following subsections. The full code is reported in **Appendix A**.

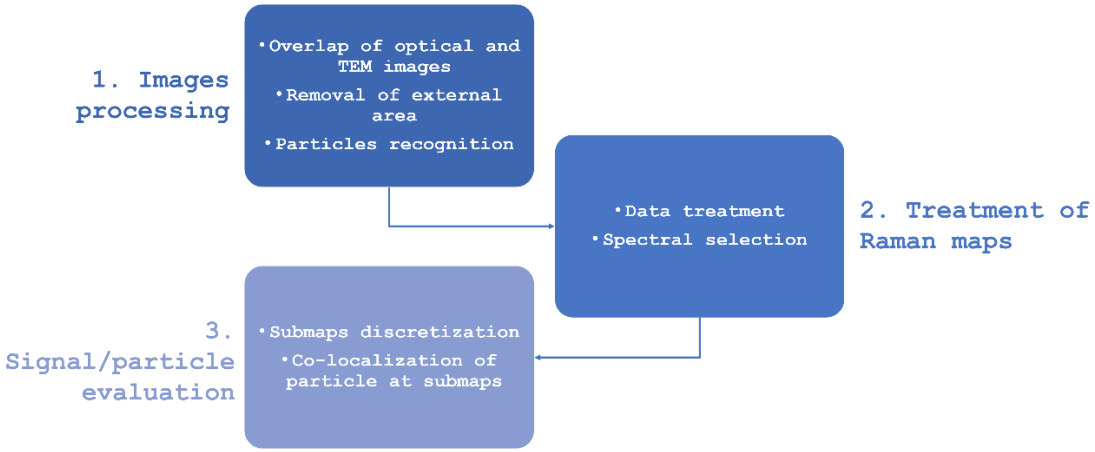

Figure 2.6 *Representation of the code block diagram, highlighting the three main steps, highlighting the main tasks for each one:* ***1)*** *imaging processing,* ***2)*** *treatment of the Raman maps,* ***3)*** *evaluation of SERS signal per particle.*

2.4.1 Image processing

For further processing, the optical image obtained from the Raman microscope (referred to as optical image in what follows) and the corresponding TEM image (saved as three RGB channels in jpeg format) are first uploaded to the application. Considering that a careful overlap between SERS map and TEM image is crucial, a tutorial video has also been provided for detailed guidance.[36] Generally, a SERS map is associated to the corresponding optical image (Raman-associated optical image), through spatial x-y coordinates. Hence, to correlate the SERS map with the TEM grid, it is possible to rotate, translate and project the TEM image onto the same coordinates grid as that for the SERS map, while maintaining the original image resolution. In the App, a guided procedure was implemented, wherein the overlap of optical and TEM images is managed by Matlab© functions. The operations work by orienting the TEM image over the optical image through spatial transformations, defined by the user. When the TEM image is uploaded, a window pops up to offer assistance with the reorientation. However, clear and recognizable features must be present in both Raman-associated optical image and TEM images, to be correctly correlated (see ***Figure 2.3B***). In ***Figure 2.7*** an example is shown, to explain how the TEM image reorientation works: the Q letter was chosen ***(1)***, which contains recognizable edges that can be used to guide the overlap the optical image ***(2)*** with the TEM image ***(3)***. Subsequently, the image is projected on the real x-y coordinates, using the reference provided by the spatial coordinates of the four vertices of

the Raman-associated optical image ***(4)***. From here on, the projected TEM image takes the place of the mentioned optical image, providing a perfect overlap. After this process, the information contained in both TEM and SERS images are computed and correlated. In particular, from the TEM image it is possible to identify and locate the NPs. For this process to be carried out automatically, the image is converted from the original format into an inverse binary image, through the definition of a threshold termed grey limit value (GLV). Considering that this parameter can strongly affect the classification of a pixel as particle or background, a default value is automatically calculated and proposed, but it can be redefined by the user if deemed appropriate. Then, automated particle detection is provided by isolating all of the white areas (corresponding to NPs) within the binary image. The quality and physical significance of this selection is influenced by several factors. In order to recognize two particles as two independent objects, a net separation between them is needed. This depends on both image resolution and the GLV threshold. The former is related to the resolution or point spread function of the instrument, whereas the GLV is a colour filter that selects the fate of grey pixels in becoming either white or black. High GLV can underestimate the real dimensions and potentially exclude blurred particles, while low GLV may overestimate particle dimensions and merge nearby particles. The user is also free to select the "Minimum Pixel Significance" parameter, namely the minimum area of a particle, expressed in pixels. This parameter has to be chosen taking into account that, in an optical microscope, the pixel size must be at least twice smaller than the features to be observed, following the Shannon-Nyquist theorem, which considers that images should be acquired with a spatial resolution at least twice smaller than the diffraction limit of the optical system.[38,39] Generally, an optical resolution of 5 times is used for imaging. In all of the examples presented here, the minimum pixel significance was fixed at 5 pixels. Once the selection parameters are set, several descriptors (such as area, perimeter, etc.) are obtained from each particle in the TEM image.

To proceed with the analysis, it is necessary to eliminate the borders that do not belong to the area of overlap between TEM and SERS images (areas between yellow and red dashed lines in ***(5)***). In fact, it is reasonable to expect that there could be several points on the Raman map located outside of the area where the particles could be imaged by TEM. This important step allows to run the analysis with precision, only in the area of the grid accessible for imaging by TEM. Another advantage of this selection is related to the fact that, in the proximity of the edges of the carbon layer one can often find defocused regions, and the grid frame can cause electron beam deviations. For this reason, it is important to remove some microns of the image close to the borders (see ***Figure 2.7 (5)***). Henceforth, in the App, both TEM image and SERS mapping are correlated and possess the same coordinates, ***(6)***.

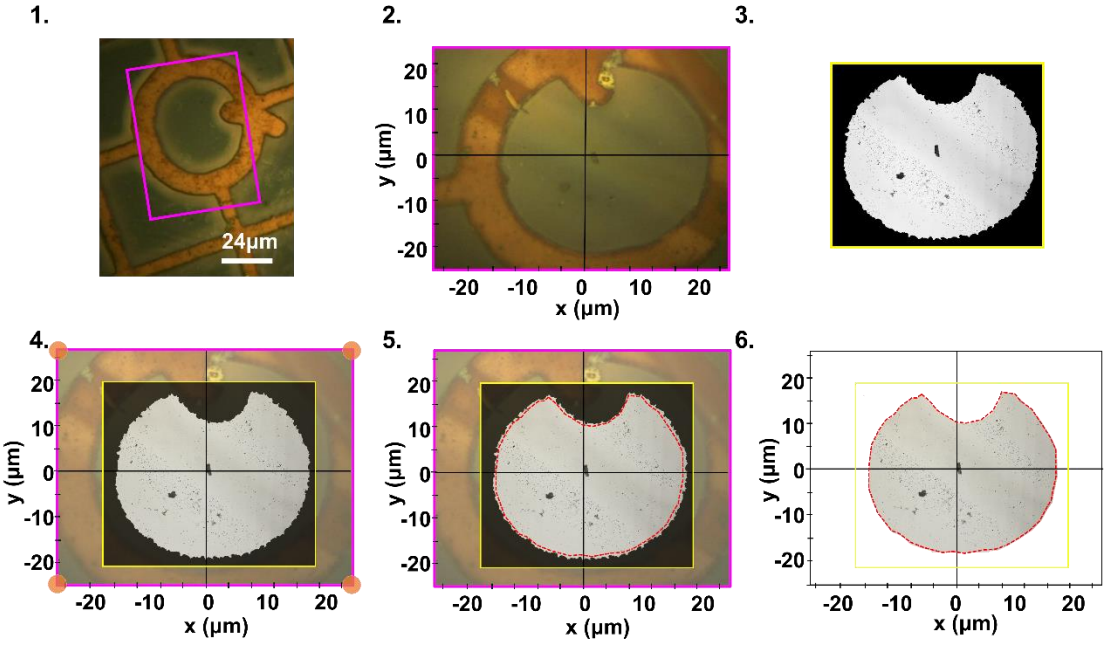

Figure 2.7 *Procedure to overlap optical and TEM images:* ***1)*** *area selected (framed in magenta);* ***2)*** *tilted optical image;* ***3)*** *TEM image (framed in yellow);* ***4)*** *the overlap process takes advantage of the spatial coordinates at the four vertices (orange circles) in the optical image;* ***5)*** *areas not to be included in the analysis (between yellow and dashed red lines) are removed from the TEM image;* ***6)*** *the relevant areas (inside the dashed red line) of the TEM image are correctly placed in the x-y plane.*

2.4.2 Treatment of Raman maps

The section of the code used to analyse the SERS maps consists of an MLRA tool, aimed at comparing each of the collected spectra in the mapping with the reference spectra.[40–43] Differently from a single peak comparison, in this kind of analyses the whole SERS spectrum is used to assign a statistical evaluation about the match with the reference spectrum in each x-y point of the map. It involves the assignment to each spectrum of the so-called b-values and the statistical p-value, as defined in **Chapter1** (**Section 2.7**). In this case, only one type of SERS tag per sample was used, and thus the analysis required only one SERS reference spectrum. Upon comparison with the reference spectrum and consequent assignment of b- and p-values, these were used as filters to select the spectra for that particular SERS tag. In ***Figure 2.8*** an example is shown to illustrate how this filtering procedure works. First, only those points for which the p-value is statistically relevant (i.e. p-value < 0.05) were selected.[44] Among the selected points, only those with a b-value related to the specific SERS tag, above an established threshold (α), were selected. The α threshold was defined according to the data features, to consider all of the spectra that are sufficiently similar to the reference spectrum. In this manner, after filtering, only those points with a significantly comparable signal to the SERS tag reference were selected.

A

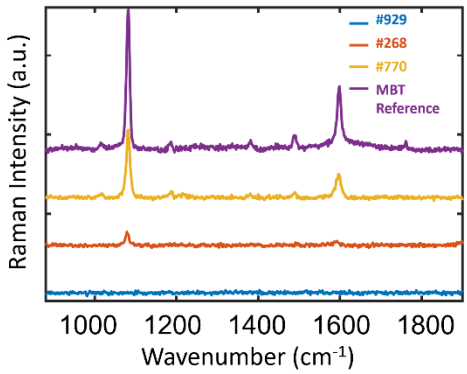

B

Spectrum #	P value	B value	P value<0.05 & B value>10
929	0.85	0.32	✗
268	$2x10^{-55}$	1.86	✗
770	$6x10^{-301}$	577	✓

Figure 2.8 *Spectra of AuNRs-MBT-PMA as an example to explain how the filters work:* ***A)*** *Three SERS spectra (#929 in blue, #268 in orange and #770 in yellow) collected from the mapping and (in purple) the reference spectrum of MBT;* ***B)*** *Parameters of each spectrum. The spectrum #929 did not pass the selection because both parameters were out of the chosen ranges (-Inf < p-value < 0.05 and 10 < b-value < Inf). This means that not only the goodness of the linear regression was not acceptable, but the spectrum was not sufficiently similar to the reference. Considering that the first applied filter was on the p-value, this spectrum was discarded because the result was not reliable. Not even spectrum #268 (in orange) passed the selections, even though it had a p-value in the correct range. This indicates that, despite the reliability of the result, the spectrum does not show the typical fingerprint of the SERS tag. It was therefore excluded, through application of the second filter on the b-value. Only the spectrum #770 (in yellow) passed both filters, indicating a statistically significant similarity with the MBT reference.*

2.4.3 Signal/NP evaluation

After the filtering procedure has been applied to the SERS map, the SERS signal per particle (SSpP) value could be calculated. This was done using the correlated TEM image and filtered SERS map, by summing up the intensities of all selected points at one of the main Raman peaks, and then dividing by the number of particles found within the mapped area. In this case, it is assumed that the entire NP population within that area contributes to the overall signal, which would be the case in a real measurement. Additionally, a deeper perspective in data analysis is provided with a dedicated option to segment the SERS map in subunits (called sub-maps in the following) of squared shape and a user-defined edge length (δ) (see ***Figure 2.9***). In this manner, it was possible to exclude those regions with no SERS signal matching the RaR reference, obtaining more precise results. The maximum allowed map subdivision depends on the spatial SERS mapping resolution, namely the grid spacing, up to the limit of considering each spectral acquisition as an independent map. Each of the sub-maps created was evaluated in a similar fashion, to obtain the SSpP. A distribution plot of the SSpP estimated from each sub-map, could thus be obtained and provided suitable statistical

calculations. In ***Figure 2.10 A-D)*** TEM images are reported for 4 sub-maps (blue squares), showing in red the edges of the NPs identified by the program. Also, the plot of the Raman signal and the SSpP obtained are reported versus the number of particles. In particular, in ***Figure 2.10E)*** the Raman signal increases when the number of NPs counted in the sub-map growths, as expected. Meanwhile, in ***Figure 2.10F)*** the values of SSpP do not scale with the number of particles, but remain almost constant, with a statistical fluctuation due to the expected particle-by-particle differences in RaR loading and SERS activity, e.g. related to different degrees of aggregation or clustering. Regarding the role of hotspots on the measured SERS signal, it can hardly be avoided that a fraction of particles is aggregated on the TEM grid. This can generate plasmon coupling between SERS tags and likely result in hotspot formation, preventing a realistic estimation. The enhancement is related to the shape of the plasmonic NPs: clustered spheres for example show additional hot-spots, increasing SERS signals by several orders of magnitude.[44] In contrast, it has been reported that the SERS signals from nanostars are almost unaffected by aggregation, as they contain intrinsic hotspots at their tips.[45] In the case of nanorods their longitudinal plasmon resonance focuses the field onto both tips, but showing weaker hotspots compared with particularly advantageous configurations such as tip-to-tip assembly.[45,46] However, it is possible to avoid plasmon coupling with an appropriate surface coating.[47] In this case, as described above, the surface of the NPs was fully covered with an inner layer of thiolated PEG and hydrophobic RaR molecules, which was subsequently wrapped with the amphiphilic polymer PMA (see ***Figure 2.1***). It has been already estimated the overall thickness of the organic shell to be around 4-5 nm in the dried state.[27] Hence, in this case, the protecting layer prevents close mutual contact between AuNPs, as well as between AuNPs and the carbon substrate on the TEM grid, providing a lower boundary to inter-NP distance of about 10 nm and thus preventing the generation of hotspots.

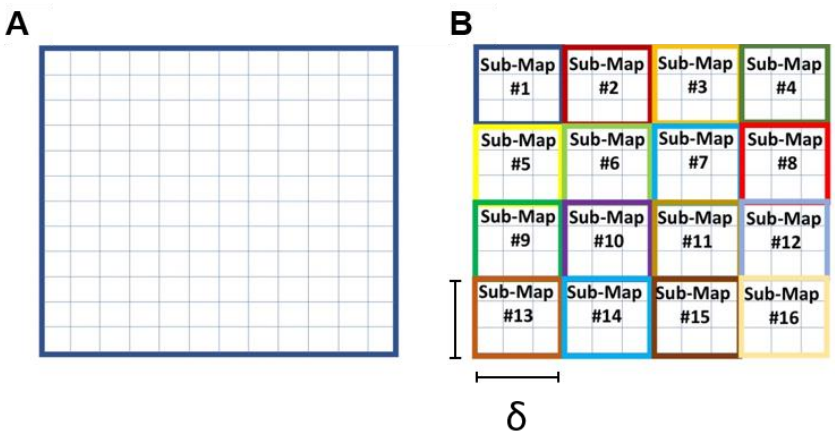

Figure 2.9 *Visual example of Raman map sectioning.* ***A)*** *The pristine Raman map is segmented in squared maps of defined dimensions (length = δ), termed sub-maps* ***B)*** *and used as independent maps.*

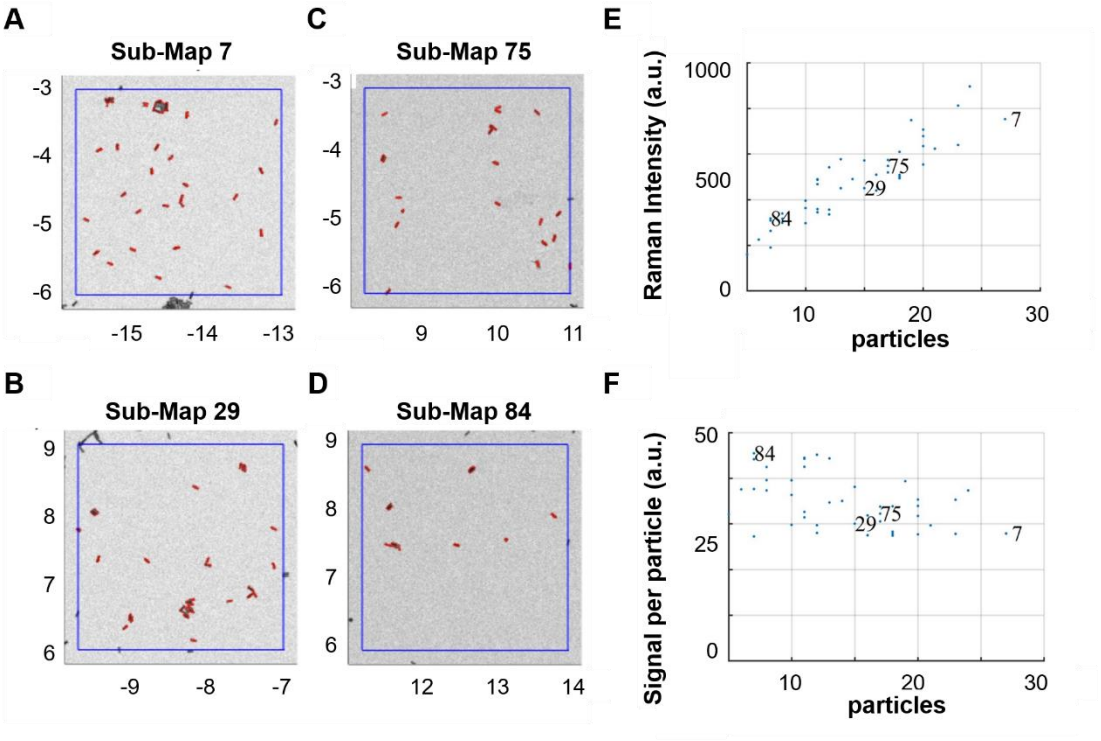

Figure 2.10 *A selection of sub-maps within the 25th and 75th percentile of the SSpP distribution.* ***A-D)*** *TEM images of sub-maps where the NP boundaries are highlighted in red and the edges of the sub-maps in blue, showing a different degree of NPs aggregation, assumed as particle clusters formed during drying.* ***E)*** *Sums of the SERS signals found in each sub-map, plotted against the number of particles, defining a directly proportional relationship. The indexes reported in the plot refer to the sub-maps at the left.* ***F)*** *SSpP plot showing that the values do not scale with the number of particles found in each sub-map.*

2.5 Results from real experiments

Several SERS tags, with variation of NP morphologies and RaR molecules, were analysed with this method. In particular, AuNRs-MBT-PM, AuNRs-BT-PMA, AuNRs-2NAT-PMA and AuNSs-BPT-PMA. In ***Table 2.2*** some additional parameters are provided, which must be selected in the analysis procedure to obtain the SSpP. The first four parameters, namely GLV, Raman shift, p-value threshold, and b-value threshold, depend on the level of contrast in the TEM image and on the signal-to-noise ratio of the SERS spectra. Standard values are suggested by default, but these have been tailored for case-by-case data analysis. The last parameters, namely Min-Max Pixels particle, and Map subdivision, depend on the properties of the sample and on the quality and dimensions of the TEM image.

The parameters were optimised for the selected maps, to obtain an efficient individualization of the particles within the TEM image with the GLV parameter and a spectral selection of only those spectra which feature the specific fingerprint of the RaR reference by the Raman shift, p-value threshold and α values. In particular, the α thresholds were selected considering the b-value distribution. Shown in ***Figure 2.11 A)*** and ***B)*** are the b-values distribution and

intensity distribution at 1078 cm^{-1}, respectively. The same distributions are presented in ***Figure 2.11 C-D)*** after the first selection done on the p-value. The reported spectra have a p-value lower than 0.05. The b-value distribution is slightly reduced, mainly on the left tail, avoiding the smallest values while the central value of intensity becomes lower. In ***Figure 2.11 E-F)*** the distributions after the b-value selection are presented: the threshold ($\alpha = 10$) was chosen in order to consider the whole distribution, eliminating only those values which correspond to spectra that are not sufficiently similar to the reference. The α threshold value was selected as the minimum value that can filter spectra with enough intensity to be able to recognize most of the spectral fingerprint in the reference spectrum. Indeed, after selection, the intensity distribution was sharper around the central value, but still presented some small values in the left tail. This indicates that only those spectra with poor match with the reference were neglected and not the ones with a low intensity.

Table 2.2 *Parameters established in the SERSTEM App to analyze samples AuNRs-BT-PMA and AuNSs-BPT-PMA.*

Sample	GLV	Raman shift	p-value threshold	b-value threshold (α)	Min-Max Pixels particle	Map subdivision (µm)
AuNRs-BT-PMA	0.5	1078	0.05	10	5-300	2
AuNSs-BPT-PMA	0.5	1594	0.05	10	5-100	1

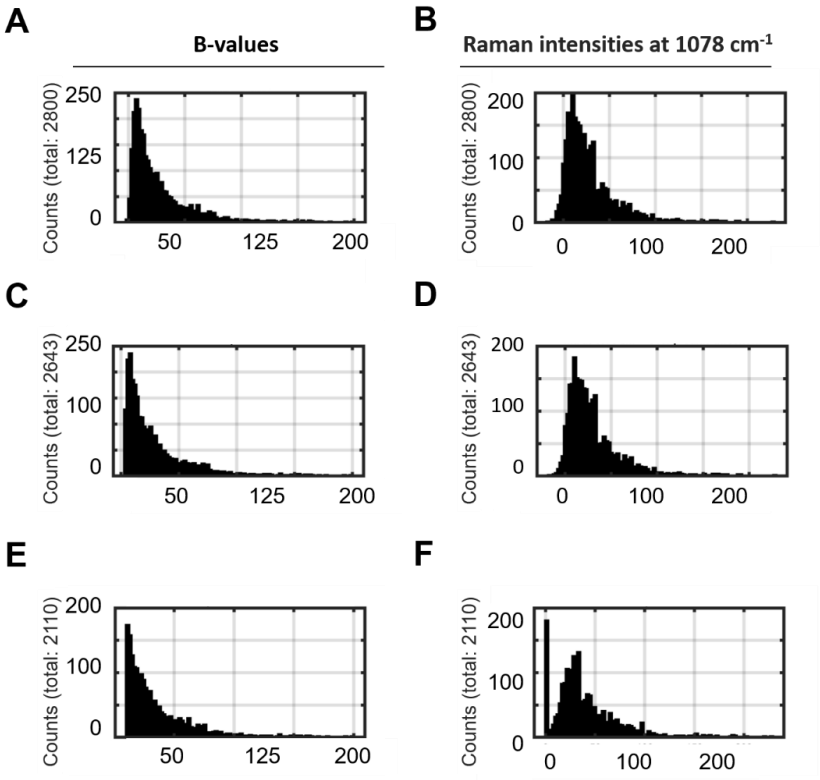

Figure 2.11 A,B) *B-values distribution and intensity distribution at 1078 cm^{-1}, respectively.* ***C,D)****: Corresponding distributions after the first selection on p-value.* ***E,F)*** *Distributions after the b-value selection with a threshold of $\alpha = 10$.*

In particular, the results presented in ***Figure 2.12A)*** were analysed using the parameters listed in ***Table 2.2*** .The map subdivision parameter was chosen to have a large number of sub-maps containing few NPs each, to obtain results that were as precise as possible, within the instrumental boundaries of the analysis. Importantly, it is not possible to choose a sub-map dimension smaller than the resolution of the map (namely, 1 μm). Indeed, the x-y step sizes used to collect the SERS maps depend on the laser spot dimension, which is strongly related to the combination of objective numerical aperture, laser intensity and material. Although it should be small enough to survey the whole sample, oversampling should be avoided. In particular, small sub-maps can provide more statistical value but the higher subdivision of the map into small parts can lead to a lower accuracy in TEM images and overlap in the SERS spectra. Otherwise, larger sub-maps are less subjected to wrong assignments at the edges, but the small number of squares generated results with poor statistics. Those sub-maps in which no particles are present or no spectra pass the filters are directly excluded from the analysis. In this manner, false positives, namely SERS signals from areas without particles, and false negatives, i.e. detected particles without SERS signal, are avoided. A minimum value of 2 μm was ultimately selected. The Minimum and Maximum pixels particle parameters were assigned through the Feret diameters estimated by the SERSTEM App, as displayed in ***Figure***

2.13. The distribution of the SSpP values calculated in all selected sub-maps is reported in ***Figure 2.12B)***. The map index is indicated along the x axis. On average, 5 AuNRs-BT-PMA NPs were calculated per 4 μm^2 box in the TEM grid. Along the z axis (i.e., the axis of the SSpP), the points appear to be clustered around an average value. In ***Figure 2.12C)*** a boxplot is included, which displays the SSpP at 1078 cm^{-1}: the median value obtained was 17.5 counts, with 50% of the values ranging between 10 and 39 counts. Choosing similar parameters in the App, the other SERS tags were analysed, and the results for AuNSs-BPT-PMA are also reported in ***Figure 2.12.*** This sample was prepared without the glow discharge treatment of the grid (see **Section 2.7.5**), which caused the particles to be closer to each other, with respect to the other samples. Considering this, a smaller submap dimension (namely, 1 µm) was chosen, to obtain areas where adjacent NPs can still be distinguished, see ***Figure 2.12A)***. Using these parameters, an average value of 6 SERS tags per 1 μm^2 area was obtained. The median SSpP at 1592cm^{-1} was found to be 17 counts. The results for the other samples, AuNRs-MBT-PMA and AuNRs-2NAT-PMA, were obtained using the parameters listed in ***Table 2.2*** and are displayed in ***Figure 2.14A)***. The first one showed a similar trend, with an average number of 6 SERS tags per 4 μm^2 area and a calculated median SSpP at 1080 cm^{-1} of 49.3 counts. Meanwhile, AuNRs-2NAT-PMA showed an average number of 25 SERS tags per 4 μm^2 square and a significantly lower SSpP at 1383 cm^{-1} (ca. 4 counts), as shown in ***Figure 2.14B-C)***. This can be explained considering that these AuNRs were smaller and had a higher amount of PEG (and therefore a reduced amount of RaRs on the surface) than those in AuNRs-MBT-PMA and AuNRs-BT-PMA. These differences are indeed expected to reduce the SERS enhancement.

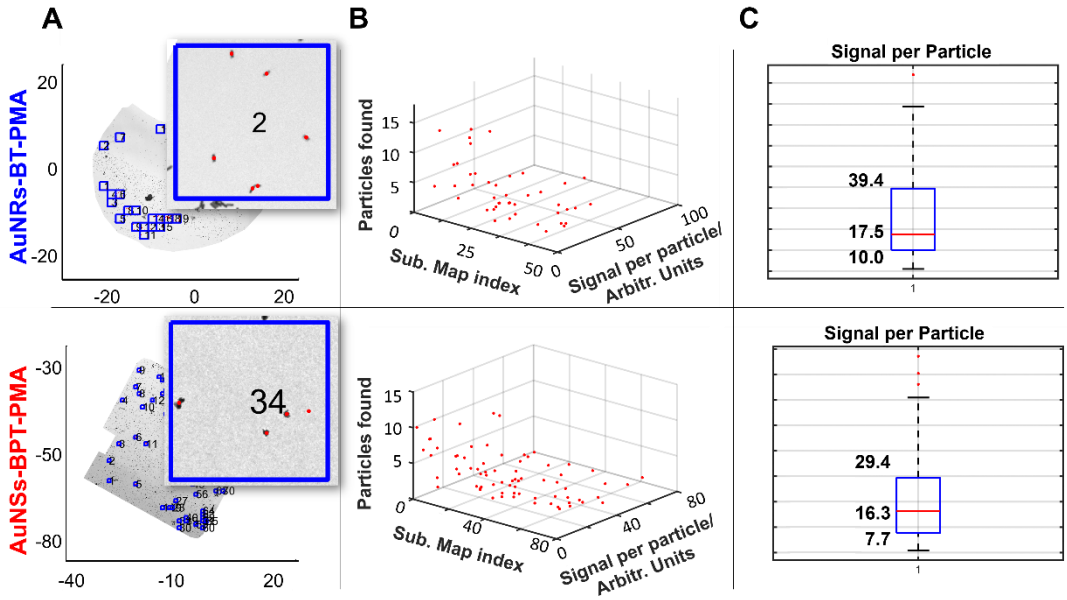

Figure 2.12 *SERSTEM App results corresponding to samples AuNRs-BT-PMA (top panel) and AuNSs-BPT-PMA (bottom panel).* ***A)*** *TEM images showing in blue those sub-maps that include points whose SERS spectra statistically matched the reference and in red the position*

of SERS tags with an area between 5 and 300 pixels. ***B)*** *SSpP of each sub-map.* ***C)*** *Box plot of the average SSpP, calculated from all selected sub-maps with evidenced the 25% and 75% percentiles of the median value.*

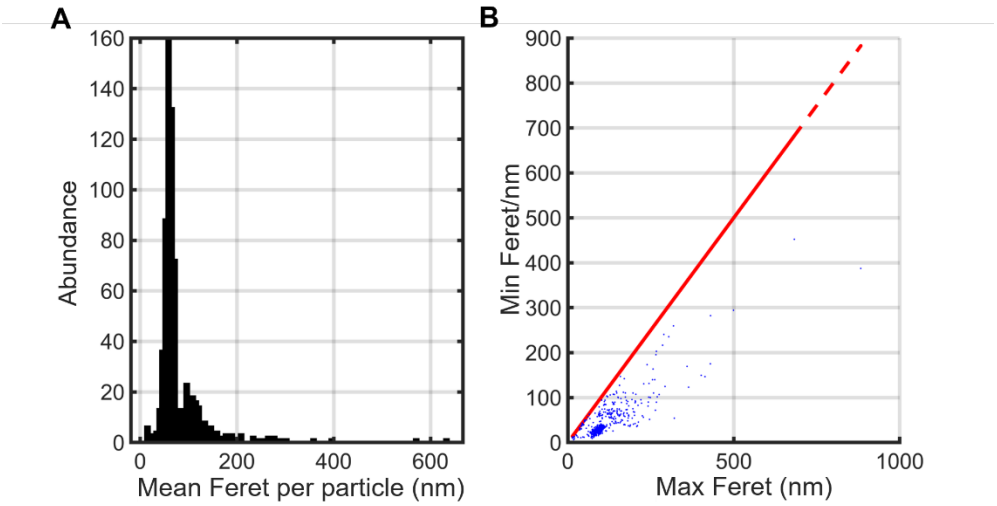

Figure 2.13 A) *Abundance of the mean Feret diameters, showing two main peaks around 60 nm and 100 nm.* ***B)*** *Scatter plot referring to the maximum and minimum Feret diameters for each particle.*

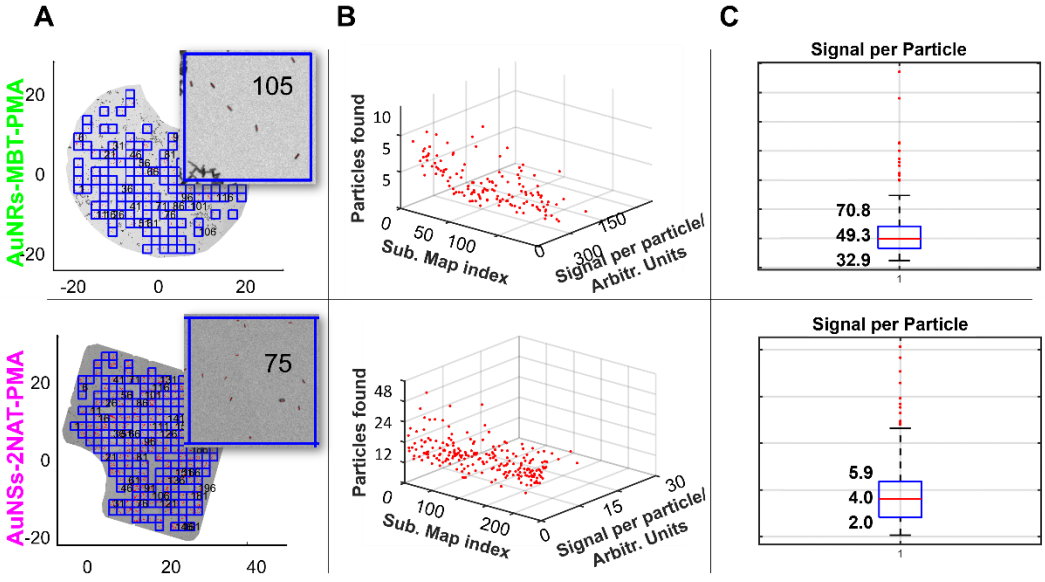

Figure 2.14 *SERSTEM App results for AuNRs-MBT-PMA (top panel) and AuNRs-2NAT-PMA (bottom panel).* ***A)*** *Analysed TEM images with sub-maps framed in blue for those points whose SERS spectra statistically matched the reference, and highlighted in red the positions of SERS tags with an area between 5 and 300 pixels.* ***B)*** *SSpP value of each submap.* ***C)*** *Boxplot of the average SSpP calculated from all the selected sub-maps were the 25% and 75% percentiles of the median value are highlighted.*

Thereafter, it was also possible to optimize the parameters, to quantify in a more reliable way the number of NPs in those spots where two or three particles were clustered close to each other. Hence, a second analysis was run to select a lower upper limit for the number of pixels per particle. The resulting SSpP changed slightly but still remained in the same range of before, as shown in ***Table 2.3***, indicating that the (few) misinterpreted NPs did not strongly influence the statistics. Again, AuNRs-2NAT-PMA yielded low intensities, while the other samples showed a similar median SSpP.

Finally, the App was tested toward quantifying the number of particles of one half of a TEM grid, assumed as an unknown sample, using the other half as the calibration sample. Hence, the Raman map was divided into two halves, reported in ***Figure 2.15A)*** and ***C)***. In this way, the same batch of particles and the same measurement setup were used, ensuring the reliability on the SSpP estimation. The first calibration half **(A)**, was subdivided in sub-maps of 3 μm edge. The resulted median SSpP was 31.9 counts, see the boxplot in ***Figure 2.15B)***. Afterwards, the number of particles (N) present in the unknown half grid **(C)** was calculated by the ratio of the sum of the SERS signals found in that half, and the previously estimated SSpP. Although the agreement between the experimental number of particles (N = 473) and those predicted (N = 560) was not perfect, it shows a reasonable reliability of the method (see ***Figure 2.15 D)***).

Table 2.3 *SERSTEM App results of the analysis performed on samples with different parameters.*

SERS tags	Raman shift	Min-Max Pixels particle	Map subdivision (μm)	Number of SERS tags per submap	Median SSpP (counts)
AuNRs-MBT-PMA	1080	5-100	2	10	34
AuNRs-BT-PMA	1078	5-300	2	5	24
AuNRs-2NAT-PMA	1383	5-80	2	16	2
AuNSs-BPT-PMA	1594	5-100	1	2	45

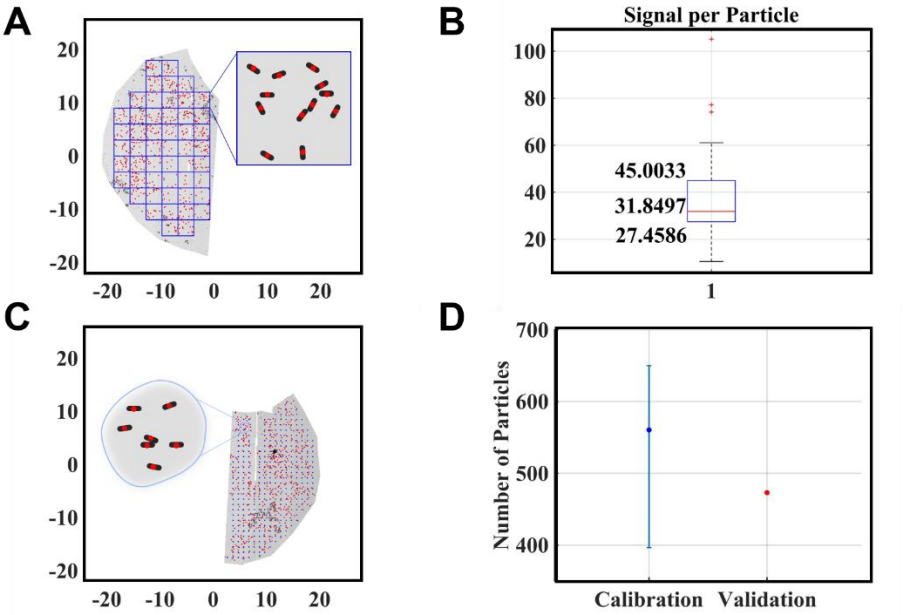

Figure 2.15 *Validation:* ***A)*** *the calibration half of the TEM grid analyzed with one highlighted sub-map and* ***B)*** *the related boxplot with median SERS signal intensity per particle of 31.9 counts.* ***C)*** *The other unknown half of the TEM grid, analysed in the same manner, without applying a segmentation in sub-maps.* ***D)*** *Number of NPs detected by the automated procedure on C) (red dot) and the calculated number of particles using the median, 25th and 75th percentiles in B) (blue dot and error bar).*

2.6 Conclusion

The developed SERSTEM App allowed us to correlate SERS maps with TEM images, with the aim of calculating the SERS signal for a single SERS tag. This method provided characterisation and accurate estimates of the signal intensity for different SERS tags, which were subsequently used in SERS bioimaging experiments, as reported in the following Chapters.

The SERS signal was collected from small recognizable areas of air-dried colloidal dispersions of SERS tags. Subsequently, the SERS tags were effectively localized through TEM images of the same areas. Correlating the positions of the NPs and their SERS signals, the App was able to estimate the signal intensity at one of the main peaks of the RaR molecule for each of the selected SERS tags. The analysis automatically excluded all those regions featuring SERS signals without a sufficient similarity to the reference, as well as empty spaces. Four different SERS tags were tested, showing that the SSpP was similar in those samples with a similar ratio RaR/PEG ratio. Only one sample with a lower RaR/PEG ratio, namely AuNRs-2NAT-PMA, showed a lower SSpP value. The estimation of the SSpP was also used to predict the number of NPs in an unknown region, obtaining a value in good agreement with the counted value.

The characterization of the signal from SERS tags via the SERSTEM App was used in **Chapter 3**, to obtain a reliable estimate of the number of NPs taken up by living cells.

2.7 Experimental section

2.7.1 Chemicals

Tetrachloroauric acid trihydrate ($HAuCl_4 \cdot 3H_2O$, ≥99%), sodium borohydride ($NaBH_4$, 99%), L-ascorbic acid (≥99%), silver nitrate ($AgNO_3$, ≥99%), hexadecyltrimethylammonium bromide (CTAB, ≥99%), n-decanol, O-[2-(3-mercaptopropionylamino)ethyl]-O'-methylpolyethylene glycol (PEG-SH, MW 5000 g/mol), benzenethiol (BT, ≥98%), 4-methylbenzenethiol (4MBT, 98%), biphenyl-4-thiol (4BPT, 97%), 2-naphthalenethiol (2NaT, 99%), poly(isobutylene-alt-maleic anhydride) (average MW ~6000 g/mol), dodecylamine (98%), tetrahydrofuran (THF, 99.85%, extra dry), chloroform ($CHCl_3$, ≥99.8%) and sodium hydroxide (NaOH, >97%) were purchased from Sigma-Aldrich. Hydrochloric acid solution (37 wt%) was purchased from Fisher Chemical. All chemicals were used without further purification. Milli-Q water (resistivity 18.2 MΩ·cm at 25 °C) was used in all experiments. All glassware was washed with aqua regia, rinsed with Milli-Q water, and dried prior to use.

2.7.2 NP synthesis

2.7.2.1 AuNRs

AuNRs with a longitudinal LSPR at around 785 nm were prepared by a modified seeded-growth method. [48] In brief, 1-2 nm gold seeds were grown in the presence of CTAB and n-decanol to form small anisotropic seeds of 7.5 nm width, which were subsequently used as seeds for the growth of larger NRs of 17 nm × 60 nm (LSPR at 785 nm).

AuNRs with a longitudinal LSPR at around 800nm and dimension of 33 nm width × 102 nm lenght, were synthetized by Dr. Xialou Zhou, one of my group member.

2.7.2.2 AuNSs

AuNSs (50 nm diameter) with a LSPR at around 785 nm were prepared by a reported seed-mediated growth method.[28,30] The seed solution was prepared by adding 5 mL of 34 mM citrate solution to 95 mL of boiling 0.5 mM $HAuCl_4$ solution, under vigorous stirring. After 15 min of boiling, the solution was cooled down and stored at 4 °C. For AuNSs synthesis, 2 mL of the citrate-stabilized seed solution was added to 50 mL of 0.25 mM $HAuCl_4$ solution (with 50 µL of 1 M HCl) in a 100 mL glass vial, at room temperature under moderate stirring. Quickly, 500 µL of 3 mM $AgNO_3$ and 500 µL of 50 mM ascorbic acid were added simultaneously. The resulting solution was mixed with 380 µL of PEG-SH 0.1 mM, stirred for 15 min, washed by centrifugation at 6500 rpm for 15 min at 20 ºC, and redispersed in water.

2.7.3 SERS tags synthesis

500 µL of AuNRs (17nm × 60 nm) at a concentration of 3.6×10^{12} NP mL^{-1} and 1 mL of AuNRs (33nm × 102 nm) at a concentration of 8×10^{11} NP mL^{-1}, were first pre-stabilized with 800 µL and 1 mL thiolated PEG 0.1 mM, respectively. Smaller AuNRs presented ~ double amount of PEG per nm^2. AuNSs were prepared to have the same RaR/PEG ratio as the larger AuNRs. The NPs were transferred to $CHCl_3$ by saturating the surface with hydrophobic RaR molecules, and subsequently wrapped with the amphiphilic co-polymer PMA, which provides colloidal stability in aqueous media thanks to its hydrophilic backbone. After washing the particles in water 4 times, the final concentrations for the experiments were fixed. Specifically, AuNRs encoded with MBT (AuNRs-MBT-PMA) were at [Au^0] = 0.25 mM, AuNRs-BT-PMA at [Au^0] = 0.17 mM, AuNRs-2NAT-PMA at [Au^0] = 0.17 mM, and AuNSs encoded with BPT (AuNSs-BPT-PMA) at [Au^0] = 0.5 mM.

2.7.4 NPs characterization

UV−vis extinction spectra were recorded using an Agilent 8453 UV−vis diode array spectrophotometer, 10 mm standard path length cuvette with 3.5 mL volume. TEM images were collected with a JEOL JEM-1400PLUS transmission electron microscope operating at 120 kV, using carbon coated 400 square mesh copper grids.

2.7.5 TEM grid with references preparation

A 200-mesh copper-carbon film London finder grid for electron microscopy was treated by glow discharge to hydrophilize the surface and obtain a homogeneous spreading of the particles. After 10 minutes in vacuum (10^{-1} mbar), a negative polarity with a coating current of 30 mA for 2 min and 30 s has been applied. Immediately after, 5µL of AuNRs-MBT-PMA at [Au^0] = 0.25 mM (2× diluted with MilliQ water), 3µL of AuNRs-BT-PMA at [Au^0] = 0.17 mM (3× diluted with MilliQ water), 3µL of AuNRs-2NAT-PMA) at [Au^0] = 0.17 mM and 5µL of AuNSs-BPT-PMA at [Au^0] = 0.5 mM, have been drop casted and left dry in air.

References:

(1) Bell, S. E. J.; Charron, G.; Cortés, E.; Kneipp, J.; de la Chapelle, M. L.; Langer, J.; Procházka, M.; Tran, V.; Schlücker, S. Towards Reliable and Quantitative Surface-Enhanced Raman Scattering (SERS): From Key Parameters to Good Analytical Practice. *Angew. Chem. Int. Ed. Engl.* **2020**, *59*, 5454–5462. https://doi.org/10.1002/ANIE.201908154.

(2) Licha, K.; Olbrich, C. Optical Imaging in Drug Discovery and Diagnostic Applications. *Advanced Drug Delivery Reviews*. June 2005, pp 1087–1108. https://doi.org/10.1016/j.addr.2005.01.021.

(3) Kong, K. V. SERS Biosensing and Bioimaging: Design and Applications in Cancer Diagnostics. In *Next Generation Point-of-care Biomedical Sensors Technologies for Cancer Diagnosis*; Springer Singapore, 2017; pp 345–364. https://doi.org/10.1007/978-981-10-4726-8_15.

(4) Ueda, S.; Kuji, I.; Shigekawa, T.; Takeuchi, H.; Sano, H.; Hirokawa, E.; Shimada, H.; Suzuki, H.; Oda, M.; Osaki, A.; et al. Optical Imaging for Monitoring Tumor Oxygenation Response after Initiation of Single-Agent Bevacizumab Followed by Cytotoxic Chemotherapy in Breast Cancer Patients. *PLoS One* **2014**, *9*, e98715. https://doi.org/10.1371/journal.pone.0098715.

(5) Lewins, J. S. Future Directions in Minimally Invasive Intervention. *Trans. Am. Clin. Climatol. Assoc.* **2017**, *128*, 346–352.

(6) Smith, B. R.; Gambhir, S. S. Nanomaterials for In Vivo Imaging. *Chem. Rev.* **2017**, *117*, 901–986. https://doi.org/10.1021/acs.chemrev.6b00073.

(7) Hillman, E. M.; Voleti, V.; Patel, K.; Li, W.; Yu, H.; Perez-Campos, C.; Benezra, S. E.; Bruno, R. M.; Galwaduge, P. T. High-Speed 3D Imaging of Cellular Activity in the Brain Using Axially-Extended Beams and Light Sheets. *Curr. Opin. Neurobiol.* **2018**, *50*, 190–200. https://doi.org/10.1016/J.CONB.2018.03.007.

(8) Combs, C. A.; Shroff, H. Fluorescence Microscopy: A Concise Guide to Current Imaging Methods. *Curr. Protoc. Neurosci.* **2017**, *79*, 2.1.1-2.1.25. https://doi.org/10.1002/cpns.29.

(9) Wolfbeis, O. S. An Overview of Nanoparticles Commonly Used in Fluorescent Bioimaging. *Chem. Soc. Rev.* **2015**, *44*, 4743–4768. https://doi.org/10.1039/c4cs00392f.

(10) Swiecicki, J. M.; Thiebaut, F.; Di Pisa, M.; Gourdin -Bertin, S.; Tailhades, J.; Mansuy, C.; Burlina, F.; Chwetzoff, S.; Trugnan, G.; Chassaing, G.; et al. How to Unveil Self-Quenched Fluorophores and Subsequently Map the Subcellular Distribution of

Exogenous Peptides. *Sci. Rep.* **2016**, *6*, 20237. https://doi.org/10.1038/srep20237.

(11) Lenzi, E.; Jiménez de Aberasturi, D.; Liz-Marzán, L. M. Surface-Enhanced Raman Scattering Tags for Three-Dimensional Bioimaging and Biomarker Detection. *ACS Sensors* **2019**, *4*, 1126–1137. https://doi.org/10.1021/acssensors.9b00321.

(12) Langer, J.; Jiménez de Aberasturi, D.; Aizpurua, J.; Alvarez-Puebla, R. A.; Auguié, B.; Baumberg, J. J.; Bazan, G. C.; Bell, S. E. J.; Boisen, A.; Brolo, A. G.; et al. Present and Future of Surface-Enhanced Raman Scattering. *ACS Nano* **2020**, *14*, 28–117. https://doi.org/10.1021/acsnano.9b04224.

(13) Strozyk, M. S.; de Aberasturi, D. J.; Gregory, J. V.; Brust, M.; Lahann, J.; Liz-Marzán, L. M. Spatial Analysis of Metal-PLGA Hybrid Microstructures Using 3D SERS Imaging. *Adv. Funct. Mater.* **2017**, *27*, 1701626. https://doi.org/10.1002/adfm.201701626.

(14) Bohndiek, S. E.; Wagadarikar, A.; Zavaleta, C. L.; Van de Sompel, D.; Garai, E.; Jokerst, J. V; Yazdanfar, S.; Gambhir, S. S. A Small Animal Raman Instrument for Rapid, Wide-Area, Spectroscopic Imaging. *Proc. Natl. Acad. Sci. U. S. A.* **2013**, *110*, 12408–12413. https://doi.org/10.1073/pnas.1301379110.

(15) Maiti, K. K.; Dinish, U. S.; Samanta, A.; Vendrell, M.; Soh, K. S.; Park, S. J.; Olivo, M.; Chang, Y. T. Multiplex Targeted in Vivo Cancer Detection Using Sensitive Near-Infrared SERS Nanotags. *Nano Today* **2012**, *7*, 85–93. https://doi.org/10.1016/j.nantod.2012.02.008.

(16) Allen, F. I.; Kim, E.; Ryu, S.-G.; Ozdol, B.; Grigoropoulos, C. P.; Minor, A. M. In-Situ Raman Spectroscopy in a TEM. *Microsc. Microanal.* **2013**, *19*, 394–395. https://doi.org/10.1017/S1431927613003966.

(17) Allen, F. I.; Kim, E.; Andresen, N. C.; Grigoropoulos, C. P.; Minor, A. M. In Situ TEM Raman Spectroscopy and Laser-Based Materials Modification. *Ultramicroscopy* **2017**, *178*, 33–37. https://doi.org/10.1016/j.ultramic.2016.06.011.

(18) Rycenga, M.; Camargo, P. H. C.; Li, W.; Moran, C. H.; Xia, Y. Understanding the SERS Effects of Single Silver Nanoparticles and Their Dimers, One at a Time. *Journal of Physical Chemistry Letters*. American Chemical Society February 2010, pp 696–703. https://doi.org/10.1021/jz900286a.

(19) Tran, V.; Thiel, C.; Svejda, J. T.; Jalali, M.; Walkenfort, B.; Erni, D.; Schlücker, S. Probing the SERS Brightness of Individual Au Nanoparticles, Hollow Au/Ag Nanoshells, Au Nanostars and Au Core/Au Satellite Particles: Single-Particle Experiments and Computer Simulations. *Nanoscale* **2018**, *10*, 21721–21731. https://doi.org/10.1039/C8NR06028B.

(20) Moran, C. H.; Xia, X.; Xia, Y. Improving Correlated SERS Measurements with Scanning Electron Microscopy: An Assessment of the Problem Arising from the Deposition of Amorphous Carbon. *Phys. Chem. Chem. Phys.* **2013**, *15*, 5400–5406. https://doi.org/10.1039/C3CP43989E.

(21) Timmermans, F. J.; Lenferink, A. T. M.; Van Wolferen, H. A. G. M.; Otto, C. Correlative SEM SERS for Quantitative Analysis of Dimer Nanoparticles. *Analyst* **2016**, *141*, 6455–6462. https://doi.org/10.1039/C6AN01648K.

(22) Yang, L.; Yan, B.; Reinhard, B. M. Correlated Optical Spectroscopy and Transmission Electron Microscopy of Individual Hollow Nanoparticles and Their Dimers. *J. Phys. Chem. C* **2008**, *112*, 15989–15996. https://doi.org/10.1021/JP804790P.

(23) Wustholz, K. L.; Henry, A.-I.; Bingham, J. M.; Kleinman, S. L.; Natan, M. J.; Griffith Freeman, R.; Van Duyne, R. P.; Wustholz, K. L. Exploring Single-Molecule SERS and Single-Nanoparticle Plasmon Microscopy. In *Plasmonics: Metallic Nanostructures and Their Optical Properties VII*; Stockman, M. I., Ed.; SPIE, 2009; Vol. 7394, pp 21–30. https://doi.org/10.1117/12.826168.

(24) Camden, J. P.; Dieringer, J. A.; Wang, Y.; Masiello, D. J.; Marks, L. D.; Schatz, G. C.; Van Duyne, R. P. Probing the Structure of Single-Molecule Surface-Enhanced Raman Scattering Hot Spots. *J. Am. Chem. Soc.* **2008**, *130*, 12616–12617. https://doi.org/10.1021/ja8051427.

(25) Amendola, V. Correlation of Surface-Enhanced Raman Scattering (SERS) with the Surface Density of Gold Nanoparticles: Evaluation of the Critical Number of SERS Tags for a Detectable Signal. *Beilstein J. Nanotechnol.* **2019**, *10*, 1016–1023. https://doi.org/10.3762/BJNANO.10.102.

(26) Shaw, C. P.; Fan, M.; Lane, C.; Barry, G.; Jirasek, A. I.; Brolo, A. G. Statistical Correlation between SERS Intensity and Nanoparticle Cluster Size. *J. Phys. Chem. C* **2013**, *117*, 16596–16605. https://doi.org/10.1021/jp404250q.

(27) Jiménez de Aberasturi, D.; Henriksen-Lacey, M.; Litti, L.; Langer, J.; Liz-Marzán, L. M. Using SERS Tags to Image the Three-Dimensional Structure of Complex Cell Models. *Adv. Funct. Mater.* **2020**, *30*, 1909655. https://doi.org/10.1002/adfm.201909655.

(28) Jiménez de Aberasturi, D.; Serrano-Montes, A. B.; Langer, J.; Henriksen-Lacey, M.; Parak, W. J.; Liz-Marzán, L. M. Surface Enhanced Raman Scattering Encoded Gold Nanostars for Multiplexed Cell Discrimination. *Chem. Mater.* **2016**, *28*, 6779–6790. https://doi.org/10.1021/acs.chemmater.6b03349.

(29) Hahn, M. A.; Singh, A. K.; Sharma, P.; Brown, S. C.; Moudgil, B. M. Nanoparticles as

Contrast Agents for In-Vivo Bioimaging: Current Status and Future Perspectives. *Analytical and Bioanalytical Chemistry*. Anal Bioanal Chem January 2011, pp 3–27. https://doi.org/10.1007/s00216-010-4207-5.

(30) Yuan, H.; Khoury, C. G.; Hwang, H.; Wilson, C. M.; Grant, G. A.; Vo-Dinh, T. Gold Nanostars: Surfactant-Free Synthesis, 3D Modelling, and Two-Photon Photoluminescence Imaging. *Nanotechnology* **2012**, *23*, 075102. https://doi.org/10.1088/0957-4484/23/7/075102.

(31) Saikin, S. K.; Olivares-Amaya, R.; Rappoport, D.; Stopa, M.; Aspuru-Guzik, A. On the Chemical Bonding Effects in the Raman Response: Benzenethiol Adsorbed on Silver Clusters. *Phys. Chem. Chem. Phys.* **2009**, *11*, 9401–9411. https://doi.org/10.1039/b906885f.

(32) Varsányi, G. *Vibrational Spectra of Benzene Derivatives*; Academic Press, 1969.

(33) Alvarez-Puebla, R. A.; Dos Santos, D. S.; Aroca, R. F. Surface-Enhanced Raman Scattering for Ultrasensitive Chemical Analysis of 1 and 2-Naphthalenethiols. *Analyst* **2004**, *129*, 1251–1256. https://doi.org/10.1039/b410488a.

(34) Kalbacova, J.; Rodriguez, R. D.; Desale, V.; Schneider, M.; Amin, I.; Jordan, R.; Zahn, D. R. T. Chemical Stability of Plasmon-Active Silver Tips for Tip-Enhanced Raman Spectroscopy. *Nanospectroscopy* **2015**, *1*. https://doi.org/10.2478/nansp-2014-0002.

(35) Chalfoun, J.; Majurski, M.; Blattner, T.; Bhadriraju, K.; Keyrouz, W.; Bajcsy, P.; Brady, M. MIST: Accurate and Scalable Microscopy Image Stitching Tool with Stage Modeling and Error Minimization. *Sci. Rep.* **2017**, *7*, 4988. https://doi.org/10.1038/s41598-017-04567-y.

(36) Nanostructure & Optics Laboratory - SERSTEM https://wwwdisc.chimica.unipd.it/nanostructures.optics/SERSTEM.html.

(37) Lenzi, E.; Litti, L.; Jimenez de Aberasturi, D.; Henriksen-Lacey, M.; Liz-Marzán, L. M. SERSTEM: An App for the Statistical Analysis of Correlative SERS and TEM Imaging and Evaluation of SERS Tags Performance. *J. Raman Spectrosc.* **2021**, *52*, 355–365. https://doi.org/10.1002/jrs.6043.

(38) Nyquist, H. Certain Topics in Telegraph Transmission Theory. *Proc. IEEE* **2002**, *90*, 280–305. https://doi.org/10.1109/5.989875.

(39) Shannon, C. E. Communication in the Presence of Noise. *Proc. IRE* **1949**, *37*, 10–21. https://doi.org/10.1109/JRPROC.1949.232969.

(40) Hoonejani, M. R.; Pallaoro, A.; Braun, G. B.; Moskovits, M.; Meinhart, C. D. Quantitative Multiplexed Simulated-Cell Identification by SERS in Microfluidic

Devices. *Nanoscale* **2015**, *7*, 16834–16840. https://doi.org/10.1039/C5NR04147C.

(41) Pallaoro, A.; Hoonejani, M. R.; Braun, G. B.; Meinhart, C. D.; Moskovits, M. Rapid Identification by Surface-Enhanced Raman Spectroscopy of Cancer Cells at Low Concentrations Flowing in a Microfluidic Channel. *ACS Nano* **2015**, *9*, 4328–4336. https://doi.org/10.1021/ACSNANO.5B00750.

(42) Zhang, Y.; Wang, Z.; Wu, L.; Zong, S.; Yun, B.; Cui, Y. Combining Multiplex SERS Nanovectors and Multivariate Analysis for In Situ Profiling of Circulating Tumor Cell Phenotype Using a Microfluidic Chip. *Small* **2018**, *14*, 1704433. https://doi.org/10.1002/SMLL.201704433.

(43) Gallagher, N. B. Classical Least Squares for Detection and Classification. *Data Handl. Sci. Technol.* **2020**, *32*, 231–246. https://doi.org/10.1016/B978-0-444-63977-6.00011-0.

(44) Litti, L.; Meneghetti, M. Predictions on the SERS Enhancement Factor of Gold Nanosphere Aggregate Samples. *Phys. Chem. Chem. Phys.* **2019**, *21*, 15515–15522. https://doi.org/10.1039/C9CP02015B.

(45) Solís, D. M.; Taboada, J. M.; Obelleiro, F.; Liz-Marzán, L. M.; García De Abajo, F. J. Optimization of Nanoparticle-Based SERS Substrates through Large-Scale Realistic Simulations. *ACS Photonics* **2017**, *4*, 329–337. https://doi.org/10.1021/acsphotonics.6b00786.

(46) González-Rubio, G.; González-Izquierdo, J.; Bañares, L.; Tardajos, G.; Rivera, A.; Altantzis, T.; Bals, S.; Peña-Rodríguez, O.; Guerrero-Martínez, A.; Liz-Marzán, L. M. Femtosecond Laser-Controlled Tip-to-Tip Assembly and Welding of Gold Nanorods. *Nano Lett.* **2015**, *15*, 8282–8288. https://doi.org/10.1021/acs.nanolett.5b03844.

(47) Romo-Herrera, J. M.; Alvarez-Puebla, R. A.; Liz-Marzán, L. M. Controlled Assembly of Plasmonic Colloidal Nanoparticle Clusters. *Nanoscale*. The Royal Society of Chemistry April 2011, pp 1304–1315. https://doi.org/10.1039/c0nr00804d.

(48) González-Rubio, G.; Kumar, V.; Llombart, P.; Díaz-Núñez, P.; Bladt, E.; Altantzis, T.; Bals, S.; Peña-Rodríguez, O.; Noya, E. G.; MacDowell, L. G.; et al. Disconnecting Symmetry Breaking from Seeded Growth for the Reproducible Synthesis of High Quality Gold Nanorods. *ACS Nano* **2019**, *13*, 4424–4435. https://doi.org/10.1021/acsnano.8b09658.

3. Study of the interaction between SERS tags and cells

Contents

3.1 Introduction

As described in the previous **Chapter 2**, we developed the SERSTEM App to correlate SERS and TEM images, which could be used to identify and quantify the signal coming from individual SERS tags. SERSTEM was validated with an example where the number of SERS tags dried on a flat surface (TEM grid) was quantified through the obtained SERS signal. In the present **Chapter 3**, the same methodology is used to quantify the number of SERS tags in a more complex sample; in this case using living cells labelled with SERS tags. The quantification of SERS tags uptaken by living cells and their evolution over time are important to understand several processes arising from the interaction of cells with nanoparticles, such as NP uptake, dwelling time during cellular division, exocytosis, among others. These processes must be considered when using such labels as contrast agent for SERS bioimaging. Moreover, a deep knowledge of such processes is fundamental to control the parameters that influence the final bioimage, such as the timeframe available for imaging or the multiplexing ability. Hence, an investigation aimed at quantifying NPs inside cells was performed through the implementation of the methodology we previously developed.

The use of NPs for bioimaging and biosensing was introduced in **Chapter 1**. However, SERS microscopy and especially confocal SERS microscopy of 3D cell models, still suffer from long acquisition times, which make repetitive measurements over short timepoints complicated. Furthermore, when considering the motile nature of living cells, experimental setups must be optimized to accurately detect SERS tags *in situ*.[1–3] Up to now, it is well known that the uptake of NPs depends on the cell type and is influenced by several factors, such as the features of the NPs (i.e. size, shape, charge and surface functionalization) and the applied procedures (time and conditions of incubation and NPs concentration).[2–4] However, it is well established that NPs with a diameter bigger than 10 nm enter the cell by endocytosis, i.e. enclosed inside small endosomes. Their transport and fate have been extensively studied,[5,6] determining both uptake[7] and division as asymmetric random processes.[3] Additionally, it has been shown that the latter process can also be influenced by exocytosis,[8] which itself is determined by the nanoparticle characteristics.[9,10] Unfortunately, the methods currently used to quantify NPs inside cells such as inductively coupled plasma mass spectrometry (ICP-MS) or flow cytometry, are destructive and, therefore, cannot always translate the biological processes into their real environment. ICP-MS based spectroscopies offer a very sensitive detection range, between parts per thousand (ppt) to parts per million (ppm),[11] while flow cytometry is used to quantify NPs functionalized with fluorescent labels, indirectly from the fluorescence signal. Although it may be possible to reach a single fluorescent tag, the resolution does not allow to individuate a single nanoparticle and the signal can be wrongly influenced by autofluorescence-induced noise or bleaching of the fluorophores.[12] Moreover, these techniques refer to the entire population of cells, whereas no studies regarding single live cells are available.[12–15] Some cases of indirect quantification

through SERS signal have been reported, based on a direct proportionality between the signal and the amount of NPs.[16] Amendola et al.[14] quantified NPs *in vitro* through correlation studies between ICP-MS and Raman signal, first testing simple colloidal solutions and then suspensions of lysated cells. On a different example, Zaveleta et al.[15] quantified five different types of SERS tags *in vivo*, obtaining a direct proportionality between tag concentration and SERS signal from a 2D map of the injection area. However, a method is still required, which can both monitor and estimate the number of NPs in a complex biological environment while remaining minimally invasive.

To address these issues, we adapted the methodology developed in **Chapter 2** to a system of human breast cancer MCF7 cells, to study the dynamics of SERS NPs inside the cells, characterizing the cellular uptake via multivariate data analysis. Considering the biologically complex microenvironment within *in vitro* samples, a data-driven supervised algorithm (SA) based on MLRA was used. In the SA, the output was compared to a reference spectrum from the SERS tags in solution, obtaining the SERS intensity recorded from a single cell containing tags. The average SERS signal of a labelled cell was then analysed with the help of the SERSTEM app to obtain the number of uptaken SERS tags. The method was compared and validated with ICP-MS analysis, yielding similar results. In the last **Section 3.4** of this chapter, we introduce the use of microfluidic devices study in more detail the dynamics of SERS tags in single cells. This part of the thesis was carried out at the International Iberian Nanotechnology Laboratory (INL) in Braga (Portugal), in collaboration with Dr. Sara Abalde-Cela. A second type of cancerous cellular line, namely SKBR3, was labelled with SERS tags to facilitate the production of cell-laden microdroplets by means of microfluidic devices. Subsequently, these microsystems were imaged over time to optimize the SERS measurement parameters.

3.2 Components and characterization

3.2.1 MCF7 cells

The MCF7 human breast cancer cell line is a widely studied epithelial cancer cell line that has characteristics of differentiated mammary epithelium. MCF7 cells are fairly large adherent cells very easy to propagate, with a typical cell size of 20-25 μm. These cells express many of the physical and morphological properties required for confocal imaging, such as adherence (enabling a fixed focal plane), immortalization (permitting changes in NP intensity to be studied in the same population over a long period of time), compact size and low aspect ratio (allowing multiple measurements on single cells to be carried out within an imaging window) (***Figure 3.1A***). Their division time of ca. 30 h, is also another characteristic that makes them attractive for 3D SERS imaging, allowing to measure cells pre- and post-division within days. Finally, they are characterized by active endocytosis, leading to high levels of SERS tag internalization, and the ability to withstand high levels of confluence without contact inhibition, which allows measuring the same area over time without detaching.

3.2.2 SKBR3 cells

The SKBR3 is a human breast cancer cell line that displays an epithelial morphology in tissue culture and can form poorly differentiated tumours. It was used as a second biological model in the realization of cell-laden microdroplets. Similarly to the MCF7, the SKBR3 average dimensions (ca. 12-18 μm), the duplication rate of ca. 28 h, as well as the compact cell size and low aspect ratio, make them a good biological model to realize the microdroplet experiments.[17]

3.2.3 SERS tags

SERS tags were prepared from AuNSs and AuNRs, both displaying LSPR at ca. 785 nm, in close resonance with the 785 nm laser typically used in Raman microscopes for bio-related experiments. AuNSs and AuNRs were decorated with the Raman reporter molecules BPT and 2NAT, respectively, coated with the PMA, and finally wrapped with the cationic polyelectrolyte poly-L-arginine hydrochloride (PA) to achieve positively charged and biocompatible SERS tags, as previously shown[18] (***Figure 3.1B***).

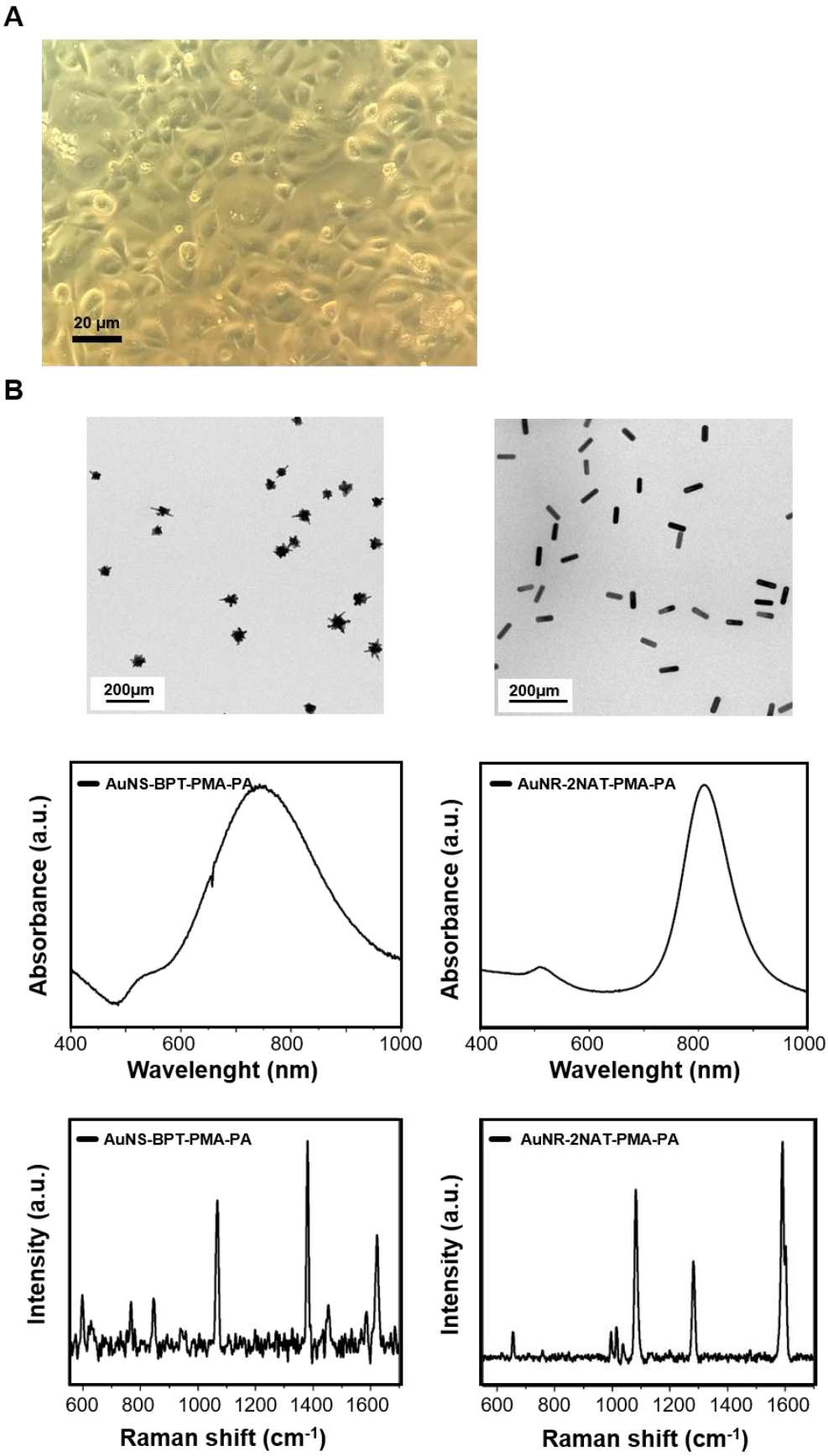

Figure 3.1 A) *Optical image of the MCF7 cells in an in vitro culture.* ***B)*** *TEM images, UV-Vis spectra and SERS spectra of AuNSs-BPT-PMA-PA (left panels) and AuNRs-2NAT-PMA-PA (right panels).*

3.3 SERS tags dynamics in 3D living cells

3.3.1 Supervised algorithm for quantification of SERS tags

The processes of SERS uptake and subsequent cellular division were modelled by means of simulated maps of SERS-labelled cells, and then analysed with an algorithm based on the MLRA method, termed supervised analysis (SA). Only those pixels inside the map whose SERS spectra match the reference spectrum of the selected SERS tags, with statistical significance, were analysed. This selection was then used to calculate the descriptive parameters of the SA, such as the surface occupancy by SERS tags inside the map or the average signal intensity, and in turn the number of SERS tags inside the map area (see ***Table 3.1***).

Table 3.1 *Descriptive parameters for a simulated map. The surface coverage (**σ**) is the number of selected spectra (**N**) in the SERS tags counting algorithm, over the total number of points inside the area (**A**). The average intensity (**$\bar{I}$**) is defined as the sum of the intensities at one of the typical wavenumbers of the selected spectra ($I_{\tilde{\nu}}$), divided by the number of the selected spectra. The relative intensity to the area (**R**) is calculated as the sum of the intensities at one of the main peaks, divided by the total number of points inside the area.*

Number of selected spectra	**Total number of spectra**	**Surface coverage (σ)**	**Intensity at $\tilde{\nu}$ one of the typical SERS tags wavenumbers**	**Average Intensity ($\bar{I}_{\tilde{\nu}}$)**	**Relative Intensity (R)**
N	A	$\sigma = \frac{N}{A}$	$I_{\tilde{\nu}}$	$\bar{I}_{\tilde{\nu}} = \frac{\Sigma I_{\tilde{\nu}}}{N}$	$R = \frac{\Sigma I_{\tilde{\nu}}}{A}$

The simulations represent SERS maps of a pre-defined number of SERS tags inside a fixed area of 400 × 400 μm^2, with a step size of 8 μm in both (X) and (Y) directions, as reported in ***Figure 3.2A***. SERS tags were randomly positioned inside the selected area, following a certain percentage of surface coverage. Each point inside the map can contain more than one SERS tag, but also none. Simulations were prepared assuming two conditions; a) each SERS tag shines with a similar SERS intensity, and b) the agglomeration of SERS tags does not lead to collective signal enhancement. These hypotheses were based on previous findings using similar SERS tags, as discussed in **Chapter 2**.[19] The intensities at the main peaks for each SERS tag signal were distributed around typical values obtained from real experiments. The background noise level was also defined from real measurements, see ***Figure 3.2B***. Simulations were devised with different total amounts of SERS tags and different surface coverages, reproducing different mapping configurations. The simulations were first used to verify that the SA worked properly to identify all SERS tags inside the simulated maps. This

control was carried out by calculating the descriptive parameters in ***Table 3.1*** for each simulation and comparing them with the parameters used to build the simulation itself (***Figure 3.2C***). Finally, it was observed that the relative SERS intensity per unit area (**R**), which is the product of the total number of selected SERS spectra inside that area (surface coverage, **σ**) times the average SERS signal per point (average intensity at a wavenumber $\tilde{\nu}$, $\bar{\mathbf{I}}_{\tilde{\nu}}$), is constant for maps containing the same number of SERS tags (***Figure 3.2C***).

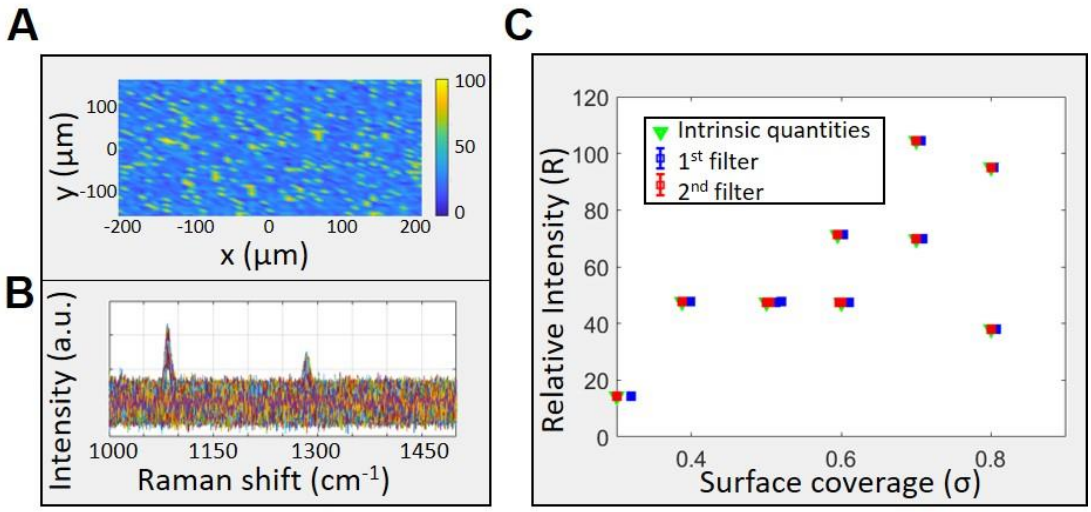

Figure 3.2 A) *Simulated 2D SERS map showing the SERS intensity at a hypothetical wavenumber of 1070 cm^{-1}.* ***B)*** *SERS spectra from all xy coordinates shown in* ***A.*** ***C)*** *Relative intensity-surface coverage graph for the intrinsic quantities (green), and for the values calculated by the program with two different filters (blue and red). Each point represents a virtual map. The orange square marks virtual maps with the same number of NPs: R is constant when the surface coverage is variable. The two different filters depend on the selection rules: the first one (as labelled) depends on the intensity value at a specific wavelength in a spectrum, while the second one is related to the b values assigned by linear regression analysis to each spectrum, with respect to the chosen reference. The second type of filter is independent of the intensity value, thus focused on the full shape and therefore more accurate than the first filter.*

Assuming that SERS tags do not leave the imaging window, on applying the SA to the same map but at a different timepoint, it is expected that **R** remains constant because the overall number of SERS tags within the cell populations remains the same. This would be explained as a contemporary increase of **σ** and decrease of $\bar{\mathbf{I}}_{\tilde{\nu}}$, due to the dilution of SERS tags into daughter cells upon cellular division. Hence, the SA was applied to experimental data obtained from real SERS maps of MCF7 cells labelled with SERS tags (added at [Au^0] = 0.1 mM, corresponding to 3.8 × 10^9 NP/mL). As expected, a reduction in the intensity and surface coverage of SERS tags over time was observed, in agreement with an increasing number of MCF7 cells in the imaging window due to cellular division (red dashed square in ***Figure 3.3***).

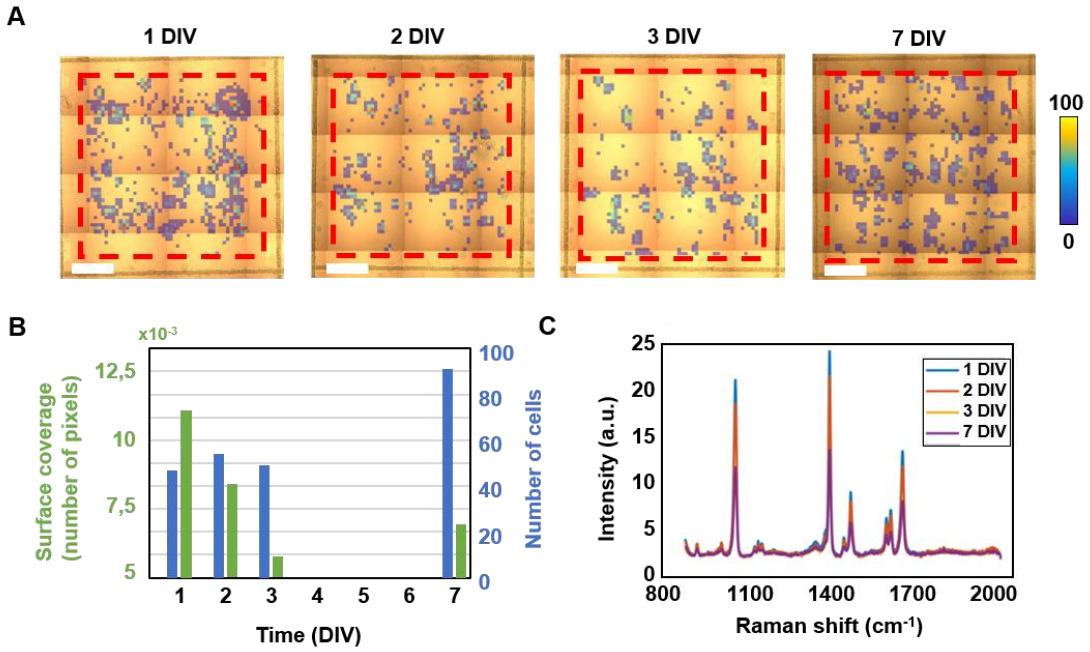

Figure 3.3 *Experimental data from 2D SERS maps of MCF7 cells labelled with SERS tags.* ***A)*** *Merged brightfield and SERS maps showing only the selected points from those SERS maps matching the reference spectrum, obtained on days 1, 2, 3, and 7 post-seeding (red dashed squares indicate the boundary of the analysed area). Scale bars: 200 µm.* ***B)*** *Cell surface coverage of SERS tag-positive pixels (left axis) and number of cells counted by optical imaging (right axis), obtained on days 1, 2, 3 and 7 post-seeding.* ***C)*** *Averaged SERS spectra for 2NAT SERS tags in the zone marked by the red dashed square in (A), showing a decrease in the average intensity over time.*

These findings suggest that MCF7 cells migrate from the imaged area during the studied time period, and that, as expected, cell division leads to dilution of SERS tags to subsequent daughter cells. The gold concentration in MCF7 cells incubated with low SERS tag concentrations was thus quantified via ICP-MS, mimicking the expected SERS tag concentrations after successive cell divisions. Specifically, the possible range (0.1 mM – 0.04 µM, corresponding to ca. $3.8 \times 10^9 - 1 \times 10^6$ NP/mL) that would be expected after 17 days *in vitro* (DIV) was analysed, based on the MCF7 doubling time and the previously used initial SERS tags concentration (3.8×10^9 NPs/mL). The results show the possibility of detecting the equivalent to 1 NP/cell in a representative sample of 200 µL, containing 2×10^4 cells (***Figure 3.4***).

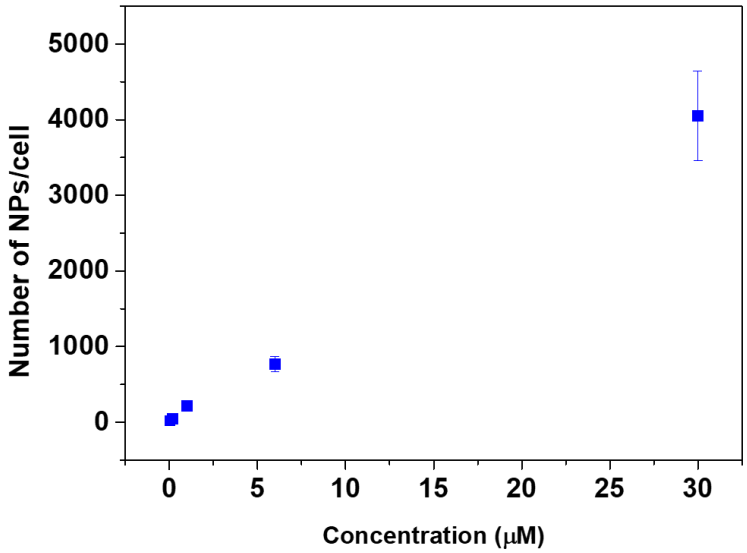

Figure 3.4 *Number of SERS tags per cell for different initial concentrations. Considering the standard conditions (100 mM NPs), the smallest concentration represents the amount of gold inside cells after three weeks of incubation. Error bars are determined from the average dimension of the SERS tags.*

3.3.2 Cellular division and exocytosis

The decrease in the number of NPs inside cells observed in the previous subsection can be related to several processes. Hence, we addressed the possibility that the decrease in SERS intensity over time may be due to cellular exocytosis, i.e., the process by which cells secret substances to the outside, including SERS tags, as opposed to cellular division (mitosis). Therefore, the amount of gold inside cells and in cell media over time was investigated by ICP-MS. MCF7 cells were incubated with SERS tags (3.8×10^9 NP/mL) for 24 hours, followed by removal of non-endocytosed NPs. According to ICP-MS analysis, approximately 57% of the added tags were internalized after 24 h. Subsequently, both cell and supernatant samples were collected at various timepoints, to measure the amount of SERS tags that were transmitted to daughter cells via mitosis and those that were exocytosed, respectively. Plotted in ***Figure 3.5A*** is the amount of NPs inside cells over time, which is observed to follow an exponential reduction (with $R^2 = 0.94$), characterized by a half-life time of $\tau = 2.2$ days, in agreement with the cellular division time of the MCF7 cell line.[20] With regards to the SERS tags released by exocytosis, once the non-endocytosed material was removed, it was observed that the number of SERS tags found in the supernatant was negligible and accounted for less than 3% of the initially endocytosed material (***Figure 3.5B***). These findings therefore suggest that, the role of exocytosis in the decrease of SERS tag signal from cells is negligible and those SERS tags that were transmitted to daughter cells retained their initial (strong) SERS

signal, thanks to the biocompatibility and high stability provided by the protective polymeric shell.

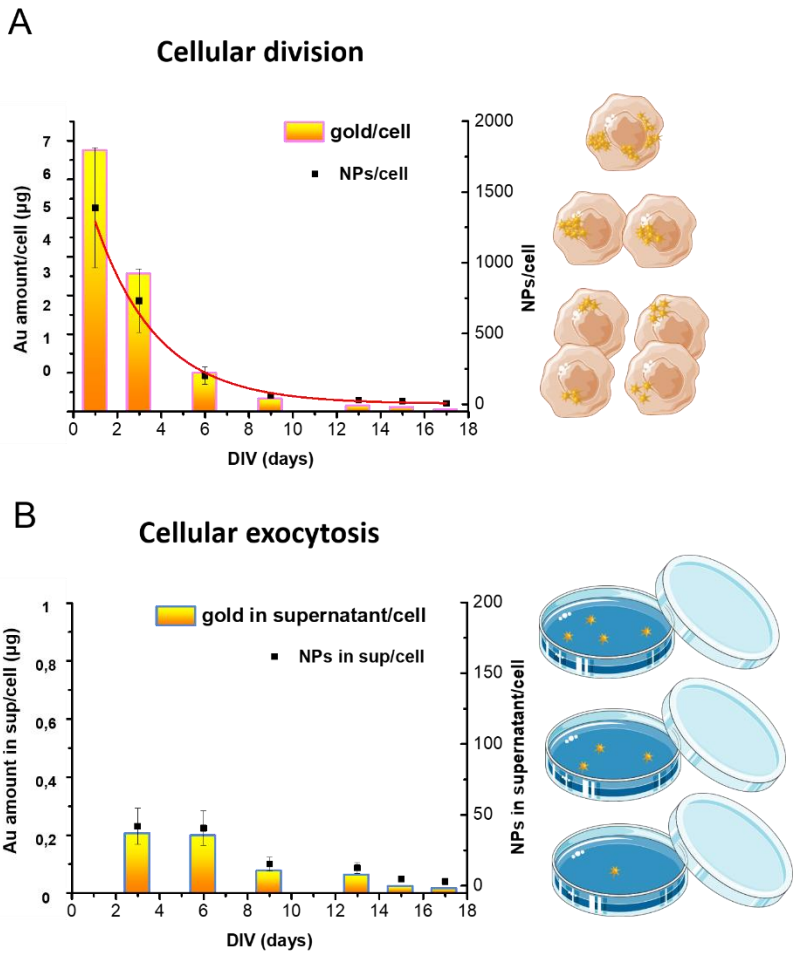

Figure 3.5 *Amount of Au per cell, obtained as the ratio between ICP-MS data and the corresponding number of cells in the sample.* ***A)*** *Amount of gold inside cells (left axis) and relative number of NPs per cell (right axis), both showing a decreasing trend. The observed reduction is in good agreement (R^2=0.89) with an exponential function characterized by a half-life time of τ =2.2 days, which is consistent with the cellular division time of the MCF7 cell line.* ***B)*** *Exocytosed NPs, presented as Au amount (left axis) and number of NPs (right axis) detected in the supernatant and correlated to the total number of cells present in the sample.*

3.3.3 Optimization of SERS measurement parameters

In order to obtain more accurate information on the number of SERS tags in an individual cell, the entire cell volume must be taken into consideration. However, realization of multiple scans at different z-depths often requires an increase in the laser energy delivered, which can have detrimental effects against cells. Hence, we investigated the risk of laser-induced (photo)toxicity and the minimum laser power required to obtain a meaningful SERS signal. These control experiments were carried out by using laser powers ranging from 3 to 20 mW,

in combination with a 20× objective lens, for measurement of SERS maps in confocal mode. As expected, increasing the laser power resulted in an increase of the recorded SERS intensity, which at high laser powers with continual irradiation resulted in extensive cell death, as confirmed by the appearance of apoptotic-like bodies and cell shrinkage (***Figure 3.6A***). Such an excessive cell death is attributed to plasmonic heating of AuNPs featuring an LSPR that accurately matches the irradiation laser wavelength. Indeed, MCF7 cells can tolerate much higher laser powers (80 mW) in the absence of SERS tags, without any apparent cytotoxic effects (***Figure 3.6B***).

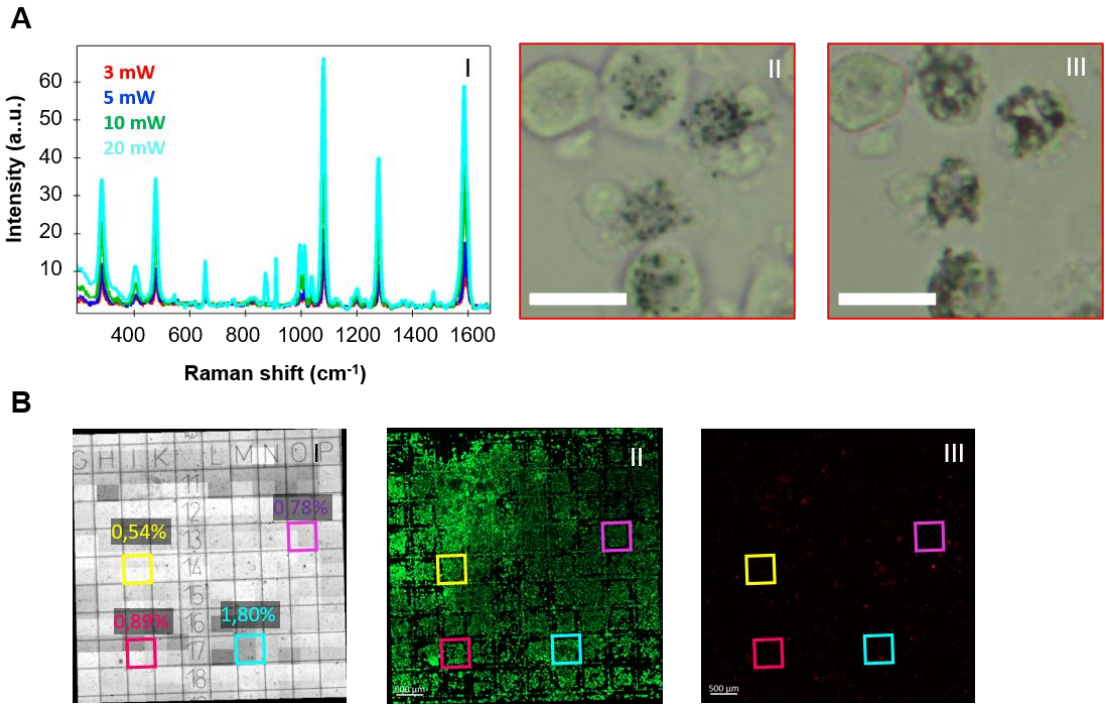

Figure 3.6 A) (I) *Average SERS signal for a fixed area* ***(II)*** *exposed to increasing laser powers (fixed step size of 5 µm and integration time of 20 ms), containing SERS-labelled MCF7 cells ([Au^0] = 0.1 mM).* ***(III)*** *Same area after all the scans: changes in cell shape and an increase in the intensity of dark areas inside cells (accumulations of SERS tags) indicates an excessive exposition to the laser. Scale bars = 20 µm.* ***B) (I)*** *Optical image of non-labelled MCF7 cells. The squares indicate areas measured under different conditions to check laser irradiation cytotoxicity: light blue is the control, non-irradiated zone; yellow is an area measured with 30 mW laser power and 20 ms accumulation time; magenta is an area measured with 30 mW and 50 ms; purple is an area measured with 80 mW and 20 ms. Fluorescence imaging showing live* ***(II)*** *and dead* ***(III)*** *cells. The corresponding percentages of dead cells in the coloured squares are indicated in A, as calculated from the ratio between live and dead cells.*

Therefore, an attempt to identify a sweet spot balancing SERS tag concentration and laser power was made, so that sufficient signal from SERS tags could be obtained while avoiding phototoxicity. Lower doses of SERS tags, coupled with a laser power of 5 mW were explored,

making sure that the SERS signal intensity was maintained above the limit of detection (***Figure 3.7A***). The brightfield images obtained pre- and post-SERS imaging show that cells retained their morphology and fluorescence live/dead assays (***Figure 3.7B***) verified their viability post-irradiation. The percentage of dead cells showed similar values in both irradiated (2.3 %) and non-irradiated areas (1.9 %), indicating that no phototoxicity effects were generated in SERS-labelled cells with [Au^0] = 0.1 mM (3.8 × 10^9 NPs/mL) and measurement parameters of 5 mW laser power and 20 ms irradiation time. These conditions were thus selected for subsequent measurements.

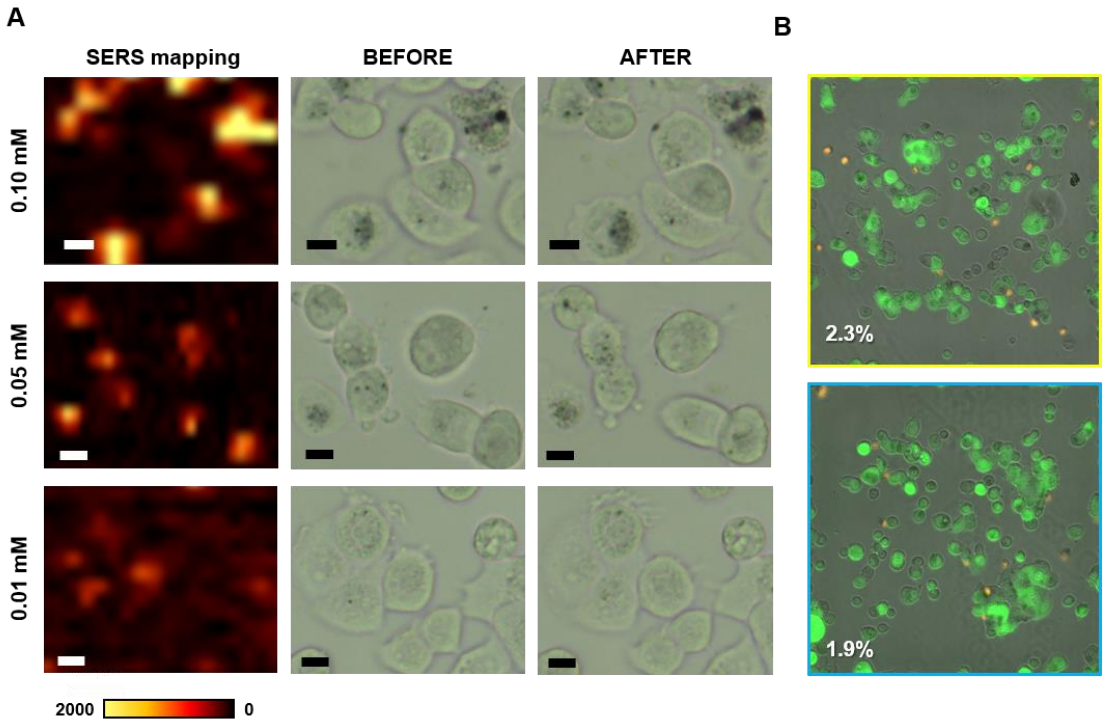

Figure 3.7 A) *SERS maps of MCF7 cells labelled with different SERS tag concentrations, imaged with a 785 nm laser at 5 mW for 20 ms, and optical images before and after irradiation. Scale bars =10 µm.* ***B)*** *Optical images of SERS-labelled MCF7 cells with [Au^0] = 0.1 mM, in irradiated (5 mW laser power and 20 ms accumulation time) (upper panel) and non-irradiated (lower panel) areas. Fluorescence maps from live (green) and propidium iodide containing dead cells (red) were overlapped to the optical images. The percentage of dead cells was calculated as the ratio between red and green areas.*

Further improvements to the SERS imaging setup were made by reducing the SERS mapping lateral step size (in the XY axis) from 5 µm to 1 µm, thereby achieving a significantly improved imaging resolution, yet avoiding laser-induced cytotoxic effects, see ***Figure 3.8***.

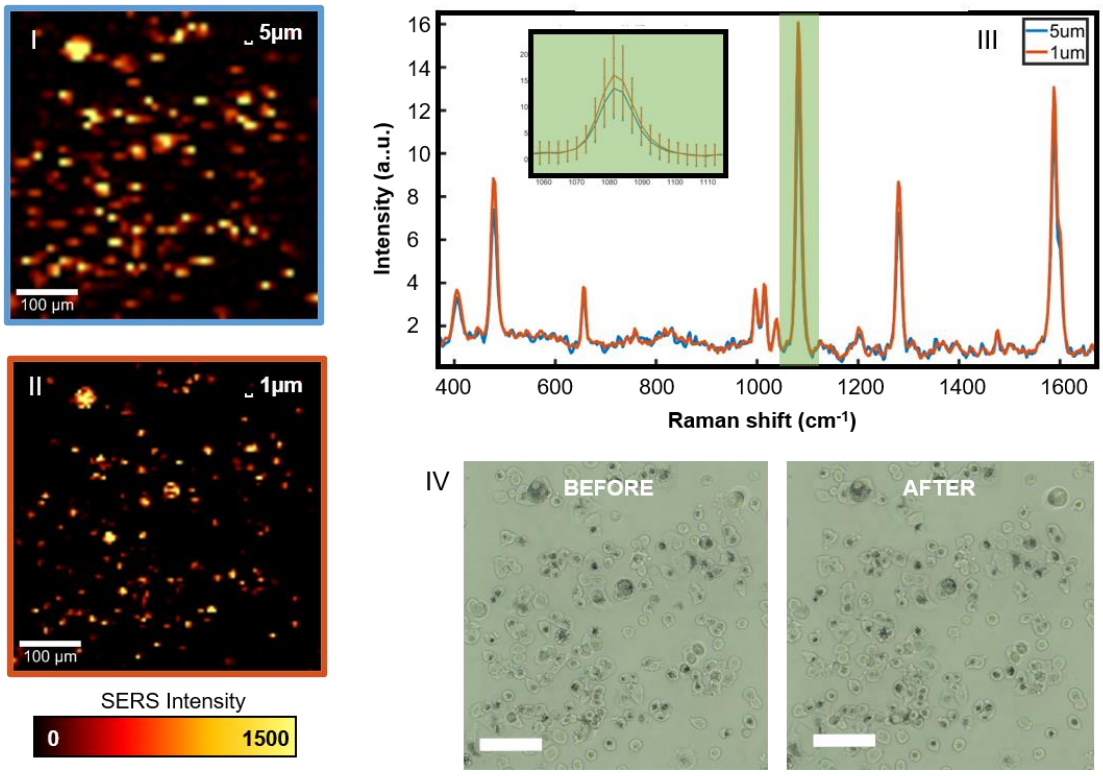

Figure 3.8 *SERS mapping of MCF7 cells labelled with 0.1 mM SERS tags, performed with 5 mW laser power, 20 ms accumulation time and two different step sizes in (XY) (5 µm* ***(I)*** *and 1 µm* ***(II)****), to study the influence of measurement conditions. Average spectra from SERS mappings* ***(III)*** *and optical images* ***(IV)*** *of cells before and after scanning, showed no considerable differences in SERS intensity resulting from the decrease in step size. Scale bars: 100 µm.*

3.3.4 Application of supervised algorithm to 3D SERS imaging

After identifying the optimal experimental conditions, including parameters such as step size, laser power, and SERS tag concentration, we proceeded to quantify the distribution of SERS tags over multiple z-planes, to obtain a representative NP/cell value for the whole 3D cellular volume. The previously used SA was implemented, by summing the SERS intensity signals derived from multiple XY images at different z-heights, to obtain the overall signal from the cellular volume (see **Experimental section 3.6** for more details). Rather than using the imaging area as a descriptive parameter for the analysis, the number of cells to be imaged was established, allowing a more accurate analysis that disregarded those cells that migrated away from the imaging field (imaging parameters are provided in ***Table 3.2***).

Table 3.2 *Real map descriptive parameters defined from the properties of the cells.*

Number of cells	**Total area**	**Surface coverage (σ_c)**	**Intensity at a typical wavenumber ($\tilde{\nu}$)**	**Average intensity per cell ($\bar{I}_{c\tilde{\nu}}$)**	**Relative intensity (R)**
η	A	$\sigma_c = \frac{\eta}{A}$	$I_{\tilde{\nu}}$	$\bar{I}_{c\tilde{\nu}} = \frac{\Sigma I_{\tilde{\nu}}}{\eta}$	$R = \bar{I}_{c\tilde{\nu}}\sigma_c$

The quantity **R** was redefined as the product of $\overline{I}_c$ and $\boldsymbol{\sigma_c}$, which are respectively the average intensity per cell and the cellular surface coverage. The cellular surface coverage was calculated as the number of cells divided by the total area, while the average intensity per cell was defined as the sum of the intensities divided by the number of cells. If the number of cells remains constant, $\boldsymbol{\sigma_c}$ can also be considered as constant. In this case, the average intensity per cell and the relative intensity follow the same trend and the former can be directly used as a descriptive parameter of the system instead of **R**. Considering that living cells were used, slightly different experimental conditions and calibration procedures were required at the different timepoints. The protocol described in **Chapter 2** to calculate the SSpP was followed, performing the measurements in water with the same objective employed to measure the cells. To ensure no changes in the NPs on the TEM grid after immersion, TEM images were taken before and after the procedure. The SERSTEM App was then used to count the tags on the grid and make sure that there are no relevant changes (***Figure 3.9A***). After this control, the signal for a single SERS tag was estimated. Raman and TEM images were correlated in three different areas of the TEM grid, and then used to generate the signal distribution for a single SERS tag, from which the median could be estimated, as well as the 25^{th} and 75^{th} percentile values, as shown in ***Figure 3.9B***.

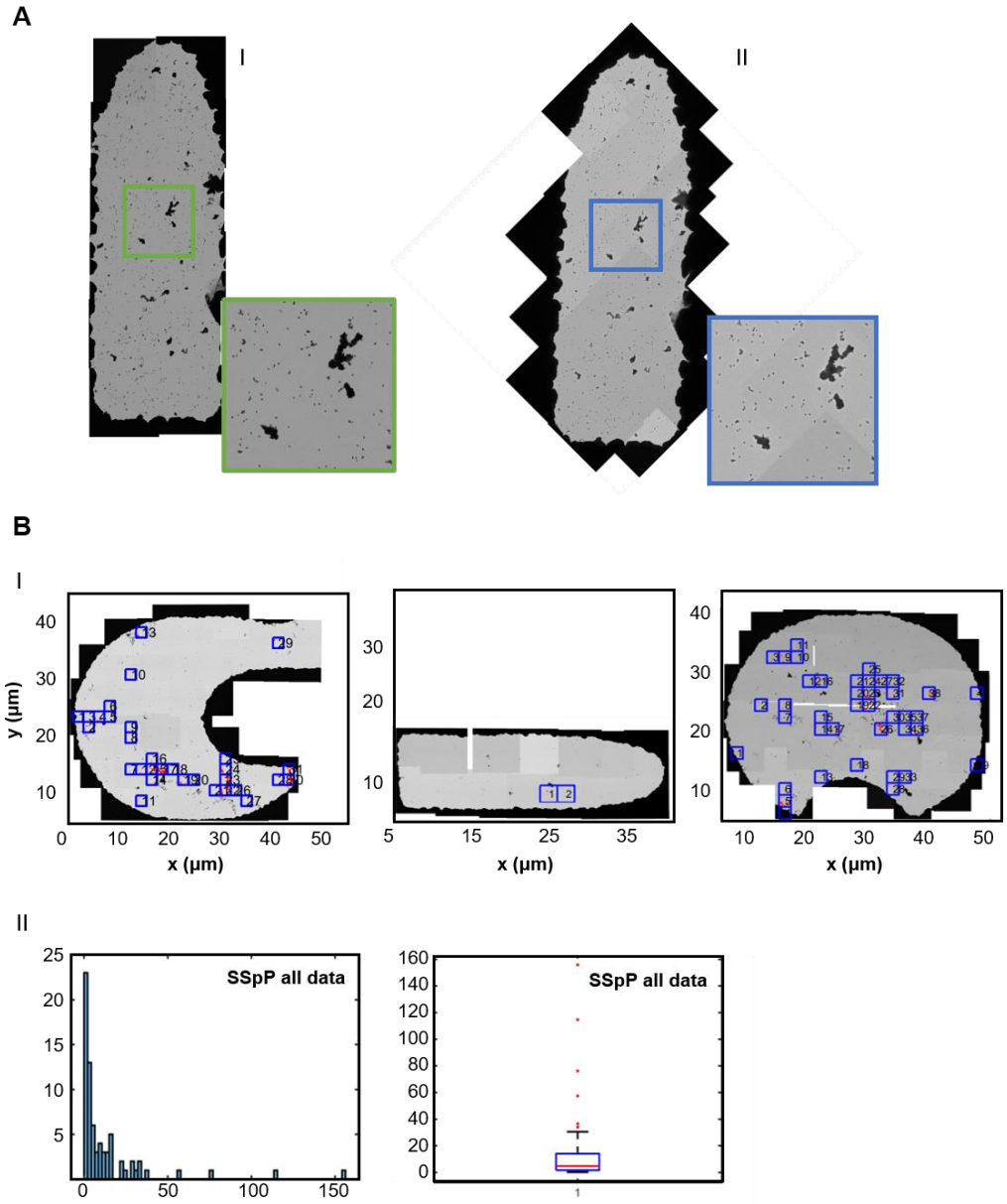

Figure 3.9 A) (I) *TEM image of the inner part of the letter P in the labelled grid, measured after preparation; the inset shows a zoom of the area marked in green.* ***(II)*** *The same area imaged by TEM after immersion in water The inset shows a zoom of the area marked in blue, equivalent to the one in green in A.* ***B) (I)*** *Three different measured areas in a TEM grid: inner parts of the letters G, P, Q, with blue squares signalling those spots where the SERSTEM App found a correlation between the presence of non-clustered nanoparticles and SERS signal. Red spots indicate the found nanoparticles. The area inside P presents a very low number of squares because it is small and the presence of clustered NPs resulted in the elimination of the majority of the area from the analysis. All maps were analysed using the following parameters: GLV = 0.2, square size = 2 µm per length, Maximum pixel number = 300, b threshold = 6.* ***(II)*** *Histogram and boxplot for the SSpP found in all three regions. Reported in the boxplot are the median signal per particle (red bar) and the 25th and 75th percentiles (lower and upper edges of the blue box). Outliers of the distribution are marked as red dots.*

To provide a realistic comparison, two different SERS tag concentrations, [Au^0] = 0.1 and 0.05 mM (3.8×10^9 NPs/mL and 1.9×10^9 NP/mL, respectively), were added to cells. Every 2-3 days for a period of 17 days, 3 – 4 volumetric areas of ca. $84 \times 84 \times 25$ μm^3 were imaged, each containing *ca.* 20 cells (hence a total of 60 - 80 cells per DIV), see ***Figure 3.10A***. Using the former SA procedure on the acquired 3D SERS images, the number of SERS tags per cell at each DIV was estimated and compared to the corresponding results obtained by ICP-MS analysis. As expected, a variation in the spatial distribution of the SERS signal over time (***Figure 3.10B***) and a decrease in the average intensity of the SERS signal per cell (see ***Figure 3.10C***) were detected. Hence, the amount of gold per cell (determined by ICP-MS) was compared to the average SERS signal intensity (at 1590 cm^{-1}) per cell, at each DIV (***Figure 3.10D***). The results are in excellent agreement, showing a decrease over time, as previously predicted by the simulations. The higher deviation noted in SERS measurements, compared to ICP-MS, is due to inhomogeneity in SERS tag uptake by cells and the fact that SERS measurements were performed on individual cells, not on the whole population. In contrast, ICP-MS measures Au in a bulk sample and the value is then correlated to the number of cells in the sample, counted using manual methods (i.e., a hemacytometer). The SA thus allowed us to monitor NP dilution in cells due to cellular mitosis, over nearly 2 weeks. It was observed that, at the latter three timepoints, SERS imaging underestimated SERS tag uptake, as compared to ICP-MS data (***Figure 3.10E***). This can be explained by the low SERS signal in cells at such latter stages. However, the estimation obtained by SERS is comparable to the experimental errors obtained by ICP-MS, indicating that this strategy may be suitable as an alternative, non-invasive, and fast method for quantification of NPs in live cells.

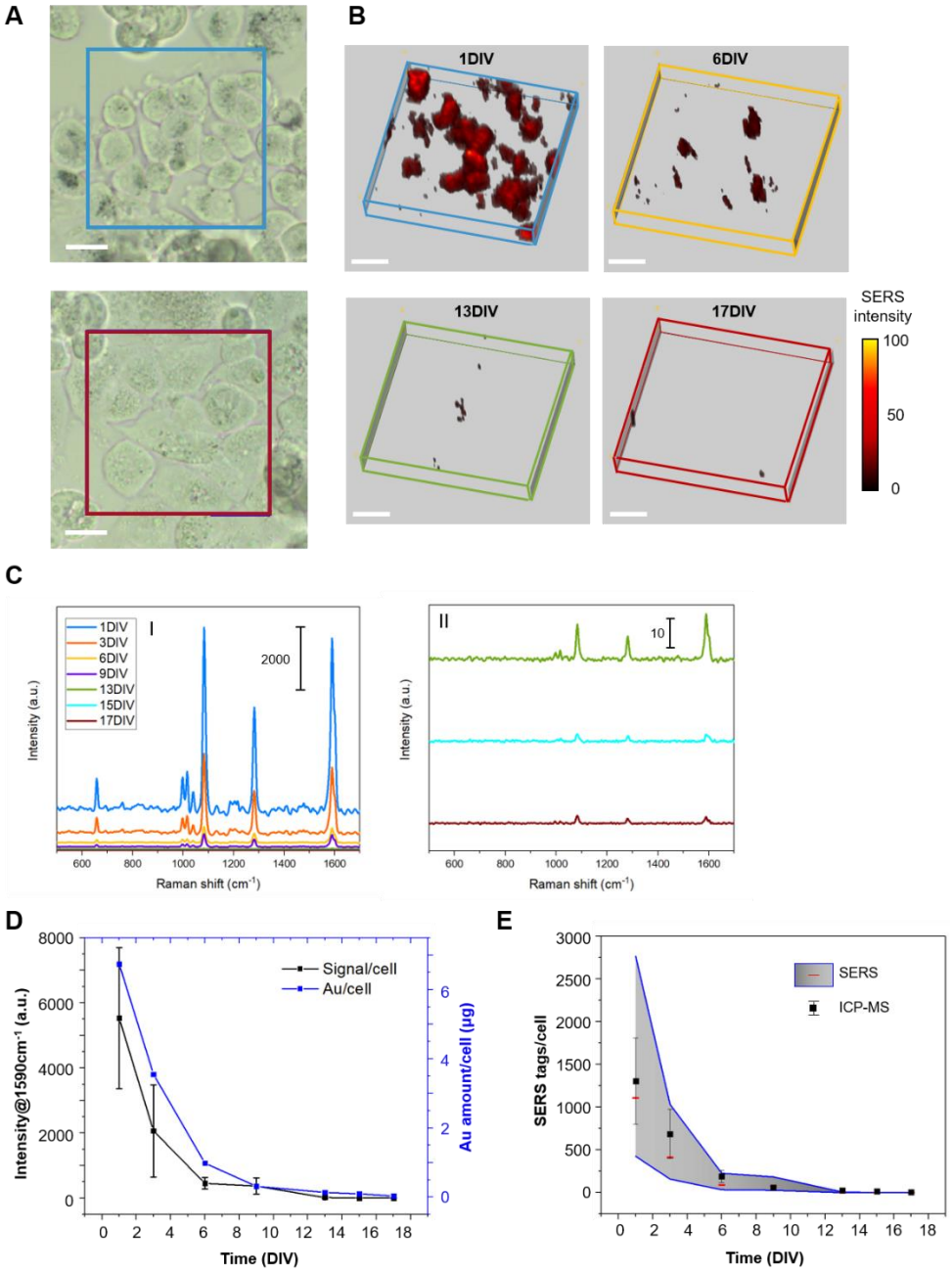

Figure 3.10 *SERS analysis by SA.* ***A)*** *Images corresponding to 1 and 17 DIV, showing labelled cells in the measured areas. Optical images were used to count the cells and subsequently calculate the SERS signal per cell. Scale bars = 20 µm.* ***B)*** *3D reconstructions of the selected SERS signal at 3 time points: 1 DIV, 13 DIV and 17 DIV. Coloured boxes measure ca. 84 × 84 × 25 µm*^{3}*.* ***C) (I)*** *Average intensity per cell ($\bar{I}_c$) obtained by applying the SERS tags voxels sum algorithm to the cellular measurements taken over time.* ***(II)*** *Zoom over the last three DIV.* ***D)*** *Comparison between the average SERS intensity per cell ($\bar{I}_c$) and the amount of gold (µg) per cell obtained via ICP-MS. Error bars indicate the standard deviations of ca. 60-80 SERS spectra recorded from single cells for SERS and triplicate measurements for ICP-MS.* ***E)*** *Number of NPs per cell, calculated from SERS analysis, using the SERS signal per particle (median value reported with a red bar, 25% and 75% are represented by a grey area), and ICP-MS, considering the average dimensions of the corresponding SERS tags.*

Indeed, similar results were also obtained for cells incubated with a lower concentration (0.05 mM, or 1.9 × 10^9 NP/mL) of SERS tags, as shown in ***Figure 3.11***. In an attempt to better resolve the differences observed at late timepoints (13 DIV onwards), the laser power was adjusted to improve SERS tag detection, taking into consideration that the number of NP/cell is considerably lower than that at 1 DIV, and hence negligible laser-induced cytotoxicity is expected.

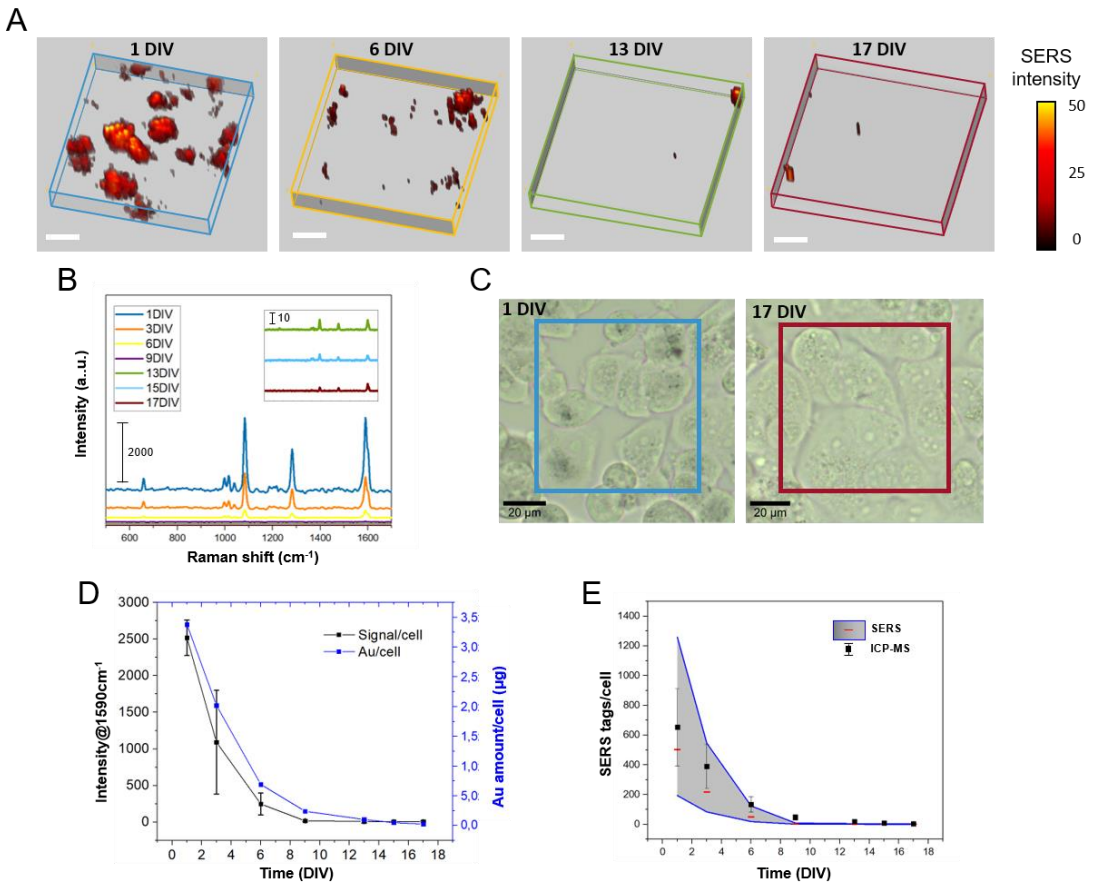

Figure 3.11 A) *3D reconstructions of the selected SERS signal at 3 time points: 1 DIV, 13 DIV and 17 DIV. Coloured boxes measure ca. 84 × 84 × 25 µm^3.* ***B)*** *Evolution of SERS spectra over time, obtained via 3D sum (orthogonal projection) of the selected SERS signals.* ***C)*** *Images of cells at the first and last days in vitro, showing labelled cells in the measured areas. The optical images were used to count the cells and obtain the SERS signal per cell.* ***D)*** *Comparison with ICP-MS results, which yield the amount of gold (µg) per cell.* ***E)*** *Number of NPs per cell calculated from both techniques: for SERS analysis, the number of NPs was estimated using the SERS signal per particle (median value reported with a red bar, 25% and 75% are represented by a grey area), while for ICP-MS it was considered the average dimensions of the corresponding SERS tags.*

As can be seen in ***Figure 3.12***, such technical adjustments allowed to better resolve the differences in SERS tag numbers at low concentrations.

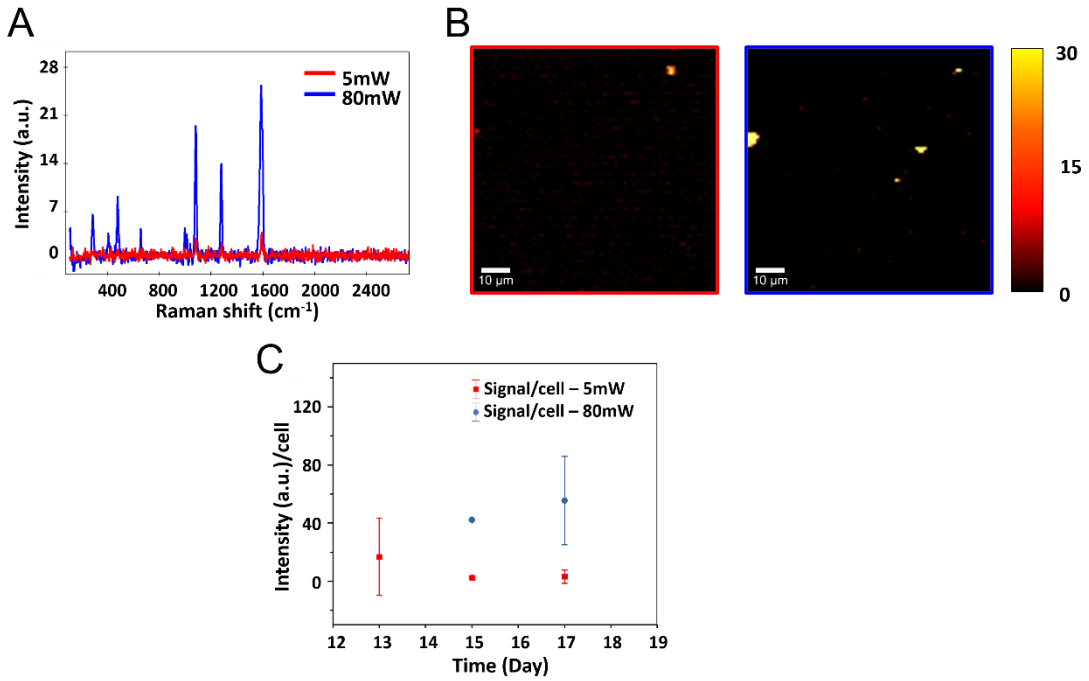

Figure 3.12 A) *Average SERS spectra from the mappings in* ***B)****, acquired with two different laser powers, 5 mW and 80 mW (as labelled), after 17 DIV.* ***C)*** *Decreasing trend of the SERS signal/cell (red squares) calculated for the measurements performed with 5mW laser power; and SERS signal/cell (blue dots) for those time points measured with a higher laser power (80 mW).*

3.4 Single cell SERS imaging in microdroplets

The previously described methodology considers an average from a large number of cells to calculate the number of SERS tags per cell. However, it is well known that the distribution of NPs uptaken by cells is not uniform.[7] Therefore, we propose a different type of study to understand such processes in more detail, by following events in single cells. Single cell studies are becoming progressively more prevalent because they can provide a more detailed insight into cellular heterogeneity and its association with physiological homeostasis in tissues, compared to traditional multicellular approaches.[21–23] One of the available measurement configurations to achieve an isolated and biocompatible environment for single cell studies, is based on the use of microdroplet-based devices in microfluidic systems. In fact, advancements in droplet-based microfluidics have allowed the systematic analysis of a large number of individual cells in a remarkably controlled manner.[24] The potential limitations and biological performance of this *in vitro* microdroplet-based single-cell model have been reported, including a great exposition and interaction of the cellular surface to the surrounding medium.[25] On the other hand, examples of droplet-based optofluidic systems which take advantage of SERS have been reported for the detection of foodborne pathogens,[26] or chemical food contamination. [27] Not only it is possible to combine SERS-based and microdroplet-based techniques, but it has also been reported the *in situ* fabrication of micro-droplet plasmonic platforms, e.g. nanocomposite beads that are able to trap and concentrate

the targeted analytes.[28] Such plasmonic microdroplet systems have been used in the development of a SERS flow cytometry platform, to achieve multiplexed and multiparametric analysis for high-throughput cellular screening. [29]

Based on these considerations, we attempted to develop a microfluidic device to study microdroplets containing individual SERS-labelled cancer cells. With this aim, an internship was carried out under the supervision of Dr. Sara Abalde-Cela of the Medical Devices Group at the INL in Braga, focused on the development and application of optofluidic platforms in the cancer research field. As previously shown in this **Chapter 3**, it is possible to image living cells containing SERS tags over long periods of time (up to approximately 3 weeks) with the techniques available at CIC biomaGUNE. However, little control over single cell analysis has been achieved in that case. The microfluidics system currently used in the Medical Devices Group provides a suitable platform to perform such an accurate study. Ideally only 1 or 2 cells can be loaded in each microgel droplet, thereby allowing a high degree of selectivity to study cellular division and crucially, what happens to SERS tags inside the cell. Indeed, by encapsulating individual cells, or low numbers of them in microgels, which support cell proliferation, the process of NP sharing or division between daughter cells can be readily studied. Hence, we attempted the encapsulation of a small amount of SERS-labelled tumour cells in single droplets by using microfluidics devices. The droplets would contain extracellular matrix, so as to allow cell proliferation, and SERS bioimaging would be used as a proof of concept to monitor them over time. Preliminary results were obtained that prove the viability of the method, which allowed us to determine the limits of detection inside these devices, by means of confocal SERS microscopy.

3.4.1 Droplet-based microfluidics

The term microfluidics device refers to any system that can process or manipulate small amounts of fluids (from nanolitres to attolitres) in channels of micrometre dimensions. The main advantages of these systems are the use of reduced volumes and the properties of fluids in micro-channels, such as laminar flow. [30]

Droplet-based microfluidic devices belong to a sub-category characterized by the use of immiscible phases to create discrete volumes. In this manner, it is possible to create highly monodisperse droplets with dimensions from nanometres to micrometres, at a rate of up to twenty thousand per second.[30] The volume of these droplets can be tuned from few picolitres to nanolitres. The inert carrier oil, in which aqueous droplets are suspended, is both hydrophobic and lipophobic, thus maintaining the cells encapsulated in viable droplets for extended periods of time without the risk of dissolving in the oil the organic molecules produced inside the droplets. Furthermore, these molecules and products secreted by the

trapped cells, can easily reach detectable concentrations due to the small volume of the microdroplets.[31]

A wide choice of materials, such as silicon, glass, polydimethylsiloxane (PDMS),[32] and other biopolymers or photocurable resins, is available to fabricate the device used to produce microdroplets, depending on the targeted application. The design of the device is one of the parameters that influences the size of the microdroplets. In fact, the latter depends basically on the flow ratio between the continuous phase (the medium in which droplets are generated, i.e. the oil phase) and the dispersed phase (the aqueous phase of the droplets), the interfacial tension between the two phases, and the geometry of the channels.[30] Some examples of geometries of passive droplet formation methods are shown in ***Figure 3.13***, namely ***A)*** cross-flowing, ***B)*** co-flowing and ***C)*** flow-focusing. In particular, in the latter configuration, the droplets result stable and uniform due to the symmetrical shear exercised by the continuous phase on the dispersed phase at the maximum shear point. In this configuration, the dimension of the droplets decreases when the flow rate of the continuous phase is increased (***Figure 3.13D***).

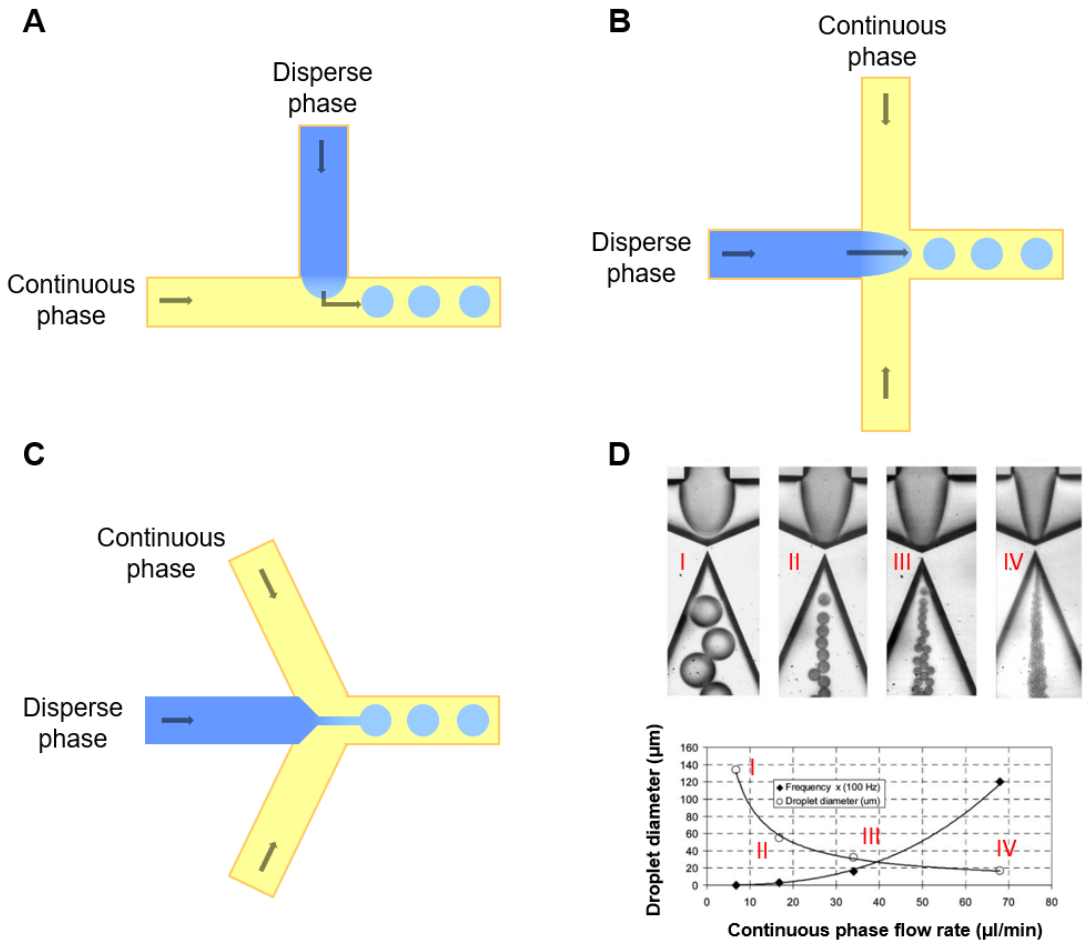

Figure 3.13 *Passive droplet-based microfluidic geometries to generate droplets in a controllable manner:* ***A)*** *cross-flowing,* ***B)*** *co-flowing and* ***C)*** *flow-focusing. Reproduced from ref* [33]. ***D)*** *Droplet formation at constant disperse phase flow rate and increasing continuous phase flow rate. Reproduced from ref.* [34]

In order to use microdroplets as small incubators for single cells, it is possible to employ cell-laden hydrogels as the disperse phase. A prediction method has been reported to assess the number of cells inside the droplets, based on the Poisson distribution, in which the probability P(X=x) of finding x cells per droplet is given by:

$$P\ (X = x) = \frac{e^{-\lambda}\,\lambda^{x}}{x!} \qquad \textit{Equation 3.1}$$

where λ is the mean number of cells in the volume of each droplet (***Figure 3.14A***). Hence, by changing the cell density in the aqueous phase it is possible to select the droplet occupancy.[31] An example is reported in ***Figure 3.14B***, where droplets of average diameters of 100 μm were realized, with a cell density of the disperse phase of 2 × 10^6 cell/mL. The majority of them was empty (ca. 70%), while just 20% and 10% contained one or two single cells, respectively.[25] In order to monitor the prepared droplets, it is possible to collect and incubate them, off-chip[35] or inside the same device throughout delay lines, traps, pillars or chamber devices. Subsequent manipulations of the droplets, such as fusion, pico-injection of reagents, splitting and sorting by dimensions are also possible procedures available to study biological processes.[24]

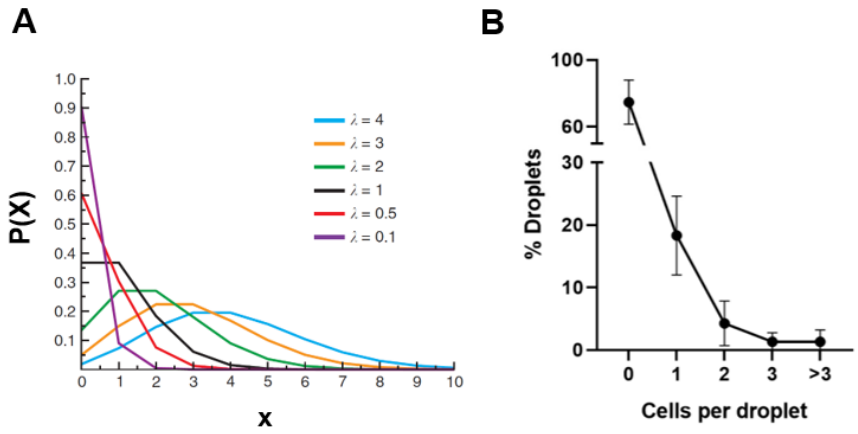

Figure 3.14 A) *Poisson probability P(X=x) of finding x cells per droplet, at different mean number of cells in the volume of each droplet (λ). Reproduced from ref.* [31]. ***B)*** *Number of cells encapsulated per microdroplet of average diameter 100 μm and disperse phase at 2 × 10^6 cell/mL cell density. Reproduced from ref .* [25].

3.4.2 Imaging in microdroplets

3.4.2.1 Preparation of the microfluidic device

The designs of the silicon master for generation and incubation of microdroplets are shown in ***Figure 3.15A*** and ***B***, respectively.[25] The flow-focusing geometry was chosen to realize the droplet generator, while pillars of 25 μm diameter positioned at 150/100/80 μm distance were employed to incubate and stabilize the microdroplets inside the reservoir devices. Shown in

Figure 3.15C is the scheme of the construction process of the microfluidic devices, which consists of realizing a stamp of *(I)* the master (with a certain height, ε=120/60 μm) from PDMS. This material was chosen due to its properties, such as the easy moldability and high elasticity, gas permeability, natural hydrophobicity, optical transparency and low autofluorescence.[36] *(II)* Then, the PDMS stamp is bound to a second PDMS layer to recreate channels and chambers with the same height of the master (*III*). In particular, as shown in ***Figure 3.15D***, a mixture of PDMS prepolymer and cross-linker (ratio 10:1, *w/w*) was poured on top of the silicon master (*I-II*), degassed and cured for 2h at 65 °C (*III*). This first layer of PDMS (ca. 5 mm thick) was cut and peeled off from the master (*IV*), and holes for tubing were made with a biopsy punch (1 mm of diameter). The PDMS containing the channels is subsequently bound to a second layer of PDMS (ca. 2 mm high), by an oxygen plasma treatment for 30 s (*V*). To guarantee the optimal and permanent bonding of all the small details within the device, a soft pressure and 10 min baking at 65 °C were applied. The channels and chambers thus realized inside the devices (***Figure 3.15E***) were functionalized by flushing a water repellent compound (Aquapel®) in order to improve their hydrophobicity and obtain a better monodispersity of the water droplets in oil. A second and third washes with biocompatible fluorinated oil (namely, HFE 7500 Novec®) were then used to remove the Aquapel® in excess, avoiding the risk of crystallization and possible channel clotting. Connecting the microdroplet generator with the reservoirs during the formation of the droplets (*III* and *IV*, respectively), allowed to fill the storage chambers formed in the replicas of the reservoir devices.

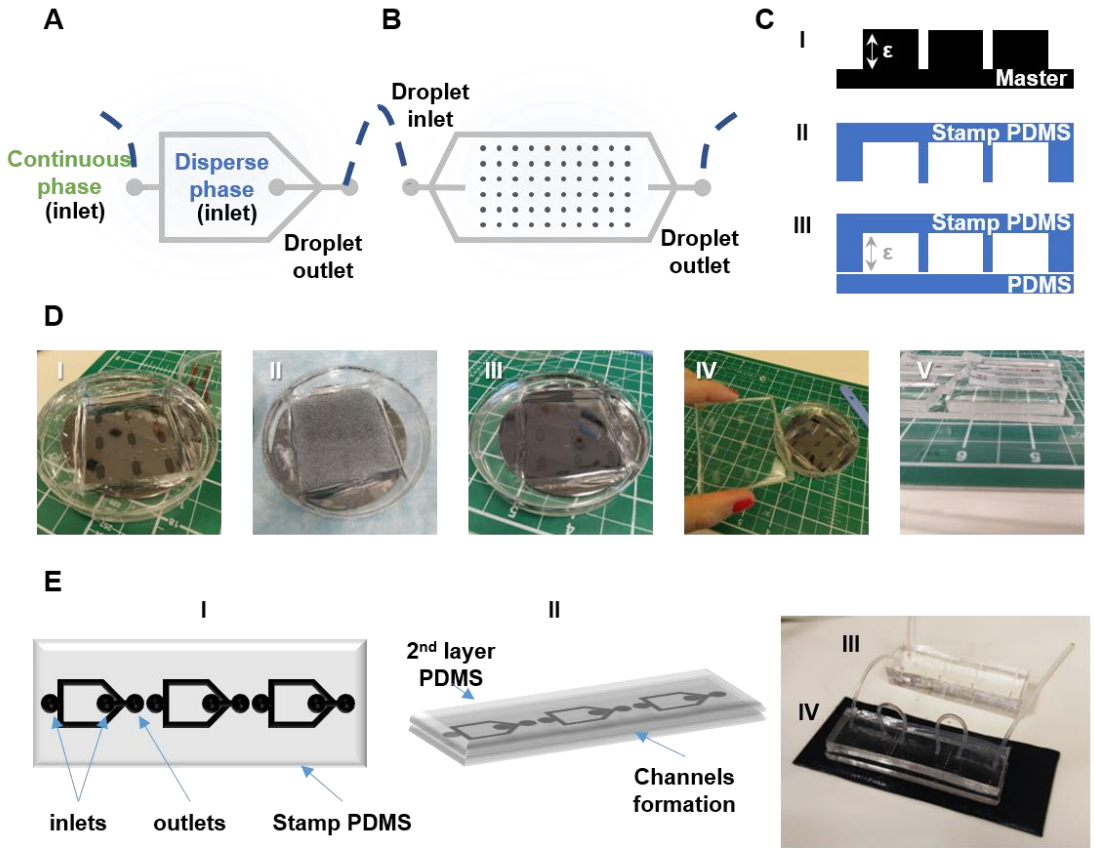

Figure 3.15 *Schematic representation of the design of* ***A)*** *the microdroplet generators and* ***B)*** *microdroplet reservoirs of the employed microfluidic devices. Reproduced from ref* [25]. ***C)*** *Scheme of microfluidic device production: I) the master is used to generate II) a stamp in PDMS of the design reported in A) that is later bound to III) a 2nd layer of PDMS to form chambers with a specific height (ε).* ***D)*** *Preparation of devices: I) silicon master and II) addition of the PDMS mixture to the silicon master; III) replicas after degassing and curing procedure and IV) cutting. V) Binding between two PDMS layers.* ***E)*** *I) PDMS replicas of the silicon masters with evidenced II) channel formation throughout its binding with a second layer of PDMS. III) Optical image of the device, connected with IV) the three replicas of the reservoirs.*

3.4.2.2 Microdroplets preparation

In order to prepare the dispersed phase, SKBR3 human breast cancer cells were previously labelled with two SERS tags, AuNSs-BPT-PMA-PA and AuNRs-2NAT-PMA-PA at [Au^0] = 0.1 mM. Therefore, 1 × 10^6 SERS-labelled cells were concentrated in 300μL of the biocompatible gel Matrigel®, diluted in cellular media at 4 °C. The continuous phase made of a biocompatible fluorocarbon oil (Fluoriner FC-40), was functionalized with a biocompatible surfactant, which acts as stabilizer of the droplets over a wide range of temperatures and biological conditions, thereby ensuring reliability and reproducibility (Pico-Surf 1-2%). Hence, two syringes of 1mL were filled with the disperse and continuous phases, maintaining the system cold, to avoid premature gellification. Afterwards, they were mounted on syringe pumps, and the tubing ends were connected to the generator microfluidic devices (***Figure 3.16A***). The syringe pumps were programmed for specific flow rates for the continuous phase of 500 μL/hr and the disperse phase of 100 μL/hr, to obtain microdroplets with diameter of 100 μm. The generated microdroplets were recovered through the outlet channel connecting the reservoirs chambers inlet (***Figure 3.16B***).

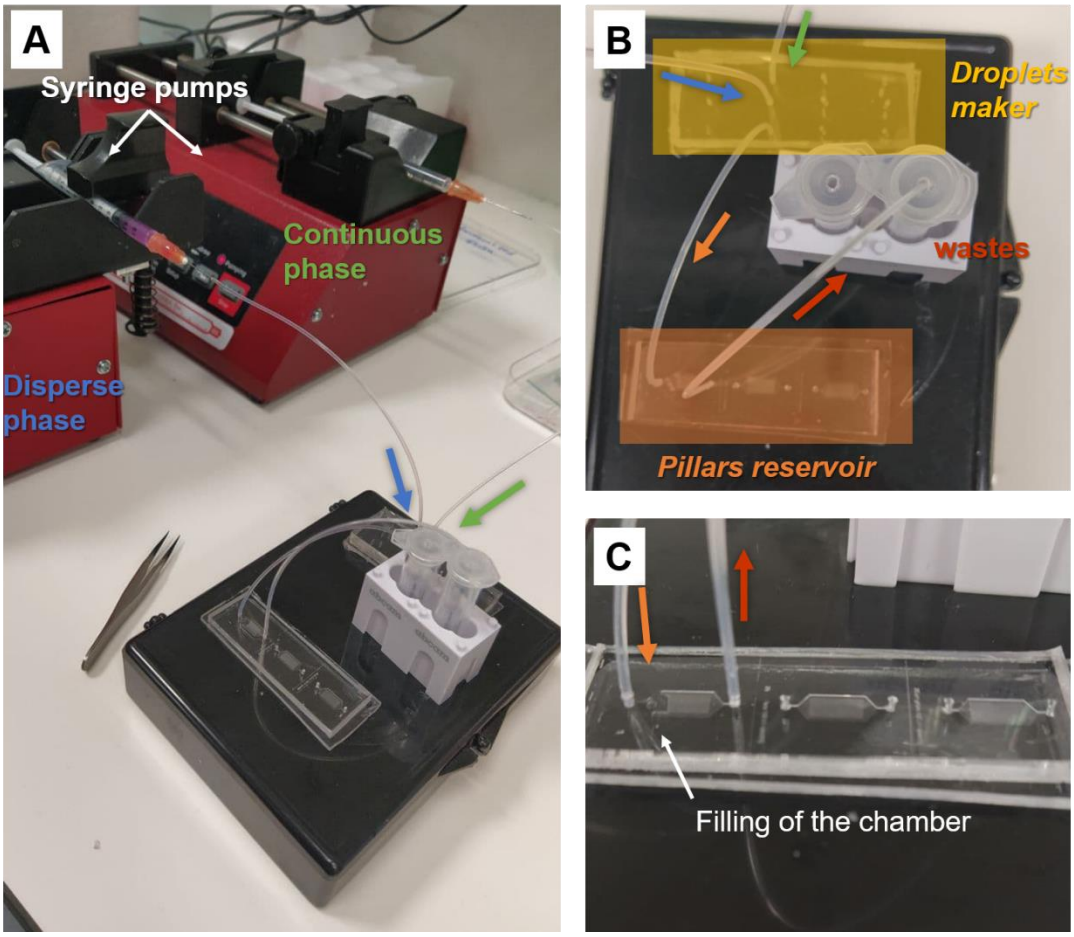

Figure 3.16 A) *System of syringe pumps of both the disperse (blue) and the continuous (green) phases connected with the microfluidic devices, with evidenced* ***B)*** *connection of the droplet generator (yellow) with the storage device (orange) and* ***C)*** *a zoom of the reservoir chamber during the filling process.*

Once these were filled, each chamber was closed (both inlet and outlet) using a flat-end tubing for storage in the incubator (hot tweezers were used to close the end of the tubing). The resulting devices for storage of the microdroplets were kept in an incubator at 37 °C, 5% CO_2 and 95% humidity. As an example, optical images of the microdroplets loaded with AuNSs-BPT-PMA-PA labelled cells on the same day of preparation are shown in ***Figure 3.17***.

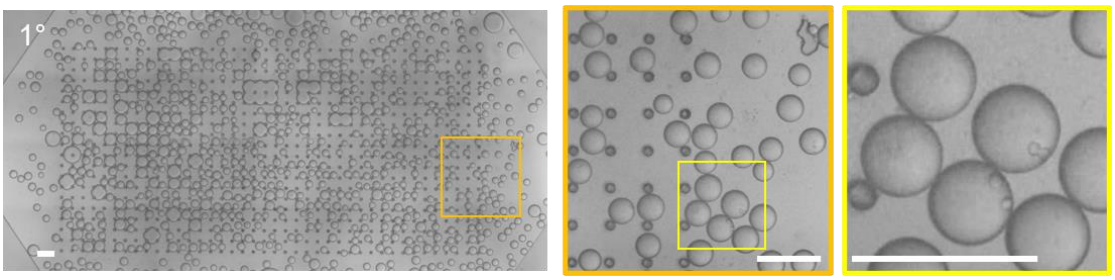

Figure 3.17 *Optical images of one reservoir chamber with AuNSs-BPT-PMA-PA labelled SKBR3 cells, at different magnifications, on the same day of preparation. Scale bars = 200 μm.*

The reservoir chambers selected had ε=120 μm height, with an intra-pillar spacing of 100 μm. In fact, among the all the combinations tested (***Table 3.3***) this one resulted the best, maintaining the microdroplets in place while avoiding their collapse.

Table 3.3 *Microfluidic device specifications tested.*

Master high (ε) [μm]	**Intra-pillars distance** [μm]
120	80
	100
	150
60	80
	100
	150

3.4.2.3 SERS imaging of cells in microdroplets

The first measured samples were chambers filled with microdroplets of SKBR3 cells labelled with AuNSs-BPT-PMA-PA. After identification of the PDMS signal (see

Table 3.4 and ***Figure 3.18A)***), it was possible to detect the typical fingerprint of the RaR only in an upside-down configuration, considering that the bottom layer of PDMS was thinner than the upper one (***Figure 3.18B** I*). In particular, we studied the effect of different laser powers on the sample and the corresponding SERS signals. Even though it was possible to detect the SERS signal of BTP using the same measurement conditions as those for PDMS, the heat generated by the nanoparticles appeared to modify irreversibly the sample structure (***Figure 3.18B***). Hence, lower laser powers were tested, showing that 5 mW was sufficient to obtain a clear typical fingerprint of BPT while avoiding damage to the sample (***Figure 3.18C*)**. Furthermore, a significantly reduced Raman signal contribution from bare PDMS was observed in the spectra acquired at lower laser power (***Figure 3.18 D***). Even in these samples measured at low laser power, the cells appeared to have moved inside the microdroplet after the measurement, likely due to excessive dilution of Matrigel® (3mg/mL) in the cell medium (***Figure 3.18E***). Optical images acquired in up-right configuration after SERS measurements (***Figure 3.18F***) showed a totally different distribution of the microdroplets inside the chamber, together with the collapse of some of them into larger droplets, probably due to the handling of the device under measurement. Additionally, the chamber presented air bubbles at the inlet and outlet extremities, indicating the need of improving the closing method of the reservoir chambers.

Table 3.4 *PDMS Raman peaks observed, and relative assignations.*

Raman shift (cm^{-1})	**Assignation**
439	Si-O sym str[37]
620	CH_3 rock[37]
713	Si-C str[38]
794	C-Si-C asym str[37]
866	CH_3 rock[37]
1270	C-H sym bend[37]
1416	C-H asym bend[37]

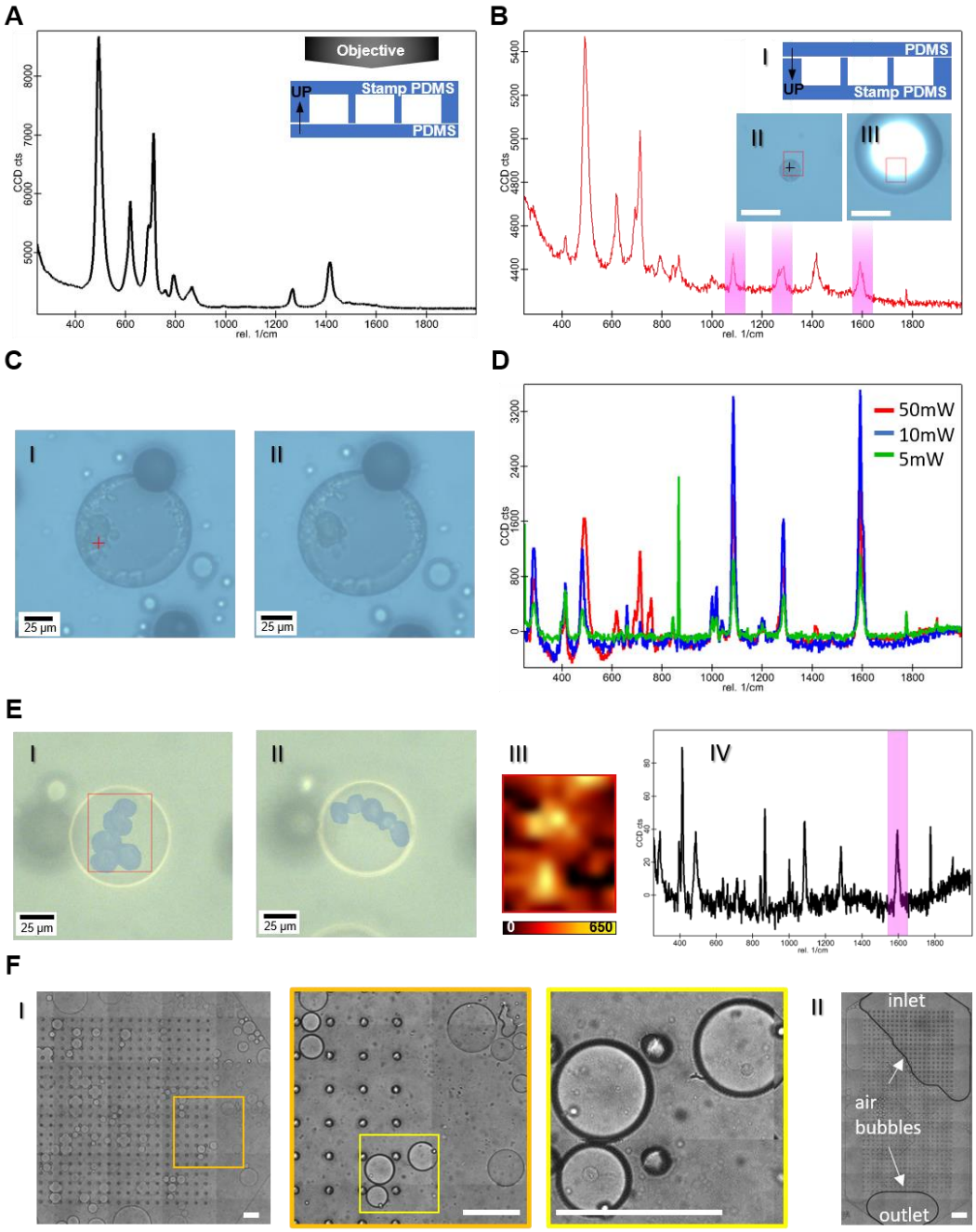

Figure 3.18 A) *Raman signal of PDMS obtained by measuring the PDMS slab with 100 mW laser power under a normal measurement configuration.* ***B)*** *SERS spectra from one point (black cross) inside the imaged area (red square), with 100 mW laser power, with evidenced in magenta the typical peaks for BPT and the I) upside-down configuration in which the optical images II) before and III) after the mapping were obtained. Scale bars = 40 µm.* ***C)*** *Optical images I) before and II) after collection of a single point SERS spectrum (red cross) at different laser powers, reported in* ***D)****.* ***E)*** *Optical images reporting the position of cells (evidenced in blue) I) before and II) after SERS mapping reported in III) at the 1594 cm^{-1} Raman shift (magenta in IV).* ***F)*** *I) Optical image of the reservoir chamber reported in* ***Figure 3.17*** *at different magnifications, after SERS mapping (2^{nd} day after preparation). Scale bar = 200 µm. II) Optical image of a second reservoir evidencing the formation of air bubbles at the inlet and outlet. Scale bar = 400 µm.*

In an attempt to optimize the system, some changes were introduced. The PDMS stamp was prepared with a smaller thickness (ca. 2-3mm), to avoid the need for measuring the device in upside down configuration and in turn excessive shaking of the droplets. The latter were realized by changing the formulation of the disperse phase, reducing the Matrigel® dilution in cellular medium (5 mg/mL) to avoid displacement of cells inside the microdroplets. Moreover, the storage arrangement was improved by introducing a paper wet with distilled water at the bottom part of the devices, to maintain the correct humidity and avoid the formation of air bubbles inside the chambers. The improved conditions are shown in the optical images in ***Figure 3.19A***. A more homogenous and stable droplet distribution over time was observed, allowing to recognize the same microdroplets after the 2nd day of incubation. It was possible to capture the nanoparticle distributions in both the SKBR3 cells labelled with AuNSs-BPT-PMA-PA and AuNRs-2NAT-PMA-PA (***Figure 3.19B-C)***, without causing any intra-droplet displacement even when using the higher laser power of 30 mW (***Figure 3.19D***). After 6 days in the incubator, the sample showed a lower SERS signal than the previous days, indicating a possible dilution of the NPs inside the cells due to mitosis, as shown in ***Figure 3.19E***. Hence, in order to verify the normal cellular division, a kit to test the viability of the cells was used. A first attempt of implementing the trypan blue dye, which is commonly used to mark dead cells in blue, was executed inside the microdroplets during their formation. The results showed that it is possible to distinguish live from dead cells using a very low concentration of the dye in the disperse phase (1:10), see ***Figure 3.20***. Nevertheless, further studies are needed to validate this procedure.

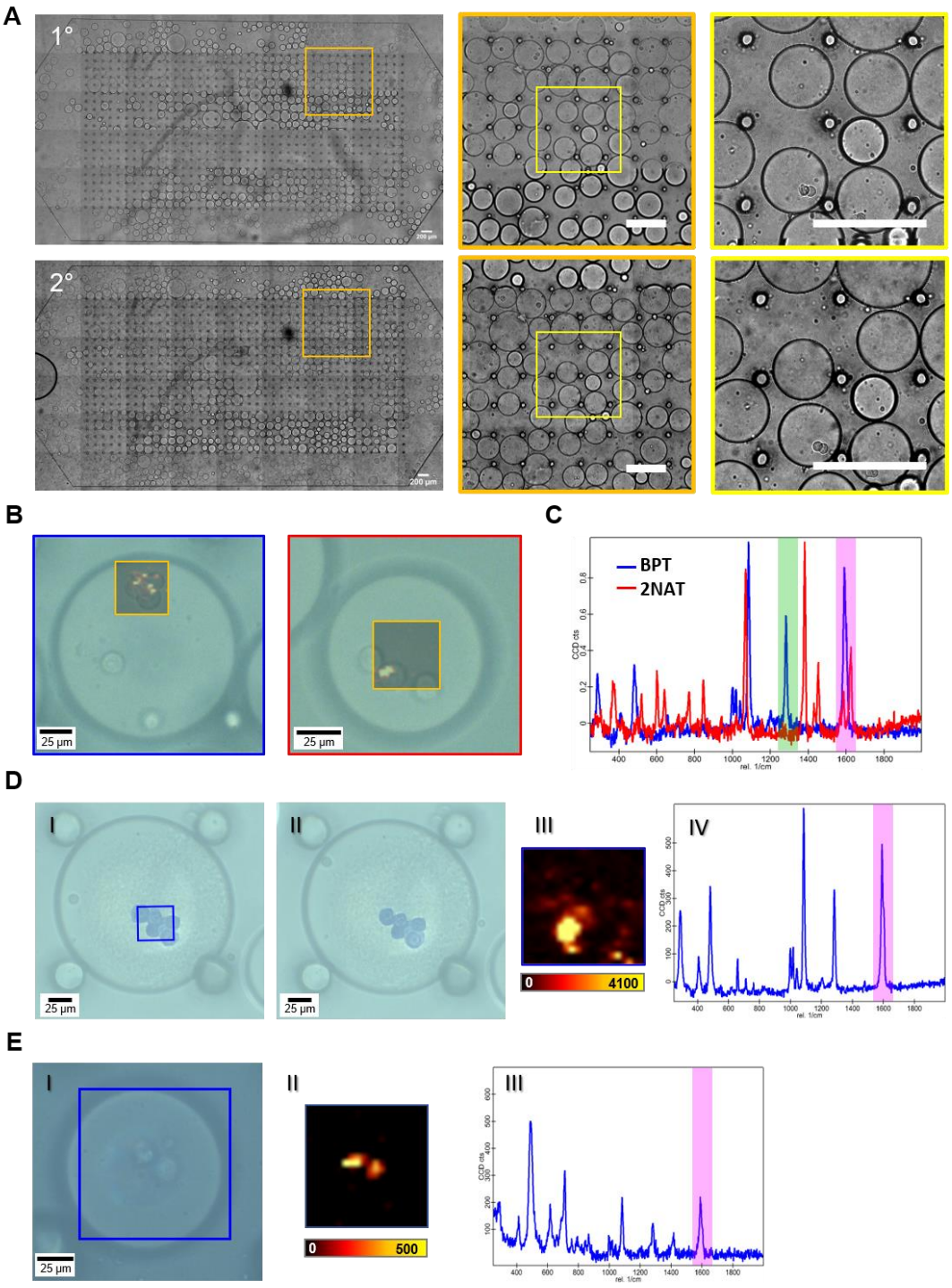

Figure 3.19 A) *Optical images of a reservoir chamber for AuNSs-BPT-PMA-PA labelled SKBR3 cells, at different magnifications, during the 1st and 2nd days after preparation. Scale bars = 200 µm.* ***B)*** *Optical images of SKBR3 cells labelled with I) AuNSs-BPT-PMA-PA and II) AuNRs-2NAT-PMA-PA, with the SERS mappings (in the orange square) taken the 2nd day after the preparation of the sample and* ***C)*** *the correlated SERS signal. In green and magenta are highlighted the two main peaks of the 2NAT and BPT RaRs.* ***D)*** *Optical images reporting the position of the cells (in blue) I) before and II) after the SERS mapping reported in III) at the 1594 cm-1 Raman shift (magenta in IV).* ***E)*** *I) Optical image taken at the 6th day after preparation, with correlated II) SERS mapping collected at 30 mW and 2 µm of step size, and III) SERS signal.*

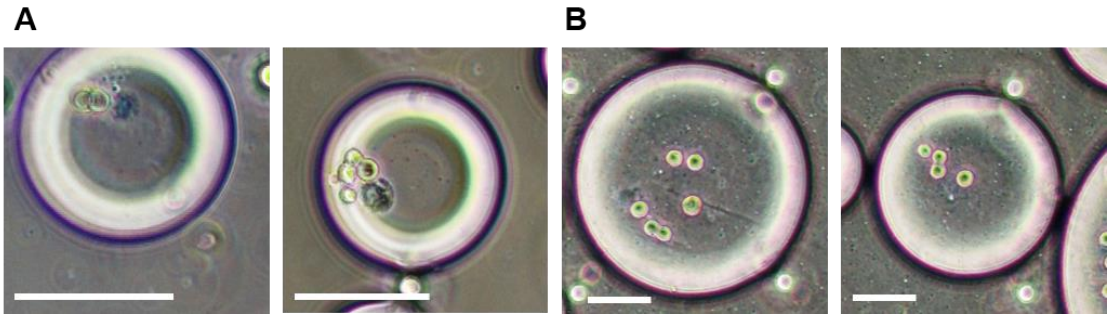

Figure 3.20 *Optical image of a droplet containing SERS-labelled cells realized with trypan blue at* ***A)****1:10 and* ***B)*** *1:20 dilutions in the disperse phase. Scale bars = 50 μm.*

3.5 Conclusions

A method to quantify the intracellular amount of SERS tags was developed, with the aim to characterize NP uptake and their dilution into daughter cells *in vitro* or due to exocytosis. The method was based on the supervised analytical method MLRA (supervised algorithm, SA), by comparing the spectra with a reference spectrum and validated by ICP-MS analysis, which is often used to quantify cell uptake of metal-containing NPs. By using this approach, a good estimation of the number of NP/cell was obtained from an analysis based on 3D SERS measurements of individual MCF7 live cells, with no undesired cytotoxicity from excessive laser exposure. Hence, it was possible to track the dilution of SERS tags into daughter cells for more than 2 weeks, ensuring the long-term labelling capacity of these biocompatible and optically sensitive labels. The decrease in SERS tag intensity over time was analysed in terms of cellular division and exocytosis, identifying cellular division as the principal source of SERS tag dilution after 1 DIV. The presented approach for the quantification of SERS tags via SERS mapping opens up the use of this methodology to study the interaction of SERS tags with live cells *in vitro* with minimal invasion and characterizing important parameters, such as dwelling time, which may vary depending on the NPs and cell line used.

Moreover, the realization procedure of 100 μm-diameter microdroplets containing SERS-labelled adhesive breast cancer cells aiming at performing single cell study, was shown. The production and the parameters for SERS measurements of cell-laden microdroplets were optimized to obtain sharp and clear SERS images. The results demonstrate a promising combination of microfluidic devices with SERS technology to study the intracellular distribution of the SERS tags in live cancer cells. Further investigations are required to improve the storage conditions and cellular viability tests over time.

These findings are important to study increasingly complex 3D cellular systems through SERS imaging as those presented in the following **Chapter 4**, with control over all parameters affecting SERS bioimaging of live cells. In this case, the long dwelling time of SERS tags (over 2 weeks), coupled with their non-toxic nature and high multiplexing ability, offers an interesting opportunity to use them in 3D cell models, even at low concentrations.

3.6 Experimental section

3.6.1 Chemicals

Tetrachloroauric acid trihydrate ($HAuCl_4 \cdot 3H_2O$, ≥99%), citric acid (≥99.5%), L-ascorbic acid (≥99%), silver nitrate ($AgNO_3$, ≥99%), hexadecyltrimethylammonium bromide (CTAB, ≥99%), O-[2-(3-mercaptopropionylamino)ethyl]-O'-methylpolyethylene glycol (PEG-SH, MW 5000 g/mol), biphenyl-4-thiol (BPT, 97%), 2-naphthalenethiol (2NAT, 99%), poly(isobutylene-alt-maleic anhydride) (average MW ~6000 g/mol), dodecylamine (98%),1-decanol, tetrahydrofuran (THF, 99.85%, extra dry), chloroform ($CHCl_3$, ≥99.8%), sodium hydroxide (NaOH, >97%), polydimethylsiloxane (PDMS) Sylgard® 184, and Fluorinert FC-40 were purchased from Sigma-Aldrich. Hydrochloric acid solution (37 wt%) was purchased from Fisher Chemical. All chemicals were used without further purification. Milli-Q water (resistivity 18.2 MΩ·cm at 25 °C) was used in all experiments. All glassware was washed with aqua regia, rinsed with Milli-Q water, and dried prior to use. Dulbecco's modified eagle medium (DMEM), fetal bovine serum (FBS), penicillin-streptomycin (PS) were purchased from Invitrogen. FBS and PS were used at 10% and 1%, respectively, to prepare complete DMEM (cDMEM). All cells were grown in cDMEM and Trypsin-EDTA was used for cell passage. HFE-7500 Novec fluorinated oil ($C_9H_5F_{15}O$, 99%) was purchased from 3M Company and Pico-Surf 2% (w/w) in FC-40 was purchased from SphereFluidic.

3.6.2 SERS tags synthesis

AuNSs and AuNRs were synthetize, respectively encoded with BPT and 2NAT, and coated with PMA as described in **Chapter 2**, obtaining AuNSs-BPT-PMA (50 nm diameter) and AuNRs-2NAT-PMA (17 nm width × 60 nm length) with LSPRs at around 785nm. Then an additional coating layer was carried out with PA, following a previously described protocol.[18] Briefly, 1 mL of AuNPs-RaR-PMA at $[Au^0]$ = 0.5 mM were centrifugated and after removing the supernatant, were resuspended in 1 mL of 1mg/mL stock solution of PA, under sonication. The mixture was leaved 1 h in a mechanical shaker and then washed with water 4 times to remove the excess of PA. The final concentration of SERS tags after the preparations was $[Au^0]$ = 0.5 mM, corresponding to ca. 1.9×10^{10} NP/mL.

3.6.3 NP characterization

TEM images were collected with a JEOL JEM-1400PLUS transmission electron microscope operating at 120 kV, using carbon-coated 400 square mesh copper grids. UV−vis optical extinction spectra were recorded using an Agilent 8453 UV−vis diode array spectrophotometer, 10 mm standard path length cuvette with 3.5 mL volume.

3.6.4 Cell preparation for SERS imaging

For the quantification of NPs over time in epithelial breast cancer cells (MCF7, ATCC#® HTB-22™), every 3-4 days the following protocol was repeated to prepare samples for SERS imaging and quantification of NPs inside cells and in the supernatant by ICP-MS. MCF7 cells

were seeded at 5.7 × 10^4 cells/cm^2 on glass-bottomed dishes of 3.5 cm^2 area (Ibidi) and incubated for 24 h. Then, DMEM cell media containing 10% FBS (herefrom cDMEM) was replaced with NPs dispersed in cDMEM and cells were incubated for an additional 24 h to allow NP uptake. Subsequently, the sample was divided: first, cell media was collected to quantify NPs in the supernatant by ICP-MS. Then, the cells were detached, counted and separated as follows: 5 × 10^4 cells were resuspended in PBS and used to measure NPs in cells by ICP-MS (see details below), and 7 × 10^4 cells were transferred to an in-house designed SERS imaging holder (details reported in ***Figure 3.21***). Finally, 2 × 10^5 cells were re-seeded to continue the experiments on the following days. The SERS imaging holder comprised a quartz slide and a polylactic acid (PLA) 3D-printed cell culture adaptor, designed with Autodesk Inventor Software (Autodesk Inc. CA, USA) and fabricated with an Ultimaker 2 printer. Prior to cell seeding, the holder was cleaned using ethanol, dried, and glued to the quartz slide, followed by sterilization by UV light. SERS measurements were performed 2 h after plating the cells, to allow them to adhere onto the substrate.

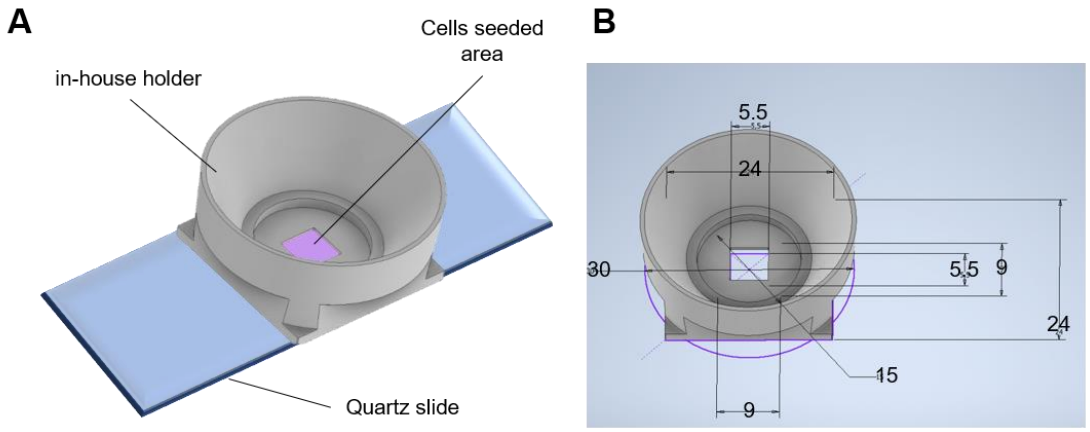

Figure 3.21 *Illustration* ***A)*** *and dimensions in mm* ***B)*** *of an in-house holder designed with Autodesk Inventor Software (Autodesk Inc. CA, USA). Cells were seeded inside an area of 30.25mm^2 in a minimum volume of 100 µL. Once adhered, additional media (<1.5 mL) could be added to perform SERS measurements with immersion objectives.*

3.6.5 Cell preparation for ICP-MS

Each 3-4 days, 2 × 10^5 MCF7 cells were centrifuged at 1200 rpm for 5 minutes. Two freeze-thaw cycles were performed to promote cell lysis. Then, the cell pellet (50 µL) was redispersed in aqua regia (450 µL) for subsequent digestion.

3.6.6 Cell preparation for viability assay

MCF7 cells were seeded at 2.8 × 10^4 cells/cm^2 on a dish with an imaging grid of 500 µm repeat distance (Ibidi). Once adhered, cells were irradiated with different laser powers using a Raman confocal microscope equipped with a 785 nm laser. After 24h, cell viability was monitored using a live/dead cell assay (ab115347, Abcam). For each irradiated section of the

grid, the percentage of dead cells was quantified and represented by the number of dead cells with respect to the area of live cells (***Figure 3.6B***).

3.6.7 TEM grid preparation for SERS tag signal analysis

A 200-mesh copper-carbon film London finder grid for electron microscopy was treated by glow discharge to hydrophilise the surface and obtain a homogeneous spreading of the particles. After 10 min in vacuum (10^{-1} mbar), a negative polarity with a coating current of 30 mA was applied for 2.5 min. Immediately after, 3µL of SERS tags at [Au^0] = 0.5 mM (1.9×10^{10} NP/mL) was drop-casted and let dry in air.

3.6.8 SERS imaging specifications

3.6.8.1 SERS tags supervised counting algorithm.

SERS measurements were performed with a confocal Raman microscope (Renishaw inVia) equipped with 1024 × 512 CCD detectors, using a 785 nm laser excitation source (maximum output 270 mW), a pinhole to obtain a circular laser spot geometry, and a 1200 l/mm diffraction grating. SERS maps were recorded in static mode (centre of scattered wavenumber 1450 cm^{-1}) using a 50× long working distance objective (NA = 0.5; Leica Microsystems, Wetzlar, Germany). For ***Figure 3.3***, an area of 400 × 400 μm^2 was imaged with 0.8s integration time, at 8.48 mW laser power and step size of 10 µm.

3.6.8.2 Phototoxicity

SERS measurements were performed with a confocal Raman microscope (Alpha300 R – Confocal Raman Imaging Microscope, Witec) equipped with 1024 × 512 CCD detectors, using a 785 nm laser excitation source (maximum output 79 mW) and a 300 l/mm diffraction grating. The signal was recorded in static mode (centre of scattered wavenumber 1450 cm^{-1}) using a 20× immersion long working distance objective (numerical aperture, NA = 0.5; Zeiss, Jena, Germany). The following settings were used in the figures, as indicated. An area of 150 × 115 μm^2 was scanned, with a step size of 5 µm and integration time of 0.02 s, increasing the laser power from 3 mW to 20 mW (***Figure 3.6A***). Two layers of 500 × 500 μm^2, at 5 µm distance between each other, were scanned with different integration times (0.02 s and 0.05 s) and laser powers (30 mW and 80 mW), and 10 µm step size. Each map took approximately 6 min to be completed (***Figure 3.6B***). Areas of ca. 60 × 80 μm^2 were scanned with 5 mW laser power, 0.02 s integration time and 5 µm step size (***Figure 3.7A***). Two layers of 500 × 500 μm^2 at 5 µm distance between each other were scanned with 5 mW laser power, 0.02 s integration time and 10 µm step size (***Figure 3.7B***). An area of 500 × 500 μm^2 was scanned with 5mW laser power, 0.02 s integration time and two different step sizes of 5 µm and 1 µm, as explained in ***Figure 3.8***.

3.6.8.3 3D SERS tags supervised counting algorithm

SERS measurements were performed with the Witec Alpha300 R. The signal was recorded using a 20× immersion long working distance objective. Per each DIV, 2 to 3 volumetric

regions (average dimensions 84 × 84 × 25 μm^3, which contained around 20 - 30 cells) were imaged with 5 mW laser power, 0.02 s integration time and step sizes of 1µm in x and y, and 4 µm in z (***Figure 3.10*** and ***Figure 3.11***). An area of ca. 84 × 84 μm^2 was imaged with 0.02 s integration time, 1 µm step size, and two different laser powers (5 mW and 80 mW) as, explained in ***Figure 3.12***.

3.6.8.4 SERS data analysis

Data obtained with the Renishaw Raman microscope were first analysed with the equipment's own program (WiRE4.4), to correct the baseline in the spectra (i.e., intelligent 11^{th} polynomial order) and to eliminate cosmic rays. Data obtained from the Witec confocal Raman microscope were analysed with the Project5 software, to correct the baseline (shape subtraction, furnished by the program) and eliminate cosmic rays.

3.6.8.5 Supervised algorithm

The spectra in 2D SERS mappings were analysed by MLRA (Regress function in Matlab) as in the previous **Chapter 2**,[39–41] which considers the full spectrum to assign a percentage of the presence of references, which are the typical fingerprints of SERS tags. This procedure assigns to each spectrum a so-called b value, one for each chosen reference, plus one b value for the background. It also provides a statistical p value for each assignment, which indicates the reliability of the analysis itself. Thus, it was possible to select only those points whose spectra had a certain percentage of similarity with the references: the first applied filter was on p values (i.e., p values < 0.05), neglecting those points that could not be properly assigned by the analysis; then, the second filter was applied to the b values, selecting only those above a second threshold called β, which was defined by the data features (here, b values > β=6). In this way a new 2D map containing only the spectra corresponding to the selected labels was obtained.

3.6.8.6 SA applied to 3D images

In the case of the 3D sum, SA was applied to all the layers of the scanned volume in a certain region and then the selected spectra were summed together. The cells were counted from the optical image and then the previous sum was divided by this number, obtaining the average SERS intensity per cell. The number of SERS tags per cell was estimated by dividing the average SERS signal per cell by the signal of a single SERS tag, obtained from the analysis of SERS tags deposited onto TEM grids, adapting the protocol presented in **Chapter 2**. In ***Figure 3.10E***, the median value is reported with a red bar, while the 25% and 75% are represented by a grey area and used to calculate the error on the number of NP/cell.

References:

(1) Bhamidipati, M.; Fabris, L. Multiparametric Assessment of Gold Nanoparticle Cytotoxicity in Cancerous and Healthy Cells: The Role of Size, Shape, and Surface Chemistry. *Bioconjug. Chem.* **2017**, *28*, 449–460. https://doi.org/10.1021/acs.bioconjchem.6b00605.

(2) Mosquera, J.; García, I.; Liz-Marzán, L. M. Cellular Uptake of Nanoparticles versus Small Molecules: A Matter of Size. *Acc. Chem. Res.* **2018**, *51*, 2305–2313. https://doi.org/10.1021/acs.accounts.8b00292.

(3) Bourquin, J.; Septiadi, D.; Vanhecke, D.; Balog, S.; Steinmetz, L.; Spuch-Calvar, M.; Taladriz-Blanco, P.; Petri-Fink, A.; Rothen-Rutishauser, B. Reduction of Nanoparticle Load in Cells by Mitosis but Not Exocytosis. *ACS Nano* **2019**, *13*, 7759–7770. https://doi.org/10.1021/acsnano.9b01604.

(4) Behzadi, S.; Serpooshan, V.; Tao, W.; Hamaly, M. A.; Alkawareek, M. Y.; Dreaden, E. C.; Brown, D.; Alkilany, A. M.; Farokhzad, O. C.; Mahmoudi, M. Cellular Uptake of Nanoparticles: Journey inside the Cell. *Chemical Society Reviews*. Royal Society of Chemistry July 2017, pp 4218–4244. https://doi.org/10.1039/c6cs00636a.

(5) Foroozandeh, P.; Aziz, A. A. Insight into Cellular Uptake and Intracellular Trafficking of Nanoparticles. *Nanoscale Res. Lett.* **2018**, *13*, 339. https://doi.org/10.1186/s11671-018-2728-6.

(6) Kapara, A.; Brunton, V.; Graham, D.; Faulds, K. Investigation of Cellular Uptake Mechanism of Functionalised Gold Nanoparticles into Breast Cancer Using SERS. *Chem. Sci.* **2020**, *11*, 5819–5829. https://doi.org/10.1039/d0sc01255f.

(7) Summers, H. D.; Rees, P.; Holton, M. D.; Rowan Brown, M.; Chappell, S. C.; Smith, P. J.; Errington, R. J. Statistical Analysis of Nanoparticle Dosing in a Dynamic Cellular System. *Nat. Nanotechnol.* **2011**, *6*, 170–174. https://doi.org/10.1038/nnano.2010.277.

(8) Ha, S. W.; Camalier, C. E.; Weitzmann, M. N.; Beck, G. R.; Lee, J. K. Long-Term Monitoring of the Physicochemical Properties of Silica-Based Nanoparticles on the Rate of Endocytosis and Exocytosis and Consequences of Cell Division. *Soft Mater.* **2013**, *11*, 195–203. https://doi.org/10.1080/1539445X.2012.617641.

(9) Kim, C. S.; Le, N. D. B.; Xing, Y.; Yan, B.; Tonga, G. Y.; Kim, C.; Vachet, R. W.; Rotello, V. M. The Role of Surface Functionality in Nanoparticle Exocytosis. *Adv. Healthc. Mater.* **2014**, *3*, 1200–1202. https://doi.org/10.1002/adhm.201400001.

(10) Oh, N.; Park, J. H. Surface Chemistry of Gold Nanoparticles Mediates Their Exocytosis in Macrophages. *ACS Nano* **2014**, *8*, 6232–6241. https://doi.org/10.1021/nn501668a.

(11) Scheffer, A.; Engelhard, C.; Sperling, M.; Buscher, W. ICP-MS as a New Tool for the Determination of Gold Nanoparticles in Bioanalytical Applications. *Anal. Bioanal. Chem.* **2008**, *390*, 249–252. https://doi.org/10.1007/S00216-007-1576-5.

(12) Drasler, B.; Vanhecke, D.; Rodriguez-Lorenzo, L.; Petri-Fink, A.; Rothen-Rutishauser, B. Quantifying Nanoparticle Cellular Uptake: Which Method Is Best? *Nanomedicine* **2017**, *12*, 1095–1099. https://doi.org/10.2217/nnm-2017-0071.

(13) Sujai, P. T.; Joseph, M. M.; Saranya, G.; Nair, J. B.; Murali, V. P.; Maiti, K. K. Surface Charge Modulates the Internalization: Vs. Penetration of Gold Nanoparticles: Comprehensive Scrutiny on Monolayer Cancer Cells, Multicellular Spheroids and Solid Tumors by SERS Modality. *Nanoscale* **2020**, *12*, 6971–6975. https://doi.org/10.1039/d0nr00809e.

(14) Amendola, V. Correlation of Surface-Enhanced Raman Scattering (SERS) with the Surface Density of Gold Nanoparticles: Evaluation of the Critical Number of SERS

Tags for a Detectable Signal. *Beilstein J. Nanotechnol.* **2019**, *10*, 1016–1023. https://doi.org/10.3762/BJNANO.10.102.

(15) Zavaleta, C. L.; Smith, B. R.; Walton, I.; Doering, W.; Davis, G.; Shojaei, B.; Natan, M. J.; Gambhir, S. S. Multiplexed Imaging of Surface Enhanced Raman Scattering Nanotags in Living Mice Using Noninvasive Raman Spectroscopy. *Proc. Natl. Acad. Sci. U. S. A.* **2009**, *106*, 13511–13516. https://doi.org/10.1073/pnas.0813327106.

(16) Schlücker, S. SERS Microscopy: Nanoparticle Probes and Biomedical Applications. *ChemPhysChem*. Wiley-VCH Verlag July 2009, pp 1344–1354. https://doi.org/10.1002/cphc.200900119.

(17) Fogh, J.; Fogh, J. M.; Orfeo, T. One Hundred and Twenty-Seven Cultured Human Tumor Cell Lines Producing Tumors in Nude Mice. *J. Natl. Cancer Inst.* **1977**, *59*, 221–226. https://doi.org/10.1093/JNCI/59.1.221.

(18) Jiménez de Aberasturi, D.; Henriksen-Lacey, M.; Litti, L.; Langer, J.; Liz-Marzán, L. M. Using SERS Tags to Image the Three-Dimensional Structure of Complex Cell Models. *Adv. Funct. Mater.* **2020**, *30*, 1909655. https://doi.org/10.1002/adfm.201909655.

(19) Lenzi, E.; Litti, L.; Jimenez de Aberasturi, D.; Henriksen-Lacey, M.; Liz-Marzán, L. M. SERSTEM: An App for the Statistical Analysis of Correlative SERS and TEM Imaging and Evaluation of SERS Tags Performance. *J. Raman Spectrosc.* **2021**, *52*, 355–365. https://doi.org/10.1002/jrs.6043.

(20) Furuya, Y.; Kohno, N.; Fujiwara, Y.; Saitoh, Y. Mechanisms of Estrogen Action on the Proliferation of MCF-7 Human Breast Cancer Cells in an Improved Culture Medium. *Cancer Res.* **1989**, *49*, 6670–6674.

(21) Tian, H.; Liu, H.; Zhu, Y.; Xing, D.; Wang, B. The Trends of Single-Cell Analysis: A Global Study. *Biomed Res. Int.* **2020**, *2020*, 7425397. https://doi.org/10.1155/2020/7425397.

(22) Hodzic, E. Single-Cell Analysis: Advances and Future Perspectives. *Bosn. J. Basic Med. Sci.* **2016**, *16*, 313–314. https://doi.org/10.17305/BJBMS.2016.1371.

(23) Stuart, T.; Satija, R. Integrative Single-Cell Analysis. *Nat. Rev. Genet. 2019 205* **2019**, *20*, 257–272. https://doi.org/10.1038/s41576-019-0093-7.

(24) Rakszewska, A.; Tel, J.; Chokkalingam, V.; Huck, W. T. S. One Drop at a Time: Toward Droplet Microfluidics as a Versatile Tool for Single-Cell Analysis. *NPG Asia Mater. 2014 610* **2014**, *6*, e133. https://doi.org/10.1038/am.2014.86.

(25) Paris, J. L.; Coelho, F.; Teixeira, A.; Diéguez, L.; Silva, B. F. B.; Abalde-Cela, S. In Vitro Evaluation of Lipopolyplexes for Gene Transfection: Comparing 2D, 3D and Microdroplet-Enabled Cell Culture. *Molecules* **2020**, *25*, 3277. https://doi.org/10.3390/MOLECULES25143277.

(26) Teixeira, A.; Paris, J. L.; Roumani, F.; Diéguez, L.; Prado, M.; Espiña, B.; Abalde-Cela, S.; Garrido-Maestu, A.; Rodriguez-Lorenzo, L. Multifuntional Gold Nanoparticles for the SERS Detection of Pathogens Combined with a LAMP-in-Microdroplets Approach. *Mater. (Basel, Switzerland)* **2020**, *13*, 1934. https://doi.org/10.3390/MA13081934.

(27) He, X.; Yang, S.; Xu, T.; Song, Y.; Zhang, X. Microdroplet-Captured Tapes for Rapid Sampling and SERS Detection of Food Contaminants. *Biosens. Bioelectron.* **2020**, *152*, 112013. https://doi.org/10.1016/J.BIOS.2020.112013.

(28) Abalde-Cela, S.; Auguié, B.; Fischlechner, M.; Huck, W. T. S.; Alvarez-Puebla, R. A.; Liz-Marzán, L. M.; Abell, C. Microdroplet Fabrication of Silver–Agarose Nanocomposite Beads for SERS Optical Accumulation. *Soft Matter* **2011**, *7*, 1321–1325. https://doi.org/10.1039/C0SM00601G.

(29) Nolan, J. P.; Duggan, E.; Liu, E.; Condello, D.; Dave, I.; Stoner, S. A. Single Cell Analysis Using Surface Enhanced Raman Scattering (SERS) Tags. *Methods* **2012**, *57*, 272–279. https://doi.org/10.1016/J.YMETH.2012.03.024.

(30) Sohrabi, S.; Kassir, N.; Keshavarz Moraveji, M. Droplet Microfluidics: Fundamentals and Its Advanced Applications. *RSC Adv.* **2020**, *10*, 27560–27574. https://doi.org/10.1039/D0RA04566G.

(31) Mazutis, L.; Gilbert, J.; Ung, W. L.; Weitz, D. A.; Griffiths, A. D.; Heyman, J. A. Single-Cell Analysis and Sorting Using Droplet-Based Microfluidics. *Nat. Protoc.* **2013**, *8*, 870–891. https://doi.org/10.1038/NPROT.2013.046.

(32) Fujii, T. PDMS-Based Microfluidic Devices for Biomedical Applications. *Microelectron. Eng.* **2002**, *61–62*, 907–914. https://doi.org/10.1016/S0167-9317(02)00494-X.

(33) Damiati, S.; Kompella, U. B.; Damiati, S. A.; Kodzius, R. Microfluidic Devices for Drug Delivery Systems and Drug Screening. *Genes (Basel)* **2018**, *9*, 103. https://doi.org/10.3390/GENES9020103.

(34) Yobas, L.; Martens, S.; Ong, W. L.; Ranganathan, N. High-Performance Flow-Focusing Geometry for Spontaneous Generation of Monodispersed Droplets. *Lab Chip* **2006**, *6*, 1073–1079. https://doi.org/10.1039/B602240E.

(35) Eastburn, D. J.; Sciambi, A.; Abate, A. R. Ultrahigh-Throughput Mammalian Single-Cell Reverse-Transcriptase Polymerase Chain Reaction in Microfluidic Drops. *Anal. Chem.* **2013**, *85*, 8016–8021. https://doi.org/10.1021/AC402057Q.

(36) Niculescu, A. G.; Chircov, C.; Bîrcă, A. C.; Grumezescu, A. M. Fabrication and Applications of Microfluidic Devices: A Review. *Int. J. Mol. Sci.* **2021**, *22*, 1–26. https://doi.org/10.3390/IJMS22042011.

(37) Jayes, L.; Hard, A. P.; Séné, C.; Parker, S. F.; Jayasooriya, U. A. Vibrational Spectroscopic Analysis of Silicones: A Fourier Transform-Raman and Inelastic Neutron Scattering Investigation. *Anal. Chem.* **2003**, *75*, 742–746. https://doi.org/10.1021/AC026012F.

(38) Durkin, A. J.; Ediger, M. N.; Pettit, G. H. Quantification of Polydimethylsiloxane Concentration in Turbid Samples Using Raman Spectroscopy and the Method of Partial Least Squares. *Lasers Med Sci* **1998**, *13*, 32–41.

(39) Brereton, R. G. Evolutionary Signals. In *Chemometrics*; John Wiley & Sons, Ltd, 2003; pp 339–407. https://doi.org/10.1002/0470863242.CH6.

(40) Zhang, Y.; Wang, Z.; Wu, L.; Zong, S.; Yun, B.; Cui, Y. Combining Multiplex SERS Nanovectors and Multivariate Analysis for In Situ Profiling of Circulating Tumor Cell Phenotype Using a Microfluidic Chip. *Small* **2018**, *14*, 1704433. https://doi.org/10.1002/SMLL.201704433.

(41) Pallaoro, A.; Hoonejani, M. R.; Braun, G. B.; Meinhart, C. D.; Moskovits, M. Rapid Identification by Surface-Enhanced Raman Spectroscopy of Cancer Cells at Low Concentrations Flowing in a Microfluidic Channel. *ACS Nano* **2015**, *9*, 4328–4336. https://doi.org/10.1021/ACSNANO.5B00750.

4. Optimization of SERS measurement parameters in 3D cell models

Contents

4.1 Introduction

In the previous **Chapter 3**, a methodology was developed to quantify the number of SERS tags inside live cells using 2D SERS mapping, which allows a better understanding of SERS-labelled cells over time. In this **Chapter 4**, we have investigated the fundamental parameters to optimize live SERS tomography, which is still under development and requires the use of sophisticated microscopes but also the optimization of measurement parameters and complex data analysis, towards achieving an accurate characterization of 3D cell models over time. Indeed, the translation from 2D to 3D cell models is not trivial,[1] and suffers from a lack of standardization in the emerging characterization techniques.[2] Specifically, we were able to study different parameters such as imaging acquisition time, resolution, signal intensity, and light penetration depth into 3D cell models. 3D-printed scaffolds were used to realize different 3D cell models, giving structural support and allowing the cells to grow in an *in vivo*-like environment. Indeed, as previously introduced in **Chapter 1,** 3D printing of polymeric scaffold provides numerous possibilities to customize the final design toward reproducible fabrication.[3,4] In particular, the simplest 3D cellular model is reported in **Section 4.2**, where a multimodal tessellated scaffold made of PLGA and printed by means of 3D jet printing technology, was employed to grow a thin layer of HDF cells in 3D. This 3D cellular model was used to study the imaging parameters by means of a comparison with the most commonly used imagining technique, i.e. fluorescence. Toward improving the 3D cellular model and obtaining more realistic 3D culture models, a second type of scaffold, printed via direct ink writing, is introduced in **Section 4.3**. By incorporating plasmonic NPs inside the ink formulation of the hydrogel-based printed scaffolds, they could be used as both SERS imaging references and biomolecular sensors. The SERS detection properties of these plasmonic structures were thus investigated. In **Section 4.4** hydrogel-based structures with improved formulation were employed to obtain a better defined structure along the z direction. Such scaffolds were employed with MCF7 and HDF cells to realize 3D cellular models with a high spatial resolution, which better resembled real tumorigenic aggregates. Imaging and detection parameters were surveyed for these models, obtaining sharp and bright SERS images of the 3D cellular model, thereby opening the possibility to monitor the production of cancer-related biomolecules, with high spatial and temporal resolution.

4.2 Multimodal tessellated scaffold

As a first model for 3D-printed polymeric scaffolds, we explored the use of biocompatible scaffolds, with micron-scale resolution over wide areas, prepared by means of 3D jet writing, a modified electrospinning process.[5–8] Using this technique, tessellated structures with unmatched spatial precision and 3D resolution can be produced.[5] This technique has also been previously reported to be suitable for printing polymer inks containing NPs, as well as other molecules such as fluorophores, thereby achieving hybrid materials with potential applications in drug release and multimodal imaging.[9,10] Our interest regarding these hybrid structures was

the possibility of expanding standard characterization methods, such as transmission electron microscopy (TEM), scanning electron microscopy (SEM) and fluorescence microscopy, through their combination with the complementary information provided by SERS.[11,12]

Based on this premise, we first studied a cellular model based on a 3D printed multimodal tessellated scaffold, labelled with SERS encoded AuNPs and a fluorescently labelled polymer. The scaffold was used as a support frame for the long-term 3D growth of 5 μm high human dermal fibroblast (HDF) cells,[13] in optical transparency conditions, suitable for both SERS and fluorescence imaging. In their natural setting, HDFs are the main cellular constituent of the dermis layer of the skin and represent a crucial element to maintain the structural integrity of this connective tissue. Importantly, it has been reported that HDF cells induce adhesion and invasion of tumour cells, promoting the formation of 3D cellular structures.[14,15] In this study, HDFs were labelled with two different SERS tags to achieve multiplex imaging and study the movement of the two different HDF populations, thanks to the presence of a different set of SERS-encoded AuNPs inside the scaffold. The results were validated *via* fluorescence imaging.

4.2.1 Components and characterization

3D printed scaffold

The multimodal tessellated scaffolds were fabricated by the group of Prof. Joerg Lahann, at the Biointerfaces Institute of the University of Michigan. Different scaffolds were prepared with fibres made of either monocompartmental or bicompartmental section, by embedding two different fluorescently labelled polymers and/or two different SERS-encoded AuNPs within the PLGA polymer matrix. As plasmonic NPs for SERS tags, we selected AuNSs with an LSPR maximum around 800 nm, i.e. in close resonance with the 785nm laser wavelength typically employed in biological experiments. After synthesis of AuNSs (50 nm diameter) in aqueous solution, they were transferred into chloroform ($CHCl_3$) by adsorption of the aromatic RaR BPT, yielding hydrophobic AuNSs-BPT (see ***Figure 4.1A***). In order to prepare the ink for 3D printing, AuNSs-BPT in $CHCl_3$ were mixed with PLGA and fluorescently labelled polymers (namely (poly[(mphenylenevinylene)-alt-(2,5-dihexyloxy-p-phenylenevinylene], and poly[tris(2,5-bis(hexyloxy)-1,4-phenylenevinylene)-alt-(1,3-phenylenevinylene)])) dissolved in $CHCl_3$, which were chosen to avoid overlap with the BPT SERS signal and *vice versa* (see Experimental section for more details). The scaffolds were printed using the 3D jet writing technique,[9] with either 5 or 10 aligned fibres of 10 μm diameter, resulting in a 10 × 10 mm^2 mesh with individual 500 × 500 μm^2 squares (***Figure 4.1B,C***). Shown in ***Figure 4.1D,E*** are a confocal fluorescence image of the scaffold containing the fluorescently labelled blue and green polymers (**D**) and a SERS image based on the AuNSs-BPT signal, which is detectable in the whole scaffold (**E**). To ensure cell adhesion onto the scaffold, it was covered with a thin layer of fibronectin, by adding a drop of a fibronectin solution (1mg/mL) at 37 °C and incubating for 30 min.

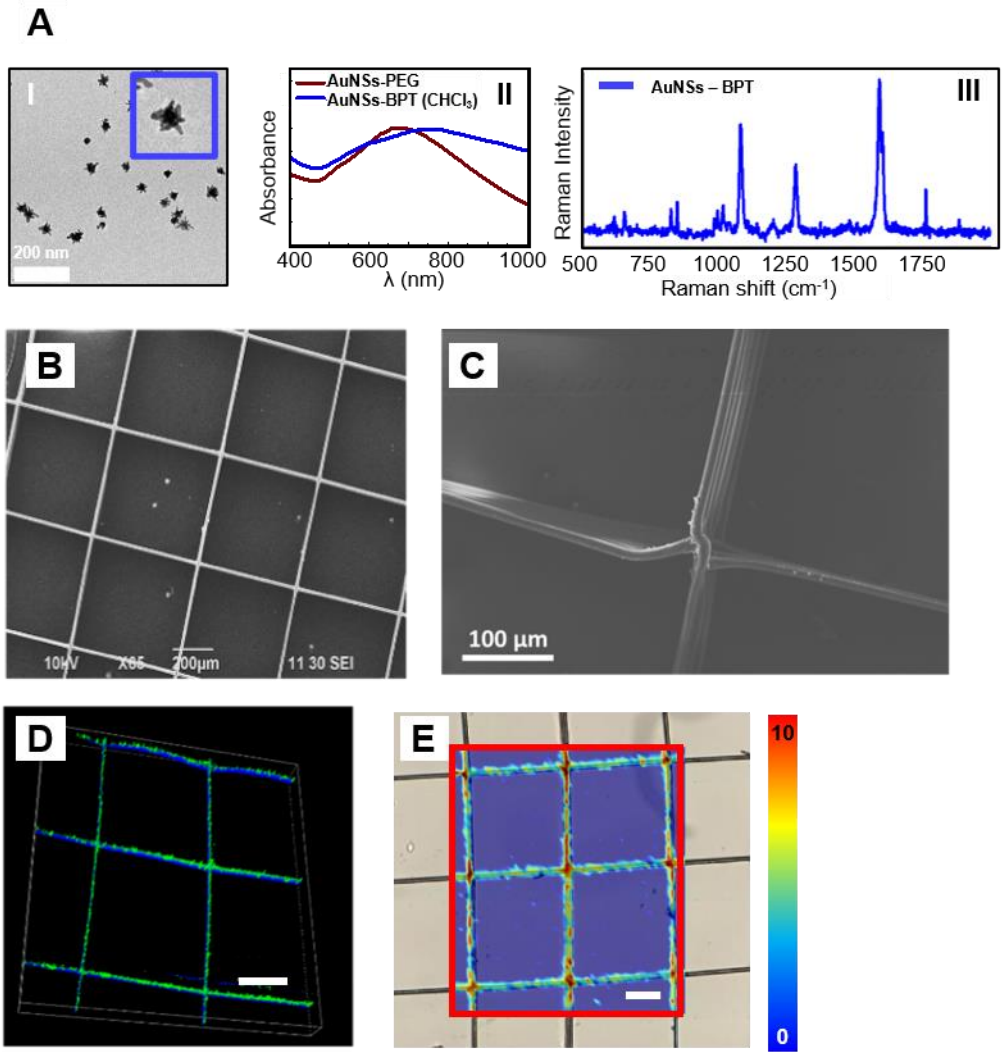

Figure 4.1 A) *(I) TEM image ,(II) UV-Vis spectra and (III) characteristic SERS signal of AuNS-BPT in* $CHCl_3$*.* ***B)*** *Representative SEM image of the hybrid scaffolds.* ***C)*** *SEM image of an intersection of the tessellated 500 × 500* μm^2 *squares.* ***D)*** *Fluorescence confocal microscopy image showing the fluorescence signals from blue and green labelled compartments.* ***E)*** *SERS signal provided by AuNS-4BPT SERS tags distributed throughout the PLGA fibres. Scale bars in (**D**) and (**E**) =200 µm.*

SERS-labelled HDF cells

It has been shown in literature that, HDF cells readily uptake positively-charged SERS tags and can retain them for long periods of *ca.* 2 weeks.[13] Therefore, HDFs were incubated with different types of SERS tags, namely AuNSs capped with 1NAT, 2NAT and MBT RaRs, and subsequently covered with a first PMA layer and an outermost positively charged layer made of PA. The selected RaRs have clearly distinguishable fingerprints (***Figure 4.2***), as shown by a post-processing analysis. The HDFs were incubated with SERS tags at a final concentration of $[Au^0]$ = 0.1 mM in FBS-containing media, after 24h serum starvation so that all cells were encouraged to endocytose SERS tags at a similar rate.[16]

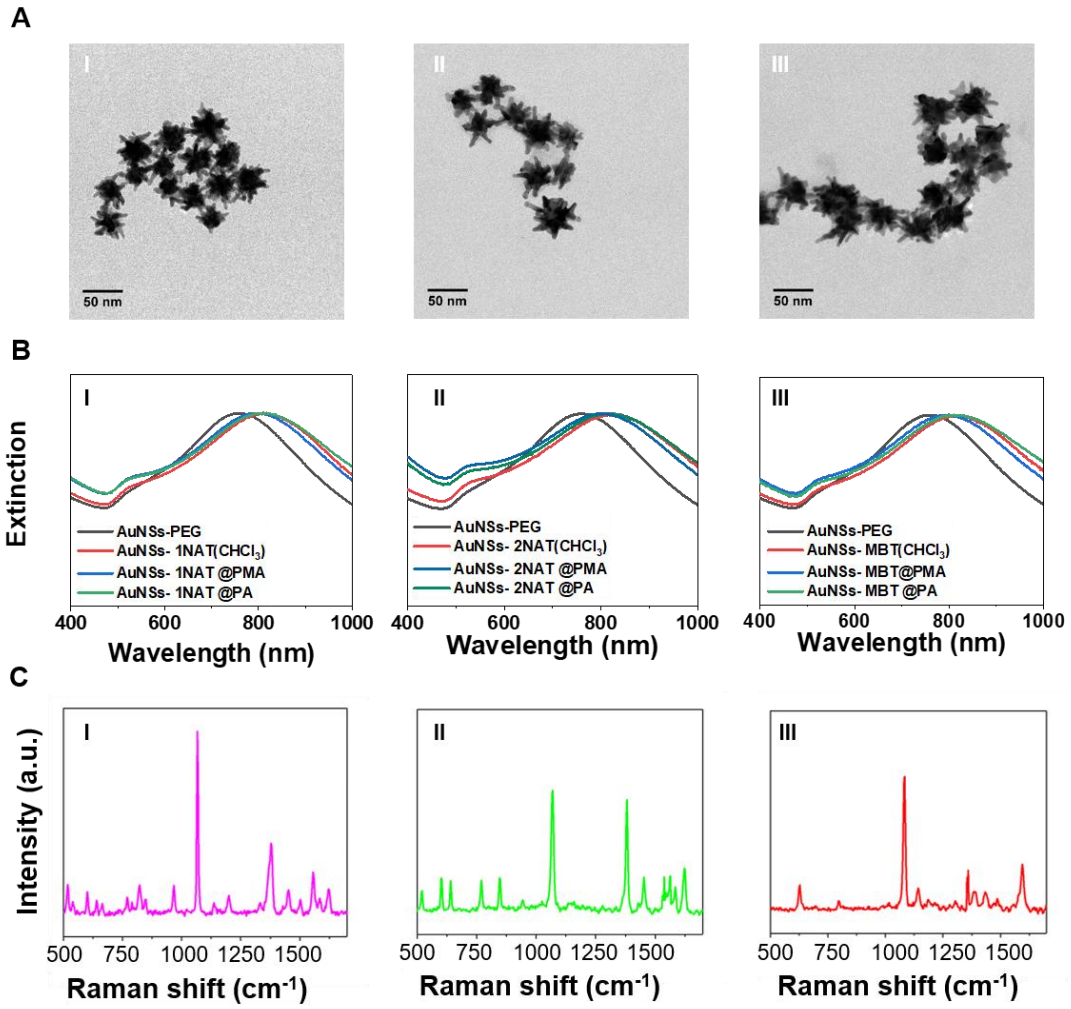

Figure 4.2 A) *TEM images,* ***B)*** *UV-Vis spectra and* ***C)*** *SERS spectra of (I) AuNSs-1NAT, (II) AuNSs-2NAT and (III) AuNSs-MBT.*

Shown in ***Figure 4.3*** are 3D confocal Raman measurements of cells labelled with *(I)* AuNSs-1NAT, *(II)* AuNSs-2NAT and *(III)* AuNSs-MBT, where it can be appreciated that they were encapsulated within endosomes located at the peri-nuclear area. Aiming at studying their behaviour in the 3D model for long-term imaging, we first explored changes in the SERS intensity over time, in a similar manner as reported for SERS-labelled MCF7 cells in the previous **Chapter 3**. The average SERS signal collected during the first 5 DIV showed little change in intensity, whereas after 9 DIV the intensity was reduced by approximately half (***Figure 4.4***). Measurements over time were performed using a longer integration time (0.05 s vs. 0.02 s) and a higher laser power (10 mW vs. 5 mW) than those for the initial characterization (***Figure 4.3A,B***), with the aim of obtaining clear signals. Shown in ***Figure 4.4C*** are higher SERS signal intensities measurements achieved by further increasing the excitation laser power intensity up to 30 mW, while working in a non-toxic laser power range. This ensured a suitable range of working parameters that could be used for imaging 3D cellular models over long periods of time.

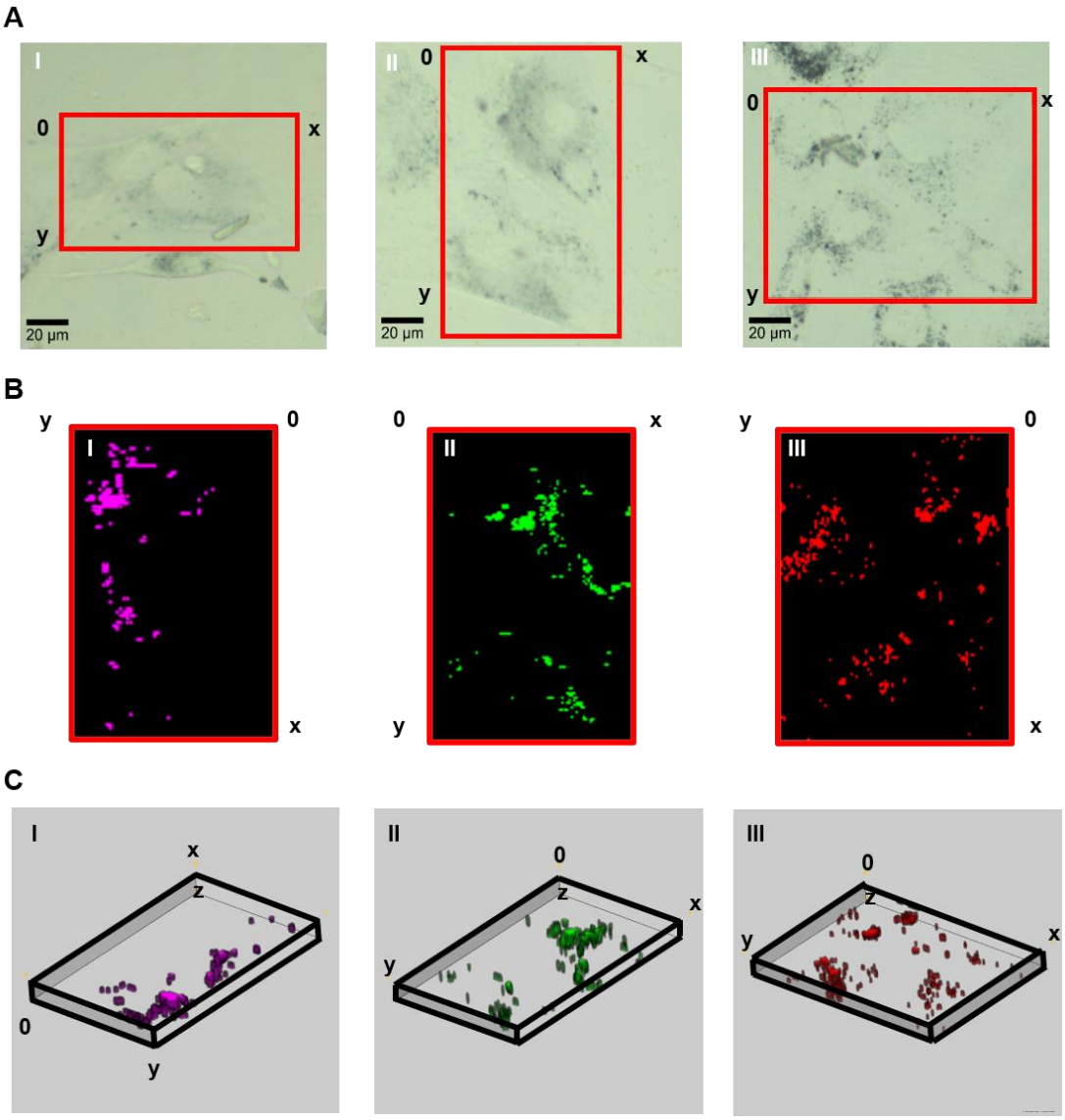

Figure 4.3 ***A)*** *Brightfield images of cells labelled with (I) AuNSs-1NAT, (II) AuNSs-2NAT and (III) AuNSs-MBT; red boxes indicate areas selected for SERS imaging.* ***B)*** *maximum intensity projection SERS maps showing distribution of signals corresponding to the separate SERS tags.* ***C)*** *3D volume reconstruction of z-stack SERS maps. SERS imaging was conducted using a 0.02 s integration time with 5 mW laser power, and 1 × 1 × 4 µm^3 step size (XYZ).*

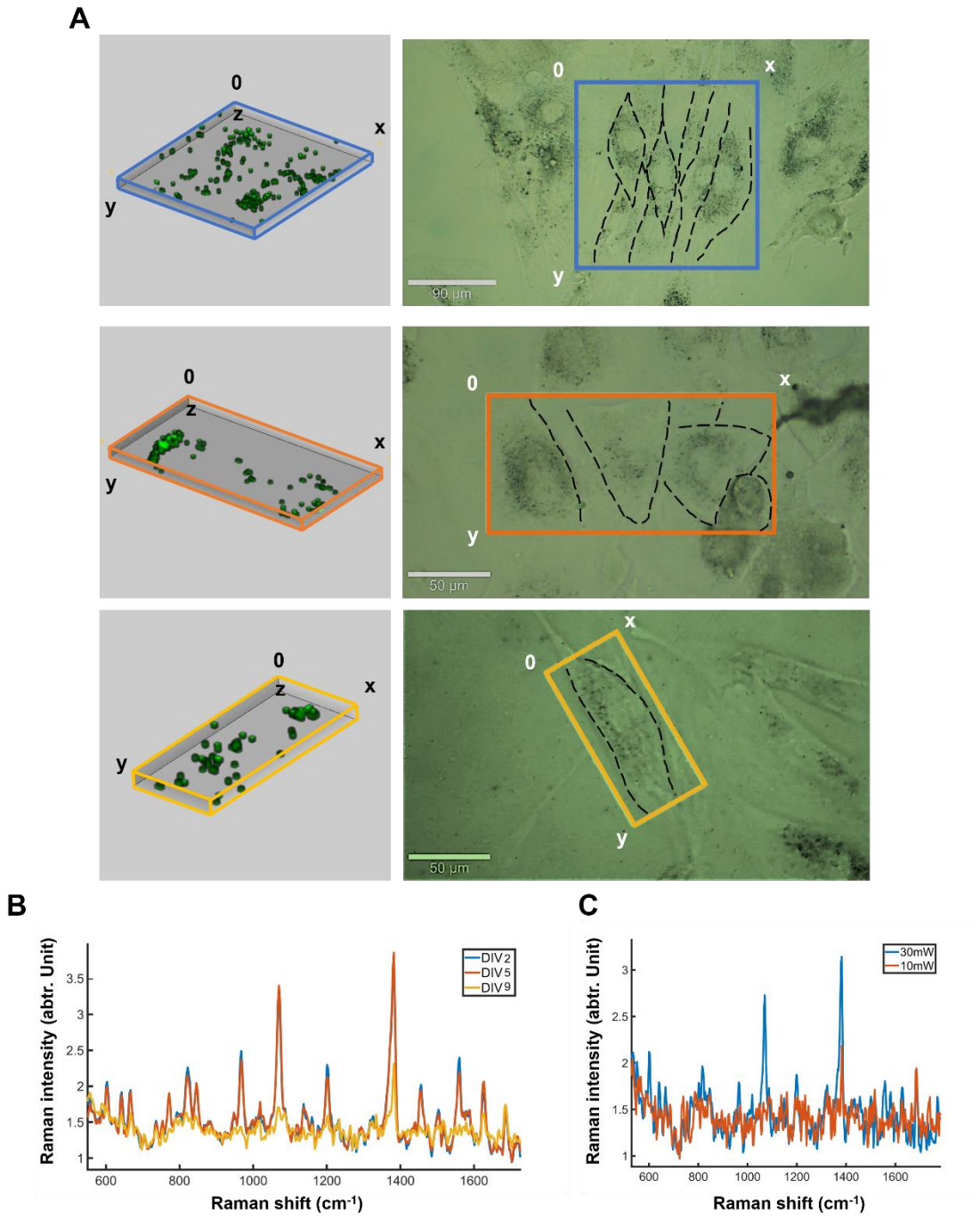

Figure 4.4 *3D measurements over time of HDF cells labelled with AuNS-2NAT.* ***A)*** *SERS tag volume reconstructions (left) of the areas containing HDF cells indicated in the brightfield optical images (right), collected at 2 DIV (blue), 5 DIV (orange), and 9 DIV (yellow).* ***B)*** *The average SERS signal from 2 DIV, 5 DIV and 9 DIV, calculated from the whole imaging volume. SERS imaging was conducted using 0.05 s integration time with 10 mW laser power, and 1 × 1 × 4 µm^3 step size (XYZ).* ***C)*** *Average spectra collected at 10 and 30 mW of laser irradiation power.*

4.2.2 3D SERS imaging

Confocal Raman microscopy offers the ability to image a sample using a NIR laser, which has a deeper penetration depth as compared to fluorescence confocal microscopy, typically based on laser excitation in the visible.[13,17] This feature is of particular interest in the

characterization of *in vitro* and *in vivo* 3D cellular models, where non-invasive imaging over time is required. However, optimization of the SERS imaging conditions and parameters is necessary to properly assess the limitations and advantages of SERS for 3D bioimaging. In order to study the kinetics of the cellular growth via SERS, three HDF cells populations labelled each of them with a different SERS tag were seeded onto a hybrid scaffold, using a fibronectin layer to increase cellular adherence. This cellular model was relatively easy to realize, considering that the cells stick and proliferate quickly on the fibronectin layer, but it is not properly considered an extended 3D model. Notwithstanding, this 3D model represents a convenient starting point to study the measurement parameters, which can be subsequently applied in the characterization of more complex systems. Cellular growth was first assessed with fluorescence, using green fluorescence protein (GFP)-transfected HDFs, which were found to form a film with a thickness of 100 μm over the printed scaffold within 14 days, thanks to the production of their own ECM (***Figure 4.5***).

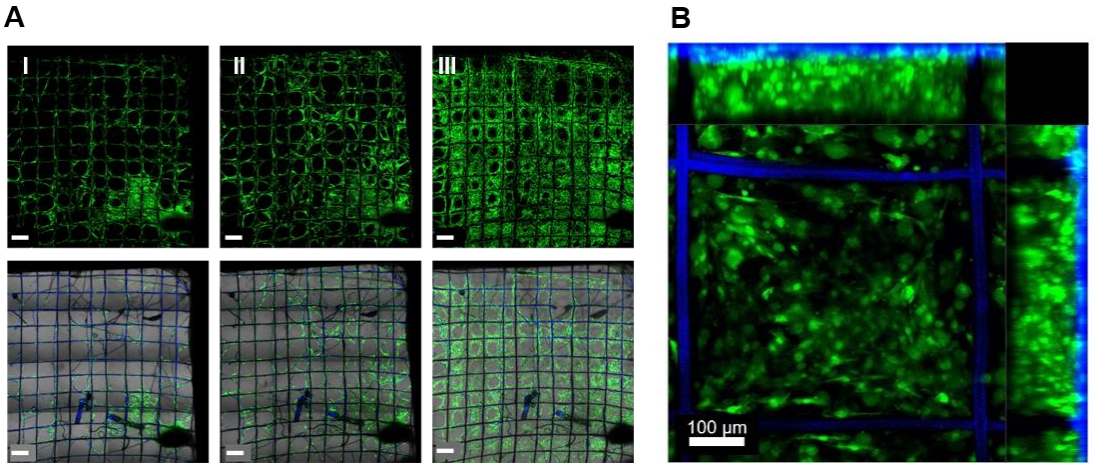

Figure 4.5 A) *Evolution of HDF cell growth and scaffold structure over a 2-week period: (I) 5DIV, (II) 7DIV and (III) 14DIV. HDFs cells were transfected to express GFP (green), the scaffold is labelled in blue. The upper panels display fluorescence images of the cells, overlaid with the scaffold, while the lower panels are optical bright field images. Scale bars: 500 μm.* ***B)*** *Maximum intensity projection (MIP) of a z-stack (ca. 150 μm thick) showing HDF 3D organization in the scaffold.*

SERS spectra were collected every 3-5 days for a period of 20 days. The same measurement parameters as those for the characterization over time were employed to obtain a good intensity signal during the latest days of measurement, namely 0.05 s integration time and 10 mW laser power. The HDFs grew into a 3D matrix layer, which was easy to image via SERS microscopy. Shown in ***Figure 4.6*** are 2D bright field images of the same area over time, overlayed by the signals identified for all three SERS tags. The SERS signals indicate a cellular spreading towards the centre of the squares from the fibres edges, where the HDFs initially attached due to the fibronectin coating layer.

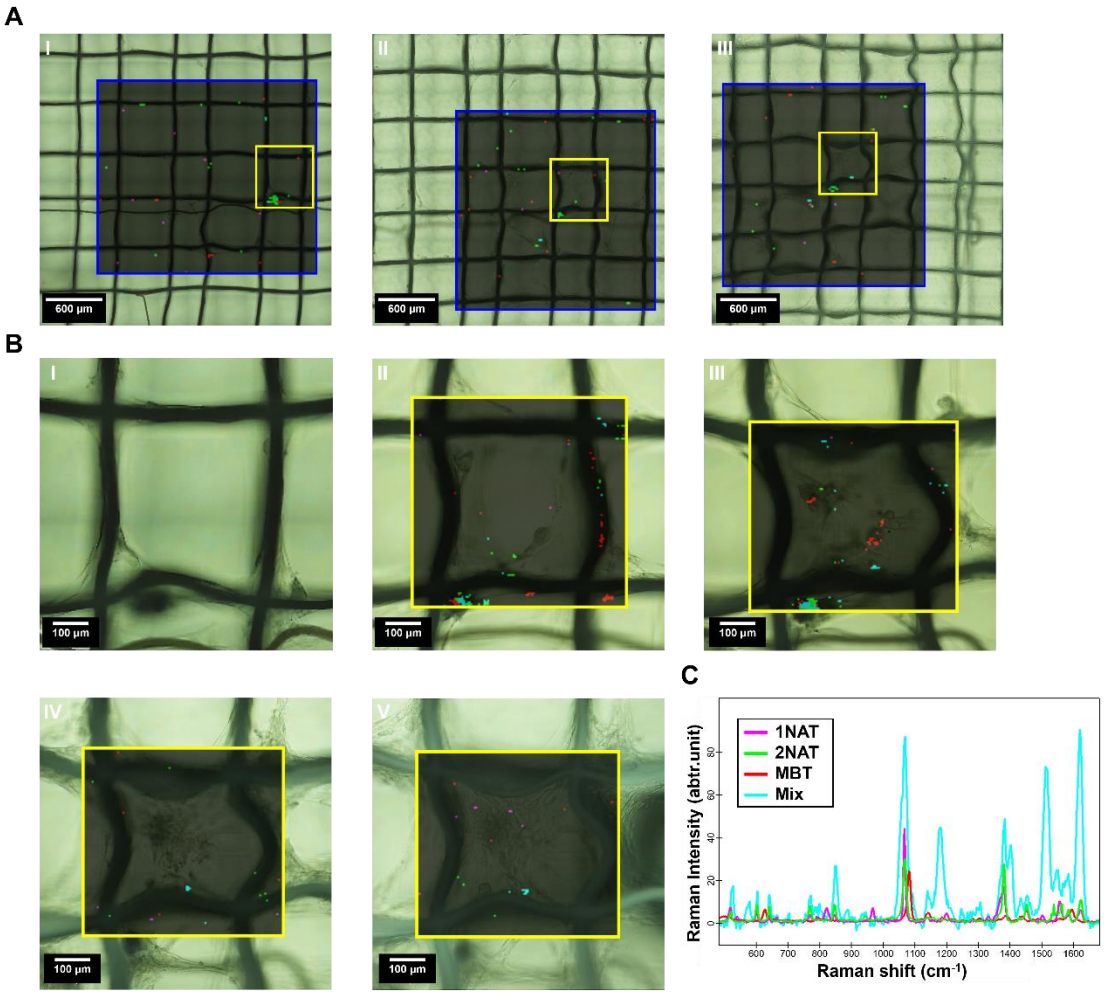

Figure 4.6 A) *HDF cells growth, proliferation and migration on a tessellated scaffold, over a 2 weeks period. The cells were labelled with AuNS-1NAT (magenta), AuNS-2NAT (green), and AuNS-MBT (red). The blue square overlaid on the brightfield image was scanned every 3-5 days: (I) 1 DIV, (II) 6 DIV, (III) 10 DIV. The mappings were analysed with the TCA tool, which correctly identifying each of the three SERS tags, plus a component in which all three tags were observed in the same voxel (depicted in cyan). SERS imaging was conducted with 0.05 s integration time, 10 mW laser power and a 100 × 100* µm^2 step size (XY). *The yellow boxes correspond to the same area displayed in* ***B)*** *and observed over time: (I) 1 DIV, (II) 6 DIV, (III) 10 DIV, (IV) 14 DIV and (V) 20 DIV. The brightfield images were laid over the SERS maps.* ***C)*** *Average SERS spectra for the SERS tags, and the mixed component achieved with the TCA tool. SERS imaging was conducted with 0.05 s integration time, 10 mW laser power and a 5 × 5* µm^2 step size (XY).

A 3D SERS measurement was then performed by confocal Raman microscopy, to obtain information about the 3D cellular distribution, initially observed by fluorescence microscopy, within a thickness of 100 µm (***Figure 4.7***). One can clearly observe the homogeneous presence of several HDF cells, labelled with the different SERS tags, throughout the whole field of view. Although it was necessary to measure during 12 hours to obtain such an image (600 × 600 × 100 µm^3 in XYZ) with a fine step size of 5 µm in all directions, SERS maintains

several advantages compared to fluorescence microscopy, such as the lack of photo-induced cytotoxicity and probe bleaching.

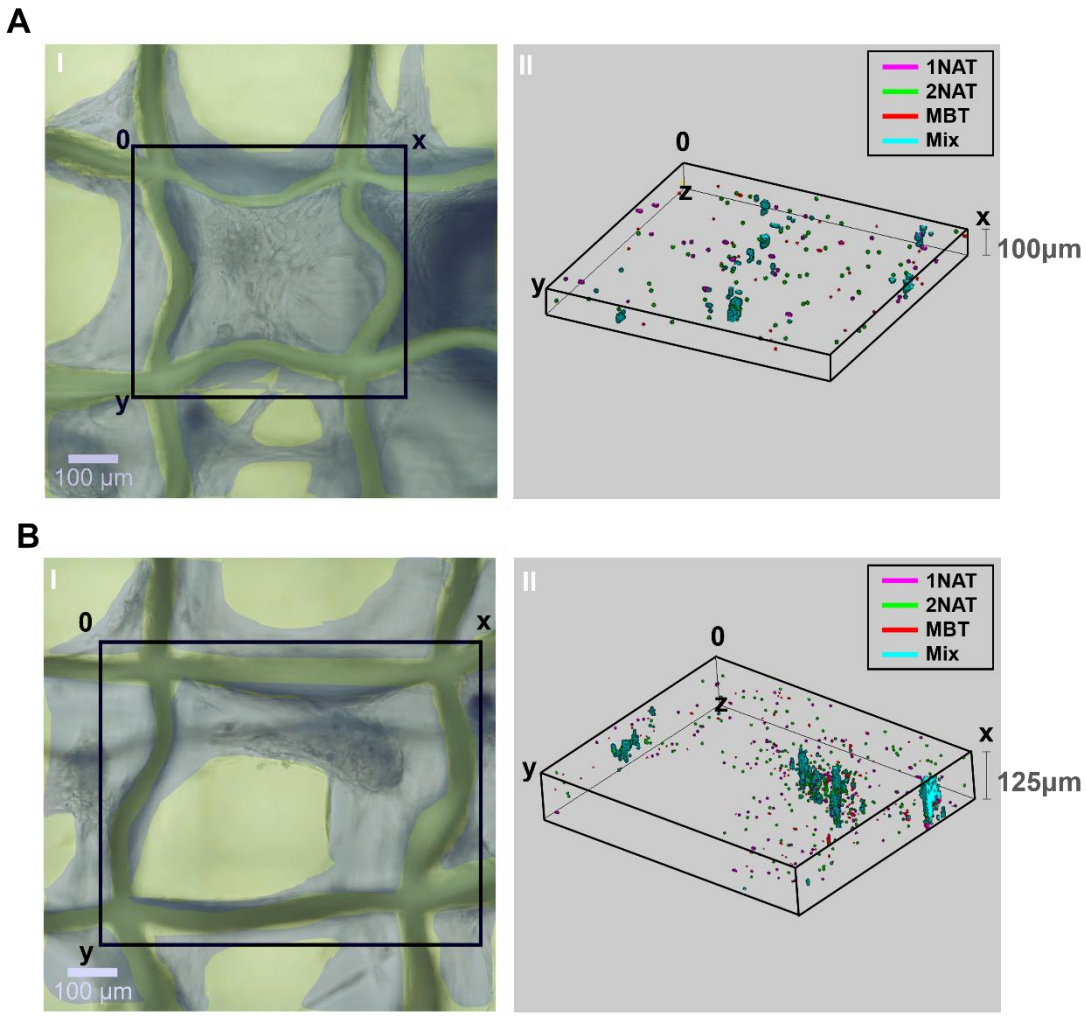

Figure 4.7 A, B) *3D SERS images of two different areas (black squares) inside the tessellated scaffold, analysed with TCA. SERS images were collected with 0.05 s integration time, 30 mW laser power, and a 5 × 5 × 5 µm^3 step size (XYZ). (I) Brightfield image of HDFs distribution after 25 DIV, with the cells highlighted in grey. II) 3D volume reconstruction of the SERS signals collected from the area indicated with a black square in (I).*

Aiming at highlighting these aspects, a bleaching experiment was conducted, where HDF cells labelled with SERS tags (2NAT) or AF488-labelled actin fluorophores were imaged using SERS and fluorescence microscopy, respectively. The tessellated scaffold was labelled with BPT for SERS or with a fluorescently labelled (blue) polymer for fluorescence microscopy. The fluorescence bleaching test was executed by imaging sequentially the same area (345 × 345 µm^2) for 60s seven times, using a resonant laser with the scaffold fluorophore (405nm laser), while the green fluorophore in the labelled cells remained unaffected, thereby providing an internal control to the experiment. On the other hand, the SERS bleaching test was conducted by imaging sequentially the same 2D area (250 × 250 µm^2) four times with 5

µm step size (XY), with a laser in resonance with both SERS tags labelling the scaffold and cells, for a total illumination time of 4h. Shown in ***Figure 4.8*** are the results for the **A)** SERS and **B)** fluorescence tests. Whereas SERS spectroscopy revealed no changes over time in either BPT (scaffold) or 2NAT (cells) signal intensity, a clear decrease was recorded in the fluorescence intensity of the blue channel (scaffold) in resonance with the excitation laser. These results confirm that, opposite to fluorescence microscopy, SERS can be used for repetitive measurements without causing any significant variations in signal intensity due to photo-induced chemical changes in the RaR molecules. Additionally, the BPT SERS signal hardly showed any fluctuations over time, indicating again a high signal stability, as required in long-term irradiation measurements.

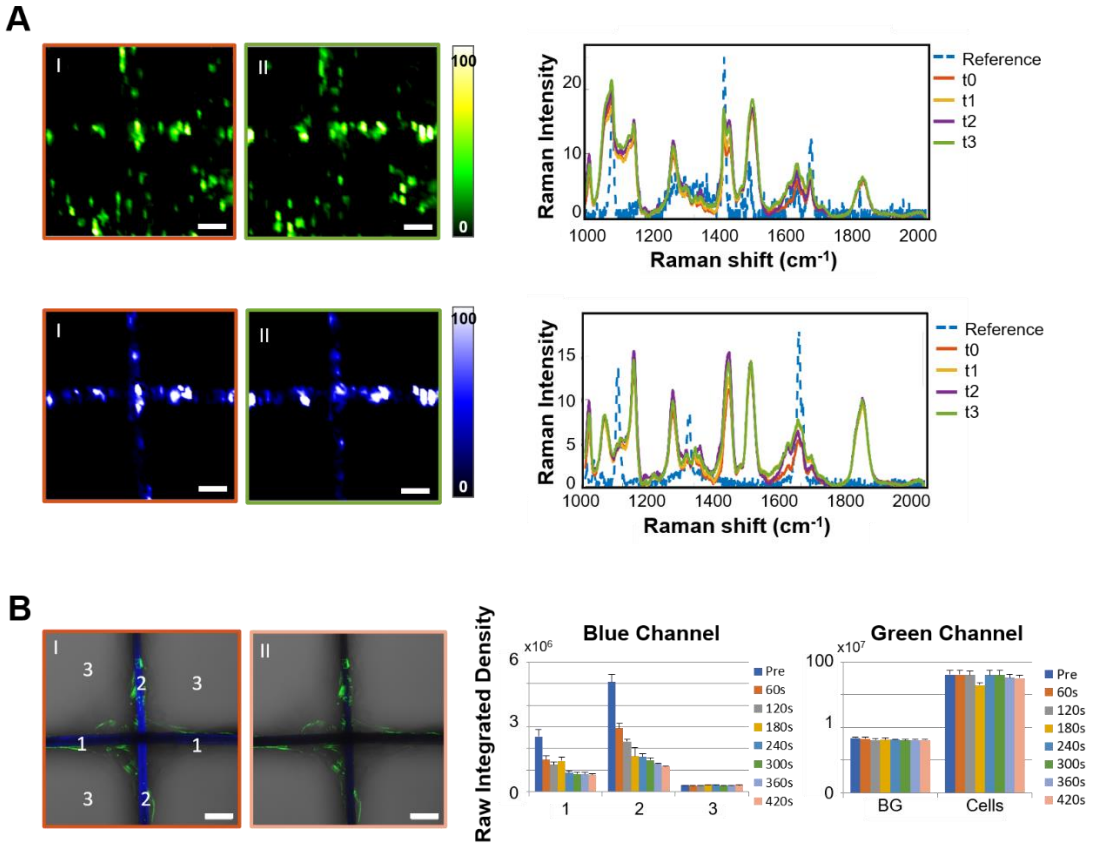

Figure 4.8 *Comparison of SERS and fluorescence stability upon sequential beaching.* ***A)*** *SERS bleaching test on HDFs cells labelled with AuNR-2NAT (green), grown inside a tessellated scaffold, correspondingly labelled with AuNS-BPT (blue). The figures show SERS maps reported at the I) first and last II) illuminations. The collected average spectra are displayed on the right panels.* ***B)*** *Fluorescence bleaching test on HDF cells labelled with green fluorescently labelled polymer (green) grown inside a tessellated scaffold labelled with blue fluorescently labelled polymer (blue). The figures show optical images overlaid with the blue and green channels, at the I) first and last II) illuminations. The evolution of fluorescence intensity in both fluorophores is shown in the histograms on the right panel. Scale bars = 50 µm.*

An additional sample was prepared, containing SERS tags with different NP morphologies, AuNRs and AuNSs, both displaying LSPRs in resonance with the Raman excitation wavelength (785nm) used for imaging. AuNRs were encoded with 2NAT, AuNSs with MBT RaR molecules (see ***Figure 4.9***). As a result, the 3D cell model was marked with three different SERS tags, namely AuNS-BPT in the scaffold, and AuNR-2NAT and AuNS-MBT in the cells. A SERS imaging study of the cellular growth inside the scaffold was then performed for 2 weeks.

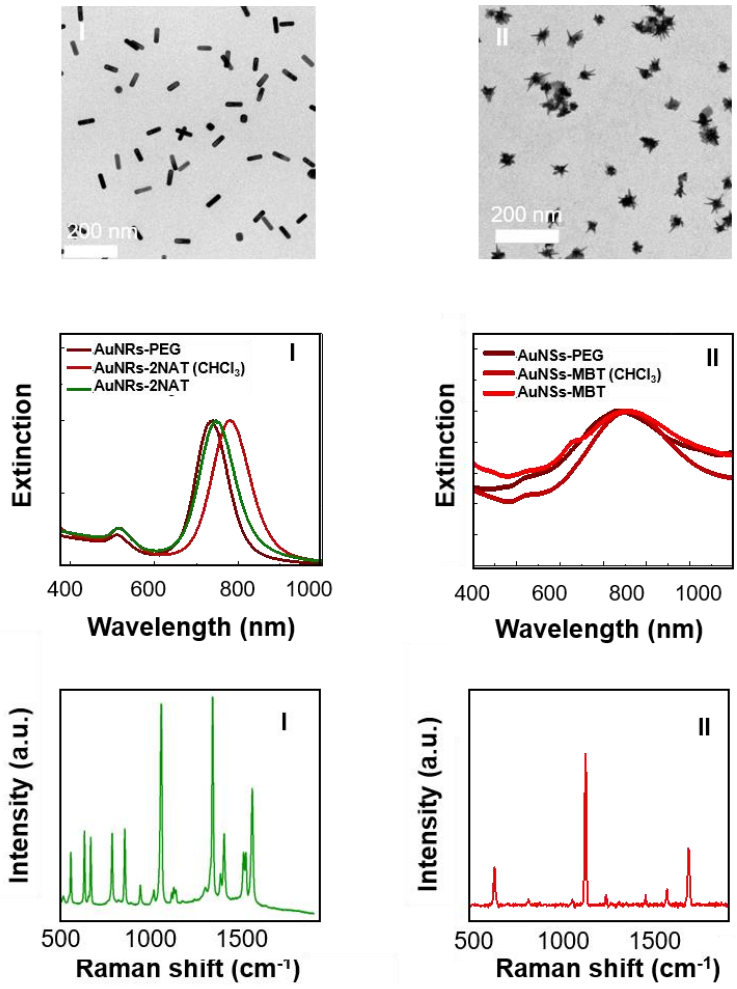

Figure 4.9 *TEM images, UV-Vis spectra and SERS spectra for I) AuNRs-2NAT and II) AuNSs-MBT.*

With this system, it was possible to follow the spreading and proliferation of SERS-labelled HDF cells inside the tessellated scaffold, using non-invasive and stable SERS signals, as shown in ***Figure 4.10***.

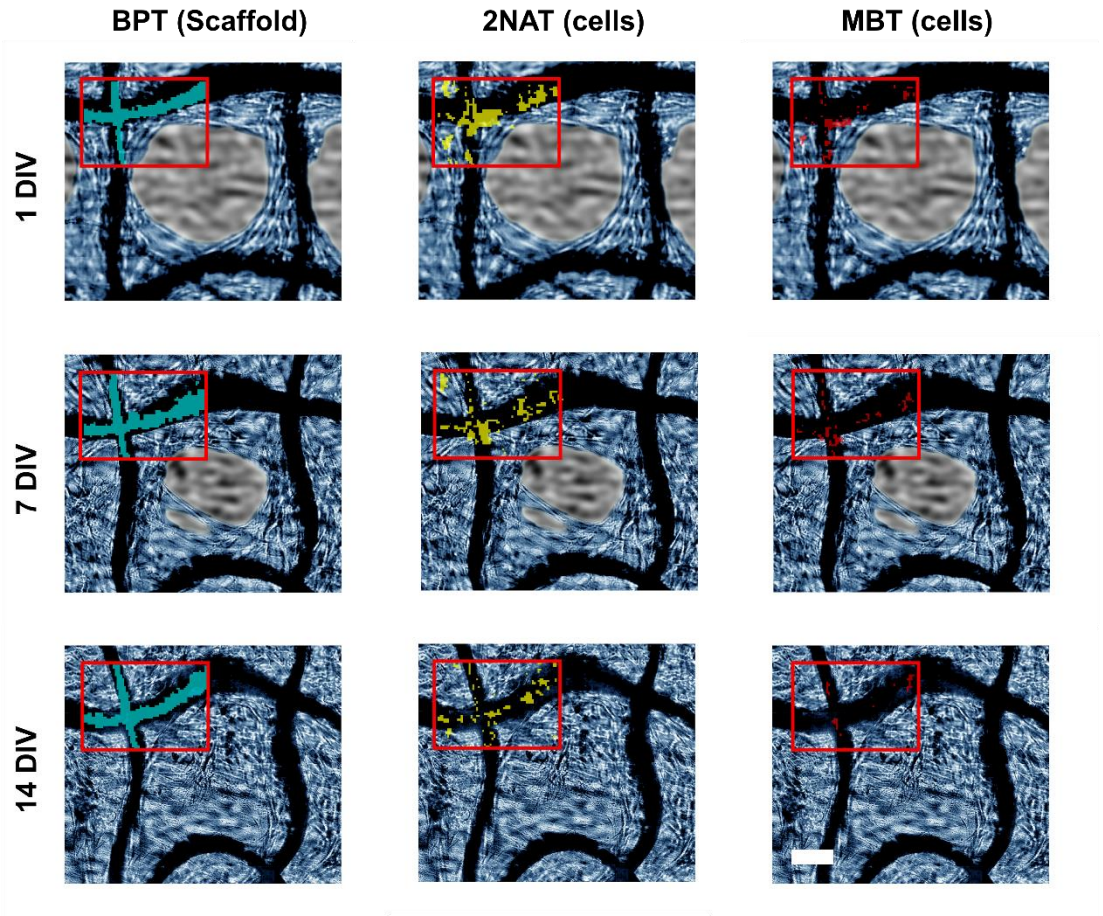

Figure 4.10 *SERS mapping of HDF cell growth over time in a hybrid scaffold. Imaging areas, indicated by red squares, were merged with optical images (HDF cells are false-coloured in blue). Coloured SERS maps represent the b values, presented in the previous* ***Chapter 3****, for the AuNS-4BPT (cyan), AuNR-2NAT (yellow), and AuNS-MBT (red). SERS imaging was conducted using 0.8 s integration time and 3.1 mW laser power, with a resolution of 5 × 5 µm^2 (XY). Scale bar: 100 µm.*

Also in this case, a 3D SERS image was performed, confirming the multiplexing capabilities of the technique in 3D measurements. Shown in ***Figure 4.12*** are the 3D reconstructions of the three different components separately, which confirmed that two different NP morphologies with two different Raman reporter molecules can indeed be used for cell imaging in 3D. Apart from the additional flexibility regarding the synthesis of SERS tags using NRs and NSs, the use of NPs with significantly different morphologies may additionally provide a method to undoubtedly distinguish them in TEM (see ***Figure 4.11***).

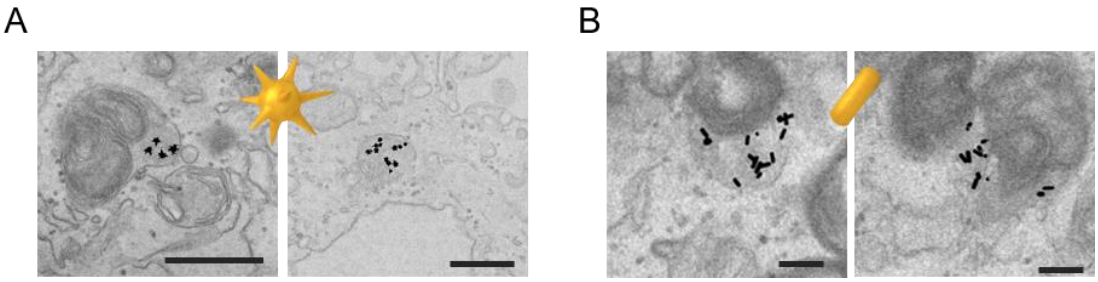

Figure 4.11 *Representative TEM images showing the uptake of (**A**) AuNS-MBT and (**B**) AuNR-2NAT into HDF cells. Scale bars = 500 nm.*

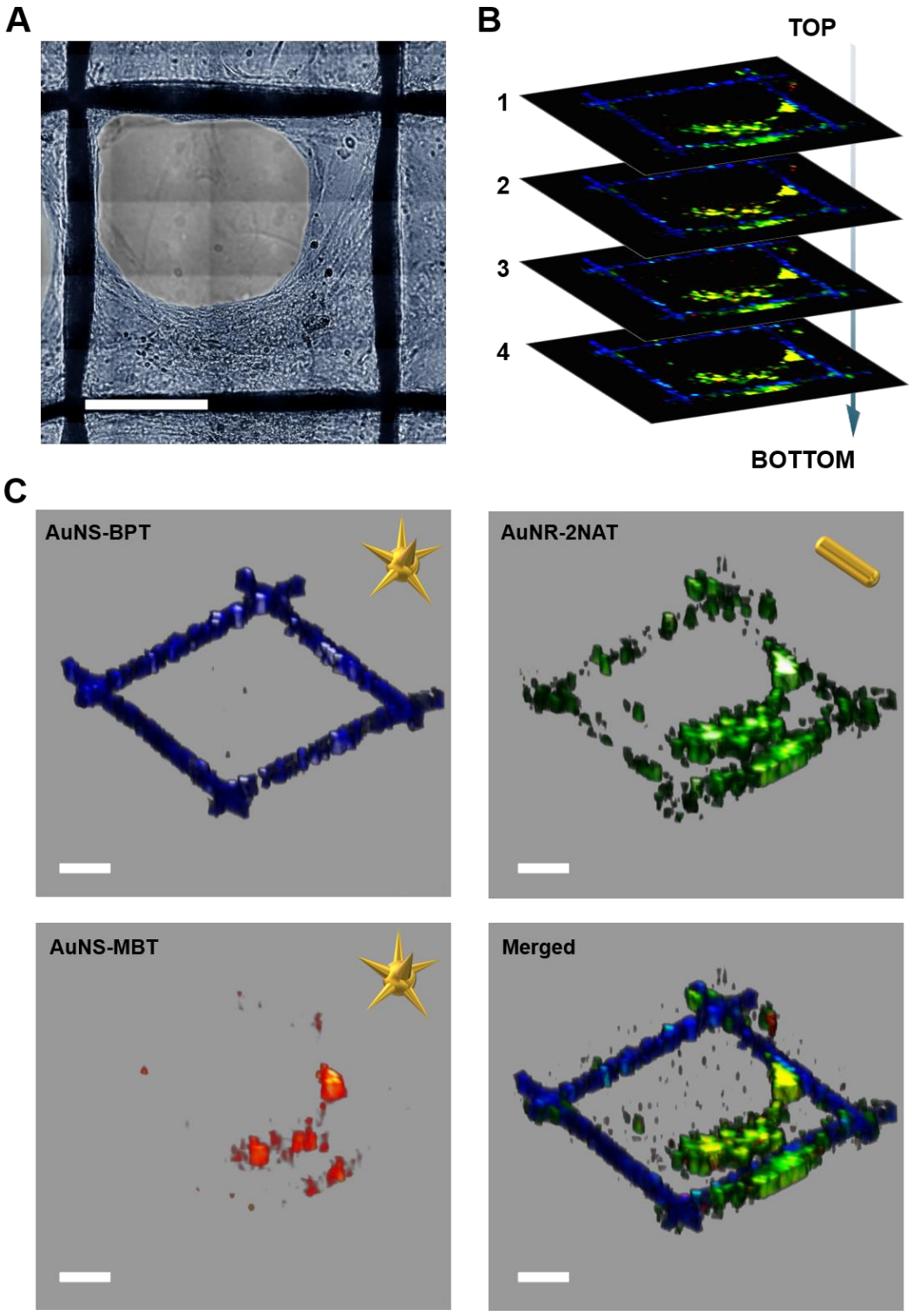

Figure 4.12 A) *Optical image of the area selected for full 3D SERS mapping.* ***B)*** *Four different layers from different z-stack measurements, on which pixels containing AuNS-BPT (blue), AuNR-2NAT (green) and AuNS-MBT (red) were highlighted. AuNS-BPT corresponds to signal from the scaffold, whereas AuNR-2NAT and AuNS-MBT corresponds to signal from HDF cells.* ***C)*** *Individual and merged 3D reconstructions of B). SERS measurement performed with 1s integration time, 29.55mW and step size of 8 × 8 × 20 µm^3. Scale bar = 200 µm.*

4.3 Hydrogel-based scaffold (sensing)

As mentioned in **Chapter 1**, another fundamental aspect to take into consideration when studying tumor cells is the production of cancer-related biomolecules. For this reason, it was important to realize an imaging system that allowed detailed monitoring of the behaviour of cells involved in the tumor model, as well as of their biomarkers production, over extended period of time.

In order to address these needs, a second type of 3D complex cellular model was prepared by using as support a 3D-printed scaffold made of a porous ink with bare AuNPs embedded in it. As briefly introduced in **Chapter 1**, SERS can be used as an ultrasensitive analytical tool for the label-free detection of a wide variety of molecules with high specificity and sensitivity. Hence, the presence of plasmonic NPs within a permeable structure is expected to allow the detection of analytes when they reach the close proximity to the plasmonic NPs surface. In this manner, the supporting structure can be also used as an *in situ* monitoring platform of the 3D culture. The scaffold was realized by Dr. Clara Garcia Astrain at the Bionanoplasmonics Laboratory, using a hydrogel-based ink, which properties were extensively presented in the introduction of this thesis, **Chapter 1**. Importantly, the high water content and porous network of the scaffolds make them resemble natural tissues, thereby favouring nutrient and oxygen transport within the gel. Also, their rich structural chemistry opens the way to various synthetic strategies focused on creating adhesion sites to promote cell proliferation and tuneable degradation properties to promote tissue growth. There are several works which reported the incorporation of NPs inside hydrogel sensors, including the use of hydrogel-based inks for 3D printing.[18,19] In our case, a composite ink containing AuNPs was used to fabricate scaffolds via DIW-3D printing, focusing on the study of both the ink formulation and the detection parameters of the scaffolds. We first carried out a 3D characterization of the detection of model Raman molecules, to evaluate the performance of the scaffolds as a monitoring platform for target biomolecules produced by cancer cells during tumour growth or metastasis, within 3D cellular models.

4.3.1 Components and characterization

3D printed scaffold

AuNPs were incorporated within a mixture of biopolymers that are commonly used in 3D printing, including alginate, methacrylated hyaluronic acid (HAMA) and κ-carrageenan. The advantages gained by using these materials included the rapid gelation of alginate upon $CaCl_2$ cross-linking, the strong elasticity of κ-carrageenan, the rapid photo-crosslinking of HAMA, and the ability of hyaluronic acid to regulate various cellular behaviours. AuNRs and AuNSs were synthetized to display LSPRs closely matching the 785 nm wavelength of the excitation laser, commonly used to work in the NIR transparency window (***Figure 4.13A***). The NPs were stabilized by two different surfactants to test the sensing properties, namely CTAB and thiolated PEG (PEG-SH), by slightly modifying previously described protocols.[20,21] Hence,

four ink formulations were obtained, including AuNRs-PEG, AuNRs-CTAB, AuNSs-PEG, AuNSs-CTAB. The scaffold was printed into a square-shaped design with 800 μm spacing between neighbouring fibres, and an initial height of 300 μm and 8 layers, ***Figure 4.13B,C***. [22]

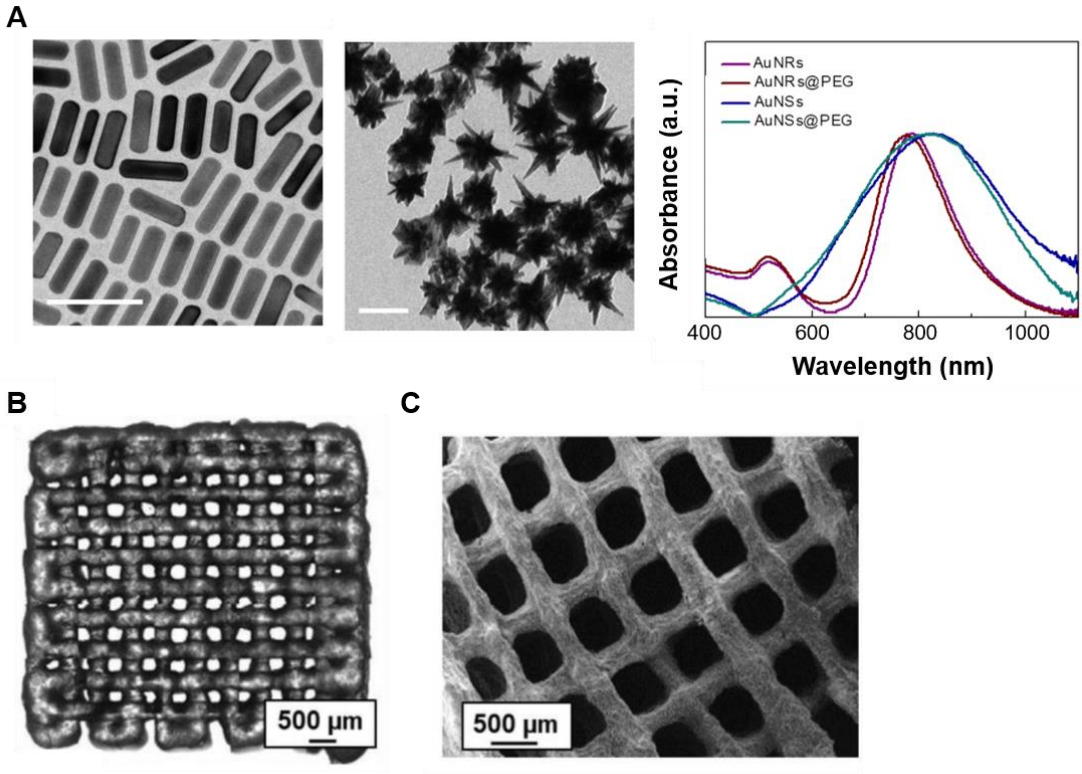

Figure 4.13 A) *TEM images and UV-Vis spectra of AuNRs and AuNSs employed as plasmonic enhancers inside the 3D-printed scaffold. Scale bars =100 nm.* ***B)*** *Epifluorescence microscopy image of a hydrated 3D-printed scaffold.* ***C)*** *SEM image of a freeze-dried scaffold.*

4.3.2 SERS sensing of metabolites

MBA, a Raman-active thiolated molecule that can readily adsorb onto gold NP surface, was used as model analyte to evaluate the SERS sensing efficiency of the plasmonic scaffolds. The scaffolds were tested by immersing them for 30 minutes in an MBA solution and subsequently imaging by SERS microscopy. 2D maps were taken over areas of ca. 2000 × 2000 μm^2 with a step size of 100 μm, confirming a homogeneous distribution of MBA signal throughout the whole scaffold, as well as a higher signal in the presence of a higher concentration of NPs in the ink formulation (***Figure 4.14A***). The scaffold with the best performance, namely 1mM AuNRs concentration, was incubated with decreasing concentrations of MBA to determine the limit of detection (***Figure 4.14B***). This model analyte could be detected at concentrations down to 100 nM, which lies within the range typically observed in biological and tumour environments.[23] By comparing the average signal collected from 2D SERS maps of the scaffolds prepared with the four different formulations at a fixed AuNP concentration of 1 mM, we concluded that AuNRs provided a better

performance with respect to AuNSs, and also that functionalization with PEG strongly hindered access of the analyte to the AuNP surface (***Figure 4.14C***).

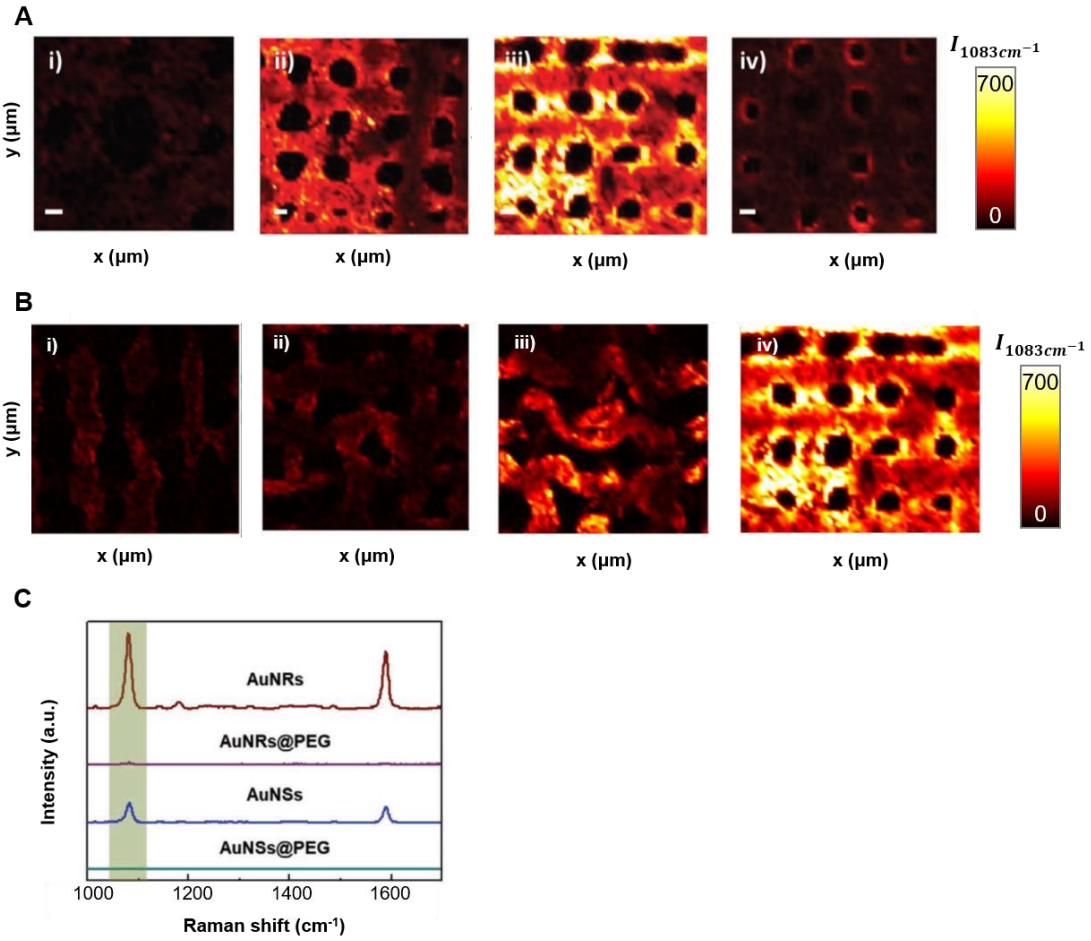

Figure 4.14 *SERS intensity images at one of the main peaks of MBA, 1083 cm^{-1}.*[24] ***A)*** *SERS maps of the scaffold realized from ink formulations with increasing AuNRs concentration: i) 0.1 mM, ii) 0.5 mM, iii) 1 mM, and iv) 1.5 mM. The highest concentration was found to hinder the SERS signal intensity, presumably due to the corresponding decrease in transparency of the scaffold. Scale bars = 200 µm.* ***B)*** *SERS maps of the scaffold containing 1 mM AuNR concentration, incubated in different concentrations of MBA: i) 100 nM, ii) 1 µM, iii) 100 µM, and iv) 1 mM.* ***C)*** *Average SERS spectra for maps collected from scaffolds containing 1 mM AuNRs and AuNSs, with different surface functionalizations. Highlighted in green is the 1083 cm^{-1} peak, major fingerprint of the MBA molecule.*

The sensing performance was also assessed along the (Z) direction, to explore the scaffolds sensing capacity for their application in 3D cell culture models. Hence, 3D SERS maps were performed by collecting the signal from 2D maps in the (XY) plane at different depths, with separation distances of 200 µm in (Z). Although a reduction in the SERS signal was observed for deeper maps, a significant SERS signal was still recorded from a plane situated at a depth of 1400 µm from the top of the scaffold (***Figure 4.15A***). Other in depth measurements were performed, in the (XZ) plane, in an area of ca. 2000 µm^2, with and without vertical holes, to evaluate the signal profile along the (Z) direction (***Figure 4.15B,C***). In a similar manner to the

SERS maps on the (XY) plane, the signal of MBA on the (XZ) plane reproduced well the features of the scaffold, showing the locations of the vertical holes with long vertical black areas (no signal) and of the fibre with a horizontal white line along the scaffold (highest signal). Shown in ***Figure 4.15D*** is a depth map in the (XZ) plane with a smaller step size in (Z) than before, namely 50 µm, to identify with more precision the deepest signal detectable, which was found to be at 1500 µm from the surface of the scaffold.

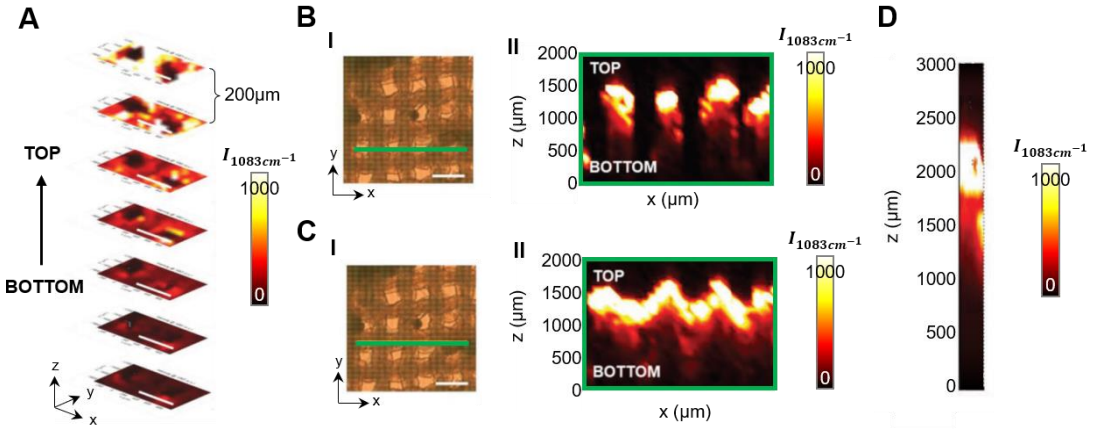

Figure 4.15 *SERS map of a scaffold containing 1mM AuNRs, incubated with 1 mM MBA.* ***A)*** *2D (XY) maps performed at different Z heights, with 200 µm of separation distance in (Z) between each other.* ***B,C)*** *Optical images* ***(I)*** *with evidenced in green the (XZ) maps of 1000 × 2000 µm^2* ***(II)****, following respectively a hole/printed line and a continuous printed pattern.* ***D)*** *(XZ) map of 400 × 3000 µm^2 collected each 50µm in Z. Scale bars =500 µm.*

After demonstration of the uniform and sensitive detection of a model analyte, adenosine was selected as a biologically relevant analyte, as it has been reported to play an important role in the development of primary tumours and metastasis, therefore being used as a cancer biomarker.[25,26] The detection of adenine required a longer incubation time, likely due to the lack of a functional group with high affinity for the gold surface, such as the thiol group in MBA.[27] We also propose that the diffusion within the scaffold is slower because of the higher molecular weight of adenosine, compared to MBA. Shown in ***Figure 4.16A*** are SERS spectra from the evaluation of three different adenosine concentrations. Similar average SERS intensities were determined after 12h of incubation, with a higher signal from the 1 mM adenosine concentration. Finally, the influence of cell media on the collected SERS signal was addressed, aiming to apply the scaffold for *in situ* SERS sensing of metabolites produced from 3D cancer cell models. As expected, the SERS signal of both MBA and adenosine was reduced in cell media, in which the presence of proteins likely hindered the contact of the analyte with the gold surface (***Figure 4.16B,C***). Notwithstanding, the scaffold detected a SERS signal sufficiently high to allow detection of the analyte under realistic conditions.

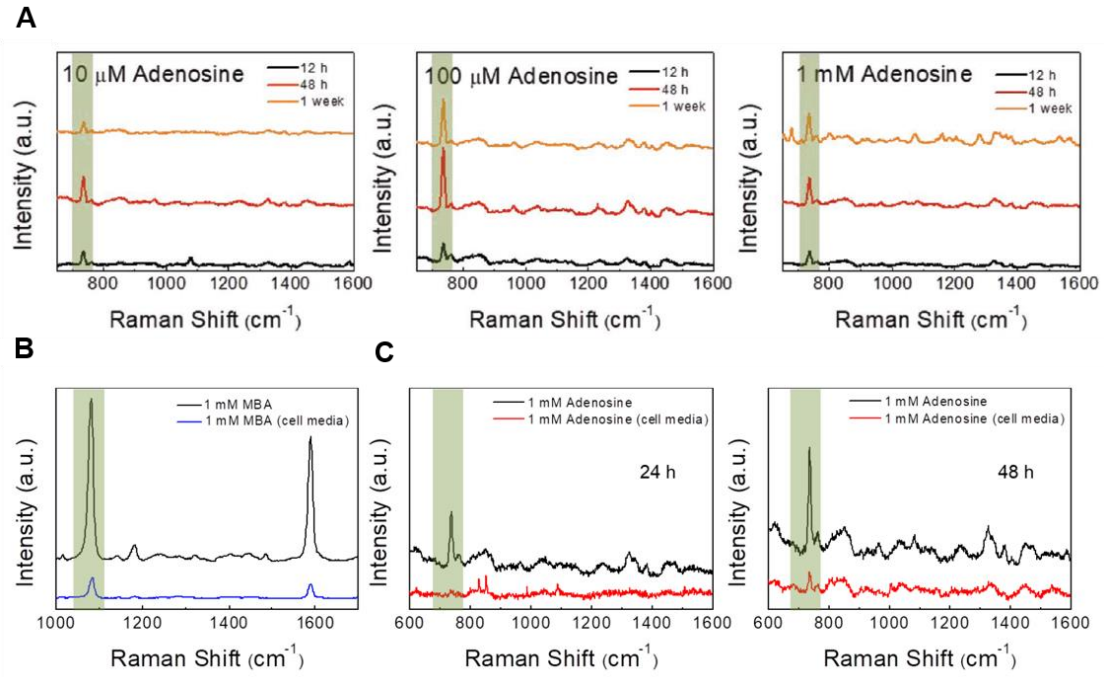

Figure 4.16 *Average SERS spectra from (XY) SERS maps of scaffolds containing 1 mM AuNRs.* ***A)*** *Scaffolds incubated in solutions containing increasing concentrations of adenosine.* ***B)*** *Scaffolds incubated in 1 mM MBA and* ***C)*** *1 mM adenosine at different times, both in aqueous solution and in cell media.*

4.4 Hydrogel-based scaffold (imaging and sensing)

Once SERS bioimaging parameters have been stablished for cells (**Chapter 3**) and scaffolds (**Section 4.2**), and the sensing conditions to detect cancer-related biomolecules have been adjusted (**Section 4.3**), a complex realistic system made of a 3D-printed hydrogel-based scaffold and embedded cells was produced to combine both techniques. The structure of this model differs from the scaffold presented in **Section 4.3,** mainly in the printing resolution in (Z) direction, which was largely improved by slightly changing the formulation and gaining a more realistic 3D cellular model.

Based on these conditions, the 3D cellular model was made of a 3D-printed hydrogel-based scaffold, incorporating both SERS-encoded and free AuNPs. In this manner, the scaffold acted as support for the 3D growth of a MCF7 cellular line, thereby behaving as both a reference for SERS imaging and a sensing platform. Several works reported the capacity of MCF7 cells to form aggregates and 3D structures, with and without 3D supports.[13,28,29] Herein, their nature was employed to grow tissue-like structures over the hydrogel-based scaffold, to obtain a 3D cellular model that can be imaged and chemically monitored with SERS. Thus, MCF7 cells were labelled with a SERS tag that was different to that used to encode the scaffold. In this manner, we intended to study the growth and expansion of the cellular population.

4.4.1 Components

3D-printed scaffold

Hydrogel-based scaffolds were fabricated by Dr. Clara Garcia Astrain, printing a mixture of polymers, biopolymers and NPs, namely PEGDA, κ-carrageenan and silica, by means of DIW, slightly changing a previously reported protocol (details in the **Experimental Section**).[22] Additionally, AuNSs and AuNRs were synthesized with LSPR maxima located around 800 nm, in resonance with the 785 nm excitation laser wavelength (***Figure 4.17A***). AuNSs were encoded with BPT as RaR (AuNSs-BPT), and then wrapped with PMA to obtain SERS-labelled NPs of 50 nm diameter, which were then used as the SERS reference in the scaffold. AuNRs were synthesized using CTAB as surface stabilizing surfactant, which is well-known to display cytotoxic properties, and was therefore extensively washed. Finally, both AuNPs were stabilized within the ink formulation. The printed scaffold presented a square-shaped design with an interlinear distance of 500 μm and 4 layers (***Figure 4.17B***).

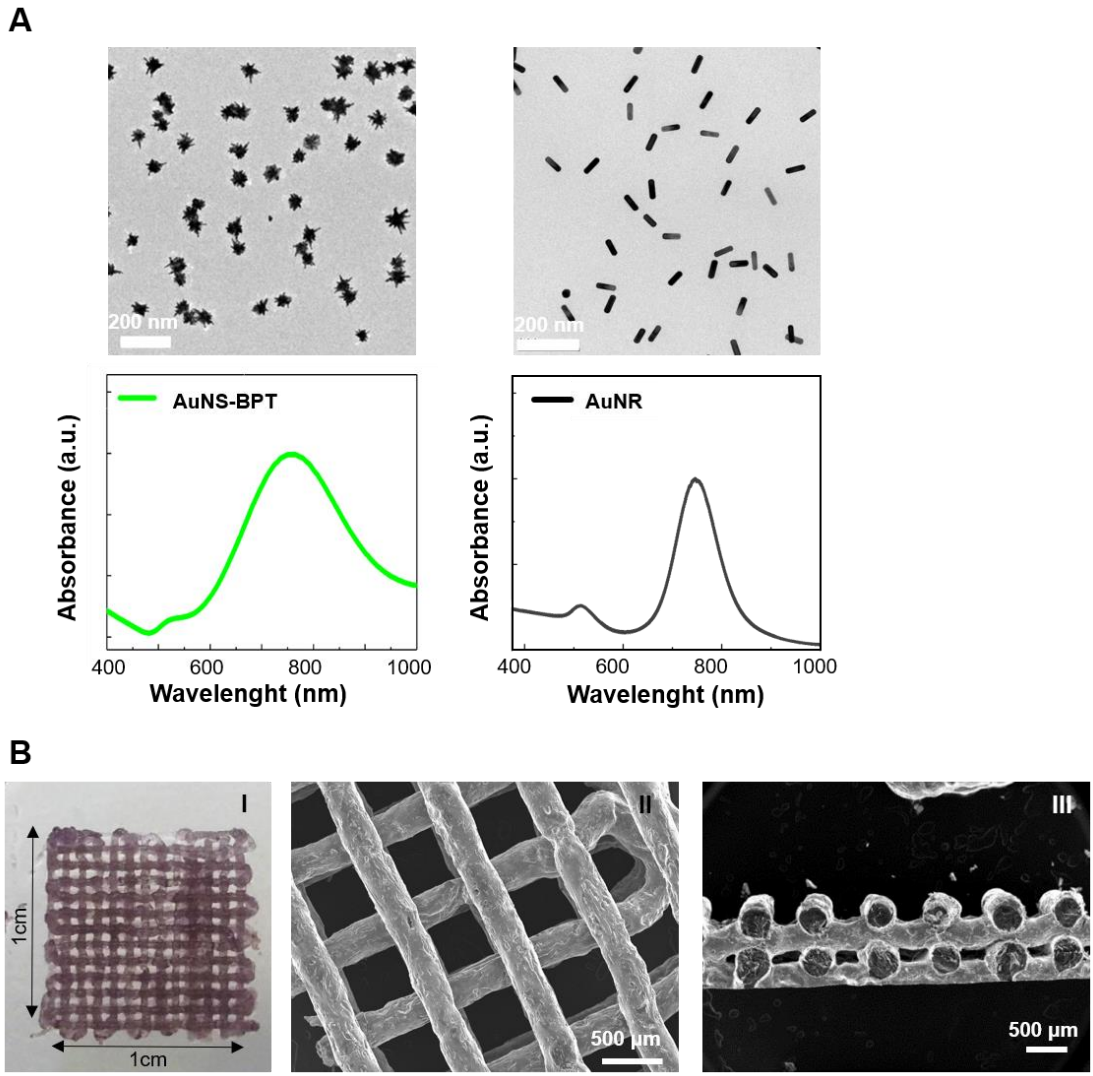

Figure 4.17 A) *TEM images and UV-Vis spectra of AuNSs-BPT-PMA (AuNS-BPT) used to label the scaffold for SERS and bare AuNRs used as plasmonic sensors inside the scaffold.* ***B) (I)*** *Optical and* ***(II-III)*** *SEM images of the hydrogel-based scaffold.*

In **Chapter 3** it was shown that MCF7 cells uptake positively-charged SERS tags, allowing the determination of the correct parameters to image them for long periods of time (*ca.* 2 weeks). Therefore, MCF7 were selected to realize a 3D cellular culture supported by the hydrogel-based scaffold. They were incubated with AuNRs that had been encoded with BT, covered with a PMA layer and functionalized with positively charged PA (AuNRs-BT), in order to obtain a clearly distinguishable fingerprint from the scaffold (***Figure 4.18***).

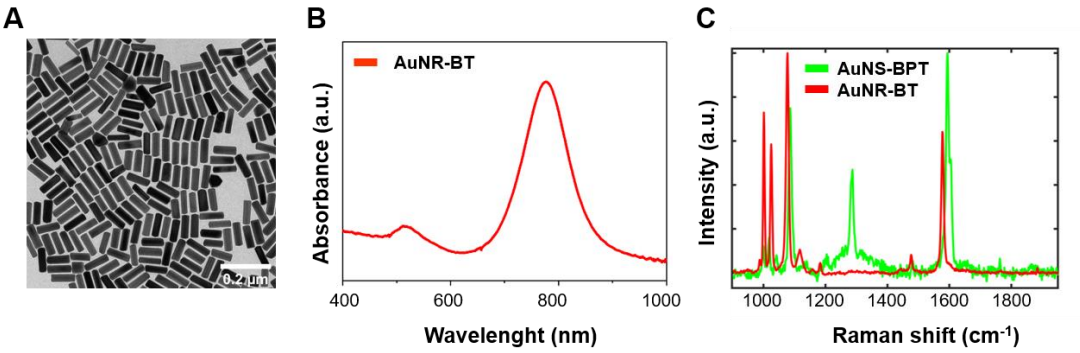

Figure 4.18 A) *TEM image and* ***B)*** *absorbance spectrum of AuNR-BT-PMA-PA (AuNR-BT) used to label MCF7 cells.* ***C)*** *SERS spectra of the SERS tags used to label the scaffold (green) and the cells (red).*

4.4.2 3D SERS measurements

The 3D cellular model was measured after 24 h of incubation at 37 °C and 5% of CO_2 (1 day in vitro, DIV) to check the SERS signal of both the scaffold and MCF7 cells, using the previously identified parameters, namely 10% power of the 785 nm laser and integration time of 0.8 s. We selected a step size of 60 µm in (XY) directions to quickly image the entire space formed between the fibres, where it was expected that the cells grow and expand. This area is indicated in ***Figure 4.19A*** within the rest of the scaffold. A depth measurement was first performed to identify the correct hight along the (Z) direction where the signal come from, see *(I-II)* in ***Figure 4.19B***. Hence, an area of ca. 700 × 700 µm^2 was imaged at 9 different planes (XY) with 100 µm of separation distance in (Z) between each other, in only 15 minutes. The recorded SERS maps were analysed by MLRA to identify the signal coming from the scaffold and the cells. Shown in *III* is the 3D volume reconstruction of the signals corresponding to the scaffold (AuNS-BPT, green) and the cells (AuNR-BT, red). The same area was imaged at 2 DIV, showing almost no variation in the signal of the scaffold but a substantial decrease of the signal corresponding to the cells (***Figure 4.19C***). This indicated a possible detachment of the cells from the scaffold with time.

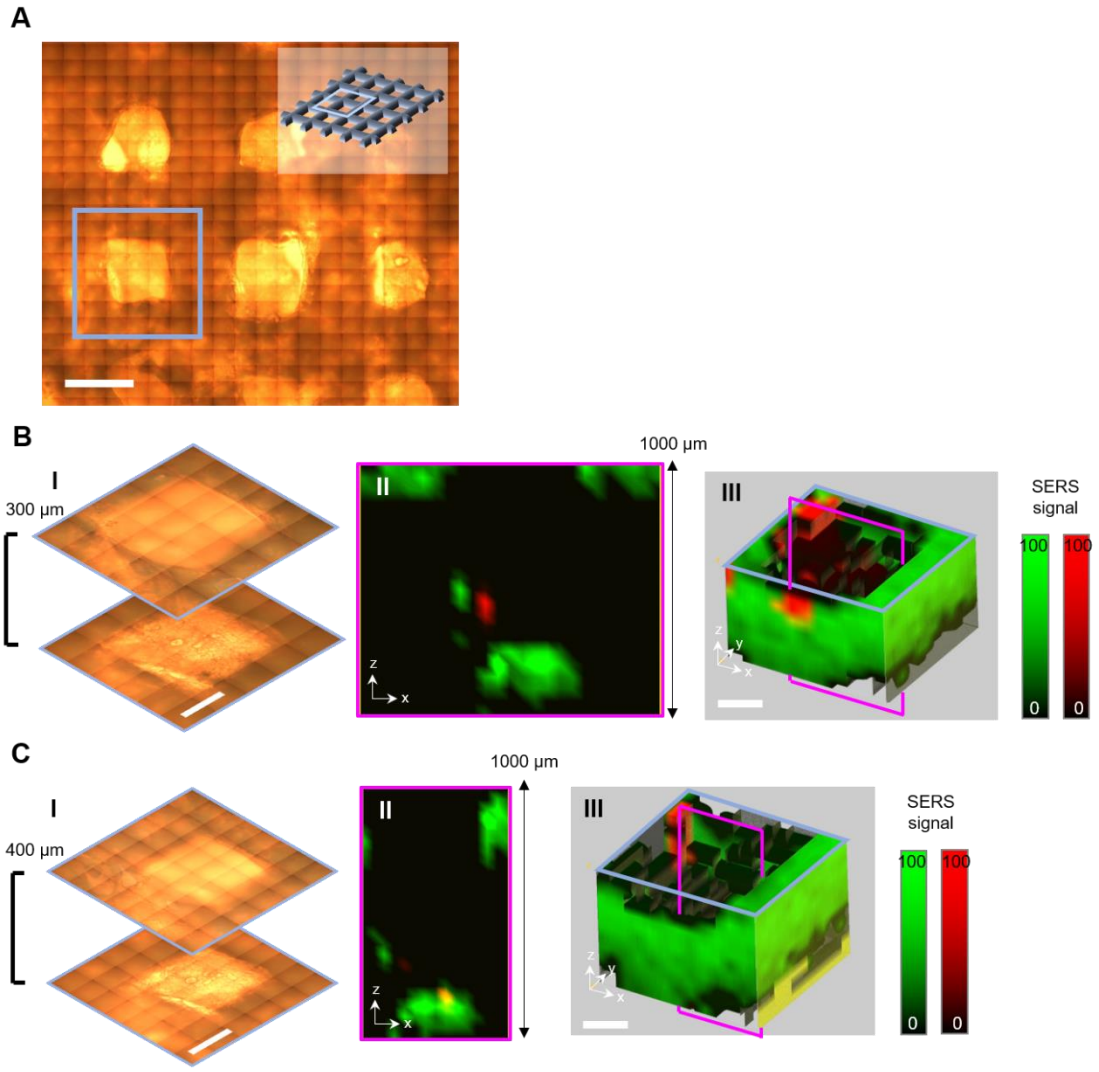

Figure 4.19 A) *Optical image of a hydrogel-based scaffold, indicating by a blue square the volumetric region imaged with 60 µm step size (XY) and 100 µm (Z). Scale bar =500 µm.* ***B)*** *SERS mapping after 1 DIV:* ***I)*** *Optical images of the area, scanned at the highest and lowest planes.* ***II)*** *Depth measurement for 1000 µm throughout the scaffold (green) and cells (red), with a 60 µm step size in (XZ).* ***III)*** *3D reconstruction of the SERS signals, collected from 9 different (XY) planes over (Z) with 100 µm step size.* ***C)*** *SERS measurement after 2 DIV:* ***I)*** *Optical images of the same area, scanned at the highest and lowest planes.* ***II)*** *Depth measurement for 1000 µm throughout the scaffold (green) and cells (red), with 60 µm step size in (XZ).* ***III)*** *3D reconstruction of the SERS signals, collected from 11 different (XY) planes over (Z) with 100 µm step size. Scale bars = 200 µm.*

A similar behaviour was observed in a second area of the same sample, which showed an important reduction of the signal correlated to the MCF7 cells, after 6 DIV (***Figure 4.20***).

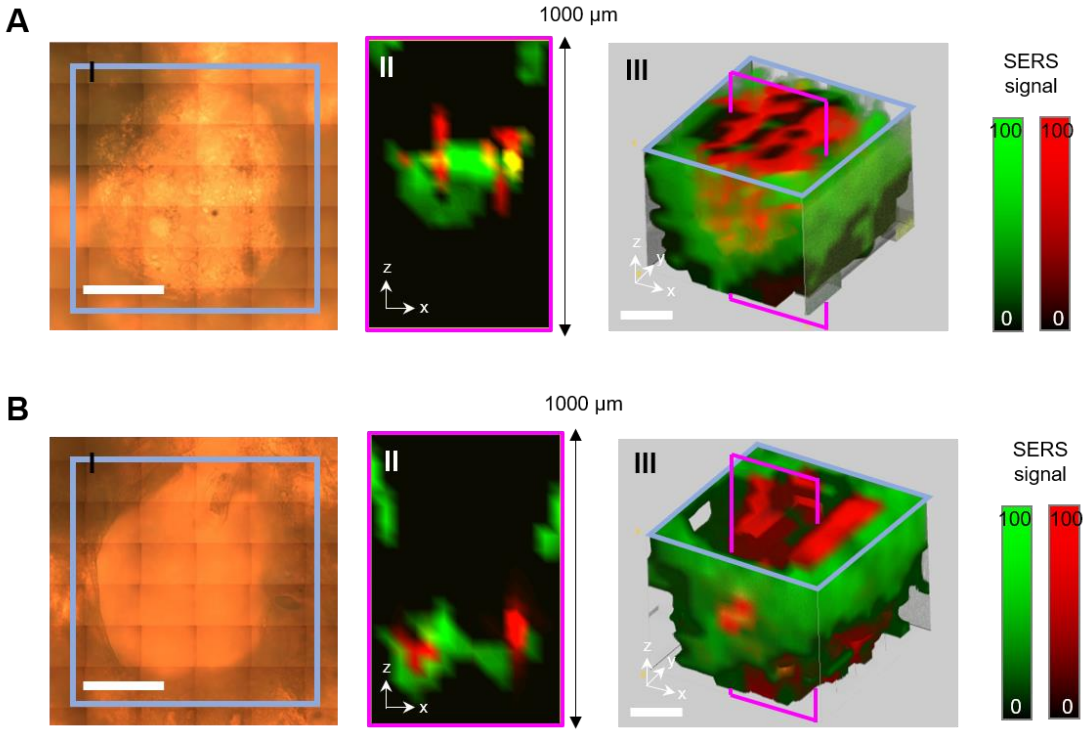

Figure 4.20 *SERS measurement of a second area, after* ***A)*** *2 DIV and* ***B)*** *6DIV:* ***I)*** *Optical images of the area scanned at the highest plane.* ***II)*** *Depth measurement for 1000 µm throughout the scaffold (green) and cells (red), with 60 µm step size in (XZ).* ***III)*** *3D reconstruction of the SERS signals, collected from 11 different (XY) planes over (Z) with 100 µm step size. Scale bars = 200 µm.*

Hence, the 3D cellular model was prepared by increasing the concentration of fibronectin by 10 times, namely 1mg/mL, aiming at improving cellular adhesion. Shown in ***Figure 4.21A*** are SERS measurements at 1DIV of a larger area than before, ca. 2000 × 2000 µm^2 in (XY) directions. As in the previous sample, the (XY) SERS maps were recorded at different heights and individuated throughout depth measurements for ca. 1000 µm, executed along the (XZ) and (YZ) directions with 60 × 100 µm^2 of step size (***Figure 4.21B***). When the SERS signal of the cells inside the scaffold was monitored over several days, it was observed a significant improvement of cellular adhesion. Nevertheless, the strong decrease of the SERS signal related to the cells after 16 DIV suggested a decrease in the cellular population, see ***Figure 4.21C, D***. Additionally, by observing the reduction of the signal during the first 9 DIV, it was not possible to establish whether cellular division was the only cause behind the intensity reduction of the SERS signal.

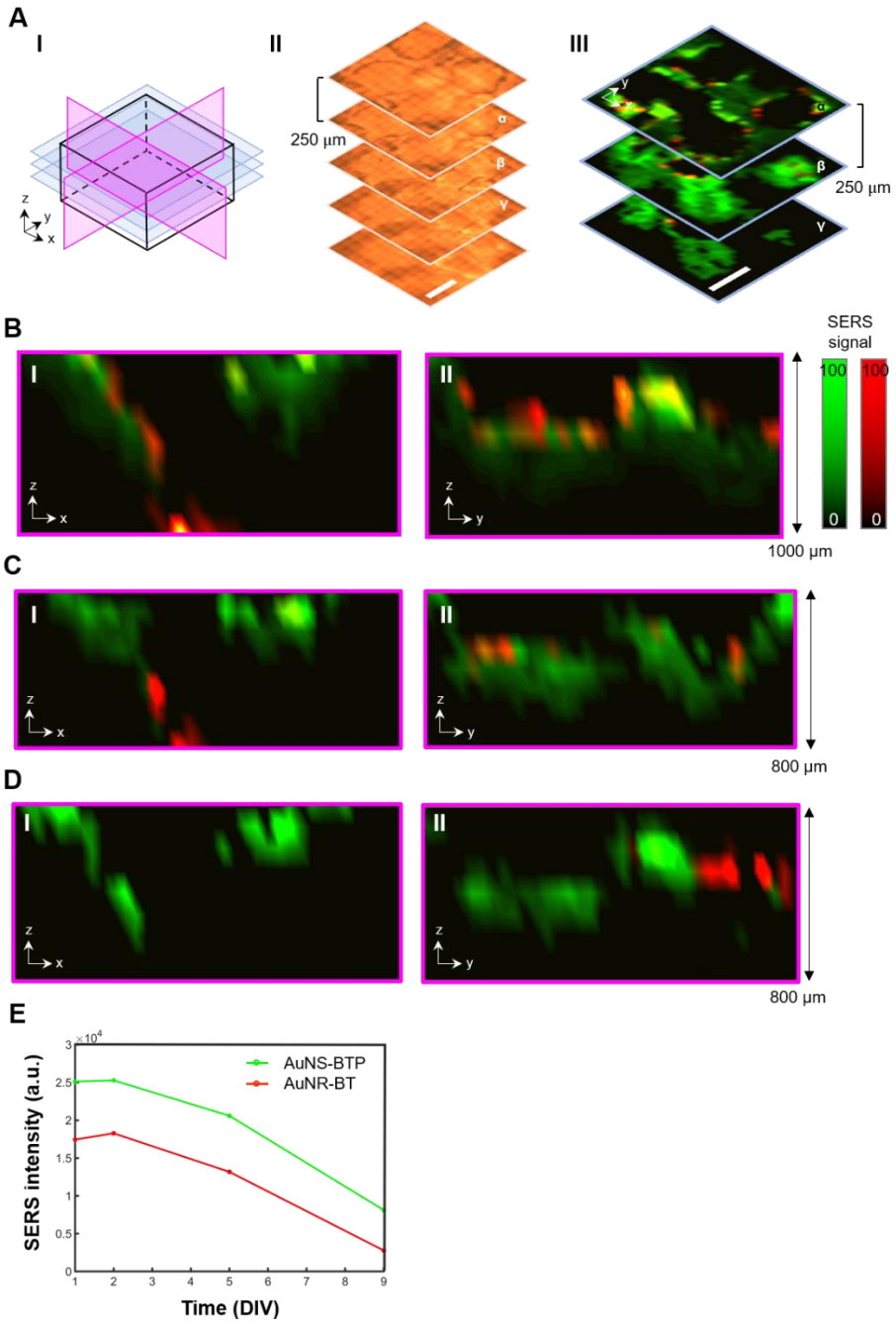

Figure 4.21 *Sample with a higher fibronectin content.* ***A)*** ***(I)*** *Scheme of the (XY) measurements (light blue) and depth measurements (magenta) performed in the scaffold.* ***(II)*** *Optical images taken each 250 µm along the (Z) direction.* ***(III)*** *(XY) SERS maps of ca. 2000 × 2000 µm^2 collected from the three central heights after 1DIV, with a step size of 60 × 60 µm^2. Reported in green and red are the signals of the scaffold (AuNS-BPT) and MCF7 cells (AuNR-BT), respectively. Scale bar = 500 µm. Depth SERS maps at* ***B)*** *1DIV,* ***C)*** *9DIV* ***D)*** *and 16DIV of ca. 1500 × 1000 µm^2 in the* ***(I)*** *(XZ) and* ***(II)*** *(YZ) planes after 1DIV. All data were analysed with MLRA.* ***E)*** *SERS intensities at the main peaks of each RaR (1592 cm^{-1}, green; 1577cm^{-1}, red) obtained as the sum of the collected spectra from the three layers indicated in A), over the first 9 DIV. The trend of this decreasing curve was not similar to the one observed in* ***Chapter 3*** *regarding the SERS signal dilution of the labelled MCF7 cells, suggesting that the reduction of the signal was not related only to cell division.*

To address this issue, a biocompatible gel was used in combination with the scaffold to realize an improved 3D cell culture. Previously labelled MCF7 and HDF cells were thus incorporated inside Matrigel©, which was then used to cover the whole hydrogel-based scaffold. In this manner, the plasmonic structure still acted as a reference for SERS imaging and detector for biomolecular sensing. Additionally, the properties of this gel-based cellular model were also exploited, such as the capacity of stimulating cell adhesion, proliferation and invading behaviour, as well as cell differentiation, tissue organization and tissue growth.[30–32] Hence, the hydrogel-based scaffold was labelled with AuNSs-2NAT-PMA and bare NRs. The cellular lines, MCF7 and HDF, were labelled respectively with AuNSs-MBT-PMA-PA and AuNSs-BPT-PMA-PA, and then incorporated inside Matrigel©, which was drop casted on top of the scaffold. Shown in ***Figure 4.22*** are 2D and 3D SERS images of both cellular lines inside the hydrogel-based scaffold. In addition, HDF and MCF7 cells were transfected respectively with GFP and Red Fluorescence Protein (RFP), so that fluorescence images of the same structure could also be acquired.

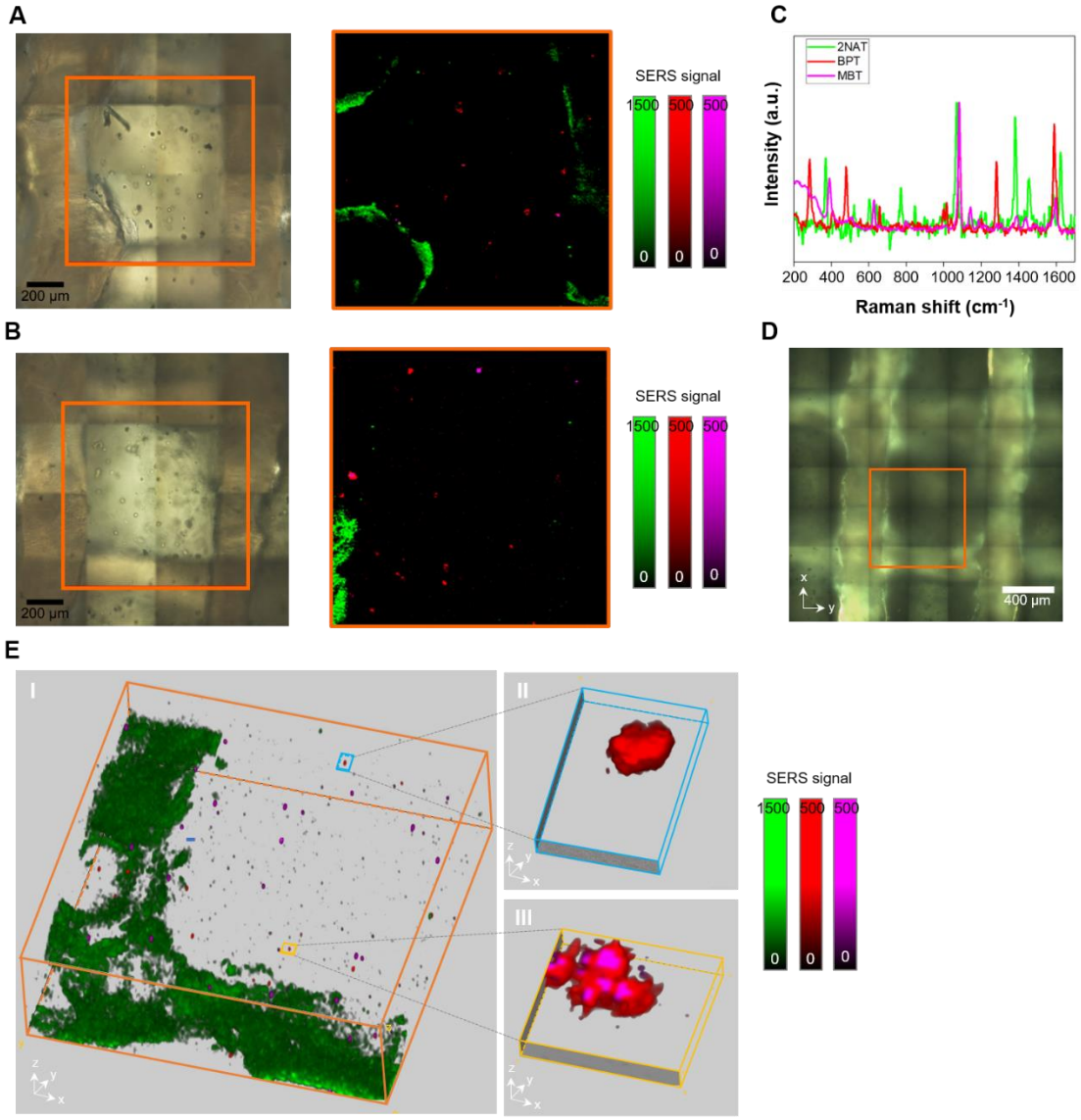

Figure 4.22 SERS images of a hydrogel-based scaffold, with MCF7 and HDF cells growth inside Matrigel©. A) *and* ***B)*** *Optical images and correlated 2D SERS maps of 1000 × 1000 μm^2 areas of the scaffold in the (XY) plane, with 5 μm step size in both directions. The signal of the hydrogel-based scaffold labelled with AuNS-2NAT, and the two types of cells, MCF7 labelled with AuNS-MBT-PMA-PA and HDFs labelled with AuNS-BPT-PMA-PA are reported respectively in green, red and magenta.* ***C)*** *The three components obtained with the TCA tool, show the typical peaks for each SERS tag, namely 1070 cm^{-1}, 1383 cm^{-1} and 1626 cm^{-1} for the 2NAT component; 1084 cm^{-1}, 1593 $cm^{-1}$and 1604 cm^{-1} for the BPT component; and 1082 cm^{-1} and 1597 cm^{-1} for the MBT component.*[33–35] ***D)*** *Optical image of the scaffold after 5 DIV, with highlighted in orange the volumetric region imaged in live conditions: 750 × 750 × 500 μm^3, with step sizes of 5 × 5 × 20 μm^3 in (XYZ) directions.* ***E)*** *3D volume reconstruction of the SERS map with highlighted volumetric regions* ***(I)*** *of a single HDF cell in light blue* ***(III)*** *and of two MCF7 and HDF cells in yellow* ***(IV)****.*

Reported in ***Figure 4.23*** are fluorescence images corresponding to the scaffold. It was not possible to image the same area due to the different measurement configurations of both

techniques, for example using the objective from the top in SERS and from the bottom in fluorescence, and the thickness of the sample. In spite of this issue, SERS and fluorescence images showed comparable features, such as the number of cells, or their displacement inside the Matrigel© matrix.

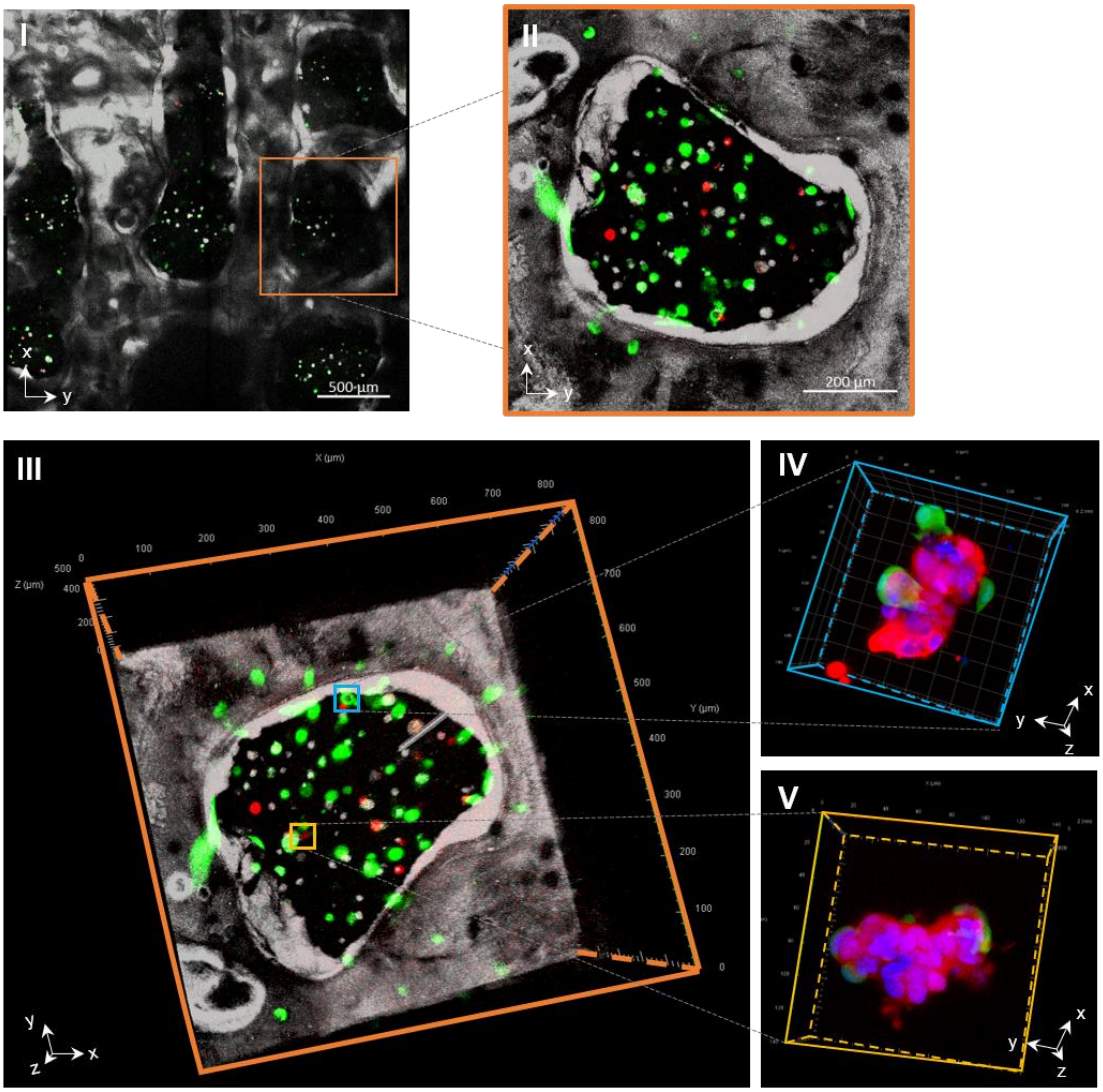

Figure 4.23 *Fluorescence images of a hydrogel-based scaffold, with MCF7 and HDF cells growth inside Matrigel©.* ***(I)*** *Overlap of the optical and fluorescence images of the scaffold after 4 DIV, with marked HDFs (green) and MCF7 (red) cells. Highlighted in orange is the* ***(II)*** *area of 850 × 850 × 400 µm^3 of the scaffold imaged along the (Z) direction. In* ***(III)*** *the 3D reconstruction of the image and two zoomed images of MCF7 and HDF cell aggregates* ***(IV-V)****, with the nuclei marked in blue.*

With the aim of testing the plasmonic properties of the hydrogel-based sensor, non-labelled scaffolds with only bare AuNRs were treated with fibronectin as previously described, to simplify the detection analysis. In ***Figure 4.24A*** are reported the SERS spectra obtained as the average from a SERS map collected from an area of 300 × 300 µm^2, measured with a step size of 20 µm in both directions, along the scaffold fibre. In order to identify metabolites produced from the MCF7 cancer cells, the corresponding non-tumorigenic epithelial breast cell line

(MCF10) was used as reference. Cellular media were collected from the flask cultures after 3 DIV and used to incubate the scaffold for 48 h under shaking to improve the permeation of molecules throughout the scaffold, down to the AuNRs and thus increase an eventual SERS signal. Some changes related to the peaks around 960 cm^{-1} and 1227 cm^{-1} Raman shifts were observed and confirmed by the results obtained with MCF7 cells after 5 DIV. Furthermore, to assess the detection capacity of the plasmonic platform in the presence of cells treated with an external agent, the Fulvestrant anticancer drug was employed. The latter is a commonly used antiestrogen, which induces proliferation arrest and apoptosis of estrogen-dependent breast cancer cells, such as MCF7 cells.[36] The drug was applied in a 70% ethanol solution and the obtained Raman spectrum was therefore screened by a strong ethanol signal, even if further diluted at 5 μM in cellular medium (***Figure 4.24B***). Indeed, the average spectrum collected from the scaffold fibers incubated with Fulvestrant solution at 5 μM in cellular medium, on an area of 300 × 300 μm^2 with a 20 μm step size, showed only a small peak at *879* cm^{-1} related to the ethanol fingerprint (***Figure 4.24C***). Finally, the cellular medium collected from a culture of 1×10^5 cells pre-incubated for 24h with Fulvestrant at 50 μM was tested. The cytotoxicity of the drug was also verified, causing a reduction of 20% in the viability of the MCF7 cells. Shown in ***Figure 4.24D*** are average spectra obtained from an area of 300 × 300 μm^2 with a 20 μm step size: two peaks which may be related to metabolites produced by dead cells due to the drug, appeared at 751 cm^{-1} and 1001 cm^{-1}. Although these results were preliminary and further investigations are needed to confirm the outcome and to identify the best measurement conditions, the plasmonic platforms did show a detection capacity required to monitor 3D cellular models.

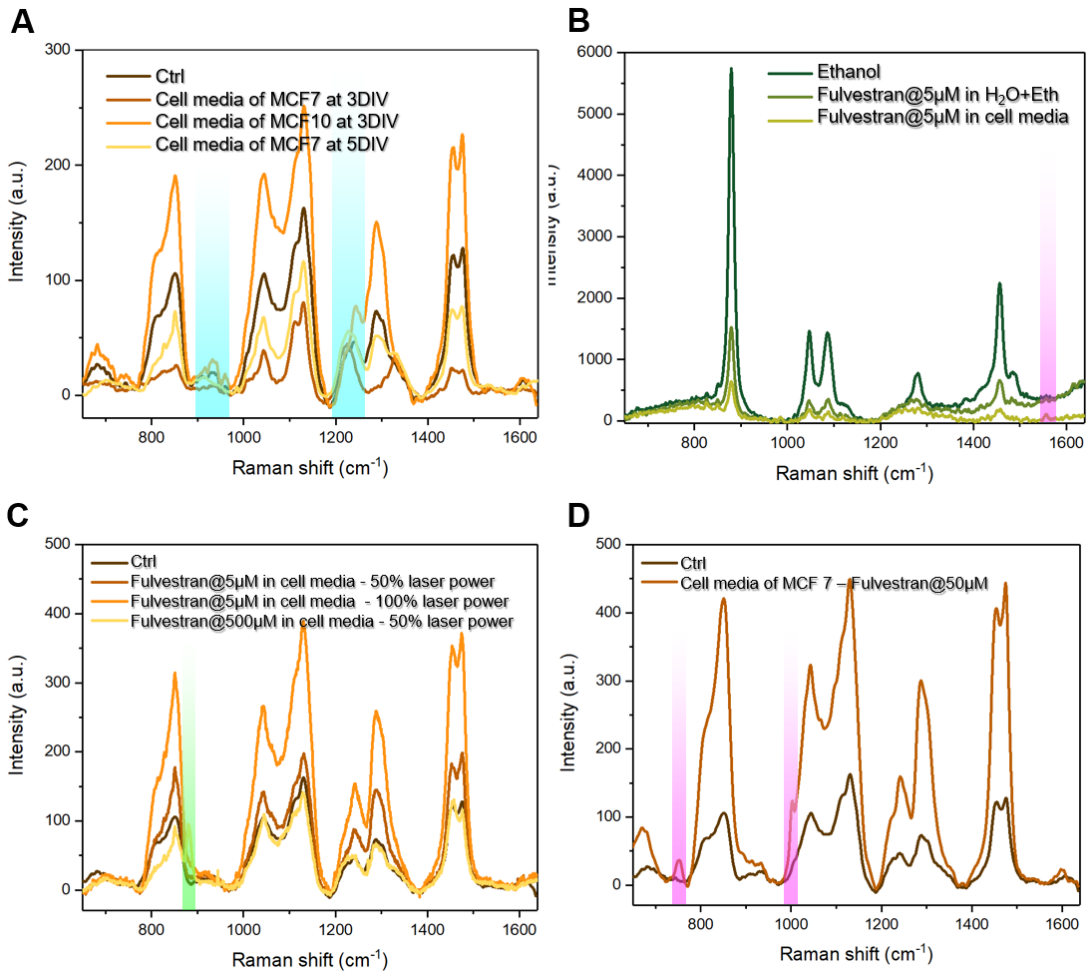

Figure 4.24 A) *SERS spectra of a hydrogel-based scaffold incubated for 48 h under shaking with the cellular media of MCF7 and MCF10 cells at different DIV. Highlighted in clear blue are two spectral areas around 960 cm^{-1} and 1227 cm^{-1} which presented small variations.* ***B)*** *SERS spectra of Fulvestrant drug diluted at 5 μM concentration in 70% ethanol solution and in cellular media, together with the pure ethanol scaffold as reference. A small peak of the Fulvestrant spectra (magenta) can be used to detect the presence of the drug inside the scaffold.* ***C)*** *SERS spectra of the scaffold incubated for 48h under shaking with Fulvestrant diluted in cellular media at 5 μM and 500 μM, under different measurement conditions. A peak corresponding to the main molecular vibration of ethanol at 879 cm^{-1} is shown in green.* ***D)*** *SERS spectra of the scaffold incubated for 48 h under shaking with the cellular media of 1 × 10^5 MCF7 cells, treated 24h with 50 μM Fulvestrant. Two peaks at 751 cm^{-1} and 1001 cm^{-1} (magenta) can be related to metabolites produced by dead cells.*

4.5 Conclusions

In **Section 4.2** it was shown the determination of appropriate imaging parameters to better characterize 3D cellular models in live conditions. The 3D cell model was built using the support of a 3D printed scaffold made of PLGA through jet printing technology and it was marked with two types of labels: SERS tags and fluorescently labelled polymers. The latter, currently used to characterize these kinds of samples, were chosen on one hand to have a

control over the information gained by SERS and on the other to eventually combine the information of both techniques as a means to study the system. The HDF cells were selected because of their capacity to form an interlaced 3D film whose growth can be supported by the tessellated scaffold. In this manner it was possible to study a real 3D sample, with a thickness of ca. 100μm and assessed the depth issue of measuring SERS through a living cellular layer. Mainly three parameters were addressed in measuring the live 3D cellular model: the laser power that should be used to obtain a sufficiently high intensity of the SERS signal without inducing photo-toxicity effects in the SERS tags; the step size that should be used in order to obtain detailed SERS images, where is possible to distinguish two cellular populations proliferating and migrating while representing a sufficiently large area to achieve a significant characterization of a millimetric sample; and finally, the study of the non-photobleaching quality of the SERS tags, particularly interesting for 3D cell models, where long 3D measurements are needed for monitoring the evolution of the sample. In detail, it was shown that for a thickness of 100μm of SERS-labelled HDFs with AuNS-1NAT, AuNS-2NAT, AuNS-MBT, it was possible to detect and clearly distinguish the three SERS signals through all the depth of the 3D cellular model using 30mW with an integration time of 0.05s in a confocal microscope. Whereas, lower laser powers were sufficient to image 2D planes of the SERS-labelled cells inside the cell model during the first days of growth or to perform 3D images of a simple 2D layer of cells. The step size chosen in the latter to clearly image the SERS tags inside the HDFs, catching more than one spot per cell, was $1 \times 1 \times 4$ μm^3 in (XYZ). A larger step size of 5 μm^3 was rather used to perform large but still detailed image of the 3D cellular model. In this way ca. 4 points were necessary to image each SERS-labelled cell and the monitoring of the evolution of two differently labelled populations of cells over large areas of the scaffold was possible, thereby obtaining a more realistic view of the true cell density within the scaffold. Hence, the proliferation and migration of HDFs cells inside the tessellated scaffold were reported over a period of ca. 3 weeks, proving also the stability of the SERS tags signal inside a living cellular environment. In addition, the non-photodegradation of the SERS labels was addressed in comparison with the typical fluorescence dyes performing several sequential measurements of the same area and proving the need of the SERS-based labels in long and repetitive 3D characterizations of 3D cell models.

After having characterized the multimodal imaging parameters of a PLGA scaffolds with HDFs cells grown in a fibronectin layer (in **Section 4.2**), we used a different support to designed a more realistic cellular model, namely 3D-printed hydrogel-based scaffold. In addition, the scaffolds were functionalized with bare AuNPs, aiming at exploiting them not only as SERS imaging reference, but also as plasmonic detector. In **Section 4.3)** the sensing properties of the scaffolds were characterized. In detail, SERS maps were first performed by immersion for 30 minutes with a Raman molecule model (MBA) to characterize the homogeneous absorption of the analyte by the scaffold and to evaluate the AuNPs type and concentration needed in order to obtain a sufficient SERS signal, identifying 1mM as the best

concentration. Afterwards, the latter configuration was used to estimate the limit of detection for the MBA molecule, which was 100nM in aqueous solution. Also, a characterization of the SERS signal detection along the (Z) direction was performed, estimating as maximum 1500μm of depth from the scaffold surface. After the demonstration of the sensing properties of these plasmonic platforms with an analyte model, a real biomolecule, used as cancer biomarkers was used to evaluate the sensing properties of the hydrogel-based scaffolds. In particular, the adenosine molecule required higher incubation time, and it was established that a minimum of 24h were needed to detect a stable SERS signal from the scaffold. Finally, it was assessed the influence on the SERS signal collected from measurements performed in real conditions, such as the signal-reduction effect generated by presence of the cellular media. Despite the signal reduction, it was still possible to detect a bio-relevant molecule in real like conditions, throughout the 3D-printed hydrogel-based scaffolds, ensuring the possibly of monitoring the production of analytes of a 3D cellular model over time.

Finally in **Section 4.4,** the plasmonic platforms evaluated in the previous **Section 4.3**, were used as support to grow cancerous cells, monitoring the evolution of the system via SERS images and detection of biomolecules. First, 3D-printed hydrogel-based scaffolds, marked with a different SERS tags from MCF7 cells, were employed to identify the imaging parameters. Several 3D measurements and depth measurements were performed over large areas of the systems. The same areas were imaged each 2-3 days, for a total period of 16 days showing the presence of the cellular SERS tags signal inside the scaffold, in both 3D and depth images. A reduction of the SERS signal over time was observed, most likely related to the detachment of the cells from the scaffold instead of to the cellular division, resulting different from the outcomes achieved in **Chapter3**. To overcome this problem, a second type of system was designed, where the SERS-labelled cells were placed inside the SERS-labelled scaffold, embedded in a biocompatible gel, which allowed the cells to grow and spread, inside the plasmonic scaffold. Moreover, two fluorescent-transfected cellular line were used, namely MCF7 with RFP and HDF with GFP, allowing the imaging of the 3D cellular model with both SERS and fluorescence techniques. Indeed, the SERS and fluorescence 3D images performed on this second system, confirmed the presence of the cells inside the scaffold. In order to address the sensing properties of the system, non-labelled scaffolds designed with bare AuNRs were employed for the detection of cancer-related metabolites, via 48h-incubation with the cellular media of cancerous and normal cells, namely MCF7 and MCF10. Some changes around the 960cm^{-1} and 1227cm^{-1} Raman shifts were observed, which can be related to different biomolecules produced by the healthy and malignant cells. Moreover, the detection properties of the hydrogel-based scaffolds were tested with the incubation of cellular media collected from MCF7 cells treated with an anticancer drug, i.e., Fulvestrant. In the scaffolds incubated with the treated MCF7, two peaks were observed at 751cm^{-1} and 1001cm^{-1} Raman shifts, which can be related to metabolites produced by drug-killed cells. Undoubtedly,

further investigations are needed in order to precisely identify the peaks and assess their relationship with the metabolic pathways of the cellular lines employed. However, the encouraging results revealed the remarkable potentialities of the plasmonic scaffolds, which were used as growth cellular support in real like conditions, SERS imaging reference and ultrasensitive metabolic detector of 3D cellular models over time.

In conclusion, based on the knowledge achieved on the signal of single SERS tag (**Chapter2**) it was possible to calculated the signal collected from a unique SERS-labeled cell (**Chapter3**). The investigation in the evolution of the SERS signal coming from a single cell in 2D cultures over time allowed to study the imaging parameters of SERS-labelled cells, such as the power and exposure time of the laser in relationship with the NPs concentration used to mark the cells. These findings were later used in this **Chapter4** to characterize the SERS imaging parameters of different 3D cellular models, as the step size and the depth of measurement in such complex structures. 3D sharp and bright images of MCF7 and HDF living cell lines inside the scaffold were achieved by SERS tomography. Finally, the optimization of the 3D imaging parameters had allowed also to study the sensing properties of the hydrogel-based scaffold, in detecting Raman model-molecules and biomolecules produced from the cells. The sensing capacity of the plasmonic structures applied on cellular media of 2D cultures, opened the way to the identification of cancerogenic MCF7 cells from healthy MCF10 cells as well as to the detection of anti-cancer drugs effects of MCF7 cells.

4.6 Experimental section

4.6.1 Chemicals

Tetrachloroauric acid trihydrate ($HAuCl_4 \cdot 3H_2O$, ≥99%), citric acid (≥99.5%), sodium borohydride ($NaBH_4$, 99%), L-ascorbic acid (≥99%), silver nitrate ($AgNO_3$, ≥99%), hexadecyltrimethylammonium bromide (CTAB, ≥99%), O-[2-(3-mercaptopropionylamino)ethyl]-O'-methylpolyethylene glycol (PEG, MW 5000 g mol^{-1}), 2-naphthalenethiol (2NAT, 99%), 4-methylbenzenethiol (MBT, 98%), biphenyl-4-thiol (BPT, 97%), poly-L-arginine hydrochloride (PA, Aldrich #26982-20-7>70,000 Da), poly(isobutylene-alt-maleic anhydride) (average MW ~6000 g mol^{-1}), dodecylamine (98%),1-decanol, tetrahydrofuran (THF, 99.85%, extra dry), chloroform ($CHCl_3$, ≥99.8%) and sodium hydroxide (NaOH, >97%) were purchased from Sigma-Aldrich. Hydrochloric acid solution (37 wt %) was purchased from Fisher Chemical. All chemicals were used without further purification. Milli-Q water (resistivity 18.2 MΩ cm at 25 °C) was used in all experiments. All glassware was washed with aqua regia, rinsed with Milli-Q water, and dried prior to use.

4.6.2 SERS tags synthesis

The SERS tags used to label the cells, namely AuNSs (50 nm diameter) and AuNRs (17 nm width × 60 nm length) with LSPR around 785 nm, were synthetized, labelled and functionalized with positive charge, as described in **Chapter 3**. The final concentration of the SERS tags after the preparation was [Au^0] = 0.5 mM.

The AuNSs-PEG and AuNRs-CTAB used to realize the inks for the 3D-printed scaffolds were prepared by Dr. Clara Garcia Astrain following well-established procedures,[20,37] and slightly changing the protocols to realize the AuNSs-CTAB and AuNRs-PEG-SH with LSPR at around 800 nm.[22]

4.6.3 NP characterization

TEM images were collected with a JEOL JEM-1400PLUS transmission electron microscope operating at 120 kV, using carbon-coated 400 square mesh copper grids. UV−vis optical extinction spectra were recorded using an Agilent 8453 UV−Vis diode array spectrophotometer, 10 mm standard path length cuvette with 3.5 mL volume.

4.6.4 Scaffold fabrication

4.6.4.1 Multimodal tessellated PLGA scaffold

The mono- and bi-compartmental fibres of tessellated scaffolds were fabricated by a 3D jet writing technique,[9] using an ink made of 50-75 kDa PLGA (30 wt/vol%), AuNS-BPT ([Au^0] = 3 mM) SERS tags dispersed in $CHCl_3$ and the fluorescently labelled polymers (poly[(mphenylenevinylene)-alt-(2,5-dihexyloxy-p-phenylenevinylene], and poly[tris(2,5-bis(hexyloxy)-1,4-phenylenevinylene)-alt-(1,3-phenylenevinylene)]).

4.6.4.2 Hydrogel-based scaffold for sensing

The AuNPs used to realize the inks for the scaffold were prepared as reported in **Section 4.6.2-3**. The hydrogel-based inks of scaffolds were realized of HAMA (1 wt%), alginate (1 wt%) and κ-carragenean (2 wt%) dissolved in aqueous AuNPs suspensions and mixed using a Thinky Mixer at 3500 rpm for 1 min. Upon complete polymer dissolution, fumed silica (4 wt%) and 2-Hydroxy-4′-(2-hydroxyethoxy) 2-methylpropiophenone (0.25 wt%) were added and mixed again (3500 rpm, 1 min). The scaffold was printed via DIW technique using a multi-headed 3D Discovery bioprinter (RegenHU, Switzerland). A high precision plunger dispenser was used at a constant volume flow rate of 2 μL s^{-1} and a stainless steel needle with an inner diameter of 0.25 mm. The code for square scaffold was produced using BIOCAD software (RegenHU, Switzerland) with 0.8 mm spacing between fibers and an initial height of 300 μm. The collector plate speed was set at 20 mm s^{-1} and after each layer was deposited, HAMA was cross-linked in situ using the light curing kit cartridge at 365 nm (output power of 500 mW). Once printing was completed, the scaffolds were immersed in a 5% w/v calcium chloride (CaCl2) solution for 5 min. [22]

4.6.4.3 Hydrogel-based scaffold for imaging

The AuNPs and SERS tags used to realize the inks for the scaffold were prepared as reported in **Section 4.6.2-3**. The hydrogel-based scaffolds were realized and printed as reported in **Section 4.6.4.2,** by slightly changing the formulation.

4.6.5 Scaffold preparation for *in vitro* studies

4.6.5.1 Multimodal tessellated PLGA scaffold

HDF cells were purchased from Invitrogen and grown in DMEM supplemented with 10% FBS and 1% penicillin-streptomycin (PS) (herein termed complete DMEM, cDMEM). To expose cells to NPs for uptake, HDF were seeded in 24 plates (3×10^4 cells per well) and allowed to adhere before replacing media with a solution of NPs diluted in cDMEM. NPs were added at a final concentration of $[Au^0] = 0.1$ mM. After 24 h, non-uptaken NPs were removed by washing the adhered HDF cell monolayer and the adhered cells were detached using Trypsin. After re-counting, cells were added to the scaffold.

A modified previously reported protocol[38] for preparation of NP-loaded scaffolds was used for imaging experiments. Scaffolds were sandwiched between two metallic windows (0.5×1 cm^2) and placed in a 2 mL sterile Eppendorf tube. 50 µL of human fibronectin (50 µg) was placed on top of the scaffold which lay suspended in the centre of the Eppendorf tube. The fibronectin was allowed to adhere to the scaffold fibres at 37 °C for 30 min. SERS-labelled HDF cells were washed, trypsinised, counted and readjusted to a concentration of $4 – 8 \times 10^5$ cells mL^{-1}. A concentrated drop of SERS tag-incubated cells (100 µL) was then added to the scaffold and allowed to incubate for approximately 30 min before transferring the scaffold to a 24-well plate and adding cDMEM. Either mixed SERS tag-cell populations or single SERS tag populations were used. The scaffolds were stored for approximately 2 weeks to allow cells to form a 3D mesh around the scaffold. cDMEM was carefully replaced every 2-3 days without disturbing the scaffold.

4.6.5.2 Hydrogel-based scaffold

MCF7 cells were purchased from Invitrogen and grown in DMEM supplemented with 10% FBS and 1% PS cDMEM. To expose cells to NPs for uptake, MCF7 were seeded in 24 plates (3×10^4 cells per well) and allowed to adhere before replacing media with a solution of NPs diluted in cDMEM. AuNRs-BP were added at a final concentration of $[Au^0] = 0.1$ mM. After 24h, non-uptaken NPs were removed by washing the adhered MCF7 cell monolayer and the adhered cells were detached using Trypsin. After re-counting, cells were added to the scaffold.

In order to increase the cellular adhesion, the scaffold was fully covered with a fibronectin layer, thought 24h incubation at 37 °C with a solution of fibronectin at 100 µg/mL. The scaffold was then rinsed, sterilized, and glued onto the quartz slide with a thin layer of dental glue on the edges of the scaffolds. A home-made holder was then placed on top of the configuration, as shown in ***Figure 4.25***. Previously labelled cells were lifted and concentrated in order to be placed inside the scaffold at the minimal volume possible (50k cells per 50 µL) to promote the cellular adhesion. After 2h of incubation at 37 °C, additional cell medium was carefully added to the 3D cellular model to perform live SERS measurements (see ***Figure 4.25C***).

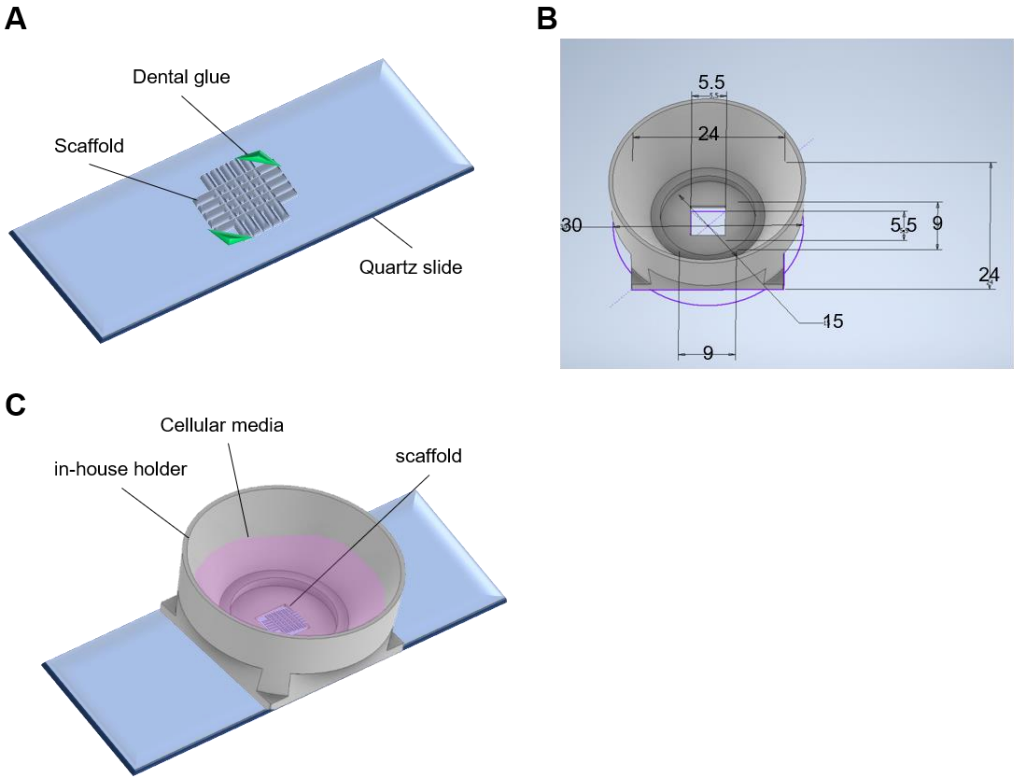

Figure 4.25 ***A)*** *The scaffold was glued directly to the quartz slide with dental glue in a wet state. Dimensions in mm* ***B)*** *and illustration* ***C)*** *of the in-house holder designed with Autodesk Inventor Software (Autodesk Inc. CA, USA). Once dried, additional media (<1.5 mL) could be added to perform SERS measurements with immersion objectives.*

4.6.6 SERS imaging

4.6.6.1 Multimodal tessellated PLGA scaffold with HDF cells

For live SERS imaging of the scaffold, the metal frames were picked up with tweezers and the whole component (scaffold and frames) was transferred to a quartz slide with an adhered in-house 3D printed well,[13] which allowed long-term cell growth and insertion of an immersion objective without disturbing the cells. The metal holder lays flat on the base allowing upright and inverted imaging. For high resolution SERS imaging of AuNS-1NAT, AuNS-2NAT, and AuNS-MBT NPs incubated with HDF cells, measurements were performed with a confocal Raman microscope (Alpha300 R – Confocal Raman Imaging Microscope, Witec) equipped with 1024 × 512 CCD detectors. A 785 nm laser excitation source (maximum output 79 mW) and a 300 l/mm diffraction grating were used. Measurements were recorded in static mode (centre of scattered wavenumber 1450 cm^{-1}) using a 20× immersion long working distance objective (numerical aperture, NA = 0.5; Zeiss, Jena, Germany). The integration time and laser power varied between 0.02 – 0.05 s, and 5 – 30 mW, respectively. Exact values are given in the legend of each figure. SERS data were analysed using True Component Analysis provided by the Witec microscope software. This is a non-open access script which is described by Witec as: “The unique post-processing function for confocal Raman imaging measurements automatically establishes the number of components in a sample, locates them

in the image, and differentiates their individual spectra. It delivers meaningful results in a fast and convenient way."

SERS measurements of HDF cells incubated with AuNR-2NAT and AuNS-MBT SERS tags were performed with a confocal Raman microscope (Renishaw inVia) equipped with 1024 × 512 CCD detectors, using a 785 nm laser excitation source (maximum output 270 mW) and a 1200 l/mm diffraction grating. SERS maps were recorded in static mode (centre of scattered wavenumber 1450 cm^{-1}). For imaging over time, a 40× immersion objective (numerical aperture, NA = 0.8; Nikon, Tokyo, Japan) with 0.8s integration time, at 3.1 mW laser power was used. The map of one selected area (325 × 225 μm^2) was acquired with a resolution of 5 µm in X and Y, and required approximately 1 h and 10 min to be completed. For 3D imaging, a 50× long distance objective (N.A. = 0.5; Leica Microsystems, Wetzlar, Germany), with 1s integration time, at 29.55 mW laser power was used. The map of one selected area (584 × 584 × 60 μm^3) was acquired with a resolution of 8 µm in X and Y, and 20 µm in Z, and the total four layers required approximately 2 h and 30 min to be completed.

SERS reference spectra were collected from a 5 µL drop of the SERS tags ($[Au]^0$ = 0.5 mM) on top of a quartz slide. We used a 50× long working distance objective (NA = 0.5; Leica Microsystems, Wetzlar, Germany) in expanded scan mode with an integration time of 10 s, at a laser power of 1.11 mW and five accumulative scans. SERS data were analysed using MLRA (*regress* function of Matlab).[39]

4.6.6.2 SERS bleaching test experiment of multimodal tessellated PLGA scaffold with HDF cells

Maps of a fixed area – different from that tested by fluorescence – were acquired four times with a resolution of 5 µm in X and Y using a 50× long distance objective (N.A. = 0.5; Leica Microsystems, Wetzlar, Germany), a full-1200 l/mm diffraction grating and a 785 nm HeNe laser. Each point was exposed to 1.11 mW of laser power for 1s. Each map has a dimension of 250 × 250 μm^2 and took approximately 1 h to complete. Reference spectra: Raman measurements of colloidal SERS tags ain solution were performed with a 50× long distance objective (N.A. = 0.5; Leica Microsystems, Wetzlar, Germany), a full-1200 l/mm diffraction grating and a 785 nm HeNe laser. The volume of the sample was exposed for 10s in total during scanning; the PLGA Raman spectrum was obtained by measuring a scaffold without SERS tags, with a 50× long distance objective (N.A. = 0.5; Leica Microsystems, Wetzlar, Germany), a full-1200 l/mm diffraction grating and a 785 nm HeNe laser. The analysis was performed as presented in **Chapter 3**.

4.6.6.3 SERS imaging of hydrogel-based scaffold for sensing

Raman spectra were acquired using an inVia Renishaw Raman microscope, excited through a 50× Leica objective with a 785 nm diode laser at 10% power for 10 s. Each scaffold was swollen in a 1 mM MBA solution (Sigma Aldrich) for 30 min. The scaffold was then placed on a quartz slide and covered with a drop of water to prevent drying during the measurement. Scaffolds were also incubated in MBA and adenosine solutions of varying concentrations,

from 100 nM to 1 mM for MBA; 10 μM, 100 μM, and 1 mM for adenosine. In the case of adenosine, the incubation time was increased to 12 h. Control experiments were conducted by incubating the scaffolds in cDMEM. For MBA detection, the scaffolds were first incubated in cell media for 12 h and subsequently incubated in 1 mM MBA solution for 30 min. For adenosine detection, the incubation with the analyte was performed for 24 and 48 h (1 mM adenosine in cDMEM). For depth measurements, scaffolds prepared with 1 mM AuNRs were excited through a 40× Leica immersion objective with a 758 nm diode laser at a 50% power. Raman spectra were taken in a small region with step sizes of 100 × 50 μm^2 (XZ) and at longer regions of 100 × 100 μm^2 (XZ).

4.6.6.4 SERS imaging of hydrogel-based scaffold with MCF7/HDF cells

Scaffold covered with fibronectin and MCF7 deposited on top: SERS measurements were performed with a confocal Raman microscope (Renishaw inVia) equipped with 1024 × 512 CCD detectors, using a 785 nm laser excitation source (maximum output 270 mW), a pinhole to obtain a circular laser spot geometry, and a 1200 l/mm diffraction grating. SERS maps were recorded in static mode (center of scattered wavenumber 1450 cm^{-1}) using a 40× immersion long working distance objective (NA = 0.8; Leica Microsystems, Wetzlar, Germany). The scaffold was placed in the quartz slice through an in-house made holder, as reported in ***Figure 4.25***. In ***Figure 4.19***, volumetric regions of ca. 700 × 700 × 900 μm^3 were imaged with 0.8 s integration time, at 12.08 mW laser power and step size of 60 μm in (XY) and 100 μm (Z). The depth areas of ca. 1200 × 1000 μm^2 and 600 × 1000 μm^2 in (XZ) were imaged with 0.8 s integration time, at 12.08 mW laser power and step size of 60 μm in (X) and (Z). In ***Figure 4.20***, volumetric regions of ca. 700 × 700 × 900 μm^3 were imaged with 0.8 s integration time, at 12.08 mW laser power and step size of 60 μm in (XY) and 100 μm (Z). Depth areas of ca. 600 × 1000 μm^2 in (XZ) were imaged with 0.8 s integration time, at 12.08 mW laser power and step size of 60 μm in (X) and (Z). In ***Figure 4.21*** a volumetric region of ca. 2000 × 2000 × 750 μm^3 was imaged with 0.8 s integration time, at 12.08 mW laser power and step size of 60 μm in (XY) and 250 μm (Z). Depth areas of ca. 1500 × 1000 and 1500 × 800 μm^2 in (XZ) and (YZ) were imaged with 0.8 s integration time, at 12.08 mW laser power and step size of 60 μm in all directions. Spectra were analyzed with MLRA using the previously obtained reference spectra, as reported in **Chapter 3**.

Scaffold filled with Matrigel with embedded MCF7 and HDF: SERS measurements were performed with a confocal Raman microscope (Alpha300 R – Confocal Raman Imaging Microscope, Witec) equipped with 1024 × 512 CCD detectors, using a 785 nm laser excitation source (maximum output 79 mW) and a 300 l/mm diffraction grating. The signal was recorded in static mode (center of scattered wavenumber 1450 cm−1) using a 20× immersion long working distance objective (numerical aperture, NA = 0.5; Zeiss, Jena, Germany). In ***Figure 4.22*** the 2D areas in the (XY) plane of ca. 1000 × 1000 μm^2 were imaged with 0.02 s integration time, at 10mW laser power and step size of 5 μm in both directions. A volumetric

region of ca. 750 × 750 × 500 μm^3 was imaged with 0.05 s integration time, at 10% laser power and step size of 5 μm in (XY) and 20 μm (Z). Spectra were analyzed with the TCA tool, and the components are reported in the figure.

Scaffold incubated with cellular media: SERS measurements were performed with a confocal Raman microscope (Renishaw inVia) equipped with 1024 × 512 CCD detectors, using a 785 nm laser excitation source (maximum output 270 mW), a pinhole to obtain a circular laser spot geometry, and a 1200 l/mm diffraction grating. SERS maps were recorded in static mode (center of scattered wavenumber 1450 cm^{-1}) using a 40× immersion long working distance objective (NA = 0.8; Leica Microsystems, Wetzlar, Germany). In ***Figure 4.24A,C,D*** the spectra were calculated as average of SERS map of ca. 300 × 300 μm^2 in (XY) plane were imaged with 1s, at 42.0 mW laser power and step size of 20 μm. In ***Figure 4.24B*** the spectra were obtained using a 50× long working distance objective (NA = 0.5; Leica Microsystems, Wetzlar, Germany) with 10s integration time and 58.3 mW laser power in extended mode.

4.6.7 Fluorescence imaging

4.6.7.1 Fluorescence imaging of multimodal tessellated PLGA scaffold with HDF cells

For live fluorescence imaging, HDF cells were transfected to express GFP using a multiplicity of infection (MOI) of 10 and hygromycin for selection, allowing imaging using 488 nm excitation. For fixed cell imaging, cell-containing scaffolds were fixed *in situ* with the metal holder in the 24-well plate. To do so, a 4% solution of formaldehyde was used at RT for 20 min, followed by washing with PBS. Immunocytochemical staining using anti-fibronectin (F3648 clone) with AF633 labelled anti-rabbit secondary antibody was conducted to image fibronectin.

4.6.7.2 Fluorescence bleaching test experiment of multimodal tessellated PLGA scaffold with HDF cells

HDF cells were grown on scaffolds containing a blue fluorophore, using the method described above to seed cells. Cells were fixed with formaldehyde and then stained with Actin 488 ReadyProbes fluorophore (Invitrogen). The sample was sandwiched between two quartz coverslips using mounting media to provide physical and chemical stability. To conduct the experiment, the sample was alternatively irradiated with a 405 nm laser for 60 s, and then imaged using the same 405 nm laser and a 488 nm laser, thereby exciting the fluorophores in the scaffold and in the cells, respectively. A Plan-Apochromat 20× objective (0.8 N.A.) was used throughout and the pinhole was set to 24 μm for both bleaching and imaging. Images were transferred to ImageJ and, by working with the blue and the green channels separately, ROIs were drawn to represent the scaffold (blue channel), the cells (green channel), and their corresponding backgrounds. In the case of the ROIs representing signal from the blue channel, they were 10 × 10 μm^2. In the case of the ROIs representing signal from the green channel, they measured 200 × 100 μm^2, to capture a brighter signal (which comes from the actin cytoskeleton and is therefore sparser). Using ImageJ, the Raw Integrated Density of each ROI

was calculated (that is, the sum of the pixel intensities in that ROI) and the average of each area was plotted. Images for visual understanding were post-processed with a 3-pixel median filter for clarity.

References:

(1) Charwat, V.; Schütze, K.; Holnthoner, W.; Lavrentieva, A.; Gangnus, R.; Hofbauer, P.; Hoffmann, C.; Angres, B.; Kasper, C. Potential and Limitations of Microscopy and Raman Spectroscopy for Live-Cell Analysis of 3D Cell Cultures. *J. Biotechnol.* **2015**, *205*, 70–81. https://doi.org/10.1016/J.JBIOTEC.2015.02.007.

(2) Placone, J. K.; Mahadik, B.; Fisher, J. P. Addressing Present Pitfalls in 3D Printing for Tissue Engineering to Enhance Future Potential. *APL Bioeng.* **2020**, *4*, 010901. https://doi.org/10.1063/1.5127860.

(3) Wang, X.; Jiang, M.; Zhou, Z.; Gou, J.; Hui, D. 3D Printing of Polymer Matrix Composites: A Review and Prospective. *Compos. Part B Eng.* **2017**, *110*, 442–458. https://doi.org/10.1016/J.COMPOSITESB.2016.11.034.

(4) Tamay, D. G.; Usal, T. D.; Alagoz, A. S.; Yucel, D.; Hasirci, N.; Hasirci, V. 3D and 4D Printing of Polymers for Tissue Engineering Applications. *Front. Bioeng. Biotechnol.* **2019**, *7*, 164. https://doi.org/10.3389/FBIOE.2019.00164.

(5) Jordahl, J. H.; Solorio, L.; Sun, H.; Ramcharan, S.; Teeple, C. B.; Haley, H. R.; Lee, K. J.; Eyster, T. W.; Luker, G. D.; Krebsbach, P. H. 3D Jet Writing : Functional Microtissues Based on Tessellated Scaffold Architectures. **2018**, *30*, 1707196. https://doi.org/10.1002/adma.201707196.

(6) Jordahl, S.; Solorio, L.; Neale, D. B.; McDermott, S.; Jordahl, J. H.; Fox, A.; Dunlay, C.; Xiao, A.; Brown, M.; Wicha, M.; et al. Engineered Fibrillar Fibronectin Networks as Three-Dimensional Tissue Scaffolds. *Adv. Mater.* **2019**, *31*, 1904580. https://doi.org/10.1002/ADMA.201904580.

(7) Steier, A.; Schmieg, B.; Irtel von Brenndorff, Y.; Meier, M.; Nirschl, H.; Franzreb, M.; Lahann, J.; Steier, A.; Schmieg, B.; Irtel von Brenndorff, Y.; et al. Enzyme Scaffolds with Hierarchically Defined Properties via 3D Jet Writing. *Macromol. Biosci.* **2020**, *20*, e2000154. https://doi.org/10.1002/MABI.202000154.

(8) Moon, S.; Jones, M. S.; Seo, E.; Lee, J.; Lahann, L.; Jordahl, J. H.; Lee, K. J.; Lahann, J. 3D Jet Writing of Mechanically Actuated Tandem Scaffolds. *Sci. Adv.* **2021**, *7*, eabf5289. https://doi.org/10.1126/SCIADV.ABF5289.

(9) Strozyk, M. S.; de Aberasturi, D. J.; Gregory, J. V.; Brust, M.; Lahann, J.; Liz-Marzán, L. M. Spatial Analysis of Metal–PLGA Hybrid Microstructures Using 3D SERS Imaging. *Adv. Funct. Mater.* **2017**, *27*, 1701626. https://doi.org/10.1002/adfm.201701626.

(10) Gregory, J. V.; Vogus, D. R.; Barajas, A.; Cadena, M. A.; Mitragotri, S.; Lahann, J. Programmable Delivery of Synergistic Cancer Drug Combinations Using Bicompartmental Nanoparticles. *Adv. Healthc. Mater.* **2020**, *9*, 2000564. https://doi.org/10.1002/ADHM.202000564.

(11) Campbell, J. L.; SoRelle, E. D.; Ilovich, O.; Liba, O.; James, M. L.; Qiu, Z.; Perez, V.; Chan, C. T.; de la Zerda, A.; Zavaleta, C. Multimodal Assessment of SERS Nanoparticle Biodistribution Post Ingestion Reveals New Potential for Clinical Translation of Raman Imaging. *Biomaterials* **2017**, *135*, 42–52. https://doi.org/10.1016/J.BIOMATERIALS.2017.04.045.

(12) Walter, A.; Paul-Gilloteaux, P.; Plochberger, B.; Sefc, L.; Verkade, P.; Mannheim, J. G.; Slezak, P.; Unterhuber, A.; Marchetti-Deschmann, M.; Ogris, M.; et al. Correlated Multimodal Imaging in Life Sciences: Expanding the Biomedical Horizon. *Front. Phys.* **2020**, *8*, 47. https://doi.org/10.3389/FPHY.2020.00047/BIBTEX.

(13) Jiménez de Aberasturi, D.; Henriksen-Lacey, M.; Litti, L.; Langer, J.; Liz-Marzán, L. M. Using SERS Tags to Image the Three-Dimensional Structure of Complex Cell Models. *Adv. Funct. Mater.* **2020**, *30*, 1909655. https://doi.org/10.1002/adfm.201909655.

(14) Olsen, C. J.; Moreira, J.; Lukanidin, E. M.; Ambartsumian, N. S. Human Mammary Fibroblasts Stimulate Invasion of Breast Cancer Cells in a Three-Dimensional Culture and Increase Stroma Development in Mouse Xenografts. *BMC Cancer* **2010**, *10*, 444. https://doi.org/10.1186/1471-2407-10-444.

(15) Ilina, O.; Gritsenko, P. G.; Syga, S.; Lippoldt, J.; La Porta, C. A. M.; Chepizhko, O.; Grosser, S.; Vullings, M.; Bakker, G. J.; Starruß, J.; et al. Cell–Cell Adhesion and 3D Matrix Confinement Determine Jamming Transitions in Breast Cancer Invasion. *Nat. Cell Biol. 2020 229* **2020**, *22*, 1103–1115. https://doi.org/10.1038/s41556-020-0552-6.

(16) Chen, M.; Huang, J.; Yang, X.; Liu, B.; Zhang, W.; Huang, L.; Deng, F.; Ma, J.; Bai, Y.; Lu, R.; et al. Serum Starvation Induced Cell Cycle Synchronization Facilitates Human Somatic Cells Reprogramming. *PLoS One* **2012**, *7*, e28203. https://doi.org/10.1371/JOURNAL.PONE.0028203.

(17) Barbora, A.; Bohar, O.; Sivan, A. A.; Magory, E.; Nause, A.; Minnes, R. Higher Pulse Frequency of Near-Infrared Laser Irradiation Increases Penetration Depth for Novel Biomedical Applications. *PLoS One* **2021**, *16*, e0245350. https://doi.org/10.1371/JOURNAL.PONE.0245350.

(18) Yetisen, A. K.; Butt, H.; Volpatti, L. R.; Pavlichenko, I.; Humar, M.; Kwok, S. J. J.; Koo, H.; Kim, K. S.; Naydenova, I.; Khademhosseini, A.; et al. Photonic Hydrogel Sensors. *Biotechnol. Adv.* **2016**, *34*, 250–271. https://doi.org/10.1016/J.BIOTECHADV.2015.10.005.

(19) Haring, A. P.; Khan, A. U.; Liu, G.; Johnson, B. N. 3D Printed Functionally Graded Plasmonic Constructs. *Adv. Opt. Mater.* **2017**, *5*, 1700367. https://doi.org/10.1002/ADOM.201700367.

(20) Scarabelli, L.; Grzelczak, M.; Liz-Marzán, L. M. Tuning Gold Nanorod Synthesis through Prereduction with Salicylic Acid. *Chem. Mater.* **2013**, *25*, 4232–4238. https://doi.org/10.1021/CM402177B.

(21) Jiménez de Aberasturi, D.; Serrano-Montes, A. B.; Langer, J.; Henriksen-Lacey, M.; Parak, W. J.; Liz-Marzán, L. M. Surface Enhanced Raman Scattering Encoded Gold Nanostars for Multiplexed Cell Discrimination. *Chem. Mater.* **2016**, *28*, 6779–6790. https://doi.org/10.1021/acs.chemmater.6b03349.

(22) García-Astrain, C.; Lenzi, E.; Jiménez de Aberasturi, D.; Henriksen-Lacey, M.; Binelli, M. R.; Liz-Marzán, L. M. 3D-Printed Biocompatible Scaffolds with Built-In Nanoplasmonic Sensors. *Adv. Funct. Mater.* **2020**, *30*, 2005407. https://doi.org/10.1002/ADFM.202005407.

(23) Plou, J.; García, I.; Charconnet, M.; Astobiza, I.; García-Astrain, C.; Matricardi, C.; Mihi, A.; Carracedo, A.; Liz-Marzán, L. M. Multiplex SERS Detection of Metabolic Alterations in Tumor Extracellular Media. *Adv. Funct. Mater.* **2020**, *30*, 1910335. https://doi.org/10.1002/adfm.201910335.

(24) Scarpitti, B. T.; Morrison, A. M.; Buyanova, M.; Schultz, Z. D. Comparison of 4-Mercaptobenzoic Acid Surface-Enhanced Raman Spectroscopy-Based Methods for PH Determination in Cells. *Appl. Spectrosc.* **2020**, *74*, 1423–1432. https://doi.org/10.1177/0003702820950768.

(25) Yang, T.; Guo, X.; Wu, Y.; Wang, H.; Fu, S.; Wen, Y.; Yang, H. Facile and Label-Free Detection of Lung Cancer Biomarker in Urine by Magnetically Assisted Surface-Enhanced Raman Scattering. *ACS Appl. Mater. Interfaces* **2014**, *6*, 20985–20993. https://doi.org/10.1021/AM5057536.

(26) Vijayan, D.; Young, A.; Teng, M. W. L.; Smyth, M. J. Targeting Immunosuppressive Adenosine in Cancer. *Nat. Rev. Cancer* **2017**, *17*, 709–724. https://doi.org/10.1038/NRC.2017.86.

(27) Serrano-Montes, A. B.; Jimenez de Aberasturi, D.; Langer, J.; Giner-Casares, J. J.;

Scarabelli, L.; Herrero, A.; Liz-Marzán, L. M. A General Method for Solvent Exchange of Plasmonic Nanoparticles and Self-Assembly into SERS-Active Monolayers. *Langmuir* **2015**, *31*, 9205–9213. https://doi.org/10.1021/acs.langmuir.5b01838.

(28) Jensen, C.; Teng, Y. Is It Time to Start Transitioning From 2D to 3D Cell Culture? *Front. Mol. Biosci.* **2020**, *7*, 33. https://doi.org/10.3389/FMOLB.2020.00033/BIBTEX.

(29) Unnikrishnan, K.; Thomas, L. V.; Ram Kumar, R. M. Advancement of Scaffold-Based 3D Cellular Models in Cancer Tissue Engineering: An Update. *Front. Oncol.* **2021**, *11*, 733652. https://doi.org/10.3389/FONC.2021.733652.

(30) Habanjar, O.; Diab-Assaf, M.; Caldefie-Chezet, F.; Delort, L. 3D Cell Culture Systems: Tumor Application, Advantages, and Disadvantages. *Int. J. Mol. Sci.* **2021**, *22*, 12200. https://doi.org/10.3390/IJMS222212200.

(31) Benton, G.; Arnaoutova, I.; George, J.; Kleinman, H. K.; Koblinski, J. Matrigel: From Discovery and ECM Mimicry to Assays and Models for Cancer Research. *Adv. Drug Deliv. Rev.* **2014**, *79–80*, 3–18. https://doi.org/10.1016/J.ADDR.2014.06.005.

(32) Baharvand, H.; Hashemi, S. M.; Ashtiani, S. K.; Farrokhi, A. Differentiation of Human Embryonic Stem Cells into Hepatocytes in 2D and 3D Culture Systems in Vitro. *Int. J. Dev. Biol.* **2006**, *50*, 645–652. https://doi.org/10.1387/IJDB.052072HB.

(33) Alvarez-Puebla, R. A.; Dos Santos, D. S.; Aroca, R. F. Surface-Enhanced Raman Scattering for Ultrasensitive Chemical Analysis of 1 and 2-Naphthalenethiols. *Analyst* **2004**, *129*, 1251–1256. https://doi.org/10.1039/b410488a.

(34) Kalbacova, J.; Rodriguez, R. D.; Desale, V.; Schneider, M.; Amin, I.; Jordan, R.; Zahn, D. R. T. Chemical Stability of Plasmon-Active Silver Tips for Tip-Enhanced Raman Spectroscopy. *Nanospectroscopy* **2015**, *1*. https://doi.org/10.2478/nansp-2014-0002.

(35) Saikin, S. K.; Olivares-Amaya, R.; Rappoport, D.; Stopa, M.; Aspuru-Guzik, A. On the Chemical Bonding Effects in the Raman Response: Benzenethiol Adsorbed on Silver Clusters. *Phys. Chem. Chem. Phys.* **2009**, *11*, 9401–9411. https://doi.org/10.1039/b906885f.

(36) Yeh, W. L.; Shioda, K.; Coser, K. R.; Rivizzigno, D.; McSweeney, K. R.; Shioda, T. Fulvestrant-Induced Cell Death and Proteasomal Degradation of Estrogen Receptor α Protein in MCF-7 Cells Require the CSK c-Src Tyrosine Kinase. *PLoS One* **2013**, *8*, e60889. https://doi.org/10.1371/JOURNAL.PONE.0060889.

(37) Scarabelli, L.; Sánchez-Iglesias, A.; Pérez-Juste, J.; Liz-Marzán, L. M. A "Tips and Tricks" Practical Guide to the Synthesis of Gold Nanorods. *J. Phys. Chem. Lett.* **2015**, *6*, 4270–4279. https://doi.org/10.1021/acs.jpclett.5b02123.

(38) Jordahl, S.; Solorio, L.; Neale, D. B.; McDermott, S.; Jordahl, J. H.; Fox, A.; Dunlay, C.; Xiao, A.; Brown, M.; Wicha, M.; et al. Engineered Fibrillar Fibronectin Networks as Three-Dimensional Tissue Scaffolds. *Adv. Mater.* **2019**, *31*, 1904580. https://doi.org/10.1002/adma.201904580.

(39) Lenzi, E.; Litti, L.; Jimenez de Aberasturi, D.; Henriksen-Lacey, M.; Liz-Marzán, L. M. SERSTEM: An App for the Statistical Analysis of Correlative SERS and TEM Imaging and Evaluation of SERS Tags Performance. *J. Raman Spectrosc.* **2021**, *52*, 355–365. https://doi.org/10.1002/jrs.6043.

5. Conclusions

This thesis has demonstrated the possibility of performing a comprehensive characterization of 3D biological systems of tumorous cells via SERS tomographic bioimaging, using SERS-encoded nanoparticles as contrast agents. As a first step, a quantification method was presented in **Chapter 2**, to calculate the SERS signal corresponding to a single SERS tag. The SERSTEM App was developed to correlate SERS maps with TEM images, with the aim of evaluating the number of SERS tags on the basis on the recorded SERS signal. The App was built to correlate the positions of NPs in TEM images with the SERS signals collected from the same recognizable areas of air-dried colloidal dispersions of SERS tags. The SERS signals were identified in the mappings via MLRA, which was used as a filter. In this manner, the analysis automatically excluded those regions featuring SERS signals without a sufficient similarity to the reference, as well as empty spaces. This procedure allowed us to estimate the signal intensity at one of the main peaks of the RaR molecule, for each of the four different SERS tags tested, showing a similar SERS signal per particle (SSpP) for those samples with a similar RaR/PEG ratio. The SSpP was also used to predict the number of NPs in an unknown 2D region, obtaining a value in good agreement with the value counted in TEM images. This analytical tool, developed for 2D SERS mapping, was then optimized for to obtain a reliable estimation in 3D of the number of NPs taken up by living cells. In **Chapter 3**, the intracellular amount of SERS tags was evaluated from an analysis based on 3D SERS measurements of individual breast cancer (MCF7) live cells, with no undesired cytotoxicity from excessive laser exposure. The methodology was developed with the aim of characterizing *in vitro* the process of NP uptake, NP dilution into daughter cells and exocytosis. The dilution of SERS tags into daughter cells was tracked for more than 2 weeks, thereby ensuring the long-term labelling capacity of these biocompatible and optically sensitive labels. The observed decrease in SERS tag intensity over time was analysed in terms of cellular division and exocytosis, identifying cellular division as the principal source of SERS tag dilution after 1 DIV. The quantification of SERS tags via non-invasive 3D SERS mapping *in vitro*, allowed us to identify important parameters required for live-cell imaging of single cells. In particular, the long dwelling time of SERS tags (over 2 weeks), coupled with their non-toxic nature and high multiplexing ability, offered an interesting opportunity for their use in 3D cell models, even at low concentrations. Moreover, with the aim to perform single cell studies of the intracellular distribution of the SERS tags in live cancer cells, the production and the parameters for SERS measurements of cell-laden microdroplets (100 μm diameter) were optimized. These findings were used in **Chapter 4** to study increasingly complex 3D cell culture systems, controlling all of the parameters that can affect SERS bioimaging. As a first complex system, a 3D printed scaffold made of PLGA with embedded SERS tags and fluorescently labelled polymers, was used as support for the growth of an interlaced 3D film of HDF cells. The thick tissue (100 μm) was used to assess the penetration depth possible for SERS measurements through a

living cellular layer, evaluating the parameters needed to obtain sharp and clear SERS images. In particular, the employed laser power was studied to obtain a sufficiently high intensity of the SERS signal without inducing photo-toxicity effects from the SERS tags, identifying 30 mW as the maximum laser power, with an integration time of 0.05 s, in a confocal microscope. The step size used to obtain detailed SERS images, with the ability to distinguish two cellular populations proliferating and migrating, while representing a sufficiently large area to achieve a significant characterization of a millimetric sample, was 5 μm^3. Finally, the stability and lack of photodegradation of SERS tags signal within a living cellular environment were also verified, demonstrating the imaging of a 3D cellular model for over a period of ca. 3 weeks. After having characterized these parameters, we used a different support, namely a 3D-printed hydrogel-based scaffold functionalized with bare AuNPs, with the aim of exploiting the scaffolds not only as a SERS imaging reference, but also as a plasmonic detector. To characterize the sensing properties of the plasmonic scaffolds, the MBA molecule was first used as a model, which confirmed a homogeneous adsorption of the analyte throughout the scaffold. AuNRs were identified as the best performing type of AuNPs, at a concentration of $[Au^0]$ = 1mM, to obtain a sufficiently high SERS signal from the analyte. Under these conditions, 100 nM in aqueous solution was evaluated as the detection limit of the MBA molecule, and 1500 μm depth from the scaffold surface was identified as the maximum detection depth of the SERS signal in the (Z) direction. After the demonstration of the sensing properties of these plasmonic platforms, a cancer biomarker (adenosine) was used as the analyte. Despite a longer incubation time (24h) and signal reduction, it was possible to detect the biomolecule in realistic concentrations, thereby ensuring the possibly of monitoring the production of biomarkers over time. Finally, the 3D-printed hydrogel-based scaffolds were used as supports to grow cancer cells, so the evolution of the system could be monitored via SERS bioimaging and biomolecule detection. Several 3D measurements and depth measurements over large areas were performed to assess the cellular distribution and organization. Specifically, it was decided to place SERS-labelled cells in the scaffolds by embedding them in a biocompatible gel. This environment allowed the cells to grow and spread within the plasmonic scaffolds. Additionally, the detection of cancer-related metabolites in cellular media was addressed by comparing the SERS signal obtained from healthy (MCF10) and malignant cells (MCF7), as well as malignant cells treated and non-treated with an anticancer drug, namely Fulvestrant. Some changes were observed around the 960 cm^{-1} and 1227 cm^{-1} Raman shifts, which can be related to different biomolecules produced by healthy and malignant cells. On the other hand, the presence of two peaks at 751cm^{-1} and 1001cm^{-1} Raman shifts in cells treated with Fulvestrant, suggested the possible detection of metabolites related to the anticancer drug.

Although further investigations are surely needed, the encouraging results of this thesis revealed the remarkable potential of SERS-related analytical techniques. Both the methodology developed to identify the appropriate measurement parameters and their values

are useful tools toward employing plasmonic scaffolds as both SERS bioimaging reference and ultrasensitive metabolic detectors of 3D cellular models for preclinical studies.

Appendix A

Contents

A.1 SERSTEM app

The SERSTEM app was developed in collaboration with Dr. Lucio Litti of University of Padova, Padova (Italy).

A.1.1 Application code

```
classdef SERSTEM2017b < matlab.apps.AppBase
    % Properties that correspond to app components
    properties (Access = public)
        UIFigure                        matlab.ui.Figure
        NewMenu                         matlab.ui.container.Menu
        ExportMenu_2                    matlab.ui.container.Menu
        ResultsmatvariableMenu          matlab.ui.container.Menu
        MapTEMpictureMenu               matlab.ui.container.Menu
        ScatterplotMenu                 matlab.ui.container.Menu
        BoxPlotMenu                     matlab.ui.container.Menu
        FeretImagesMenu                 matlab.ui.container.Menu
        CreditsMenu                     matlab.ui.container.Menu
        UIAxes                          matlab.ui.control.UIAxes
        TabGroup                        matlab.ui.container.TabGroup
        ImageTab                        matlab.ui.container.Tab
        GreyLimitValueEditFieldLabel    matlab.ui.control.Label
        GreyLimitValueEditField
matlab.ui.control.NumericEditField
        MinPixelSignificanceEditFieldLabel  matlab.ui.control.Label
        MinPixelSignificanceEditField
matlab.ui.control.NumericEditField
        UpdateButton_img                matlab.ui.control.Button
        MinPixelParticleEditFieldLabel  matlab.ui.control.Label
        MinPixelParticleEditField
matlab.ui.control.NumericEditField
        MaxPixelParticleEditFieldLabel  matlab.ui.control.Label
        MaxPixelParticleEditField
matlab.ui.control.NumericEditField
        RamanTab                        matlab.ui.container.Tab
        MapsubdivisionmEditFieldLabel   matlab.ui.control.Label
        MapsubdivisionmEditField
matlab.ui.control.NumericEditField
        pValuethresholdEditFieldLabel   matlab.ui.control.Label
        pValuethresholdEditField
matlab.ui.control.NumericEditField
        bValuethresholdEditFieldLabel   matlab.ui.control.Label
        bValuethresholdEditField
matlab.ui.control.NumericEditField
        IntensitythresholdEditFieldLabel  matlab.ui.control.Label
        IntensitythresholdEditField
matlab.ui.control.NumericEditField
        UpdateButton_ram                matlab.ui.control.Button
        RamanShiftLabel                 matlab.ui.control.Label
        RamanShiftEditField
matlab.ui.control.NumericEditField
        GraphTab                        matlab.ui.container.Tab
        SubMapNumberEditFieldLabel      matlab.ui.control.Label
        SubMapNumberEditField
matlab.ui.control.NumericEditField
        ShowButton                      matlab.ui.control.Button
        ShowBButton                     matlab.ui.control.Button
```

```
        UIAxes_Scatter                  matlab.ui.control.UIAxes
        UIAxes_SigPart                  matlab.ui.control.UIAxes
        UIAxes_Feret                    matlab.ui.control.UIAxes
        LoadOpticalImgButton            matlab.ui.control.Button
        LoadTEMImgButton                matlab.ui.control.Button
        LoadReferenceSpectrumButton     matlab.ui.control.Button
        LoadRamanMapButton              matlab.ui.control.Button
        RunButton                       matlab.ui.control.Button
        UIAxes_Feret_2                  matlab.ui.control.UIAxes
        Status                          matlab.ui.control.Label
    end

    properties (Access = private)
        imageTEM % the original TEM image
        imageCamera % the original camera image from Raman map
        par % type structr, parameters for computations
        M % Raman map spectra
        res % results in terms of submaps
        imgVars % image variables
    end

    methods (Access = private)

        function par = initialization(app,par)
            app.Status.Text='Initialization...';
            app.Status.FontColor='r'; pause(0.5)
            par.significance=5;
            par.GLV=[];
            par.BLV=[0 inf];
            app.par.SubMapNumber=1;
            app.SubMapNumberEditField.Value=1;
            par.dq =Inf; %la dimensione dello spot, approssimato a
rettangolo di lato = diametro dello spot
            par.st=0; % signal treshold in "signal", section 5
            par.res=1; % in um ???
            par.alpha=0.05; % p value threshold
            par.b=10;% b value threshold
            par.rg=2; % ???
            [val,ind]=max(par.probe(:,2));
            par.RamanShift=par.probe(ind,1);
            app.RamanShiftEditField.Value=par.probe(ind,1);
        end

        function [signal,par] = mapAnalyzer(app,M,par)
            app.Status.Text='Map Analyzing...';
            app.Status.FontColor='r'; pause(0.5)
            [signal,par]=mapAnalyzer(M,par);
        end

        function res = mapShaping(app,M,signal,par,img)
            app.Status.Text='Map Shaping...';
            app.Status.FontColor='r'; pause(0.5)
            res=MapSection(M,signal{2,4}(:,1),[par.dq par.dq]);
            res=MapSelection(res,img,par);
        end

        function [Cnp,par,Bounds,Geom] = TEMimage(app,img,par)
```

```
            app.Status.Text='Image Analyzing...';
            app.Status.FontColor='r'; pause(0.5)
            [Cnp,par,Bounds,Geom]=TEMimage(img,par);
        end

        function [res,resSel,FerSel] =
SignalParticle(app,res,Cnp,par,Bounds,Geom)
            app.Status.Text='Signals Processing...';
            app.Status.FontColor='r'; pause(0.5)
            res=SignalParticle(res,Cnp,par,Bounds,Geom);
            [res,resSel,FerSel]=SquareSelection(res,par.BLV);

            % Graphs
            var=res;
            img=app.imageTEM;
            par=app.par;

            % app.UIAxes - image
            ax=app.UIAxes;
            cla(ax,'reset')
            app.Status.Text='Plotting...';
            app.Status.FontColor='r'; pause(0.5)
            try
            hold(ax,'on')

image(ax,'XData',linspace(par.imgX(1),par.imgX(2),size(img,2)),'YData',l
inspace(par.imgY(1),par.imgY(2),size(img,1)),'CData',img)
            if size(var,2)==1
                    scatter(ax,var{4,1}(:,1),var{4,1}(:,2),'.r')
                    scatter(ax,var{1,1}(:,1),var{1,1}(:,2),'.b')
            elseif size(var,2)<100
                for i=1:size(var,2)
                    scatter(ax,var{4,i}(:,1),var{4,i}(:,2),'r.')
                    plot(ax,[var{3,i}(:,1);
var{3,i}(1,1)],[var{3,i}(:,2); var{3,i}(1,2)],'b');

text(ax,mean(var{3,i}(:,1)),mean(var{3,i}(:,2)),num2str(i))
                end
            else
                for i=1:size(var,2)
                    scatter(ax,var{4,i}(:,1),var{4,i}(:,2),'r.')
                    plot(ax,[var{3,i}(:,1);
var{3,i}(1,1)],[var{3,i}(:,2); var{3,i}(1,2)],'b');
                end
                for i=1:5:size(var,2)

text(ax,mean(var{3,i}(:,1)),mean(var{3,i}(:,2)),num2str(i))
                end
            end
            hold(ax,'off'); axis(ax,'tight'); axis(ax,'equal');

            % UIAxes_Scatter - scatter plot signal/particle vs particles
found vs sub-map index
            ax=app.UIAxes_Scatter;
            cla(ax,'reset')
            hold(ax,'on')
                for i=1:size(var,2)
```

```
scatter3(ax,i,var{2,i}{2,3},var{2,i}{2,1},50,'filled','MarkerFaceColor',
[1 0 0]) % signal/particle vs particle
                end
            hold(ax,'off')
            xlabel(ax,'Sub-Map index');
            ylabel(ax,'signal per particle');
            zlabel(ax,'particles found'); view(ax,[40,30])
            grid(ax,'on')

            % UIAxes_SigPart - boxplot signal per particles
            ax=app.UIAxes_SigPart;
            cla(ax,'reset')
            if size(var,2)>1
                temp=zeros(size(var,2),1);
                for i=1:size(var,2)
                    temp(i,1)=var{2,i}{2,3}; % signal per particle
                    temp(i,2)=var{2,i}{2,1}; % particles found
                end
                title(ax,'Signal per Particle')
            else
                temp(:,1)=var{1,1}(var{1,1}(:,3)>par.st,3);
                title(ax,'Signals over Threshold')
            end
             hold(ax,"on")
             boxplot(ax,temp(:,1)); grid(ax,'on')

text(ax,0.6,prctile(temp(:,1),75),num2str(prctile(temp(:,1),75)))
              text(ax,0.6,median(temp(:,1)),num2str(median(temp(:,1))))

text(ax,0.6,prctile(temp(:,1),25),num2str(prctile(temp(:,1),25)))
              hold(ax,"off")

              % app.UIAxes_Feret - plot Feret distribution
              ax=app.UIAxes_Feret;
              cla(ax,'reset')
              histogram(ax,mean(FerSel(:,2:3),2),100)
              xlabel(ax,'Mean Feret per particle (nm)');
              ylabel(ax,'Aboundance');
              grid(ax,'on')

              % app.UIAxes_Feret_2 - plot min e max Feret
              ax=app.UIAxes_Feret_2;
              cla(ax,'reset')
              hold(ax,"on")
              plot(ax,FerSel(:,2),FerSel(:,2),'--r')
              scatter(ax,FerSel(:,2),FerSel(:,3),'.b')
              hold(ax,"off")
              xlabel(ax,'Max Feret (nm)');
              ylabel(ax,'Min Feret (nm)');
              grid(ax,'on')
            catch
               text(app.UIAxes,1,1,'SERSTEM Warning: Wrong Parameters')
               axis(app.UIAxes,[0.5 5 0.5 1.5])
               cla(app.UIAxes_Scatter,'reset')
               cla(app.UIAxes_SigPart,'reset')
               cla(app.UIAxes_Feret,'reset')
```

```
                cla(app.UIAxes_Feret_2,'reset')
            end
        end

        function results = loadings(app,form)

            switch form
                case '*.jpg'
                    curr=pwd;
                    [name,path]=uigetfile(form);
                    cd(path)
                    results=imread(name);
                    cd(curr);
                case '*.mat'
                    curr=pwd;
                    [name,path]=uigetfile(form);
                    cd(path)
                    results=load(name);
                    cd(curr);
                case 'Raman'
                    curr=pwd;
                    [name,path]=uigetfile('*.wdf','*.wip');
                    if strcmp(name(1,end-3:end),'.wdf')
                        results=datagen(name,path,curr);
                    elseif strcmp(name(1,end-3:end),'.wip')
                        % to do
                    end
                case '*.txt'
                    curr=pwd;
                    [name,path]=uigetfile(form);
                    cd(path)
%                     results=importdata(name);
                    FileID=fopen(name);
                    Count=textscan(FileID,'%s %s',1);
                    Count=textscan(FileID,'%f %f');
                    results=[Count{1,1} Count{1,2}];
                    fclose(FileID);
                    cd(curr);
            end
        end

        function app=start(app)
            app.UpdateButton_img.Text='Running';
            app.UpdateButton_img.FontColor='red';
            pause(0.5)

            % initialization and data loading
            app.par = initialization(app,app.par);

app.MinPixelSignificanceEditField.Value=app.par.significance;
            app.MinPixelParticleEditField.Value=app.par.BLV(1);
            app.MaxPixelParticleEditField.Value=app.par.BLV(2);
            app.pValuethresholdEditField.Value=app.par.alpha;
            app.bValuethresholdEditField.Value=app.par.b;
            app.IntensitythresholdEditField.Value=app.par.st;
            app.MapsubdivisionmEditField.Value=app.par.dq;
            app.par.GLV=[];
```

```
            % Raman Map Analysis
            [signal,app.par] = mapAnalyzer(app,app.M,app.par);

            % Map reshaping and selection
            app.res = mapShaping(app,app.M,signal,app.par,app.imageTEM);

            % TEM image analysis

[app.imgVars.Cnp,app.par,app.imgVars.Bounds,app.imgVars.Geom] =
TEMimage(app,app.imageTEM,app.par);
            app.GreyLimitValueEditField.Value=app.par.GLV;

            % Signal per Particle evaluation
            [app.res, app.imgVars.resSel, app.imgVars.FerSel] =
SignalParticle(app,app.res,app.imgVars.Cnp,app.par,app.imgVars.Bounds,ap
p.imgVars.Geom);

            app.UpdateButton_img.FontColor='green';
            app.UpdateButton_ram.FontColor='green';
            app.UpdateButton_img.Text='Update';
        end
    end

    methods (Access = private)
        % Menu selected function: NewMenu
        function NewMenuSelected(app, event)
            app.par.loading=[0 0 0 0];
            app.LoadOpticalImgButton.FontColor='red';
            app.LoadRamanMapButton.FontColor='red';
            app.LoadTEMImgButton.FontColor='red';
            app.LoadReferenceSpectrumButton.FontColor='red';
            app.UpdateButton_img.Enable='off';
            app.ShowButton.Enable='off';
            app.UpdateButton_ram.Enable='off';
            app.RunButton.Enable='off';
            app.RunButton.FontColor='red';
            app.ResultsmatvariableMenu.Enable='off';
            app.MapTEMpictureMenu.Enable='off';
            app.ScatterplotMenu.Enable='off';
            app.BoxPlotMenu.Enable='off';
            app.FeretImagesMenu.Enable='off';

            app.M=[]; app.imageTEM=[]; app.imageCamera=[]; app.par=[];
app.res=[]; app.imgVars=[];

            cla(app.UIAxes,'reset');
            cla(app.UIAxes_Feret,'reset');
            cla(app.UIAxes_Feret_2,'reset');
            cla(app.UIAxes_Scatter,'reset');
            cla(app.UIAxes_SigPart,'reset');

        end
        % Value changed function: GreyLimitValueEditField
        function GreyLimitValueEditFieldValueChanged(app, event)
            app.par.GLV = app.GreyLimitValueEditField.Value;
            app.UpdateButton_img.FontColor='red';
```

```
        end
        % Value changed function: MinPixelParticleEditField
        function MinPixelParticleEditFieldValueChanged(app, event)
            app.par.BLV(1) = app.MinPixelParticleEditField.Value;
            app.UpdateButton_img.FontColor='red';
        end
        % Button pushed function: UpdateButton_img
        function UpdateButton_imgPushed(app, event)
            app.UpdateButton_img.Text='Running'; pause(0.5)
            % Raman Map Analysis
            [signal,app.par] = mapAnalyzer(app,app.M,app.par);
            % Map reshaping and selection
            app.res = mapShaping(app,app.M,signal,app.par,app.imageTEM);
            % TEM image analysis

[app.imgVars.Cnp,app.par,app.imgVars.Bounds,app.imgVars.Geom] =
TEMimage(app,app.imageTEM,app.par);
            % Signal per Particle evaluation
            [app.res, app.imgVars.resSel, app.imgVars.FerSel] =
SignalParticle(app,app.res,app.imgVars.Cnp,app.par,app.imgVars.Bounds,ap
p.imgVars.Geom);            app.UpdateButton_img.FontColor='green';
            app.UpdateButton_img.Text='Update';
            app.Status.Text='Ready';
            app.Status.FontColor='k';
        end
        % Button pushed function: UpdateButton_ram
        function UpdateButton_ramPushed(app, event)
            app.UpdateButton_ram.Text='Running'; pause(0.5)
            % Raman Map Analysis
            [signal,app.par] = mapAnalyzer(app,app.M,app.par);
            % Map reshaping and selection
            app.res = mapShaping(app,app.M,signal,app.par,app.imageTEM);
            % Signal per Particle evaluation
            [app.res, app.imgVars.resSel, app.imgVars.FerSel] =
SignalParticle(app,app.res,app.imgVars.Cnp,app.par,app.imgVars.Bounds,ap
p.imgVars.Geom);            app.UpdateButton_ram.FontColor='green';
            app.UpdateButton_ram.Text='Update';
            app.Status.Text='Ready';
            app.Status.FontColor='k';
        end
        % Value changed function: MaxPixelParticleEditField
        function MaxPixelParticleEditFieldValueChanged(app, event)
            app.par.BLV(2) = app.MaxPixelParticleEditField.Value;
            app.UpdateButton_img.FontColor='red';
        end
        % Value changed function: MinPixelSignificanceEditField
        function MinPixelSignificanceEditFieldValueChanged(app, event)
            app.par.significance =
app.MinPixelSignificanceEditField.Value;
            app.UpdateButton_ram.FontColor='red';
        end
        % Value changed function: MapsubdivisionmEditField
        function MapsubdivisionmEditFieldValueChanged(app, event)
            value = app.MapsubdivisionmEditField.Value;

            temp=diff(app.M.C(:,1));
            deltaX=min(abs(temp(temp~=0)));
```

```
            temp=diff(app.M.C(:,2));
            deltaY=min(abs(temp(temp~=0)));

            if (value>=deltaX && value>=deltaY)
                app.par.dq=value;
            else
               text(app.UIAxes,1,1,'SERSTEM Warning: Map Subdivision
exceeds Map Resolution')
               axis(app.UIAxes,[0.5 5 0.5 1.5])
               cla(app.UIAxes_Scatter,'reset')
               cla(app.UIAxes_SigPart,'reset')
               cla(app.UIAxes_Feret,'reset')
               cla(app.UIAxes_Feret_2,'reset')
            end
            app.UpdateButton_ram.FontColor='red';
        end
        % Value changed function: pValuethresholdEditField
        function pValuethresholdEditFieldValueChanged(app, event)
            app.par.alpha = app.pValuethresholdEditField.Value;
            app.UpdateButton_ram.FontColor='red';
        end
        % Value changed function: bValuethresholdEditField
        function bValuethresholdEditFieldValueChanged(app, event)
            app.par.b = app.bValuethresholdEditField.Value;
            app.UpdateButton_ram.FontColor='red';
        end
        % Value changed function: IntensitythresholdEditField
        function IntensitythresholdEditFieldValueChanged(app, event)
            app.par.st = app.IntensitythresholdEditField.Value;
            app.UpdateButton_ram.FontColor='red';
        end
        % Button pushed function: LoadOpticalImgButton
        function LoadOpticalImgButtonPushed(app, event)
            app.Status.Text='Loading...';
            app.Status.FontColor='r';
            app.imageCamera=loadings(app,'*.jpg');
%             app.imageCamera=[];
            app.LoadOpticalImgButton.FontColor='green';
            app.par.loading(1)=1;
            if sum(app.par.loading,2)>=2
                if sum(app.par.loading(1,1:2),2)==2
                    global imgC imgT
                    imgC=app.imageCamera;
                    imgT=app.imageTEM;
                    run IMAGES.mlapp
                end
            end
            if sum(app.par.loading,2)==4
                app.RunButton.Enable='on';
                app.RunButton.FontColor='green';
            end
            app.Status.Text='Ready';
            app.Status.FontColor='k';

        end
        % Button pushed function: LoadTEMImgButton
        function LoadTEMImgButtonPushed(app, event)
```

```
            app.Status.Text='Loading...';
            app.Status.FontColor='r';
            app.imageTEM=loadings(app,'*.jpg');
%             results=loadings(app,'*.mat');
%             app.imageTEM=results.img;
%             app.par.imgX=results.par.imgX;
%             app.par.imgY=results.par.imgY;
            app.LoadTEMImgButton.FontColor='green';
            app.par.loading(2)=1;
            if sum(app.par.loading,2)>=2
                if sum(app.par.loading(1,1:2),2)==2
                    global imgC imgT
                    imgC=app.imageCamera;
                    imgT=app.imageTEM;
                    run IMAGES.mlapp
                end
            end
            if sum(app.par.loading,2)==4
                app.RunButton.Enable='on';
                app.RunButton.FontColor='green';
            end
            app.Status.Text='Ready';
            app.Status.FontColor='k';
        end
        % Button pushed function: LoadRamanMapButton
        function LoadRamanMapButtonPushed(app, event)
            app.Status.Text='Loading...';
            app.Status.FontColor='r';
            results=loadings(app,'Raman');
            app.M=results;
            app.LoadRamanMapButton.FontColor='green';
            app.par.loading(3)=1;
            if sum(app.par.loading,2)==4
                app.RunButton.Enable='on';
                app.RunButton.FontColor='green';
            end
            app.Status.Text='Ready';
            app.Status.FontColor='k';
        end
        % Button pushed function: LoadReferenceSpectrumButton
        function LoadReferenceSpectrumButtonPushed(app, event)
            app.Status.Text='Loading...';
            app.Status.FontColor='r';
            results=loadings(app,'*.txt');
            app.par.probe=results;
%             app.par.background=results.background;
            app.LoadReferenceSpectrumButton.FontColor='green';
            app.par.loading(4)=1;
            if sum(app.par.loading,2)==4
                app.RunButton.Enable='on';
                app.RunButton.FontColor='green';
            end
            app.Status.Text='Ready';
            app.Status.FontColor='k';
        end
        % Button pushed function: RunButton
        function RunButtonPushed(app, event)
```

```
%             try
            global imgC imgT imgXY
            app.imageCamera=imgC;
            app.imageTEM=imgT;
            app.par.imgX=imgXY(1,:);
            app.par.imgY=imgXY(2,:);
            app=start(app);
            app.UpdateButton_img.Enable='on';
            app.ShowButton.Enable='on';
            app.UpdateButton_ram.Enable='on';
            app.Status.Text='Ready';
            app.Status.FontColor='k';
            app.ResultsmatvariableMenu.Enable='on';
            app.MapTEMpictureMenu.Enable='on';
            app.ScatterplotMenu.Enable='on';
            app.BoxPlotMenu.Enable='on';
            app.FeretImagesMenu.Enable='on';
%             catch
%                 text(app.UIAxes,1,1,'SERSTEM Warning: work on IMAGES
app first')
%                axis(app.UIAxes,[0.5 5 0.5 1.5])
%                cla(app.UIAxes_Scatter,'reset')
%                cla(app.UIAxes_SigPart,'reset')
%                cla(app.UIAxes_Feret,'reset')
%                cla(app.UIAxes_Feret_2,'reset')
%             end
        end
        % Value changed function: SubMapNumberEditField
        function SubMapNumberEditFieldValueChanged(app, event)
            app.par.SubMapNumber = app.SubMapNumberEditField.Value;

        end
        % Button pushed function: ShowButton
        function ShowButtonPushed(app, event)
            app.Status.Text='Running';
            app.Status.FontColor='r';
            pause(0.5)

            var=app.res; img=app.imageTEM;
            ind=app.par.SubMapNumber; rs=app.par.RamanShift;
            a=var{2,ind}{2,1}; % particles number
            figure('units','normalized','outerposition',[0 1 0.8 0.8]);

            subplot(2,3,4) % image and bounds
            zoom=0.2;
            hold on

image('XData',linspace(app.par.imgX(1),app.par.imgX(2),size(img,2)),'YDa
ta',linspace(app.par.imgY(1),app.par.imgY(2),size(img,1)),'CData',img)
            for i=1:a

plot(var{6,ind}.Bounds{1,i}(:,1),var{6,ind}.Bounds{1,i}(:,2),'r')
            end
            if size(var,2)>1
                plot([var{3,ind}(:,1);
var{3,ind}(1,1)],[var{3,ind}(:,2); var{3,ind}(1,2)],'b');
            else
```

```
                scatter(var{1,1}(:,1),var{1,1}(:,2),'.b')
            end
            hold off
            set(gca,'DataAspectRatio',[1 1 1])
            if size(var,2)>1
                axis([min(var{3,ind}(:,1))-zoom
max(var{3,ind}(:,1))+zoom min(var{3,ind}(:,2))-zoom
max(var{3,ind}(:,2))+zoom])
            else
                axis tight
                axis equal
            end
            title(['Sub-Map ',num2str(ind)]); %axis('equal')

            subplot(2,3,1:3) % spectra
            plot(var{5,ind}(1,:),var{5,ind}(2:end,:))
            xlabel('Raman Shift (cm^-^1)')
            ylabel('Intensity (a.u.)')
            grid on

            subplot(2,3,5) % intensities
            valmin=prctile(var{5,ind}(2:end,:),25,1);
            valmax=prctile(var{5,ind}(2:end,:),75,1);
            valAver=median(var{5,ind}(2:end,:),1);
            hold on
            if size(var{5,ind}(2:end,:),1)>1
            plot(var{5,ind}(1,:),valmin,'g','displayname','25°
percentile')
            plot(var{5,ind}(1,:),valmax,'g','displayname','75°
percentile')
            end
            plot(var{5,ind}(1,:),valAver,'r','displayname','Median')
            plot([rs rs],[0 max(valmax)],'--b','displayname','Selected
Raman Shift')
            hold off
            legend
            xlabel('Raman Shift (cm^-^1)')
            ylabel('All Signals (a.u.)')
            grid on

            subplot(2,3,6) % boxplot
            temp=var{1,ind}(var{1,ind}(:,3)>app.par.st,3);
            boxplot(temp);
            text(0.6,prctile(temp,75),num2str(prctile(temp,75)))
            text(0.6,median(temp),num2str(median(temp)))
            text(0.6,prctile(temp,25),num2str(prctile(temp,25)))
            ylabel('Signals over Threshold')
            grid on

            app.Status.Text='Ready';
            app.Status.FontColor='k';

        end
        % Value changed function: RamanShiftEditField
        function RamanShiftEditFieldValueChanged(app, event)
            app.par.RamanShift = app.RamanShiftEditField.Value;
            app.UpdateButton_ram.FontColor='red';
```

```
        end
        % Button pushed function: ShowBButton
        function ShowBButtonPushed(app, event)
            figure;
            subplot(3,3,1)
            histogram(app.par.BIall(:,1),100)
            title('All b-Values')
            xlabel('b-Values'); ylabel(['Counts (tot:
',num2str(size(app.par.BIall,1)),')']); grid on

            subplot(3,3,2)
            histogram(app.par.BIall(:,2),100)
            title(['All Int. at ',num2str(round(app.par.RamanShift)),'
cm^-^1'])
            xlabel('Intensities (a.u.)'); ylabel(['Counts (tot:
',num2str(size(app.par.BIall,1)),')']); grid on

            subplot(3,3,3)
            hold on
            plot([0 max(app.par.BIall(:,1))],[0
max(app.par.BIall(:,1))],'r')
            scatter(app.par.BIall(:,1),app.par.BIall(:,2),'.b')
            hold off
            title('All b-Values and Int.'); grid on
            xlabel('b-Values'); ylabel('Intensities (a.u.)');

            subplot(3,3,4)
            histogram(app.par.BIselP(:,1),100)
            title('b-Values over p-Value threshold')
            xlabel('b-Values'); ylabel(['Counts (tot:
',num2str(size(app.par.BIselP,1)),')']); grid on

            subplot(3,3,5)
            histogram(app.par.BIselP(:,2),100)
            title(['Int. at ',num2str(round(app.par.RamanShift)),' cm^-
^1  over p-Value threshold'])
            xlabel('Intensities (a.u.)'); ylabel(['Counts (tot:
',num2str(size(app.par.BIselP,1)),')']); grid on

            subplot(3,3,6)
            hold on
            plot([0 max(app.par.BIselP(:,1))],[0
max(app.par.BIselP(:,1))],'r')
            scatter(app.par.BIselP(:,1),app.par.BIselP(:,2),'.b')
            hold off
            title('b-Values and Int. over p-Value threshold'); grid on
            xlabel('b-Values'); ylabel('Intensities (a.u.)');

            subplot(3,3,7)
            histogram(app.par.BIsel(:,1),100)
            title('b-Values over p-Value & b-Value threshold')
            xlabel('b-Values'); ylabel(['Counts (tot:
',num2str(size(app.par.BIsel,1)),')']); grid on

            subplot(3,3,8)
            histogram(app.par.BIsel(:,2),100)
```

```
            title(['Int. at ',num2str(round(app.par.RamanShift)),' cm^-
^1  over p-Value & b-Value threshold'])
            xlabel('Intensities (a.u.)'); ylabel(['Counts (tot:
',num2str(size(app.par.BIsel,1)),')']); grid on

            subplot(3,3,9)
            hold on
            plot([0 max(app.par.BIsel(:,1))],[0
max(app.par.BIsel(:,1))],'r')
            scatter(app.par.BIsel(:,1),app.par.BIsel(:,2),'.b')
            hold off
            title('b-Values and Int. over p-Value & b-Value threshold');
grid on
            xlabel('b-Values'); ylabel('Intensities (a.u.)');


        end
        % Menu selected function: ResultsmatvariableMenu
        function ResultsmatvariableMenuSelected(app, event)
            mes{1,1} = 'x,y coordinates and intensities at the selected
Raman Shift';
            mes{2,1} = 'resume of part. found, overall intensity and
Signal per Particle';
            mes{3,1} = 'edges of the sub-map used to count particles';
            mes{4,1} = 'x,y coordinates of the particles found';
            mes{5,1} = 'spectra acquired within the submap';
            mes{6,1} = 'geometrical info about particles found';
            assignin('base','Results',[mes app.res]);
            f = uifigure;
            uialert(f,'"Result" vabiable created in the main
workspace','Variable Export');
        end
        % Menu selected function: MapTEMpictureMenu
        function MapTEMpictureMenuSelected(app, event)
            figure;
            % Graphs
            var=app.res;
            img=app.imageTEM;
            par=app.par;
            hold('on')

image('XData',linspace(par.imgX(1),par.imgX(2),size(img,2)),'YData',lins
pace(par.imgY(1),par.imgY(2),size(img,1)),'CData',img)
            if size(var,2)==1
                    scatter(var{4,1}(:,1),var{4,1}(:,2),'.r')
                    scatter(var{1,1}(:,1),var{1,1}(:,2),'.b')
            elseif size(var,2)<100
                for i=1:size(var,2)
                    scatter(var{4,i}(:,1),var{4,i}(:,2),'r.')
                    plot([var{3,i}(:,1); var{3,i}(1,1)],[var{3,i}(:,2);
var{3,i}(1,2)],'b');

text(mean(var{3,i}(:,1)),mean(var{3,i}(:,2)),num2str(i))
                end
            else
                for i=1:size(var,2)
                    scatter(var{4,i}(:,1),var{4,i}(:,2),'r.')
```

```
                    plot([var{3,i}(:,1); var{3,i}(1,1)],[var{3,i}(:,2);
var{3,i}(1,2)],'b');
                end
                for i=1:5:size(var,2)

text(mean(var{3,i}(:,1)),mean(var{3,i}(:,2)),num2str(i))
                end
            end
            hold('off'); axis('tight'); axis('equal');

        end
        % Menu selected function: ScatterplotMenu
        function ScatterplotMenuSelected(app, event)
            % Graphs
            var=app.res;
            figure;
            hold('on')
                for i=1:size(var,2)

scatter3(i,var{2,i}{2,3},var{2,i}{2,1},50,'filled','MarkerFaceColor',[1
0 0]) % signal/particle vs particle
                end
            hold('off')
            xlabel('Sub-Map index');
            ylabel('signal per particle');
            zlabel('particles found'); view([40,30])
            grid('on')
        end
        % Menu selected function: BoxPlotMenu
        function BoxPlotMenuSelected(app, event)
            % Graphs
            var=app.res;
            figure
            if size(var,2)>1
                temp=zeros(size(var,2),1);
                for i=1:size(var,2)
                    temp(i,1)=var{2,i}{2,3}; % signal per particle
                    temp(i,2)=var{2,i}{2,1}; % particles found
                end
                title('Signal per Particle')
            else
                temp(:,1)=var{1,1}(var{1,1}(:,3)>app.par.st,3);
                title('Signals over Threshold')
            end
             hold('on')
             boxplot(temp(:,1)); grid('on')

text(0.6,prctile(temp(:,1),75),num2str(prctile(temp(:,1),75)))
             text(0.6,median(temp(:,1)),num2str(median(temp(:,1))))

text(0.6,prctile(temp(:,1),25),num2str(prctile(temp(:,1),25)))
             hold('off')


        end
        % Menu selected function: FeretImagesMenu
        function FeretImagesMenuSelected(app, event)
```

```
            % Graphs
            FerSel=app.imgVars.FerSel;

            figure;
            subplot(1,2,1)
             histogram(mean(FerSel(:,2:3),2),100)
             xlabel('Mean Feret per particle (nm)');
             ylabel('Aboundance');
             grid('on')

             subplot(1,2,2)
             hold('on')
             plot(FerSel(:,2),FerSel(:,2),'--r')
             scatter(FerSel(:,2),FerSel(:,3),'.b')
             hold('off')
             xlabel('Max Feret (nm)');
             ylabel('Min Feret (nm)');
             grid('on')
        end
        % Menu selected function: CreditsMenu
        function CreditsMenuSelected(app, event)
            figure
            subplot(2,1,1)
            imshow(imread('Logo_Bionanoplasmonic.jpg'))
            title('... publication reference ...')
            subplot(2,1,2)
            imshow(imread('Logo_NOL.jpg'))

        end
    end
    % App initialization and construction
    methods (Access = private)
        % Create UIFigure and components
        function createComponents(app)
            % Create UIFigure
            app.UIFigure = uifigure;
            app.UIFigure.Position = [100 100 728 456];
            app.UIFigure.Name = 'UI Figure';
            % Create NewMenu
            app.NewMenu = uimenu(app.UIFigure);
            app.NewMenu.MenuSelectedFcn = createCallbackFcn(app,
@NewMenuSelected, true);
            app.NewMenu.Text = 'New';
            % Create ExportMenu_2
            app.ExportMenu_2 = uimenu(app.UIFigure);
            app.ExportMenu_2.Text = 'Export';
            % Create ResultsmatvariableMenu
            app.ResultsmatvariableMenu = uimenu(app.ExportMenu_2);
            app.ResultsmatvariableMenu.MenuSelectedFcn =
createCallbackFcn(app, @ResultsmatvariableMenuSelected, true);
            app.ResultsmatvariableMenu.Enable = 'off';
            app.ResultsmatvariableMenu.Text = 'Results (mat variable)';
            % Create MapTEMpictureMenu
            app.MapTEMpictureMenu = uimenu(app.ExportMenu_2);
            app.MapTEMpictureMenu.MenuSelectedFcn =
createCallbackFcn(app, @MapTEMpictureMenuSelected, true);
            app.MapTEMpictureMenu.Enable = 'off';
```

```
            app.MapTEMpictureMenu.Text = 'Map & TEM picture';
            % Create ScatterplotMenu
            app.ScatterplotMenu = uimenu(app.ExportMenu_2);
            app.ScatterplotMenu.MenuSelectedFcn = createCallbackFcn(app,
@ScatterplotMenuSelected, true);
            app.ScatterplotMenu.Enable = 'off';
            app.ScatterplotMenu.Text = 'Scatter plot';
            % Create BoxPlotMenu
            app.BoxPlotMenu = uimenu(app.ExportMenu_2);
            app.BoxPlotMenu.MenuSelectedFcn = createCallbackFcn(app,
@BoxPlotMenuSelected, true);
            app.BoxPlotMenu.Enable = 'off';
            app.BoxPlotMenu.Text = 'Box Plot';
            % Create FeretImagesMenu
            app.FeretImagesMenu = uimenu(app.ExportMenu_2);
            app.FeretImagesMenu.MenuSelectedFcn = createCallbackFcn(app,
@FeretImagesMenuSelected, true);
            app.FeretImagesMenu.Enable = 'off';
            app.FeretImagesMenu.Text = 'Feret Images';
            % Create CreditsMenu
            app.CreditsMenu = uimenu(app.UIFigure);
            app.CreditsMenu.MenuSelectedFcn = createCallbackFcn(app,
@CreditsMenuSelected, true);
            app.CreditsMenu.Text = 'Credits';
            % Create UIAxes
            app.UIAxes = uiaxes(app.UIFigure);
            title(app.UIAxes, 'Title')
            xlabel(app.UIAxes, 'X')
            ylabel(app.UIAxes, 'Y')
            app.UIAxes.Position = [231 187 250 260];
            % Create TabGroup
            app.TabGroup = uitabgroup(app.UIFigure);
            app.TabGroup.Position = [11 69 210 255];
            % Create ImageTab
            app.ImageTab = uitab(app.TabGroup);
            app.ImageTab.Title = 'Image';
            % Create GreyLimitValueEditFieldLabel
            app.GreyLimitValueEditFieldLabel = uilabel(app.ImageTab);
            app.GreyLimitValueEditFieldLabel.HorizontalAlignment =
'right';
            app.GreyLimitValueEditFieldLabel.VerticalAlignment =
'center';
            app.GreyLimitValueEditFieldLabel.Position = [10 188 120 22];
            app.GreyLimitValueEditFieldLabel.Text = 'Grey Limit Value';
            % Create GreyLimitValueEditField
            app.GreyLimitValueEditField = uieditfield(app.ImageTab,
'numeric');
            app.GreyLimitValueEditField.ValueChangedFcn =
createCallbackFcn(app, @GreyLimitValueEditFieldValueChanged, true);
            app.GreyLimitValueEditField.Position = [150 188 50 22];
            % Create MinPixelSignificanceEditFieldLabel
            app.MinPixelSignificanceEditFieldLabel =
uilabel(app.ImageTab);
            app.MinPixelSignificanceEditFieldLabel.HorizontalAlignment =
'right';
            app.MinPixelSignificanceEditFieldLabel.VerticalAlignment =
'center';
```

```
            app.MinPixelSignificanceEditFieldLabel.Position = [13 158
126 22];
            app.MinPixelSignificanceEditFieldLabel.Text = 'Min. Pixel
Significance';
            % Create MinPixelSignificanceEditField
            app.MinPixelSignificanceEditField =
uieditfield(app.ImageTab, 'numeric');
            app.MinPixelSignificanceEditField.ValueChangedFcn =
createCallbackFcn(app, @MinPixelSignificanceEditFieldValueChanged,
true);
            app.MinPixelSignificanceEditField.Position = [153 158 47
22];
            % Create UpdateButton_img
            app.UpdateButton_img = uibutton(app.ImageTab, 'push');
            app.UpdateButton_img.ButtonPushedFcn =
createCallbackFcn(app, @UpdateButton_imgPushed, true);
            app.UpdateButton_img.FontColor = [1 0 0];
            app.UpdateButton_img.Enable = 'off';
            app.UpdateButton_img.Position = [56 17 100 22];
            app.UpdateButton_img.Text = 'Update';
            % Create MinPixelParticleEditFieldLabel
            app.MinPixelParticleEditFieldLabel = uilabel(app.ImageTab);
            app.MinPixelParticleEditFieldLabel.HorizontalAlignment =
'right';
            app.MinPixelParticleEditFieldLabel.VerticalAlignment =
'center';
            app.MinPixelParticleEditFieldLabel.Position = [11 128 120
22];
            app.MinPixelParticleEditFieldLabel.Text = 'Min. Pixel
Particle';
            % Create MinPixelParticleEditField
            app.MinPixelParticleEditField = uieditfield(app.ImageTab,
'numeric');
            app.MinPixelParticleEditField.ValueChangedFcn =
createCallbackFcn(app, @MinPixelParticleEditFieldValueChanged, true);
            app.MinPixelParticleEditField.Position = [151 128 50 22];
            % Create MaxPixelParticleEditFieldLabel
            app.MaxPixelParticleEditFieldLabel = uilabel(app.ImageTab);
            app.MaxPixelParticleEditFieldLabel.HorizontalAlignment =
'right';
            app.MaxPixelParticleEditFieldLabel.VerticalAlignment =
'center';
            app.MaxPixelParticleEditFieldLabel.Position = [11 98 120
22];
            app.MaxPixelParticleEditFieldLabel.Text = 'Max. Pixel
Particle';
            % Create MaxPixelParticleEditField
            app.MaxPixelParticleEditField = uieditfield(app.ImageTab,
'numeric');
            app.MaxPixelParticleEditField.ValueChangedFcn =
createCallbackFcn(app, @MaxPixelParticleEditFieldValueChanged, true);
            app.MaxPixelParticleEditField.Position = [151 98 50 22];
            % Create RamanTab
            app.RamanTab = uitab(app.TabGroup);
            app.RamanTab.Title = 'Raman';
            % Create MapsubdivisionmEditFieldLabel
            app.MapsubdivisionmEditFieldLabel = uilabel(app.RamanTab);
```

```
            app.MapsubdivisionmEditFieldLabel.HorizontalAlignment =
'right';
            app.MapsubdivisionmEditFieldLabel.VerticalAlignment =
'center';
            app.MapsubdivisionmEditFieldLabel.Position = [10 188 120
22];
            app.MapsubdivisionmEditFieldLabel.Text = 'Map subdivision
(µm)';
            % Create MapsubdivisionmEditField
            app.MapsubdivisionmEditField = uieditfield(app.RamanTab,
'numeric');
            app.MapsubdivisionmEditField.ValueChangedFcn =
createCallbackFcn(app, @MapsubdivisionmEditFieldValueChanged, true);
            app.MapsubdivisionmEditField.Position = [150 188 50 22];
            % Create pValuethresholdEditFieldLabel
            app.pValuethresholdEditFieldLabel = uilabel(app.RamanTab);
            app.pValuethresholdEditFieldLabel.HorizontalAlignment =
'right';
            app.pValuethresholdEditFieldLabel.VerticalAlignment =
'center';
            app.pValuethresholdEditFieldLabel.Position = [10 129 120
22];
            app.pValuethresholdEditFieldLabel.Text = 'p-Value
threshold';
            % Create pValuethresholdEditField
            app.pValuethresholdEditField = uieditfield(app.RamanTab,
'numeric');
            app.pValuethresholdEditField.ValueChangedFcn =
createCallbackFcn(app, @pValuethresholdEditFieldValueChanged, true);
            app.pValuethresholdEditField.Position = [150 129 50 22];
            % Create bValuethresholdEditFieldLabel
            app.bValuethresholdEditFieldLabel = uilabel(app.RamanTab);
            app.bValuethresholdEditFieldLabel.HorizontalAlignment =
'right';
            app.bValuethresholdEditFieldLabel.VerticalAlignment =
'center';
            app.bValuethresholdEditFieldLabel.Position = [10 99 120 22];
            app.bValuethresholdEditFieldLabel.Text = 'b-Value
threshold';
            % Create bValuethresholdEditField
            app.bValuethresholdEditField = uieditfield(app.RamanTab,
'numeric');
            app.bValuethresholdEditField.ValueChangedFcn =
createCallbackFcn(app, @bValuethresholdEditFieldValueChanged, true);
            app.bValuethresholdEditField.Position = [150 99 50 22];
            % Create IntensitythresholdEditFieldLabel
            app.IntensitythresholdEditFieldLabel =
uilabel(app.RamanTab);
            app.IntensitythresholdEditFieldLabel.HorizontalAlignment =
'right';
            app.IntensitythresholdEditFieldLabel.VerticalAlignment =
'center';
            app.IntensitythresholdEditFieldLabel.Position = [10 69 120
22];
            app.IntensitythresholdEditFieldLabel.Text = 'Intensity
threshold';
            % Create IntensitythresholdEditField
```

```
            app.IntensitythresholdEditField = uieditfield(app.RamanTab,
'numeric');
            app.IntensitythresholdEditField.ValueChangedFcn =
createCallbackFcn(app, @IntensitythresholdEditFieldValueChanged, true);
            app.IntensitythresholdEditField.Position = [150 69 50 22];
            % Create UpdateButton_ram
            app.UpdateButton_ram = uibutton(app.RamanTab, 'push');
            app.UpdateButton_ram.ButtonPushedFcn =
createCallbackFcn(app, @UpdateButton_ramPushed, true);
            app.UpdateButton_ram.FontColor = [1 0 0];
            app.UpdateButton_ram.Enable = 'off';
            app.UpdateButton_ram.Position = [56 17 100 22];
            app.UpdateButton_ram.Text = 'Update';
            % Create RamanShiftLabel
            app.RamanShiftLabel = uilabel(app.RamanTab);
            app.RamanShiftLabel.HorizontalAlignment = 'right';
            app.RamanShiftLabel.VerticalAlignment = 'center';
            app.RamanShiftLabel.Position = [10 159 120 22];
            app.RamanShiftLabel.Text = 'Raman Shift';
            % Create RamanShiftEditField
            app.RamanShiftEditField = uieditfield(app.RamanTab,
'numeric');
            app.RamanShiftEditField.ValueChangedFcn =
createCallbackFcn(app, @RamanShiftEditFieldValueChanged, true);
            app.RamanShiftEditField.Position = [150 159 50 22];
            % Create GraphTab
            app.GraphTab = uitab(app.TabGroup);
            app.GraphTab.Title = 'Graph';
            % Create SubMapNumberEditFieldLabel
            app.SubMapNumberEditFieldLabel = uilabel(app.GraphTab);
            app.SubMapNumberEditFieldLabel.HorizontalAlignment =
'right';
            app.SubMapNumberEditFieldLabel.VerticalAlignment = 'center';
            app.SubMapNumberEditFieldLabel.Position = [28 188 102 22];
            app.SubMapNumberEditFieldLabel.Text = 'Sub-Map Number';
            % Create SubMapNumberEditField
            app.SubMapNumberEditField = uieditfield(app.GraphTab,
'numeric');
            app.SubMapNumberEditField.ValueChangedFcn =
createCallbackFcn(app, @SubMapNumberEditFieldValueChanged, true);
            app.SubMapNumberEditField.Position = [150 188 50 22];
            % Create ShowButton
            app.ShowButton = uibutton(app.GraphTab, 'push');
            app.ShowButton.ButtonPushedFcn = createCallbackFcn(app,
@ShowButtonPushed, true);
            app.ShowButton.Position = [55 149 100 22];
            app.ShowButton.Text = 'Show';
            % Create ShowBButton
            app.ShowBButton = uibutton(app.GraphTab, 'push');
            app.ShowBButton.ButtonPushedFcn = createCallbackFcn(app,
@ShowBButtonPushed, true);
            app.ShowBButton.Position = [41.5 72 127 36];
            app.ShowBButton.Text = {'Show b-value and'; ' intensity
distribution'};
            % Create UIAxes_Scatter
            app.UIAxes_Scatter = uiaxes(app.UIFigure);
            title(app.UIAxes_Scatter, 'Title')
```

```
            xlabel(app.UIAxes_Scatter, 'X')
            ylabel(app.UIAxes_Scatter, 'Y')
            app.UIAxes_Scatter.Position = [491 187 230 260];
            % Create UIAxes_SigPart
            app.UIAxes_SigPart = uiaxes(app.UIFigure);
            title(app.UIAxes_SigPart, 'Title')
            xlabel(app.UIAxes_SigPart, 'X')
            ylabel(app.UIAxes_SigPart, 'Y')
            app.UIAxes_SigPart.Position = [580 17 141 160];
            % Create UIAxes_Feret
            app.UIAxes_Feret = uiaxes(app.UIFigure);
            title(app.UIAxes_Feret, 'Title')
            xlabel(app.UIAxes_Feret, 'X')
            ylabel(app.UIAxes_Feret, 'Y')
            app.UIAxes_Feret.Position = [241 17 160 160];
            % Create LoadOpticalImgButton
            app.LoadOpticalImgButton = uibutton(app.UIFigure, 'push');
            app.LoadOpticalImgButton.ButtonPushedFcn =
createCallbackFcn(app, @LoadOpticalImgButtonPushed, true);
            app.LoadOpticalImgButton.FontColor = [1 0 0];
            app.LoadOpticalImgButton.Position = [11 413 99 36];
            app.LoadOpticalImgButton.Text = {'Load Optical '; 'Img'};
            % Create LoadTEMImgButton
            app.LoadTEMImgButton = uibutton(app.UIFigure, 'push');
            app.LoadTEMImgButton.ButtonPushedFcn =
createCallbackFcn(app, @LoadTEMImgButtonPushed, true);
            app.LoadTEMImgButton.FontColor = [1 0 0];
            app.LoadTEMImgButton.Position = [121 413 99 36];
            app.LoadTEMImgButton.Text = {'Load TEM '; 'Img'};
            % Create LoadReferenceSpectrumButton
            app.LoadReferenceSpectrumButton = uibutton(app.UIFigure,
'push');
            app.LoadReferenceSpectrumButton.ButtonPushedFcn =
createCallbackFcn(app, @LoadReferenceSpectrumButtonPushed, true);
            app.LoadReferenceSpectrumButton.FontColor = [1 0 0];
            app.LoadReferenceSpectrumButton.Position = [118.5 366 104
36];
            app.LoadReferenceSpectrumButton.Text = {'Load Reference ';
'Spectrum'};
            % Create LoadRamanMapButton
            app.LoadRamanMapButton = uibutton(app.UIFigure, 'push');
            app.LoadRamanMapButton.ButtonPushedFcn =
createCallbackFcn(app, @LoadRamanMapButtonPushed, true);
            app.LoadRamanMapButton.FontColor = [1 0 0];
            app.LoadRamanMapButton.Position = [11 366 99 36];
            app.LoadRamanMapButton.Text = {'Load Raman '; 'Map'};
            % Create RunButton
            app.RunButton = uibutton(app.UIFigure, 'push');
            app.RunButton.ButtonPushedFcn = createCallbackFcn(app,
@RunButtonPushed, true);
            app.RunButton.FontColor = [1 0 0];
            app.RunButton.Enable = 'off';
            app.RunButton.Position = [66 335 100 22];
            app.RunButton.Text = 'Run';
            % Create UIAxes_Feret_2
            app.UIAxes_Feret_2 = uiaxes(app.UIFigure);
            title(app.UIAxes_Feret_2, 'Title')
```

```
            xlabel(app.UIAxes_Feret_2, 'X')
            ylabel(app.UIAxes_Feret_2, 'Y')
            app.UIAxes_Feret_2.Position = [411 17 160 160];
            % Create Status
            app.Status = uilabel(app.UIFigure);
            app.Status.HorizontalAlignment = 'center';
            app.Status.VerticalAlignment = 'center';
            app.Status.FontSize = 20;
            app.Status.FontWeight = 'bold';
            app.Status.Position = [12 33 208 27];
            app.Status.Text = 'Ready';
        end
    end
    methods (Access = public)
        % Construct app
        function app = SERSTEM2017b
            % Create and configure components
            createComponents(app)
            % Register the app with App Designer
            registerApp(app, app.UIFigure)
            if nargout == 0
                clear app
            end
        end
        % Code that executes before app deletion
        function delete(app)
            % Delete UIFigure when app is deleted
            delete(app.UIFigure)
        end
    end
end
```

A.1.2 Functions codes

A.1.2.1 mapAnalyzed

```
function [signal,par]=mapAnalyzer(M,par)

S_2 = M.S';
err_lato=par.res;
alfa=par.alpha; %p-value threshold, it's a fix value
soglia_b=par.b; %b-value threshold
rg=par.rg;
% background=par.background;
probe=par.probe;
rs=par.RamanShift;
wl=2;
range=[rs-rg rs+rg];
[val, ind]=min(abs(S_2(:,1)-rs)); par.rs=rs;

% reference
probe_s = spline(probe(:,1),probe(:,2),S_2(:,1));
probe_s = [S_2(:,1) probe_s];
probe_smoothed = smooth(probe_s(:,2),'sgolay',3);
[M2,I2] = min(abs(probe_s(:,1)-S_2(1,1)),[],1);
[N2,L2] = min(abs(probe_s(:,1)-S_2(end,1)),[],1);
probe_2 = probe_s(I2:L2,:);
probe_smoothed_2 = probe_smoothed(I2:L2,:);
```

```
norm = probe_2(:,2)./(max(probe_2(:,2)));
norm_probe_smoothed = probe_smoothed_2./(max(probe_smoothed_2));
resp = [ones(size(S_2,1),1) norm_probe_smoothed];
Bint_matrix=zeros(2,(size(S_2,2)-1)*2);
for k=1:size(S_2,2)-1
    S_2_norm(:,k+1)= S_2(:,k+1);
    [b, bint, r,rint,stats]=regress(S_2_norm(:,k+1),resp);
    B_matrix(:,k)=b;
    R_matrix(:,k)=r;
    R2_matrix(:,k)=stats(:,1);
    F_matrix(:,k)=stats(:,2);
    pvalue_matrix(:,k)=stats(:,3);
    var_matrix(:,k)=stats(:,4);
end
par.BIall=[B_matrix(wl,:)' S_2_norm(ind,2:end)']; % all b and Int vlaues

%p-value selection
temp_x = unique(M.C(:,1),'stable');
temp_y = unique(M.C(:,2),'stable');
lato=size(temp_x,1);
altez=size(temp_y,1);
a_mappa=lato*altez;
delta_a_mappa  = 1;
indici = find(pvalue_matrix>alfa);
S_7=S_2_norm(:,2:end);
S_7(:,indici)=NaN;
B_filtrered = B_matrix();
B_filtrered(wl,indici) = NaN;

temp=isfinite(B_filtrered(wl,:));
par.BIselP=[B_filtrered(wl,temp)' S_7(ind,temp)']; % b and Int vlaues
after p-selection

%b value selection
indici3 = find(B_filtrered(wl,:)<soglia_b);
B_filtrered_2 = B_filtrered();
B_filtrered_2(:,indici3) = NaN;
B_filtered_2_zeros = B_filtrered();
B_filtered_2_zeros(:,indici3)=0;
S_10 = S_7;
S_10(:,indici3)=NaN;
S_11=S_10;
S_11(isnan(S_11)) = 0;

signal={'Int selected','B value selected','Peak area','highest
peak';[],[],[],[]};
signal{2,1}=S_11(ind,:)';
signal{2,2}=B_filtered_2_zeros(wl,:)';
%con area
[val,ind1]=min(abs(M.S(1,:)-range(1)));
[val,ind2]=min(abs(M.S(1,:)-range(2)));
signal{2,3}=trapz(M.S(1,ind1:ind2),M.S(2:end,ind1:ind2),2);

l=0;
for kk=1:size(M.S,1)-1
    temp=0;
    [temp,pos]=findpeaks(M.S(kk+1,ind1:ind2));
```

```
    % temp is local maxima and pos the index

    if signal{2,1}(kk,1)>0
        if temp>0
            [signal{2,4}(kk,1) pos2]= max(temp);
            %  signal{2,4}(kk,2)=pos(pos2)+rs-rg;
            signal{2,4}(kk,2)=M.S(1,pos(pos2)+ind1-1);
        else
            signal{2,4}(kk,1)=signal{2,1}(kk,1);
            signal{2,4}(kk,2)=M.S(1,ind);
        end
    else
        l=l+1;
        indici4(l)=kk;
    end
end
temp=B_filtered_2_zeros(wl,:)~=0;
par.BIsel=[B_filtered_2_zeros(wl,temp)' signal{2,4}(temp,1)]; % b and
Int vlaues after p&b-selection
end
```

A.1.2.2 mapSection

```
function res=MapSection(M,signal,dim)

[x, indxa, indxb]=unique(M.C(:,1));
[y, indya, indyb]=unique(M.C(:,2));
linex=min(x):dim(1):max(x);
liney=min(y):dim(2):max(y);
temp=diff(M.C(:,1));
deltaX=min(abs(temp(temp~=0)));
temp=diff(M.C(:,2));
deltaY=min(abs(temp(temp~=0)));
if (size(linex,2)==1 || size(liney,2)==1)
    res{1,1}=[M.C(:,1:2) signal];
    res{3,1}=[];
    res{5,1}=M.S;
    for count=1:size(M.C,1)
        res{3,1}{1,count}=[M.C(count,1)-0.5*deltaX,
M.C(count,2)+0.5*deltaY;...
            M.C(count,1)+0.5*deltaX, M.C(count,2)+0.5*deltaY;...
            M.C(count,1)+0.5*deltaX, M.C(count,2)-0.5*deltaY;...
            M.C(count,1)-0.5*deltaX, M.C(count,2)-0.5*deltaY];
    end
else
    [val indLinex]=min(abs(x-linex));
    [val indLiney]=min(abs(y-liney));
    for i=1:size(indLinex,2)
        X{1,i}=[];
        try
            temp=indLinex(i):indLinex(i+1)-1;
        catch
            temp=indLinex(i):max(indxa);
        end
        for j=1:size(temp,2)
            X{1,i}=[X{1,i}; [M.C(indxb==temp(j),1:2),
signal(indxb==temp(j),1)]];
        end
```

```
    end
    for i=1:size(indLiney,2)
        Y{1,i}=[];
        try
            temp=indLiney(i):indLiney(i+1)-1;
        catch
            temp=indLiney(i):max(indya);
        end
        for j=1:size(temp,2)
            Y{1,i}=[Y{1,i}; [M.C(indyb==temp(j),1:2),
signal(indyb==temp(j),1)]];
        end
    end
    res=cell(1,size(X,2)*size(Y,2));
    count=0;
    for i=1:size(X,2)
        for j=1:size(Y,2)
            count=count+1;
            [temp, iX, iY]=intersect(X{1,i},Y{1,j},'rows');
            res{1,count}=X{1,i}(iX,:);
            res{3,count}=[min(res{1,count}(:,1))-0.5*deltaX,
max(res{1,count}(:,2))+0.5*deltaY;...
                max(res{1,count}(:,1))+0.5*deltaX,
max(res{1,count}(:,2))+0.5*deltaY;...
                max(res{1,count}(:,1))+0.5*deltaX,
min(res{1,count}(:,2))-0.5*deltaY;...
                min(res{1,count}(:,1))-0.5*deltaX,
min(res{1,count}(:,2))-0.5*deltaY];
        end
    end
    for i=1:size(res,2)
        res{5,i}=[M.S(1,:); zeros(size(res{1,i},1),size(M.S,2))];
        for j=1:size(res{1,i},1)
            testx=find(M.C(:,1)==res{1,i}(j,1));
            testy=find(M.C(:,2)==res{1,i}(j,2));
            test=intersect(testx,testy);
            res{5,i}(j+1,:)=M.S(test+1,:);
        end
    end
end
end
```

A.1.2.3 mapSelection

```
function [res,Breal]=MapSelection(res,img,par)

imgX=par.imgX;
imgY=par.imgY;
GLV=0.999;
% image in black white
imgBW=img;
imgBW = im2bw(img, GLV);
dimBW=size(imgBW); % dimensioni max img in pixel
imgBW = imcomplement(imgBW);
B = bwboundaries(imgBW,'noholes');
temp=zeros(size(B,1),1);
for i=1:size(B,1)
```

```
    temp(i,1)=size(B{i,1},1);
end
[val,ind]=max(temp); clear temp
Breal=B{ind,1}; Breal=fliplr(Breal);
Breal(:,1)=imgX(1)+(imgX(2)-imgX(1)).*Breal(:,1)./dimBW(2);
Breal(:,2)=imgY(1)+(imgY(2)-imgY(1)).*Breal(:,2)./dimBW(1);
p1=polyshape(Breal(:,1),Breal(:,2));
res2=[];
if size(res,2)>1
    for i=1:size(res,2)
        p2=polyshape(res{3,i}(:,1),res{3,i}(:,2));
        test=intersect(p1,p2);
        if area(test)==area(p2)
            res2=[res2, res(:,i)];
        end
    end
else
    val=res{3,1}; count=0; res2{5,1}(1,:)=res{5,1}(1,:);
    for i=1:size(val,2)
        p2=polyshape(val{1,i}(:,1),val{1,i}(:,2));
        test=intersect(p1,p2);
        if area(test)==area(p2)
            count=count+1;
            res2{1,1}(count,:)=res{1,1}(i,:);
            res2{3,1}{1,count}=res{3,1}{1,i};
            res2{5,1}(count+1,:)=res{5,1}(i+1,:);
        end
    end
end
res=res2;

end
```

A.1.2.4 TEMimage

```
function [coordum,par,Bsel,TC]=TEMimage(img,par)

imgX=par.imgX;
imgY=par.imgY;
if isempty(par.GLV)
    GLV=0.5;%graythresh(img); %computes a global threshold to convert an
intensity image to a binary image
    par.GLV=GLV;
else
    GLV=par.GLV;
end

% initialization
BLV=par.significance; % boundary limit value - limite per selezione
delle aree da considerare buone

c2=(linspace(min(imgX),max(imgX),size(img(:,:,1),2)))';
r2=(linspace(min(imgY),max(imgY),size(img(:,:,1),1)))';
%two vectors of image's dimensions

% image in black white
imgBW=img;
imgBW = im2bw(img, GLV); %convert image to binary image
```

```
%imgBW{1,i} = imbinarize(img{1,i}, GLV(i,1));
imgBW = imcomplement(imgBW); %image's complement

Bsel=cell(2,1);
TC=[];
coord=[];
temp=1;
B = bwboundaries(imgBW,'noholes');%traces the exterior boundaries of
objects
temp2=bwconncomp(imgBW);
PROP  = regionprops(temp2, 'area','MajorAxisLength','MinorAxisLength');
AREA=cat(1, PROP.Area);
FerM=cat(1, PROP.MajorAxisLength);
Ferm=cat(1, PROP.MinorAxisLength);
Pixnm=(imgX(2)-imgX(1))./size(img,2); % conversione µm/pixel
for i = 1:length(B)
    mediaDimensione=AREA(i,1);
    if mediaDimensione>=BLV
        Bsel{1,temp}=B{i}; %figure; imshow(handles.img{1,k})
        try
            Bsel{2,temp}=img(min(B{i}(:,1))-10:max(B{i}(:,1))+10,...
                min(B{i}(:,2))-10:max(B{i}(:,2))+10);
        catch
            Bsel{2,temp}=img(min(B{i}(:,1)):max(B{i}(:,1)),...
                min(B{i}(:,2)):max(B{i}(:,2)));
        end
        TC(temp,1)=AREA(i,1); % area della particella trovata, in pixel
        TC(temp,2)=FerM(i,1).*(Pixnm*1e3); % max Feret, in nm
        TC(temp,3)=Ferm(i,1).*(Pixnm*1e3); % min Feret, in nm

coord(temp,2)=round((max(Bsel{1,temp,1}(:,1))+min(Bsel{1,temp}(:,1)))/2)
;
coord(temp,1)=round((max(Bsel{1,temp,1}(:,2))+min(Bsel{1,temp}(:,2)))/2)
;
        temp=temp+1;
    end
end
% coordinates in um
coordum=[c2(coord(:,1),1) r2(coord(:,2),1)];
% coordum(:,:)=fix(coordum(:,:)*10)/10;
dimBW=size(imgBW); % dimensioni max img in pixel
for i=1:size(Bsel,2)
    Bsel{1,i}=fliplr(Bsel{1,i});
    Bsel{1,i}(:,1)=imgX(1)+(imgX(2)-imgX(1)).*Bsel{1,i}(:,1)./dimBW(2);
    Bsel{1,i}(:,2)=imgY(1)+(imgY(2)-imgY(1)).*Bsel{1,i}(:,2)./dimBW(1);
end
end
```

A.1.2.5 SignalParticle

```
function [res]=SignalParticle(res,Cnp,par,Bounds,Geom)
res2=[];
if size(res,2)>1
        for i=1:size(res,2)
        xm=min(res{3,i}(:,1)); xM=max(res{3,i}(:,1));
        ym=min(res{3,i}(:,2)); yM=max(res{3,i}(:,2));
        indx1=find(Cnp(:,1)>xm);% no valore, ma indice
        indx2=find(Cnp(:,1)<xM); indx=intersect(indx1,indx2);
```

```
        indy1=find(Cnp(:,2)>ym);
        indy2=find(Cnp(:,2)<yM); indy=intersect(indy1,indy2);
        ind=intersect(indx,indy); %prendo gli indici in comune
        res{4,i}=Cnp(ind,:); % salva le coordinate delle particelle
trovate
        try
            res{6,i}.Bounds=Bounds(1,ind);
            res{6,i}.Geom=Geom(ind,:);
        catch
        end
        temp=sum(res{1,i}(res{1,i}(:,3)>par.st,3));
        %sto prendendo le intensità e le filtro su b tramite st=0:
prendo solo
        %i valori che sono maggiori di zero

        res{2,i}={'particles found',['overall signal over
',num2str(par.st)],'Signal / Particle';...
            size(ind,1),temp,0};
        if (size(ind,1)>0 && temp > 0 )
            res{2,i}{2,3}=temp/size(ind,1);
            res2=[res2 res(:,i)];
        end
    end
else
    res{6,1}.Bounds=[]; res{6,1}.Geom=[];
    for i=1:size(res{3,1},2)
        xm=min(res{3,1}{1,i}(:,1)); xM=max(res{3,1}{1,i}(:,1));
        ym=min(res{3,1}{1,i}(:,2)); yM=max(res{3,1}{1,i}(:,2));
        indx1=find(Cnp(:,1)>xm);
        indx2=find(Cnp(:,1)<xM); indx=intersect(indx1,indx2);
        indy1=find(Cnp(:,2)>ym);
        indy2=find(Cnp(:,2)<yM); indy=intersect(indy1,indy2);
        ind=intersect(indx,indy);
        res{4,1}=[res{4,1}; Cnp(ind,:)];
        try
            res{6,1}.Bounds=[res{6,1}.Bounds, Bounds(1,ind)];
            res{6,1}.Geom=[res{6,1}.Geom; Geom(ind,:)];
        catch
        end
    end
    temp=sum(res{1,1}(res{1,1}(:,3)>par.st,3));
    res{2,1}={'particles found',['overall signal over
',num2str(par.st)],'Signal / Particle';...
        size(res{6,1}.Geom,1),temp,0};
    %         if (size(ind,1)>0 && temp > 0 )
    res{2,1}{2,3}=temp/res{2,1}{2,1};
    res2=res;
    % size(res{6,1}.Bounds), size(res{6,1}.Geom)%[res2 res(:,i)];
    %         end
end
res=res2;
end
```